TESIS DE LA UNIVERSIDAD DE ZARAGOZA

2013

131

Carlos Ginestra Díaz

# Characterization of scintillating bolometers for particle detection and installation of a bolometric test facility in the University of Zaragoza

Departamento
Física Teórica

Director/es
García Abancens, Eduardo



ISSN 2254-7606

Prensas de la Universidad
Universidad Zaragoza

Universidad Zaragoza
1542

Tesis Doctoral

# CHARACTERIZATION OF SCINTILLATING BOLOMETERS FOR PARTICLE DETECTION AND INSTALLATION OF A BOLOMETRIC TEST FACILITY IN THE UNIVERSITY OF ZARAGOZA


Autor

Carlos Ginestra Díaz

Director/es

García Abancens, Eduardo

**UNIVERSIDAD DE ZARAGOZA**

Física Teórica


2013

# Characterization of scintillating bolometers for particle detection and installation of a bolometric test facility in the University of Zaragoza

Memoria presentada por
**Carlos Ginestra Díaz**
para optar al grado de
Doctor en Física

Laboratorio de Física Nuclear y Astropartículas
Área de Física Atómica, Molecular y Nuclear
Departamento de Física Teórica
**Universidad de Zaragoza**

Septiembre 2013

# Contents

# Preface

In 1800 F. W. Herschel discovered the invisible infrared radiation by the temperature rise produced in a thermometer exposed to it. That was maybe the first time that radiation was detected by a thermal measurement. It was the American astronomer S. L. Langley in 1881 who invented the bolometer to measure radiation from celestial objects [1]. This first bolometer consisted of two thin metal strips forming a Wheatstone's Bridge being just one of them exposed to a radiation source. The irradiation of one of the strips induced a temperature increase that was measured as a change of resistance with a Galvanometer. The new device was named as the Greek translation of ray-meter ($\beta o \lambda \eta$ – $\mu \epsilon \tau \rho o \nu$). After some development of this new technique, F. Simon proposed and tested in 1935 the use of such devices at low temperatures, increasing the response in several orders of magnitude and being able to detect individual particles [2]. A general theory of bolometers performance applicable to all ordinary types of bolometers was developed by R. C. Jones in 1953 [3]. After several years using bolometers as infrared detectors, in the 80s, the good performance of bolometers regarding efficiency and energy resolution, made them being proposed and used as particle detectors, for example, as X–rays spectrometers [4] and for rare decays [5]. Currently bolometers are used in a wide range of applications from basic research to industry.

The Nuclear and Astroparticle Physics Research Group (GIFNA) of the University of Zaragoza, being aware of the potentiality of bolometric detectors, established a collaboration in 1997 with the group of Spectrométrie Thermique pour l'Astrophysique et la Physique (STAP) of the Institut d'Astrophysique Spatiale (IAS) of Orsay to measure with bolometers (designed and built by the French group) in the old facilities of the Canfranc Underground Laboratory (LSC), aiming to perform dark matter searches. Within this collaboration, called ROSEBUD (Rare Objects SEarch with Bolometers UndergrounD), numerous bolometers and scintillating bolometers were measured underground since 1999. For instance, in the LSC, ROSEBUD carried out the first light versus heat dark matter search with

a $CaWO_4$ scintillating bolometer [6] and several bolometric WIMP searches using simultaneously different absorbers (Ge, $Al_2O_3$ and $CaWO_4$ in [7] and $Al_2O_3$ and BGO in [8]). Recently, new targets, not only for dark matter searches but also for neutron spectroscopy and other nuclear and particle physics experiments, have been developed and tested at IAS and/or LSC. The GIFNA group has also established a collaboration with the Advanced Detectors Group (ADG) of the Lisbon University (UL) for the loan and operation in Zaragoza (and in the long-term in the LSC) of a dilution refrigerator (property of UL) to test bolometers and scintillating bolometers to be developed in Zaragoza.

This thesis presents the characterization carried out at IAS and LSC of several scintillating bolometers in the frame of the ROSEBUD collaboration and the installation and tuning of a cryogenic facility at Zaragoza to test bolometers in the frame of the collaboration with the UL.

The report starts (chapter 1) with the description of a bolometer, introducing the physics of the particle detection processes and how bolometers and scintillating bolometers work. In chapter 2 they are reviewed the applications of massive bolometers in the field of nuclear and particle physics; thanks to their excellent performance, bolometers are being used in experiments aiming to reveal some of the frontier topics in physics as dark matter, neutrino physics and other rare event searches.

The description of the experimental setups (dilution refrigerator, electronics and data acquisition, radioactive sources, etc.) used in the works carried out within the ROSEBUD collaboration in the laboratories of the IAS and the LSC is presented in chapter 3. Chapter 4 describes the preliminary analysis of the digitized pulses obtained from the bolometers.

Chapter 5 presents the characterization of scintillating bolometers of $SrF_2$, LiF, enriched $^6$LiF, LGBO, BGO and $Al_2O_3$ and their physics applications. In chapter 6 it is described the installation and tuning of a cryogenic facility in the University of Zaragoza as a new bench to test bolometers and scintillating bolometers developed there. Finally they are listed the conclusions of this thesis.

# Chapter 1

# Bolometry and scintillating bolometry

The first chapter of this thesis is devoted to describe how bolometers and scintillating bolometers work. They are introduced the concept of particle detection and the physical effects produced by the different kind of particles interacting in the material that constitutes the detector (section 1.1). Then it is explained the principle of operation of an ideal bolometer (section 1.2), describing its main components: the absorber (section 1.2.1) and the phonon sensor (section 1.2.2). The operation of the phonon sensors used in this work is described in section 1.2.3, and the physical limit for the energy resolution of such devices and the intrinsic noise contributions are discussed in section 1.2.4. Thermal models that better explain real bolometers are considered in section 1.2.5. Finally we present an introduction to inorganic scintillators (section 1.3.1) and we explain how scintillation light is collected by a secondary bolometer in the hybrid detector configuration known as scintillating bolometer (section 1.3.2).

## 1.1 Particle detection

A particle detector is a device in which a single particle is able to produce a measurable signal. The basic principle of detection consists in inducing and registering the change produced in a medium (liquid, solid or gaseous, depending on the detector) when a particle interacts with it. The alteration of that medium is converted into a measurable signal, from which information of the impinging particle can be deduced by a kind of reverse engineering process. For that, it is necessary to know and understand the interaction mechanisms of particles with matter.

Particles see matter in terms of its physical constituents, atoms composed by nuclei and electrons (and its corresponding subatomic particles). The nature of the interactions depends on the type and characteristics of the incident particle and the properties of the target material. Probability terms are involved in the process governed by the laws of quantum mechanics and the basic forces of nature. The dominant processes induced by each kind of particle in matter are briefly described in next paragraph.

Heavy charged particles interact mainly through two mechanisms: inelastic collisions with the atomic electrons of the material or elastic scattering from nuclei, although other processes as emission of Cherenkov radiation, nuclear reactions or bremsstrahlung radiation can also occur. These particles suffer many interactions while they go through matter being the final effect a cumulative result. In the interaction of electrons and positrons, bremsstrahlung, i.e., the emission of electromagnetic radiation arising from scattering in the electric field of nucleus, becomes competitive with collisions (specially at high energies) due to their small mass. The interaction of photons with matter is completely different from that of charged particles. In this case, the dominant processes are photoelectric effect, Compton scattering and pair production. These mechanisms remove the photon from the incident beam, either by complete absorption or scattering. Finally, neutrons mainly interact through the strong force with nuclei by mean of several nuclear processes depending on its energy: elastic scattering from nuclei, inelastic scattering, neutron capture reactions, fission, or hadron shower production in the very high energy region. All these mechanisms are explained in [9].

When a particle interacts with a detector it transfers some or all of its energy to the medium, resulting in some form of excitation. The excitation produced in the atoms of the detector can be of several types: ionization of electron-ion or electron-hole pairs, excitation of phonons, breakup of Cooper pairs in superconductors,

formation of superheated droplets in superfluids, excitations of optical states, etc. Each excitation mechanism has its properties but not all them are effective for particle detection. The excitation produces finally some kind of measurable magnitude, being the most commonly used heat, charge and light. Detectors are usually designed to detect one of these forms of energy, but in last years, hybrid detectors in which two magnitudes are simultaneously measured have emerged. In next section we will follow the path of the energy from its deposition in a crystal detector to its detection.

### 1.1.1 Energy partition in crystals

In crystal detectors, the energy transferred to the target material can interact with the nuclear ($S_n$) or the electronic ($S_e$) system. Depending on the systems involved, the energy follows different processes before being detected in form of charge, light or heat, or being stored in undetectable energy states. A simplified scheme of such processes is depicted in figure 1.1. All the processes shown occur in a few picoseconds.

The particle interactions with the crystal lattice, the nuclear system, consist in elastic scattering off the nuclei, producing vibrational excitations that propagate along the crystal as phonons in a complex thermalization process briefly explained below that finally is manifested in form of heat. Depending on its energy, the impinging particle could produce structural defects in the lattice or even sputtered atoms in the case of heavy ion interactions. These defects can constitute energy traps.

The energy released in the electronic channel usually produces ionization in the target, exciting electron-hole pairs. If these charge carriers are not collected by an external electric field, they can be absorbed in the medium producing phonons in the lattice or can recombine either in a radiative form, emitting scintillation photons, or in a non-radiative form. Some photons can be reabsorbed by the crystal in form of phonons. In this channel there exist also trapping phenomena of the carriers in meta-stable energy levels, impurities or defects. There are energy transfers between the nuclear and the electronic channels that, for simplicity, are not shown in figure 1.1. Only the energy appearing as heat at the bottom will contribute to the heat signal.

The first excited phonons in the crystal are very high energy phonons (Debye phonons) that follow a thermalization process in which they are divided into phonons of lower energies until they are able to cross the whole crystal without decaying.

These are called ballistic phonons and they interact with the surfaces of the crystal, where they can be detected by athermal phonon sensors (glued or deposited into the surface) or are reflected and finally thermalized in the crystal through interactions with crystal defects, with surfaces or with other phonons, reaching eventually a new thermal equilibrium state of the crystal at a temperature higher than the initial one. This process as well as the energy partition in crystals are widely explained in several references (see for example [10, 11]).

Phonons can be detected as ballistic phonons (non-equilibrium mode) or as the temperature increase produced in the crystal when they thermalize (thermal or equilibrium-mode). Ballistic phonons can be detected with fast sensors and, due to its ballistic behavior, information as the interaction position or even directionality could be obtained. Thermal sensors are slower since they wait for the full thermalization of the phonons, with time responses typically between 0.1 and 10 ms. These sensors work as thermometers and offer better energy resolution (in principle they offer the ultimate in energy resolution) since they collect many independent carriers in a single event. Thermal detectors working in this equilibrium mode are usually called perfect calorimeters. Charge carriers can be collected by an electric field and scintillation photons (light) can be detected with photomultiplier tubes, photodiodes, bolometers, etc.

The incident particle energy partition among the different detectable forms of energy (mainly charge, light and heat) depends on how the particle interacts with the crystal, on whether it does it with the nuclear system or with the electronic one, on the density of deposited energy, etc. These differences allow to discriminate between different types of particles comparing the amount of energy collected in two or more different forms.

In any case, most of the energy flows into the phonon or heat channel, while the ratio of energy producing charge is about 30% and scintillation light just around a 10% in the best scintillating materials [12]. Moreover, the energy required to produce a phonon is of the order of the Debye energy ($\sim$10 meV), while, for instance, 3 eV are needed to produce a electron-hole pair in Ge and around 25 eV to produce a scintillation photon in NaI, which are good examples of ionization and scintillation detectors respectively. The larger fraction of energy used and the higher number of carriers of the heat channel place the phonon mediated detectors in an advantageous position (energy threshold and resolution), but it requires to operate them at very low temperatures.

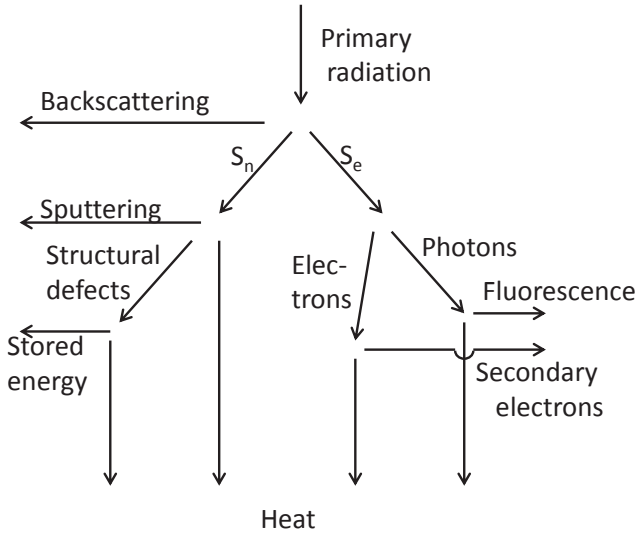


Figure 1.1: *Simplified scheme of the energy partition of an interacting particle inside a crystal detector [11].*

## 1.2 Heat collection: bolometers

A thermal equilibrium bolometer (from now on, for simplicity, we will refer to it as bolometer) is basically a heat detector, that is, a device able to detect the temperature increase produced by the thermalization of phonons after a particle interaction in a crystal. It basically consists of three parts depicted in figure 1.2a: an absorber, where the interaction happens, that absorbs and thermalizes the energy, a thermometer perfectly coupled to the absorber to detect its temperature increase, and a weak thermal link to a heat sink that keeps the absorber at a constant base temperature in absence of signal and returns it to that temperature after an interaction. The absorber is characterized by its heat capacity C, the thermal link by its thermal conductivity G and the heat sink by its constant temperature $T_b$.

When an amount of energy $\Delta$E is deposited in the absorber in an instant $t_0$, its temperature increases by $\Delta T = \Delta E/C$ and decays back to $T_b$ with a time constant $\tau = C/G$. The evolution of temperature with time in the absorber is shown in figure 1.2b and follows the expression

$$T(t > t_0) = T_b + \frac{\Delta E}{C} \exp\left(-\frac{G}{C}(t - t_0)\right) \tag{1.1}$$

Very small values of C are needed to obtain a measurable temperature increase. To achieve this goal, bolometers are usually cooled down to very low temperatures,

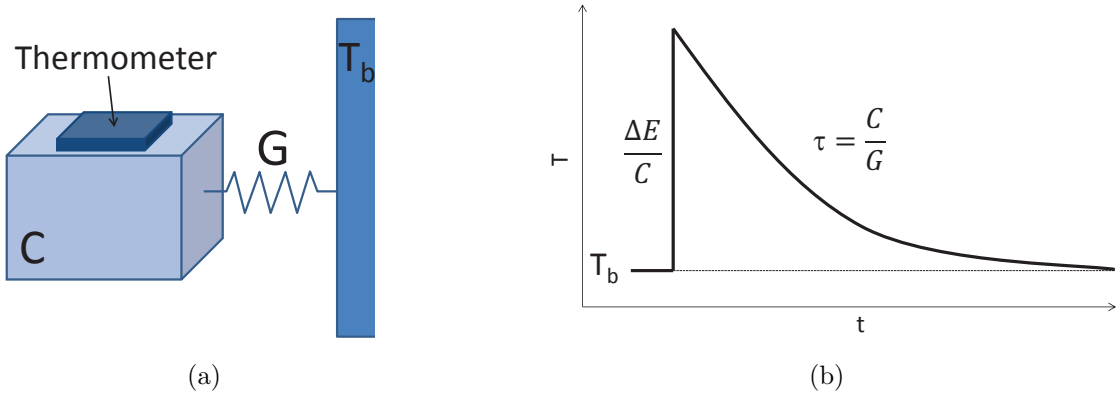


(a) (b)

Figure 1.2: *(a) Ideal simple bolometer consisting of an absorber of heat capacity $C$ with a thermometer coupled to it, and connected to a heat sink at temperature $T_b$ by a weak thermal link of conductivity $G$. (b) Its temperature response to an energy deposition $\Delta E$.*

close to the absolute zero, where the heat capacity is minimal. As a rough example, considering $C \sim R = 5.19 \cdot 10^{10}$ GeV/(K·mol) at room temperature, a particle depositing 1 MeV of energy in one mol of atoms would produce a temperature increase of about $10^{-14}$ K, an undetectable magnitude. But at temperatures of the order of tens of mK, C could be reduced down to $\sim 1$ GeV/(K·mol), producing a temperature increase of $\sim 0.1$ mK with the same deposited energy.

### 1.2.1 Absorber materials

The material used as absorber in a bolometer is required to have a heat capacity $C$ as low as possible in order to maximize the thermal response. The heat capacity, is an extensive property of matter that specifies the amount of heat required to change the temperature of a body by a certain amount (see equation 1.2, where $U$ is the internal energy of the body) and has different contributions.

$$C = \frac{\partial U}{\partial T} \tag{1.2}$$

The contribution of the lattice vibrations to the heat capacity was obtained by Debye considering the atoms in a solid as a collection of oscillators following a density of states as function of frequency $D(f) = Vf^2/2\pi^2 v^3$, being $V$ the volume and $v$ the constant velocity of sound. The Debye heat capacity for temperatures much higher than the Debye temperature ($T \gg \Theta_D$) approaches the classical value of $3Nk_B$ from the Dulong-Petit law, while at very low temperatures ($T \ll \Theta_D$) it

follows the well-known expression

$$C_l \cong \frac{12}{5}\pi^4 N k_B \left(\frac{T}{\Theta_D}\right)^3 \tag{1.3}$$

with $N$ the number of atoms and $k_B$ the Boltzmann constant.

Other contribution is that from the free electrons, particles responsible of the conductivity in metals, that can be treated as a Fermi gas. Following the Fermi statistics, it is found that at low enough temperature ($k_B T \ll T_F$), the heat capacity of a free electron gas can be written as

$$C_{el} = \frac{1}{2}\pi^2 N k_B \frac{T}{T_F} \tag{1.4}$$

being $T_F$ the Fermi temperature. The contribution of free electrons to $C$ is negligible at room temperature but it becomes important at very low temperatures.

In superconductor materials, the electronic contribution to the heat capacity follows an exponential function with argument proportional to $\propto (-T^{-1})$. They can present low heat capacity values, but during the phonon thermalization Cooper pairs can be easily broken loosing part of the energy in these quasi-particles that are not detected, so that superconductors are not a preferred material as absorber. Ferromagnetic and paramagnetic materials also contribute to $C$ with the magnetic degrees of freedom.

From this it follows that dielectric and diamagnetic materials are the most used to build bolometers since they just have the lattice contribution, that at low temperatures scales with $T^3$. This is not a very restrictive condition, so absorbers can still be chosen from a wide range of materials. This is a great advantage because it allows to choose an appropriate crystal depending on the use of the bolometer: for example, targets with nuclei that favor certain interactions as in the case of dark matter WIMPs searches or spectroscopy applications, or targets containing double beta decay nuclei that can be used in searches of the type source=detector.

An important criterion to take into account is the amount of absorber, since the heat capacity scales with it. By this reason, very large bolometers can not be built and experiments needing large detection masses resort to matrix detectors consisting of several relatively small bolometers.

### 1.2.2 Phonon sensors

The phonon sensors used in bolometers are based on a magnitude that changes with temperature, usually an electric resistance (but other magnitudes can be used). To measure the small temperature variations, high-sensitivity thermistors are needed, which means measuring magnitudes that change sharply with temperature. Another important consideration for bolometer thermistors is the heat capacity, that has to be kept as low as possible since its value is added to the absorber heat capacity. The thermistors commonly used in massive bolometers are superconductors kept at their superconducting-to-normal transition edge or semiconductor sensors properly doped close to the metal-insulator transition. They are described in the next paragraphs, emphasizing in the type of sensors used in this work (NTD-Ge semiconductor sensors). Other devices based on changes of magnetization are being used and show excellent energy resolution. These thermistors, as for example Metallic Magnetic Calorimeters (MMC) and Magnetic Penetration Thermometers (MPT), are so far installed only with small absorbers (less than 1 $mm^3$), but they show excellent performance in applications as X–ray detection, $\alpha$ spectroscopy and measurement of beta decay and electron capture of some nuclei [13–15].

#### Superconductor thermistors

The Transition Edge Sensors (TES) are thin superconducting films (usually tungsten) deposited on the absorber surface and operated around the temperature of their superconducting-to-normal transition, although bilayer films formed by a normal metal and a superconductor are also used. The latter configuration allows to tune the transition temperature by means of the layer thicknesses, fitting it to the operation temperature of detectors. TES are intrinsically fast detectors, so they can also detect ballistic phonons. The thermal pulse is detected by changes in the feedback current measured by a SQUID. These are very sensitive thermistors since their resistance varies from zero up to many k$\Omega$ (using meander lines) in a very narrow temperature interval. A drawback of these sensors is the short range of the linear response, that limits the range of detected energies. TES are versatile thermistors: they can be mounted in microbolometers for IR detection or X–ray space applications [16, 17], or in massive bolometers in large scale rare events search experiments [18, 19]. Figure 1.3 shows the typical dependence of resistance with temperature in a TES.

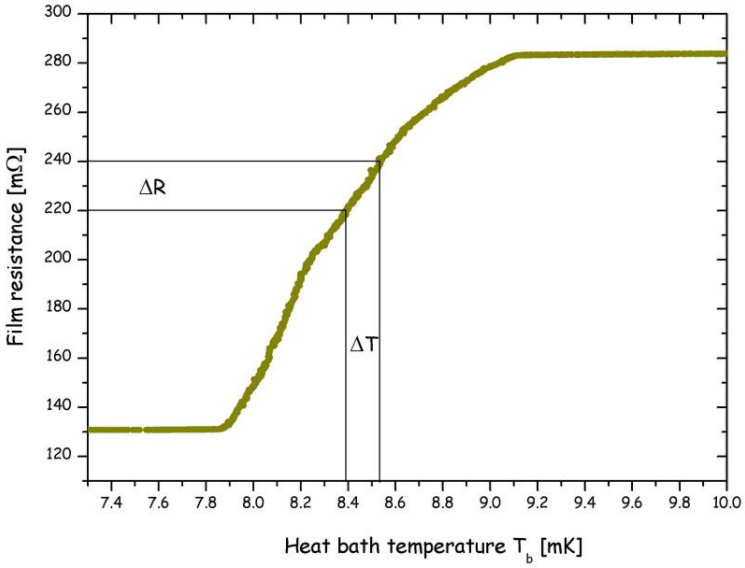


Figure 1.3: *Dependency of resistance with temperature in a TES device of tungsten in the region of the superconducting transition [20].*

### Semiconductor thermistors

Semiconductor thermistors consist of a small semiconductor crystal, usually Si or Ge, doped in a concentration just below the metal-insulator transition, and slightly compensated to enhance the conductivity. In these conditions, the conductivity of the thermistor is highly dependent on the temperature. The uniformity of the dopant distribution and the dopant concentration are critical parameters.

The expected temperature dependence of the resistance in these doped semiconductor devices for temperatures below 4 K, which follow the regime known as "variable range hopping" (for a detailed description of the theory see [21]), is

$$R(T) = R_0 \exp\left(T_0/T\right)^n \tag{1.5}$$

where $R_0$, $T_0$ and $n$ are parameters that depend on the doping concentration and must be experimentally measured for each sensor. The value of $n$ was found to be 0.5 [22], reducing the dependence to two parameters, $R_0$ and $T_0$. This dependence can be observed in figure 1.4a for a specific sensor. The physics of doped semiconductor materials, closely related with its metal-insulator transition, is widely explained in [11] and references therein.

There are some processes to introduce impurities in semiconductors. Such processes are delicate and must be precise to obtain uniformity in the doping density. Doped semiconductor thermistors can be obtained by ion implantation or using the melt doping technique, but the Neutron Transmutation Doping (NTD) allows a

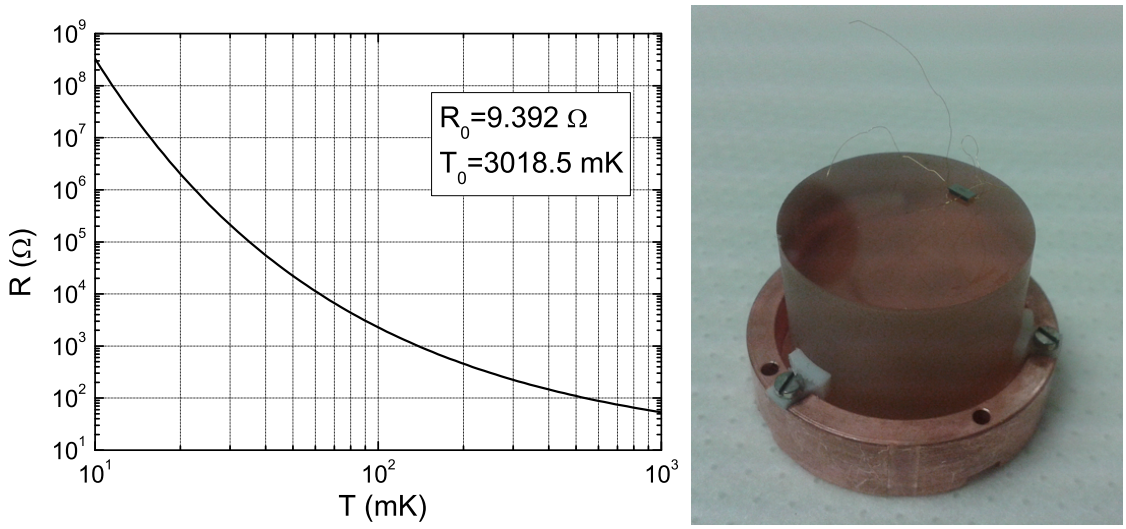


(a) (b)

Figure 1.4: *In (a) it is displayed the temperature dependence of resistance for a particular Ge–NTD sensor, following the equation 1.5 with* $n = 0.5$. *In (b) it is shown a Ge-NTD sensor glued to a* $ZnWO_4$ *absorber. Thin gold wires can also be observed.*

high uniformity in large volumes and is a very useful technique with an excellent reproducibility.

The NTD technique consists in exposing the crystal to a controlled thermal neutron flux in order to induce neutron captures in some isotopes, and to transmute them into n-type and p-type impurities. In the case of Ge, the most used material with this technique, the induced reactions are noted in table 1.1. The uniformity in the bulk volume of Ge is guaranteed since the cross sections of these processes are low, of the order of $\sim$1 barn. To obtain the thermistor, a prism of some $mm^3$ is cut from the Ge batch. The ohmic contacts are implanted as heavily doped regions and gold pads are evaporated on them. The connections are usually thin gold wires attached to the contacts (see figure 1.4b). The device is finally glued with epoxy to the absorber surface. The amount of epoxy allows to control the coupling properties.

### 1.2.3 Polarization and operation

As previously stated, in this work we used NTD–Ge semiconductor sensors. In this section we will describe the typical bias and readout circuits used with these sensors.

The thermistor attached to a bolometer absorber is biased with a steady current in order to create a voltage difference to be measured. The bias current is applied

| Isotope | Abundance (%) | Reaction | Dopant type |
|---|---|---|---|
| $^{70}$Ge | 20.5 | $^{70}$Ge(n,$\gamma$)$^{71}$Ge$\rightarrow^{71}$Ga | p |
| $^{72}$Ge | 27.4 | $^{72}$Ge(n,$\gamma$)$^{73}$Ge | – |
| $^{73}$Ge | 7.8 | $^{73}$Ge(n,$\gamma$)$^{74}$Ge | – |
| $^{74}$Ge | 36.5 | $^{74}$Ge(n,$\gamma$)$^{75}$Ge$\rightarrow^{75}$As | n |
| $^{76}$Ge | 7.8 | $^{76}$Ge(n,$\gamma$)$^{77}$Ge$\rightarrow^{77}$As$\rightarrow^{77}$Se | n |

Table 1.1: *Neutron capture reactions in natural Ge isotopes in NTD process [23].*

through a load resistor $R_L$ according to a circuit as those displayed in figure 1.5. $R(T)$ is the thermistor resistance and $V_b$ a constant voltage generator.

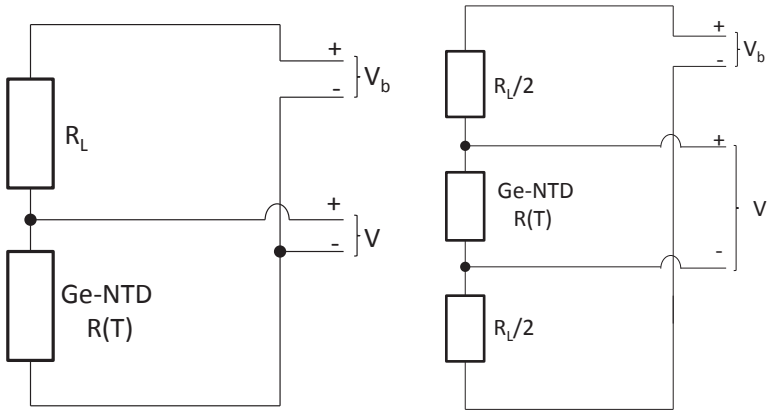


(a) (b)

Figure 1.5: *In (a) it is shown a typical electric circuit of a semiconductor sensor attached to a bolometer. Figure (b) shows a similar circuit operating in a differential mode.*

The voltage $V$ across the sensor produces a dissipation Joule power that affects the system increasing the base temperature $T_b$ up to another steady temperature $T > T_b$, and changing the voltage $V$ itself in a feedback effect called electrothermal feedback (ETF). The result is that the V-I curve in the sensor looses linearity from a certain applied bias (see figure 1.6). In the static regime, i.e., without particle interactions, the lack of linearity is observed in the curves shown in 1.6a obtained at different temperatures. In the dynamic regime, the ETF affects the output signal reducing the amplitude and shortening the return time constant. The calculations of this effect and further explanations are in references [24, 25].

The static working point of a thermistor at a certain temperature is determined by the intersection of the $V(I)$ curve with the line $V = V_b - I \cdot R_L$, as can be seen in

figure 1.6b. Higher pulse amplitudes are achieved with higher $V_b$ (with the maximum limit observed in the V-I curves, called inversion point), but a higher $V_b$ also implies an increase of the base temperature and consequently a decrease of the response. A compromise must be reached, and finally the choice of the optimal working point is usually based on the experimental behavior of the bolometer, searching for a maximum signal-to-noise ratio.

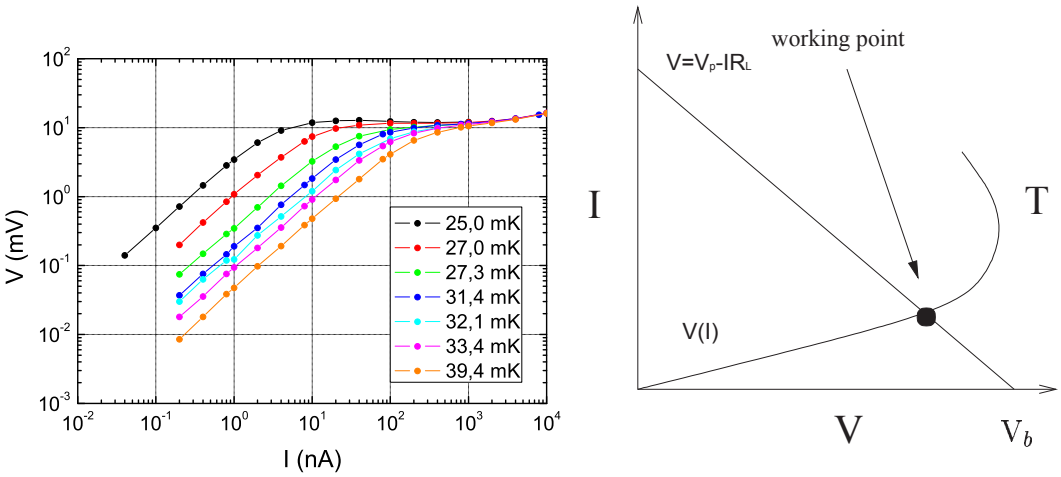


(a) (b)

Figure 1.6: *(a) V-I curves measured for a Ge–NTD sensor at several temperatures. (b) Typical load curve and working point of operation of a polarized thermistor.*

As we have already seen, the energy $E$ deposited in the absorber is converted into a temperature increase $\Delta T$. Thermistors are usually characterized by its sensitivity defined as $A = |(d\log R)/(d\log T)|$, which is measured as a voltage change $\Delta V$. Applying a linear approximation to use finite variations as infinitesimal ones, we can estimate the relationship between $\Delta V$ and the deposited energy $E$:

$$\Delta V = \frac{R_L}{R_L + R} V \frac{\Delta R}{R} = \frac{R_L}{R_L + L} V A \frac{\Delta T}{T} = \frac{R_L}{R_L + L} V A \frac{E}{CT} \tag{1.6}$$

### 1.2.4 Ultimate resolution and noise contributions

There exists an intrinsic limit in the energy resolution $\Delta E$ of bolometers due to thermodynamic considerations that can be expressed as

$$\Delta E = \sqrt{k_B T^2 C(T)} \tag{1.7}$$

This value can be understood as the thermodynamic fluctuations of the number of thermal phonons exchanged with the heat sink through the thermal conductance $G$.

According to our model of figure 1.2a, the number of phonons in the absorber at thermal equilibrium can be expressed as

$$N = \frac{E}{\epsilon} = \frac{C(T)T}{k_B T} = \frac{C(T)}{k_B} \tag{1.8}$$

where $\epsilon$ is the mean phonon energy, equal to $k_B T$. Assuming Poisson statistics we obtain

$$\Delta E = \Delta N k_B T = \sqrt{N} k_B T = \sqrt{k_B T^2 C(T)} \tag{1.9}$$

A dimensionless constant factor $\xi$ is usually added multiplying the equation 1.9. It accounts for departures of Poisson statistics and can take values of some units; it depends on some particular parameters of the detector (thermistor, G, C(T)).

It is noticeable that the ultimate energy resolution is independent on the energy of the interaction $E$, while $C$ is again a relevant parameter: materials with low heat capacity have a better ultimate energy resolution besides having a greater response. As an example, in a pure $SrF_2$ crystal of 50 g at 20 mK, the theoretical limit in the energy resolution assuming $\xi = 1$ is $\Delta E = 8$ eV.

The thermodynamic limit in resolution is hard to reach since there exist many other sources of noise that can be classified as extrinsic and intrinsic sources. The former group corresponds to noises coming from the surrounding equipment of the detector and are characteristic of each experimental setup (cryogenics, mechanical vibrations, electromagnetic pick-up, readout devices, etc.), and they are mentioned in chapters 3 and 6. Intrinsic sources of noise are those arising from the detector itself and the most important terms are described below.

- **Johnson noise:** It is a white noise, affecting equally all the frequency spectrum, caused by thermal agitation of the charge carriers (electrons) in resistors. The most important contribution of Johnson noise arises from the thermistor, with a power spectrum value of $\sqrt{4k_B RT}$. The contribution of the load resistor of the polarization circuit is proportional to $R/(R_L + R)$, so it can be done negligible choosing a large enough $R_L$ value [22].

- **Branching fluctuations:** An important noise contribution in phonon mediated detectors is that coming from the statistical energy partition in the thermalization process between the different energy channels, including energy losses in defects or meta-stable energy levels. This effect has been observed as an anti-correlation in the energy partition between heat and light in some scintillating bolometers [12, 26].

- **Other sources:** Other source of noise can be inhomogeneities in the detector leading to position-dependent fluctuations. These effects can appear specially in large detectors. A study of such effect in a 53 g $SrF_2$ bolometer is presented in section 5.1.3 of this thesis.

### 1.2.5 More realistic models

In the previous discussion, we have considered an ideal and simple thermal model of bolometer, represented in figure 1.2a, usually called monolithic thermal model. This model works well enough to understand the general behavior of a bolometer, but further considerations must be taken into account to obtain more precise results from the theoretical model. As a first step, the thermistor can not be considered as part of the absorber, and a thermal conductance $G_{abs-ph}$ appears between both elements that depends on the glue and method used to couple the thermistor to the absorber.

As shown in figure 1.6a, the V-I curves show deviations from linearity, specially at low temperatures. Two explanations are usually proposed apart from the previously mentioned electrothermal feedback. The first one is that the thermistor resistance would be affected by a electric field effect, introducing in the resistance a dependence on the electric field across the thermistor. The second explanation is usually called the hot-electron effect: it consists in a thermal decoupling between the lattice phonons and the electrons that becomes relevant at low temperatures; this effect is characterized by a thermal conductance $G_{e-ph}$ between the two systems with a exponential dependency on the temperature $T^{\alpha}$ with $\alpha \simeq 4$ [27, 28].

A more realistic model could be that depicted in figure 1.7, which considers three subsystems or nodes in the bolometer: the electronic system of the thermistor, its phononic system, and the absorber. The polarization power $P$ would be applied to the electronic system and the dynamic power $W$ from the energy deposition to the absorber. The model can be adapted to the particular configuration of the detector, and the one shown corresponds with most of the bolometers used in this thesis, with double thermalization through the absorber and the thermistor. To solve the model, a thermal equation is obtained from each node, reducing the problem to a differential equations system, including the resistance and power equations with their non-linear effects mentioned above. The values of the different heat capacities ($C_i$) and thermal conductances ($G_i$), and other input parameters must be well known to derive realistic results and are usually measured experimentally. This kind of model has been applied in several works obtaining results in reasonable agreement with

experimental performance of the corresponding bolometers [25, 27–29].

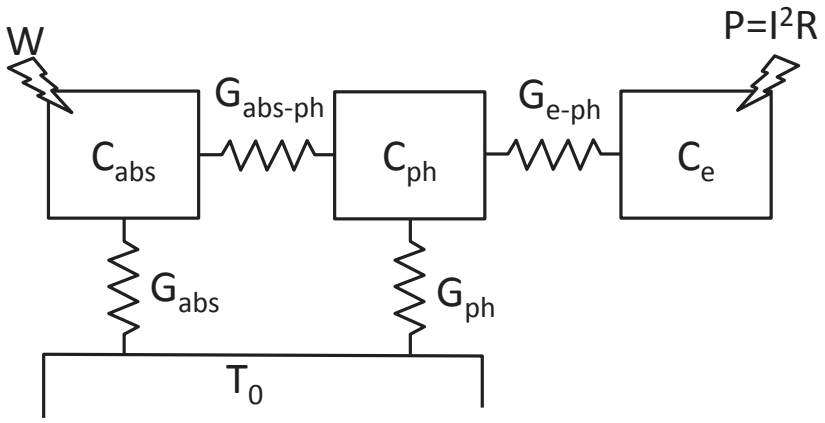


Figure 1.7: *Diagram of a more realistic thermal model of a bolometer considering the absorber as a different system from the thermistor and considering also a decoupling between the phononic and electronic systems of the thermistor.*

## 1.3 Scintillating bolometers

As mentioned previously, a fraction of the energy transferred by a particle interaction flows into energy channels not detectable with phonon sensors (see figure 1.1). However, it is possible to detect a secondary energy channel (charge or light) besides the heat in bolometers. The term scintillating bolometer refers to detectors that are capable of detecting simultaneously the heat and the scintillation light produced in a scintillating absorber, allowing particle identification through the heat/light signal ratio.

In this section, we are going to briefly explain the scintillation mechanism in an absorber and its properties, and then the design, evolution and performances of scintillating bolometers.

### 1.3.1 Inorganic scintillators

Scintillation is a property of some materials by which they emit faint light flashes when they are exposed to certain radiation. Scintillating materials are usually classified in six types: organic crystals, organic liquids, plastics, inorganic crystals,

gases and glasses. In this work, we are interested in inorganic scintillators, in which the scintillation mechanism depends on the energy states of the crystalline structure.

When electrons of an inorganic scintillator absorb enough energy to jump the energy gap that separates the valence and conduction bands, electrons of the valence band can reach the conduction band leaving the corresponding holes in the the valence one (see figure 1.8 to see the band scheme). In pure crystals, after a short time period, these electrons decay returning to the valence band with the possible emission of a photon, but as their energy is equal to the gap energy it is likely to be reabsorbed exciting another valence electron, being the photon emission process very inefficient. To avoid that, impurities or dopants are introduced in the crystal to create intermediate energy levels within the forbidden gap, allowing the emission of photons with energies lower than the gap energy. A deeper description of the scintillation mechanism can be found in references [9, 30, 31].

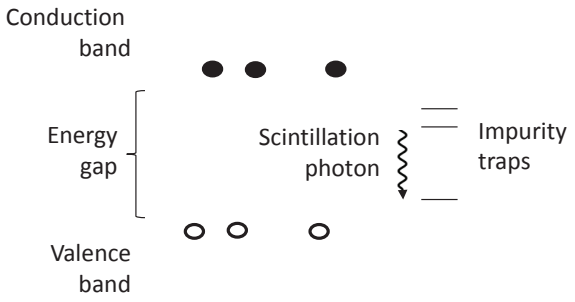


Figure 1.8: *Electronic band structure of inorganic crystals. A excitation of enough energy can create electron-hole pairs. Electrons decaying back to the valence gap through impurity traps can produce scintillation photons.*

The light yield is defined as the amount of light emitted by a scintillator per unit of energy absorbed. This is a magnitude that determines the efficiency and resolution, and therefore the quality of a scintillator. The temperature is an important factor that affects the light yield, and it is of the utmost importance for very low temperature applications. Inorganic crystals are very sensitive to variations of the temperature, with behaviors completely different from one material to another [9, 30]. The study of the scintillation properties of materials at low temperature is needed to build scintillating bolometers and several experiments have performed measurements with this goal. For example, NaI(Tl) is a very good scintillating material at room temperature, and recently its light output have been measured at low temperatures showing an increase of light emission when temperature decreases

from 300 K down to ∼125 K, then a decrease down to ∼40 K and a further increase below this temperature [32,33]. The light yield of BGO increases at low temperatures as it is evidenced in [12], offering excellent properties as low temperature scintillator. Similar behavior has been found for $Al_2O_3$(Tl) crystals [24]. The light yield of other materials at low temperature have been measured, for example for $CaWO_4$, CsI and $CdWO_4$ [34], or $ZnMoO_4$ [35], obtaining good scintillating performances.

The light yield also depends on the particle that interacts in the crystal. The measurement of the scintillation allows to discriminate among the different types of interacting particles while the heat measurement provides the energy released. Charged or electromagnetic particles as electrons, muons or photons interact mainly with the electronic system of the absorber, producing more scintillation than neutrons, which produce mainly recoiling off nuclei. Alpha particles and heavier ions excites also the electronic system, but they deposit its energy in a very short range saturating the scintillation centers, which generally reduces the amount of light emitted. But the lack of a model able to describe successfully the behavior of the inorganic crystals makes necessary the measurement of the different responses to different particles for each material. Such measurements have been performed by different groups for promising materials as for example BGO and sapphire [24,36,37]; and they have been discriminated even the different responses for the different nuclei of the same detector, as the O, Ca and W nuclei in a $CaWO_4$ crystal irradiated with monoenergetic neutrons (using a dedicated scattering facility) [34]. Surprising results like a light yield of $\alpha$ particles larger than that of electrons and photons, have been reported [38] and explanations are not clear.

### 1.3.2 Optical bolometers and the double bolometer configuration

The scintillating bolometer was firstly proposed by González-Mestres and Perret-Gallix [39] in 1988 with the name of luminescent bolometer, and it was successfully tested by Alessandrello et al. [40] using $CaF_2$(Eu) absorber crystals with a NTD–Ge as heat sensor and with a silicon photodiode as light detector, operated between 20 mK and 300 K. In 1996, Bobin et al. [41] showed their results using a secondary infrared silicon bolometer (called optical bolometer) as photon detector. The optical bolometer as light detector at low temperature is the technique currently chosen by the groups and collaborations using scintillating bolometers: our experiment ROSEBUD, the CRESST experiment [18] and the project LUCIFER [42]. This type of detector offers the possibility of working at the same temperature than the

scintillating absorber and it presents a wide photon absorbtion band (from some eV to tens of keV).

The design of the optical bolometer consists in a thin slab or substrate of a material capable to absorb scintillation photons efficiently, with a phonon sensor attached to it. Typical dimensions of the absorber are between some $\mu m^2$ and some $cm^2$ of surface, and thicknesses of tens of $\mu$m, depending on the energy of the photons to be detected. Several materials have been tested as photon absorbers (see [43] and references therein) but silicon, pure or deposited on sapphire, and germanium are the most used. The absorber surface can be texturized by a dedicated etching process to reduce the reflectivity, and antireflecting deposited coatings are sometimes used.

A complete description of the characteristics and performance of the Ge optical bolometers used by the ROSEBUD collaboration is presented in [43]. Some pictures of such detectors used by the ROSEBUD and CRESST collaborations are shown in figure 1.9.

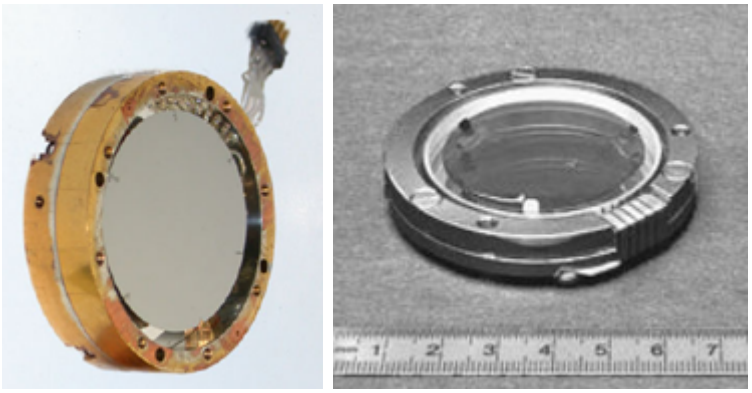

(a) (b)

Figure 1.9: *Optical bolometers: (a) Ge disk used by the ROSEBUD collaboration and (b) wafer of silicon on sapphire used by the CRESST collaboration [44].*

For the simultaneous measurement of heat and light, the optical bolometer is faced to a scintillating crystal and both are enclosed in a reflecting cavity to improve the photon collection. Each absorber has its own phonon sensor and its thermal contact to the heat sink. A schematic view of the scintillating bolometer is shown in figure 1.10. When a particle interacts with the scintillating absorber, the heat produced is measured like in a simple bolometer and the emitted photons, after several reflections in the cavity, are absorbed in the optical bolometer and detected through the temperature increase produced in it. The additional requirement for the scintillating absorber is to have a high light yield at low temperatures (besides the requirements as bolometer), although weak Cherenkov light could have been also

detected with optical bolometers in non-scintillating materials like $TeO_2$ [45].

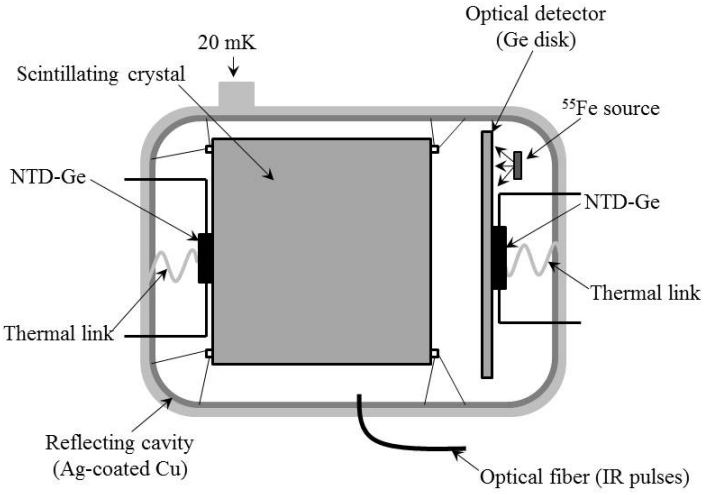


Figure 1.10: *Schematic view of a scintillating bolometer in a double bolometer configuration. There are also plotted an X–ray source and an optical fiber to inject IR pulses from a LED for calibration purposes [12].*

The fraction of energy deposited in the absorber that produces light is about the 10% for electromagnetic interactions in the best scintillators [12]. The properties of the light channel are not as good as in the heat channel, and improvements of threshold energy, resolution and sensitivity in general for this channel would be very appreciated, specially for nuclear interactions whose light yield is usually dominated by electronic noise. Different approaches can be addressed in this direction. A direct improvement would be to decrease the operation temperature. Other lines must be directed to optimize the light collection: the use of antireflection coating on the substrate, design of complex substrates to enlarge the area without losing heat conduction to the thermistor, a better design of the reflecting cavity, or the use of more than one optical bolometer as in [46]. Recently, a 20% of improvement in the light detected has been reported using $SiO_2$ coating in Ge optical bolometers [47]. The application of the so-called Neganov–Luke effect to optical bolometers has shown impressive improvements in energy resolution (10%) and signal-to-noise ratio (factor 9) in silicon substrates [48]. This effect consists in drifting the electron-hole pairs in the semiconducting substrate by applying an electric field by mean of two metallic electrodes directly evaporated into the absorber. The heat dissipated by the drifting pairs amplifies the phonon signal. The comparison of two pulses without and with bias voltage applied is shown in figure 1.11.

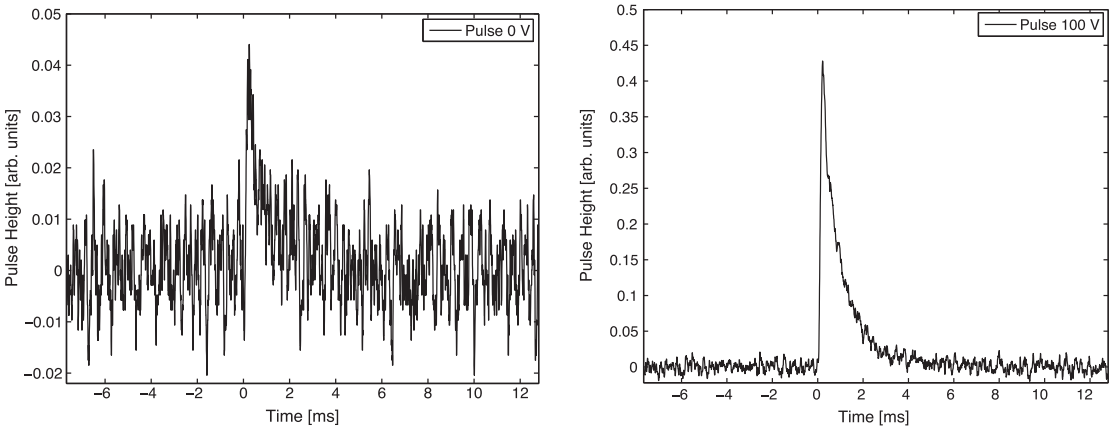


(a) (b)

Figure 1.11: *Light pulse injected by a LED source without Neganov-Luke electric field applied (a) and with a 100 V field applied (b). The signal is amplified in a factor ≃12 and the noise level is only slightly increased [48].*

# Chapter 2

# Nuclear and particle physics with bolometers and scintillating bolometers

As it was shown in the previous chapter, bolometers offer an excellent performance in particle detection with excellent energy resolution, very low energy thresholds, a wide range of materials to build the detector, and possibility of particle discrimination in the case of scintillating bolometers. Thus bolometric detectors are used in numerous fields of physics including some of the hottest topics in astrophysics and particle physics: the search for the elusive dark matter, a principal constituent of the Universe, the detection of neutrinos and/or the measurement of their fundamental properties, the search for axions, or the study of some rare decays. The so-called micro-bolometers or micro-calorimeters are widely used in interesting applications as measurements of IR radiations, X–rays and sub-millimeter waves in experiments as, for example, measuring cosmic rays or cosmic microwave background with some front-end results.

In this chapter we will focus mainly on the applications of massive bolometers with masses from grams to kilograms. A more exhaustive collection of bolometer's applications can be found, for instance, in [49].

## 2.1 Dark Matter searches

In the last decades, several observational data from different sources have established a precision cosmological model of the Universe, the so-called Standard Cosmological Model or ΛCDM. This model assumes large scale homogeneity and isotropy of the Universe, and its geometry and evolution is based on the Robertson-Walker metric and the Einstein's equations of general relativity [50]. The model can be parameterized with some fundamental cosmological parameters which, according to the observations, reveal an accelerating Universe in continuous expansion constituted by radiation, matter and dark energy.

Astrophysical measurements from such different sources as observations of Type Ia Supernovae, Barion Acoustic Oscillations (BAO) observed from clustering of galaxies and measurements of the Cosmic Microwave Background (CMB) converge on a small region of the cosmological parameter space, as is shown in figure 2.1. A major role is developed by the CMB measurements which detect the relic photons that uncoupled from matter in the early history of the Universe, when it cooled down and became transparent to them, carrying an image from 380000 years after the Big Bang. The CMB has been measured with increasing accuracy from its discovery in 1965 by Penzias and Wilson, using satellite-board instruments as COBE (launched by NASA), able to measure small inhomogeneities (related with the structures formation in the early Universe) in the sky map in 1992 [51], its successor WMAP (also launched by NASA) which after 9 years released very precise data [52], and the ESA instrument Planck, currently in orbit, that recently has shown the most accurate measurement of the CMB anisotropies so far [53] (see figure 2.2).

The fit of the cosmological model to Planck data and other observations lead to a flat Universe constituted mainly by dark energy $(68.6 \pm 2.0)\%$ responsible for the accelerated expansion and represented by the cosmological constant $\Lambda$ in the Einstein equations, being the matter content of the Universe the remaining $(31.4 \pm 2.0)\%$. But the Big Bang Nucleosynthesis (BBN), the theory which predicts the abundances of the light element isotopes, indicates that the ordinary or baryonic matter make up just a 4.9%, with the other 26.6% being cold dark matter (CDM), which has not been detected and whose nature is unknown and must be beyond the Standard Model (SM) of particle physics.

The elusiveness of dark matter leads to question its existence and some alternative theories have been proposed (see, for instance, [56]). However, there exists a relevant number of evidences that support the dark matter hypothesis.

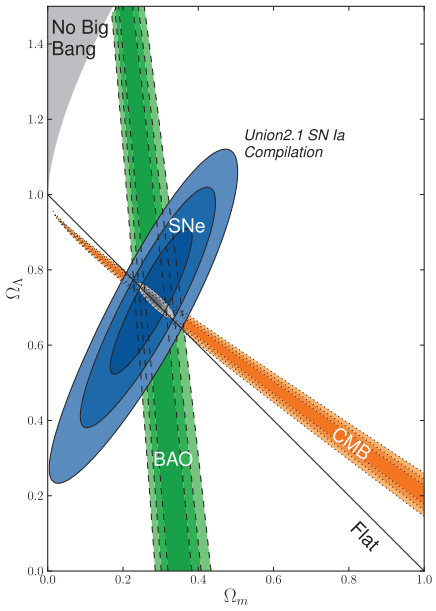


Figure 2.1: *Confidence level contours (at 68.3%, 95.4% and 99.7%) in the dark energy density ($\Omega_\Lambda$)- matter density ($\Omega_m$) plane from the Cosmic Microwave Background, Baryonic Acoustic Oscillations and the Supernovae Ia, as well as their combination [54].*

The first hint of an *invisible* matter is attributed to F. Zwicky in 1933[1] [59], who realized that the observed mass of the Coma cluster was not enough to explain the high velocity of the galaxies in its outskirts according to Newtonian dynamics. This behavior has been observed both in clusters and galaxies, always with flat dependencies of the velocity on the distance to the center $r$ instead of the expected $r^{-1/2}$ dependency (see figure 2.3a), indicating that there is more mass than that observed and it extends further than the visible matter [60]. Another important evidence is the gravitational lensing effect whereby massive objects can deviate the light passing near them, creating distorted images of galaxies placed further (see figure 2.3b). The study of these images allows to estimate the mass and size of the interposed object, which is in general more massive than it is expected from its luminosity, resulting again in a lack of matter [61]. Collisions of galaxy clusters like the recent observation of the Bullet cluster [62], which consists of two large colliding clusters, show also discrepancies between the observed distributions of gas and matter, pointing to the existence of a form of matter which weakly interacts but produces gravitational effects. The dark matter is also needed to explain the

[1]Actually, in the early 1930s J. H. Oort introduced the expression "dark matter" to explain stars motion perpendicular to Milky Way galaxy plane [57] and reference [58] mentions that in 1922 J. H. Jeans analyzed the motion of nearby stars transverse to the galactic plane concluding that the average density of DM must be roughly equal to that of luminous matter.

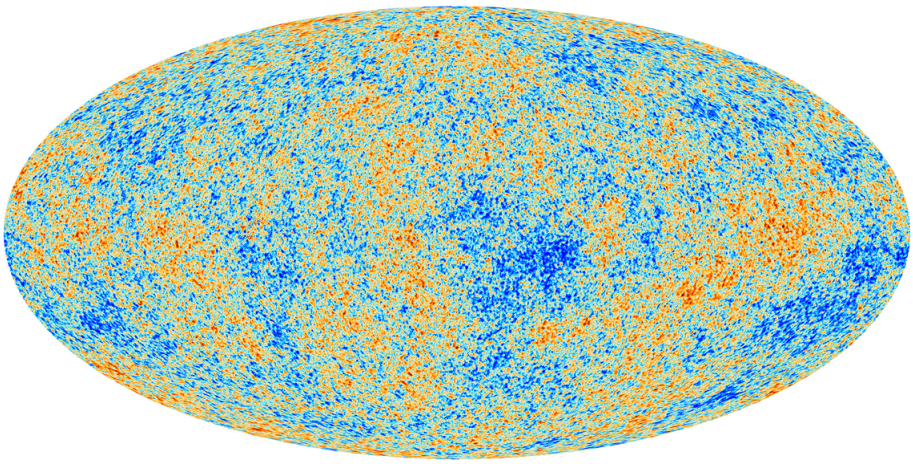

Figure 2.2: *The anisotropies of the Cosmic Microwave Background as observed by Planck [55].*

creation of structures along the Universe evolution. Complex simulations of this evolution including cold dark matter have confirmed the consistency of the ΛCDM model with the observed structures of the Universe [63]. A complete review of dark matter hints can be found in [64, 65], and an early history of dark matter in [66].

Dark matter can be classified in hot and cold dark matter. The former consists of matter relativistic at the decoupling moment. The neutrino could be a candidate, but hot dark matter can not explain the structure formation according to the anisotropies observed in the CMB, so that it can not constitute the main part of dark matter. To fulfill the requirements imposed by the numerous evidences mentioned above, dark matter particles must be cold (non relativistic when they decoupled from the rest of the Universe), massive, neutral, stable or with half-life of the order of the Universe age, weakly interacting with matter and, of course, non baryonic. There are no particles in the Standard Model (SM) of Particle Physics with these features.

One of the best positioned candidates are the WIMPs or Weakly Interacting Massive Particles, encompassing, among others, the candidates motivated by supersymmetric (SUSY) extensions of the SM. These models propose supersymmetric partners of the SM particles. Some of these SUSY particles (with masses from 10 GeV to TeV) fulfill the cold dark matter requirements as for example the neutralino. Other accepted candidate is the axion. Axions were proposed by Peccei and Quinn in 1977 [68] to explain the strong CP conservation problem in the frame of Quantum ChromoDynamics (QCD). Although not any axion is a dark matter candidate, for some specific values of the theoretical parameters the axion could form the totality of cold dark matter with masses between the $\mu$eV and the meV [69]. A

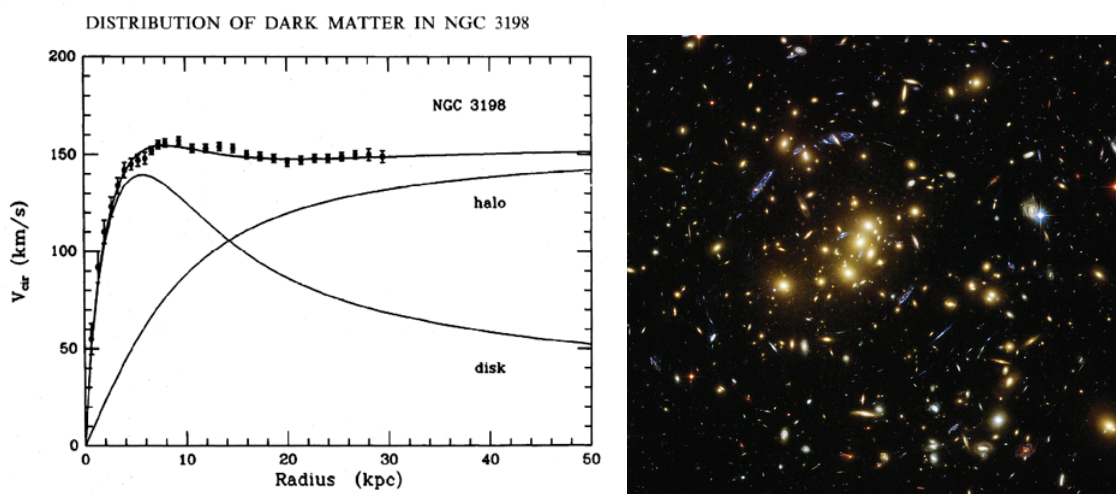


(a) (b)

Figure 2.3: *In (a) it is shown the measured rotational curve of NGC 3198 (dots), that is explained as the sum of the expected curve for the visible disk and the contribution of a invisible matter halo [67]. In (b) it is shown an image of strong gravitational lensing around galaxy cluster CL0024+17 obtained from reference [61]. The faint elongated (blue) objects are galaxies lying behind the cluster (yellow); gravitational lensing has distorted their apparent images into a series of tangential arcs centered on the foreground cluster.*

complete review of candidates to cold dark matter can be found in [65].

Numerous experimental collaborations are dedicated to detect WIMP dark matter particles using different approaches. The indirect detection of dark matter is based on the detection of the annihilation products of galactic WIMPs and their subsequent particle cascades. Among the experiments aiming to detect gamma rays, antimatter or neutrinos coming from dense regions of our galaxy, where dark matter is expected to accumulate, we can mention the Fermi Large Area space Telescope [70], the telescopes MAGIC [71], the antimatter detector AMS in the International Space Station [72], or the neutrino observatories IceCube [73] and ANTARES [74]. In direct detection techniques, the aim is to observe the recoiling off the detector nuclei induced by dark matter WIMPs. This is the approach used with bolometers and will be explained more in detail in the next subsection. SUSY particles could also be produced in accelerators as the LHC with the subsequent study of their decaying products, but no clear evidences of SUSY particles have been detected so far [75].

### 2.1.1 Direct detection of WIMPs

Although WIMPs are expected to be weakly interacting with matter and then practically invisible to our detectors, the expected density in the DM halo of our galaxy at the Sun position ($\rho_0 = 0.3$ GeV/cm$^3$ [76]) could make possible the detection of the small fraction of WIMPs colliding with nuclei of our detectors. The basic idea of direct detection is that WIMPs can produce elastic scattering off nuclei in the detector, inducing detectable nuclear recoils.

The differential event rate of interaction (in terms of counts per unit of mass, unit of time and unit of energy) for a WIMP with mass $m_\chi$ in nuclei of mass $m_N$ can be written as

$$\frac{dR}{dE_R} = \frac{\rho_0}{m_N m_W} \int_{v_{min}}^{v_{esc}} v f(v) \frac{d\sigma_{WN}}{dE_R}(v, E_R)\, dv \tag{2.1}$$

where $E_R$ is the nuclear recoil energy, $v$ and $f(v)$ the WIMP speed and its distribution in the detector frame, $v_{min}$ is determined by kinematical reasons (the minimum WIMP speed needed to produce a recoil of energy $E_R$), $v_{esc}$ is the escape speed of WIMPs gravitationally bound to the Milky Way, and $\frac{d\sigma_{WN}}{dE_R}$ the differential cross-section for the WIMP-nucleus scattering.

The differential cross-section contains the properties of the interaction of WIMPs with ordinary matter and can be separated into spin independent (SI) and spin dependent (SD) contributions, expressed in function of the nuclear form factors $F(E_R)$ which encode the dependence on the momentum transfer $q(E_R)$:

$$\frac{d\sigma_{WN}}{dE_R} = \left(\frac{d\sigma_{WN}}{dE_R}\right)_{SI} + \left(\frac{d\sigma_{WN}}{dE_R}\right)_{SD} = \frac{m_N}{2\mu_N^2 v^2}\left(\sigma_0^{SI,N} F_{SI}^2(E_R) + \sigma_0^{SD,N} F_{SD}^2(E_R)\right) \tag{2.2}$$

$\sigma_0^{SI,N}$ and $\sigma_0^{SD,N}$ are the SI and SD components of the WIMP-nucleus cross-sections at zero momentum transfer and $\mu_N$ the WIMP-nucleus reduced mass. The SI cross-section $\sigma_0^{SI,N}$ can be expressed as a function of the effective couplings to protons $f_p$ and neutrons $f_n$ that, if assumed to be equal ($f_p = f_n$), gives an expression proportional to the square of the mass number A,

$$\sigma_0^{SI,N} = \frac{4\mu_N^2 G_F^2}{\pi}\left[Z f_p + (A - Z) f_n\right]^2 \approx \left(\frac{\mu_N}{\mu_n}\right)^2 A^2 \sigma^{SI} \tag{2.3}$$

being $G_F$ the Fermi coupling constant, $\mu_n$ the WIMP-nucleon reduced mass, and $\sigma^{SI}$ the WIMP-nucleon SI cross-section.

The SD contribution comes from the coupling to the quark axial current, and can be also expressed as a function of its effective SD couplings to protons and neutrons,

$a_p$ and $a_n$ respectively,

$$\sigma_0^{SD,N} = \frac{32\mu_N^2}{\pi} G_F^2 \frac{J+1}{J} \left[a_p S_p + a_n S_n\right]^2 = \frac{4}{3}\frac{J+1}{J}\left(\frac{\mu_N}{\mu_n}\right)^2 \left(S_p\sqrt{\sigma^{SD,p}} + S_n\sqrt{\sigma^{SD,n}}\right)^2 \tag{2.4}$$

where $S_p$ and $S_n$ the spin content of the protons and neutrons in the nucleus, and $\sigma^{SD,p}$ and $\sigma^{SD,n}$ the WIMP-proton and WIMP-neutron SD cross sections. As it can be observed, the SD cross-section is proportional to a function of the total nuclear spin $J$. A rigorous description of this calculous and its necessary inputs from astrophysics and particle physics is presented in [77]. Since both SI and SD contributions are plausible, targets with heavy nuclei should be complemented with those containing light nuclei and with those containing high $J$ nuclei.

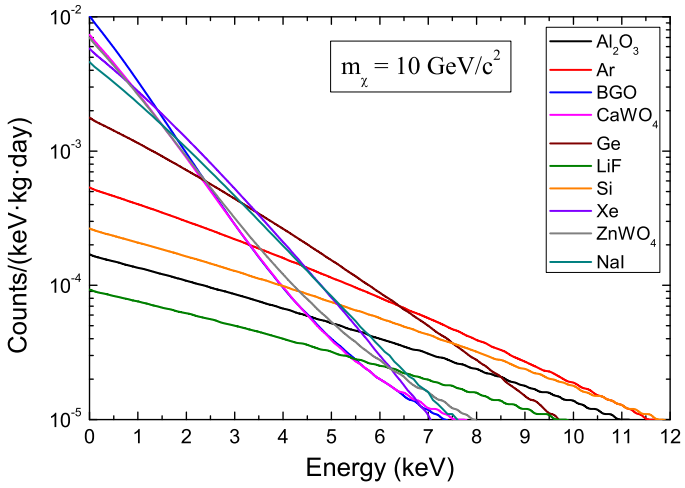


Figure 2.4: *Expected differential rates of WIMPs with mass of 10 GeV/$c^2$ interacting with several target materials considering SI interaction with $\sigma^{SI} = 10^{-8}$ pb. Figure from [36].*

Several considerations should be taken into account to select and build a WIMP detector. Figure 2.4 shows an example of how the recoil energy spectrum depends on the target nuclei properties. In all cases, recoil energy is expected to be no more than few keV, so low energy thresholds are needed because the lower the threshold energy the higher the sensitivity of the detector. Since the WIMPs detection rate is very low, large target mass is needed, and a radioactive background as low as possible is mandatory, so dark matter experiments are usually placed in underground laboratories and inside suitable shieldings. Background arising from photons, electrons, muons or $\alpha$ particles is usually rejected when using double-readout experiments as is the case of scintillating bolometers studied in this thesis; an accurate knowledge of the response to different particles is important to precisely define the region of interest for WIMP searches. This kind of study

is presented in section 5.3. In that case, the most dangerous background for dark matter experiments are neutrons, since they produce also nuclear recoils and could mimic a possible WIMP signal. Some dark matter detectors are designed to search for a distinctive dark matter signature as could be directionality or temporal dependencies. This latter approach is based in the changes of relative velocity between WIMPs and the Earth-based detector due to the diary and annual movements of the Earth around the WIMP halo considered fixed to the galaxy.

Bolometers and scintillating bolometers are attractive dark matter detectors due to their high efficiency, low energy thresholds, feasible (although not very easy) scalability, wide target choice, and the possibility of particle discrimination in hybrid configurations. Actually, some of the leading direct detection experiments consist of bolometers as it is reviewed below.

Dark matter detectors have been developed since the eighties, with different techniques and approaches, without a widely accepted dark matter positive claim. As an example, figure 2.5 illustrates the most relevant limits and positive claims obtained in the case of SI couplings. In this brief summary we will focus on the bolometric dark matter experiments, but previously it is worth mentioning some other experiments. The first experiment claiming for a positive dark matter signal was the Italian DAMA/LIBRA (previously DAMA/NaI), which shows an annual modulation of the interaction rate, compatible with the Dark Matter modulation effect, over 13 cycles of data in 250 kg of NaI scintillating crystals placed in the Gran Sasso underground laboratory [78]. After several years without another evidence of annual modulation, the experiment CoGeNT, in the Soudan Underground Laboratory, has recently claimed for a possible dark matter annual modulation in its p-type Ge detector of 440 g with very low background and electronic noise [79]. Without a positive evidence, the XENON100 experiment must be mentioned since it has reached the best limits to WIMP parameters in the SI case using a sensitive mass of 62 kg of liquid Xe in a double phase chamber with hybrid readout of light and charge [80].

Regarding cryogenic detectors, the best positioned are those using hybrid techniques, either heat-charge (CDMS and EDELWEISS) or heat-light (CRESST). The three experiments have found excess of events in their regions of interest for WIMPs recoils that are not completely explained with their expected backgrounds. CDMS uses towers of Ge bolometers (600 g) with several phonon sensors and with charge collection called ZIPs (see figure 2.6a), and with eight Si detectors [81]; it is located in the Soudan Underground Laboratory. Apart from their excess of nuclear recoils [82], they have searched for annual modulation without success [83]. They are

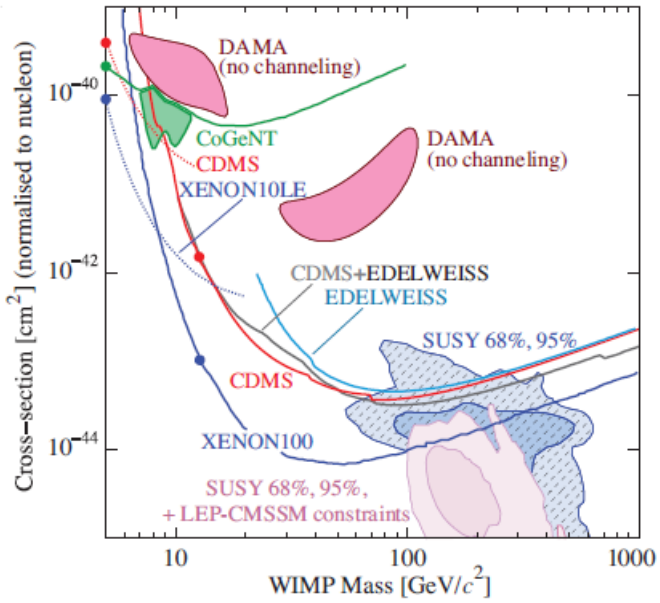


Figure 2.5: *Cross sections for spin independent coupling versus mass diagrams for different dark matter experiments. Pink shaded 68% and 95% regions are SUSY predictions, together with recent constraints (blue shaded 68% and 95% regions) set by LHC experiments (CMSSM). Equal cross sections for scattering from protons and neutrons have been assumed. Figure extracted from [58], further details and references can be found there.*

currently upgrading the experiment to SuperCDMS, with improved detectors and larger mass. The experiment EDELWEISS uses the same technique, Ge bolometers with charge collection by interleaved electrodes in the crystal (see figure 2.6b), and it is located at the Underground Laboratory of Modane. A few events appear in the WIMP search region and they derive limits for WIMP-nucleon scattering cross-section in searches optimized for WIMP masses above 50 GeV [84] and for very low masses of the order of 10 GeV [85]. A combined analysis of the results from CDMS and EDELWEISS was released giving good limits to SI WIMP interactions [86], but not as good as the XENON100 values. The experiment CRESST uses scintillating bolometers of $CaWO_4$ constituting a total of 10 kg detector in the Gran Sasso underground laboratory (see figure 2.6c). They claim for an excess of events in the nuclear recoils region of several detectors [18]. The CUORE experiment for double beta decay searches (see figure 2.6d) has recently presented a dark matter analysis of its $TeO_2$ bolometers [87], estimating the expected sensitivities of the CUORE–0 (52 bolometers) and CUORE (988 bolometers) experiments to a WIMP annual modulation signal. Our experiment, ROSEBUD, have tested small ($\sim$ 50 g) scintillating bolometers for dark matter searches in the Canfranc Underground

Laboratory since 2001 [88], and crystals of several materials have been used ($CaWO_4$, BGO, $Al_2O_3$, etc.). Although large masses of several kilograms can not be operated in our dilution refrigerator, characterization of new materials and research and development activities are being performed and they will be presented in following chapters, specially in section 5.3.

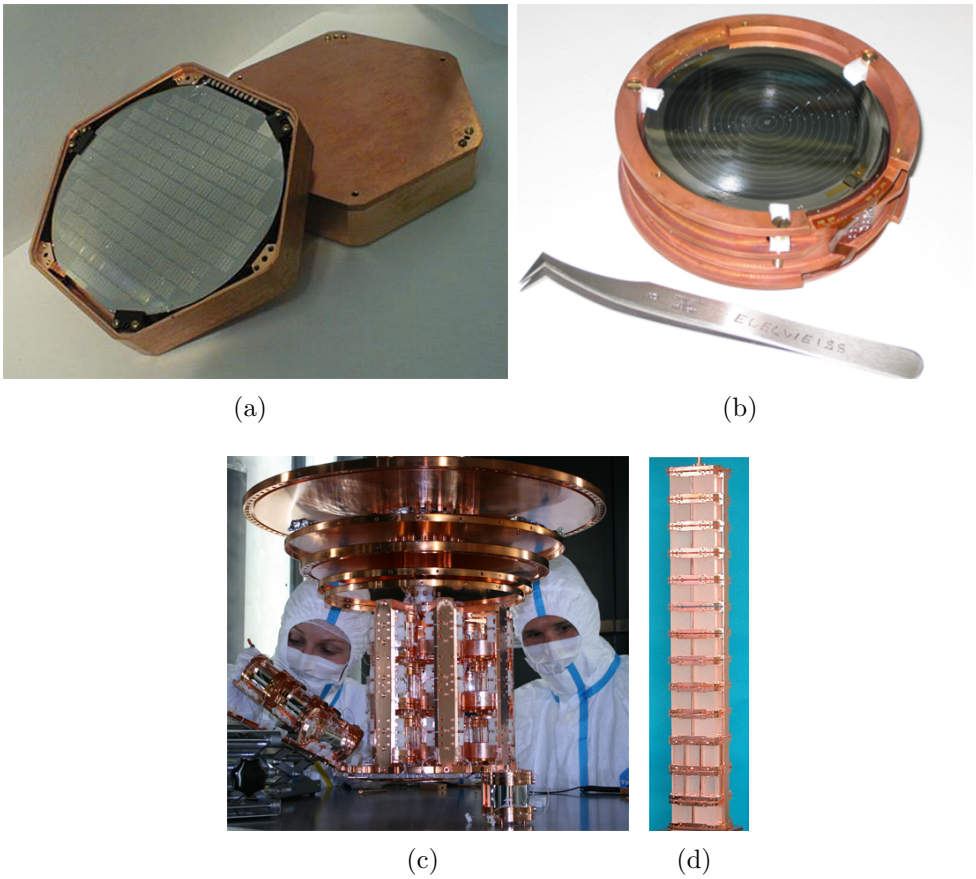

Figure 2.6: *(a) ZIP detector of the CDMS II experiment [89]. (b) EDELWEISS Ge bolometer with charge collection by interleaved electrodes [90]. (c) Structure of the CRESST experiment with $CaWO_4$ scintillating detectors [91]. (d) Detector tower of the Cuoricino experiment with $TeO_2$ bolometers, from the CUORE collaboration [92].*

The European bolometric experiments CRESST, EDELWEISS and ROSEBUD have joined efforts in a collaborative project, EURECA, aiming to build a bolometric hybrid dark matter detector with up to 1 ton of mass (Ge and $CaWO_4$ detectors in the first phase), profiting the experience of the groups involved in those experiments. The modularity allows to install different targets in the same site; this multitarget approach will allow to constrain the dark matter parameters. The experiment will be located in the extension of the Underground Laboratory of Modane. The Conceptual Design Report of EURECA has been recently sent to be published [93], and a scheme

of the project is shown in figure 2.7.

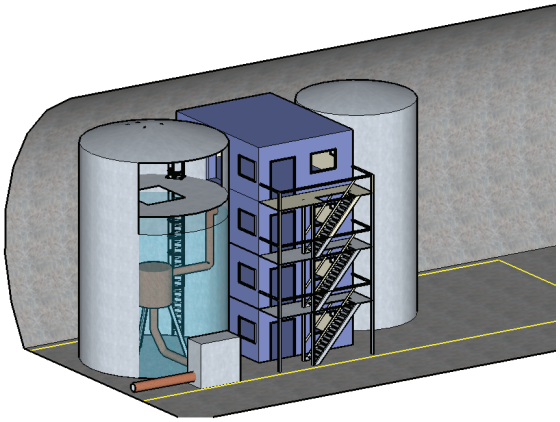

Figure 2.7: *Depict of the EURECA setup in the Underground Laboratory of Modane [93].*

### 2.1.2 Fast neutron monitoring

As mentioned above, fast neutrons are one of the most dangerous backgrounds for dark matter experiments with particle discrimination since they scatter off the detector nuclei like hypothetical WIMPs could do. Such experiments need good characterization of the fast neutron flux at which detectors are exposed. Neutrons can come from the natural radioactivity of the laboratory rocks or can be induced by muons. In underground laboratories the neutron flux arising from natural radioactivity is approximately three orders of magnitude greater than that arising from cosmic rays. Even though expected fluxes in underground laboratories are very low and can be reduced using neutron shieldings, fast neutrons can be still an annoyance for rare event searches. Estimations of the neutron background inside the detector are performed using Monte Carlo simulations methods, but uncertainties are always present. A direct measurement of the fast neutron flux at the detector position would be a relevant information.

Neutron detectors can be divided into those that just count neutrons and those able to estimate the kinetic energy of the incoming neutrons. The second group of detectors as well as the techniques used to measure the fast neutron energy are included in the category of neutron spectroscopy, in which we are interested. Some fast neutrons detectors are based on neutron moderators; they consist of neutron counters that are efficient to a certain neutron energy range (tuned with the shape

and size of a moderator surrounding a thermal neutron detector). A known example of such detectors are the Bonner spheres, that use different sizes of moderator spheres to obtain an energy spectrum by deconvolution [94, 95].

A more direct method is that based on fast neutron induced reactions. Neutrons can induce nuclear reactions in suitable materials whose products share the sum of the incoming neutron kinetic energy and the Q–value of the reaction. We can detect these products an obtain the incoming neutron energy by subtracting the Q–value. Unfortunately, cross sections for typical reactions are much lower for fast neutrons than for thermal neutrons. The most popular reactions for fast neutrons spectroscopy are $^{6}$Li(n,$\alpha$) and $^{3}$He(n,p). The first one has a cross section that drops off rather smoothly with increasing energy (it is proportional to the reciprocal of the neutron velocity) and has a pronounced resonance at 250 keV (see figure 2.8). The response of a detector based on this reactions (neglecting other competing reactions) is a single peak located at the neutron energy (250 keV) plus the Q–value (4.78 MeV), that is, centered at $\sim$5.03 MeV. An additional peak due to thermal captures is also observed at 4.78 MeV. The cross section of the $^{3}$He(n,p) reactions falls off continuously with increasing energy (figure 2.8). In this case, there is a relevant competing reaction, simple scattering of the neutrons from He nuclei, which contributes in the detector response with a continuous (due to the partial energy transfer to the He nuclei) from zero to a maximum at the 75% of the incoming neutron energy. Other technique is based on neutron elastic scattering by target nuclei. For this method, light nuclei targets (H, deuterium, He, etc.) are used to maximize their recoils, although neutron induced recoils in other targets can be also detected with bolometers as will be shown in section 5.1.3.

Scintillating bolometers are interesting as neutron detectors since absorbers can be made of materials of interest for neutron detection as Lithium-based crystals. Moreover, the discrimination capability allows to measure very low neutron backgrounds. Bolometric neutron detectors can be placed inside an experiment, next to the crystals devoted to dark matter detection or other rare events searches [97] to directly measure the neutron flux inside the experimental shielding, as it is being considered in EURECA. A characterization of bolometers for neutron detection is presented in section 5.2.

An interesting study developed in the Ph.D. thesis of T. Rolón [98] shows the possibility of measuring the differential neutron flux using neutron induced events registered in two scintillating bolometers: one of LiF (neutron captures) and another one of $Al_2O_3$ (nuclear recoils). The differential flux is reconstructed using a three parameter model and grouping the events in several energy windows. In [99] it is

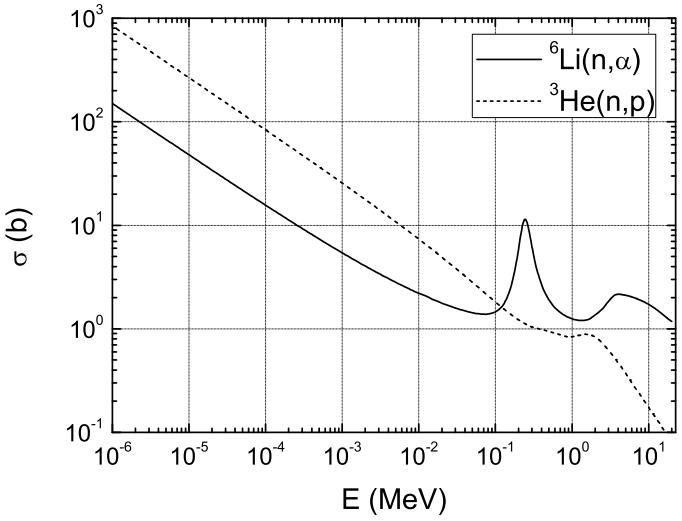


Figure 2.8: *Cross sections of the neutron captures $^6$Li(n,α) (solid line) and $^3$He(n,p) (dashed line) [96].*

described a method to recover the incident neutron energy spectra from a $^6$LiF-based cryogenic neutron spectrometer.

## 2.2 Neutrino physics

The neutrino detection and the study of its properties have constituted an issue of great interest for the scientific community since its proposal in 1930 by W. Pauli to solve the lack of energy in the final state of the beta decay processes. In 1933, E. Fermi developed and published the first theory of beta decay including the new particle, that was named neutrino. The first experimental measurement of this particle do not happened until 1956, when F. Reines and C. Cowan detected the unique signature of the capture by protons of antineutrinos arising from a nuclear reactor at Savannah River. Since then, neutrinos from other different sources have been detected: atmospheric, solar, astrophysical, and also from inside the Earth (geo-neutrinos). A complete neutrino review is presented in reference [100].

The neutrino is considered in the Standard Model of particle physics as a neutral particle with spin 1/2, weakly interacting and with zero mass, existing three families or flavours of neutrino (electron $\nu_e$, muon $\nu_\mu$ and tau $\nu_\tau$). But the study of this particle has revealed some surprising results as the fact that neutrinos actually have non zero mass. The deficit in the number of solar neutrinos detected from the expected theoretical value (first by R. Davis in the Homestake Experiment and confirmed later by other experiments) was explained by neutrino oscillations, a

mechanism that had been proposed by B. Pontecorvo in 1957 [101]. According with this concept, neutrinos can change of flavour, since flavours are linear combinations of states with a well defined mass ($\nu_1$, $\nu_2$ and $\nu_3$):

$$|\nu_l\rangle = \sum_i U_{li}|\nu_i\rangle \tag{2.5}$$

with U the mixture unitary matrix characterized by the 3 mixing angles $\theta_{ij}$ and 1 or 3 CP violation phases. Oscillations have been observed in solar, atmospheric and reactor neutrinos, and there are also strong evidences for disappearance of muon neutrinos due to neutrino oscillations in the long-baseline accelerator neutrino experiments. One of the most important implications of this process is that neutrinos have mass. These results are evidences of physics beyond the Standard Model. The oscillation experiments have allowed to measure or limit other neutrino parameters as some mixing angles $\theta_{ij}$ and the quadratic mass differences between mass states $\Delta m^2$ [102–104], remaining unknown the absolute mass values. With the known mass differences, there are two possible scenarios: in the so-called normal hierarchy of masses $m_1 < m_2 < m_3$ and $\Delta m^2_{31} > 0$, and in the inverted hierarchy $m_3 < m_1 < m_2$ and $\Delta m^2_{31} < 0$ (see figure 2.9). A third mass scale called quasi-degenerate would imply three masses of the same order but significantly larger than $\sqrt{\Delta m^2_{31}}$. Another unknown property of neutrinos is their nature as Majorana (neutrino and antineutrino would be the same particle) or Dirac particle (neutrino different from antineutrino).

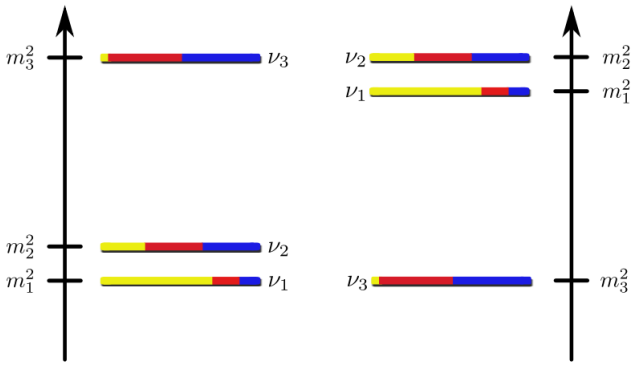


Figure 2.9: *Scheme of mass hierarchy scenarios of neutrinos, normal (left) and inverted (right). The colours represent the mixed flavours: $\nu_e$ (yellow), $\nu_\mu$ (red) and $\nu_\tau$ (blue).*

In the next subsections we will review some approaches to determine the neutrino properties, specially those in which bolometers are used. For a detailed review on neutrino nature, mass, mixing and oscillations see [58].

### 2.2.1 Double Beta Decay

Double beta decay (DBD) is a second order process in which a nucleus (A,Z) decays into an isobar changing its nuclear charge by two units (A,Z±2). It was firstly studied by M. Goeppert-Mayer in 1935 [105] on the basis of the Fermi theory of $\beta$ decay. There are several DBD possibilities combining the three single beta decay modes: double $\beta^-$, double $\beta^+$, double Electronic Capture (EC) or $\beta^+$ EC. In the first and more studied case, two electrons and two antineutrinos are emitted in the process. In the other cases are emitted positrons and neutrinos. We name in general this cases involving two neutrinos or antineutrinos as $2\nu$DBD, being a process within the Standard Model. This is a very rare decay (half-lives of the order of $10^{18}$-$10^{22}$ years) and it is disfavored against the single beta decay, so it is observed when the $\beta$ decay is energetically forbidden, what takes place in the lightest nuclei of some isobaric families with even A.

A second DBD mode was firstly considered in 1939 by W. H. Furry [106]. In the neutrinoless doble beta decay ($0\nu$DBD) neutrinos are not emitted and the lepton number is then violated. In contrast with the $2\nu$DBD, the $0\nu$DBD has not been observed so far, but its discovery would be a solid proof of physics beyond the SM. Besides, the existence of the neutrinoless mode would reveal the Majorana nature of neutrinos, being a massive neutrino also needed for this process.

Both modes could be experimentally discriminated. For instance, in the $\beta^-\beta^-$ case, they are distinguished by the energy spectra of the electrons emitted in the decay. The electrons of the $2\nu$DBD share the energy with the two neutrinos, producing a continuous from zero to the available energy $Q_{\beta\beta}$; on the contrary, the electrons of the $0\nu$DBD would produce a peak at $Q_{\beta\beta}$. Both expected spectra are shown in figure 2.10.

The probability of the $0\nu$DBD transition is normally expressed as

$$\left(T^{0\nu}_{1/2}\right)^{-1} = G^{0\nu} \left|M^{0\nu}\right|^2 \langle m_\nu \rangle^2 \tag{2.6}$$

where $G^{0\nu}$ is the kinetic phase space factor, $M^{0\nu}$ is the nuclear matrix element (NME) and $\langle m_\nu \rangle$ the effective Majorana mass defined as

$$\langle m_\nu \rangle = \sum_{i=1}^{3} m_i U_{ei}^2 \tag{2.7}$$

The phase space $G^{0\nu}$ can be accurately calculated for each particular process, but the calculations of the NME are more difficult and controversial due to its dependence

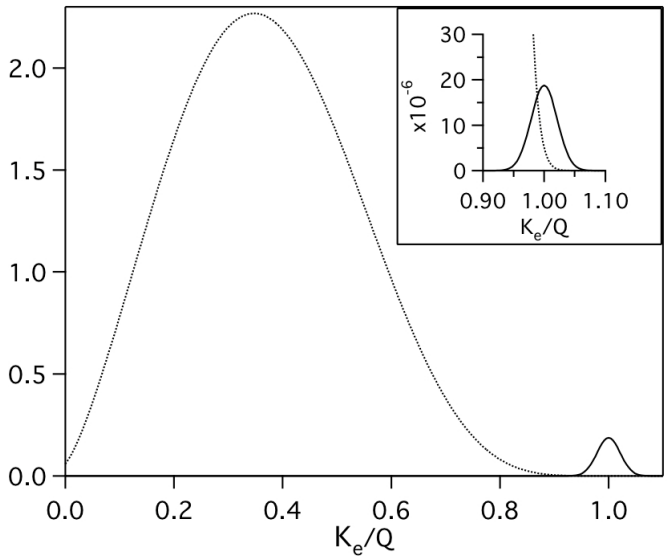


Figure 2.10: *Expected spectra of $\beta^-\beta^-2\nu$ (dotted line, on the left) and $\beta^-\beta^-0\nu$ (solid line, on the right). The finite energy resolution creates an overlap between two spectra that is zoomed in the inset of the upper right corner [107].*

on the nuclear model used and a hard work has been done in the last decades to increase its reliability. Reducing the uncertainties of the NME, a positive observation of the $0\nu$DBD would allow to know the neutrino effective mass and fix a range of absolute values of the neutrinos masses.

The neutrinoless DBD half-lives are expected to be even longer than those of the two neutrinos mode. For that, large-scale experiments with very low radioactive backgrounds and high detection efficiencies are required. But the irreducible background is that from the $2\nu$DBD process of the own isotope, because it contributes with a continuous as is shown in figure 2.10. Excellent energy resolution is needed to minimize the contribution of $2\nu$DBD events in the peak of $0\nu$DBD. DBD experiments are usually installed underground and use large volumes. Other requirement is imposed by the isotope to be studied. The list of isotopes that undergo DBD is not too long, and isotopes with high $Q_{\beta\beta}$ values are recommended to minimize the natural background.

Several experiments using a wide range of techniques have been devoted to DBD studies. A controversial positive claim on $^{76}$Ge, using enriched Ge detectors, by part of the Heidelberg-Moscow collaboration [108], later strengthened with the use of pulse shape information [109], was not widely accepted by the community and is strongly disfavoured by the recent results of GERDA Phase I using also Ge enriched detectors [110]. Presently, the experiments GERDA Phase II and MAJORANA

with large masses of segmented Ge detectors point to a further exploration of the degenerate Majorana mass scale. Other techniques are used as Time Projection Chambers (TPC) filled with gas as the project NEXT [111] or with liquid-gas bi-phase as the experiment EXO [112] to enable double readout and tracking; large tanks of scintillating liquid as KamLAND-Zen [113] and SNO+ [114], profiting the cavities of old neutrinos observatories; or tracking calorimeters as the experiment NEMO and its upgrading SuperNEMO [115].

Bolometers are an excellent possibility for DBD searches, since they can be built with materials containing DBD isotopes, they offer an excellent energy resolution and the possibility of background rejection. The experiment CUORICINO used 40 kg of $TeO_2$ shared in 62 bolometers to study the $0\nu$DBD of $^{130}$Te and has been taking data since 2003 in the Gran Sasso underground laboratory, providing the best limits to the $^{130}$Te half-life [116] and being a demonstrator of its evolution CUORE, scaling up to 750 kg of $TeO_2$ (see an artistic view of the final configuration in figure 2.11a) that is currently under construction and with validation runs [117]. Some experiments in development phase are testing scintillating bolometers which provide excellent background rejection at the energies of interest: the AMoRE experiment uses $CaMoO_4$ crystals (see figure 2.11b) in the Yangyang underground laboratory with the aim of reaching a total mass of 100 kg to study the $0\nu$DBD of $^{100}$Mo [118], the project LUCIFER is testing ZnSe scintillating bolometers to study the $^{84}$Se [42], and the recent project LUMINEU is testing scintillating bolometers of $ZnMoO_4$, also focused on $^{100}$Mo [119].

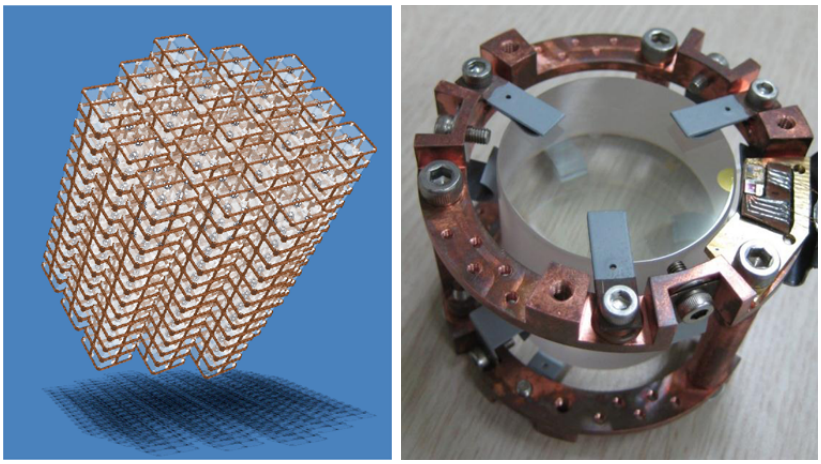

(a) (b)

Figure 2.11: *(a) Artistic view of the bolometers arrays in the final CUORE configuration. (b) A $CaMoO_4$ bolometer from the AMoRE experiment.*

### 2.2.2 Neutrino mass from beta decay

The accurate measurement of the single beta decay spectrum is the most direct method to investigate the electron-neutrino mass. The continuous spectrum of the electron energy in the beta decay ranges from zero to the available energy in the process, that for a pure beta-emitter (decay to the daughter nucleus ground state), considering a massive neutrino, corresponds to the differences of atomic masses in the decay $Q_\beta$ minus the effective neutrino mass $m_\nu c^2$ defined in the following equation

$$\left(m_\nu c^2\right)^2 = \sum_{i=1}^{3} m_i^2 |U_{ei}|^2 \tag{2.8}$$

Since the neutrino mass is expected to be very low, the difference in the end-point $(Q_\beta - m_\nu c^2)$ of this spectrum with the spectrum of a massless neutrino is quite small (see figure 2.12). A precise measurement of this difference would be a direct measurement of $m_\nu$ based on kinematics and without further assumptions.

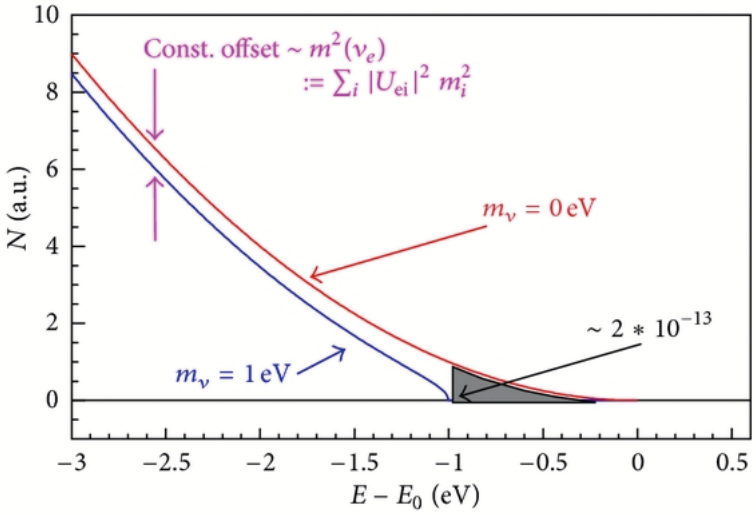


Figure 2.12: *Expanded region of interest of the energy spectrum for $^3H$ beta decay for the hypothetical arbitrary case of decay with a neutrino of $m_\nu c^2 = 1$ eV and the massless neutrino case. The gray-shaded area corresponds to a fraction of $2{\cdot}10^{-13}$ of all tritium $\beta$ decays [120]. $E_0$ represents the energy available in the case of a massless neutrino, that is, $Q_\beta$ in the case of a pure beta-emitter.*

The difficulty of this measurement is that, at the end of the spectrum, the counting rate of electrons is very low, and excellent resolution is needed since the expected mass is the order of meV. The end-point energies of the isotopes usually used are of low energy (of the order of some keV), because a lower energy means a

higher fraction of events in the region of interest. At this energies the background contributions are quite significant and rejection techniques become mandatory.

Since the sixties, many experiments have studied the spectrum of tritium ($^3$H) beta decay ($Q_\beta = 18.6$ keV) using magnetic or electrostatic spectrometers to measure the electrons energy, being upgraded by using adiabatic magnetic collimation, reaching upper limits to the neutrino mass of 2.3 eV/c$^2$ by the Mainz collaboration [121] and 2.5 eV/c$^2$ by the experiment Troitsk [122]. These are the most stringent limits on $m_\nu$ to date. The experiment KATRIN is currently under construction following the same measurement technique, with prospects of reaching limits down to 0.2 eV/c$^2$.

Bolometers, in this case arrays of microcalorimeters, are also being used in this field. Using absorbers containing the source isotope, all the energy released in the decay, except that of the neutrino, can be detected as a sum allowing to use isotopes with complex electronic structure. Small bolometers are used to keep fast time constants and avoid pile-up, but they are installed in arrays to increase the sensitivity. The MARE project (Microcalorimeter Array for a Rhenium Experiment) uses $AgReO_4$ calorimeters (see figure 2.13) to study the $\beta$ decay of $^{187}$Re, although they are also considering sources of $^{163}$Ho, that undergoes Electron Capture. They aim, in the long term, to be able to explore the sub-eV region of the electron-neutrino mass using arrays with tens of thousands microcalorimeters [123]. The ECHO (the Electron Capture $^{163}$Ho experiment) collaboration is also exploring the possibility of studying $^{163}$Ho embebed in metallic magnetic calorimeters [124].

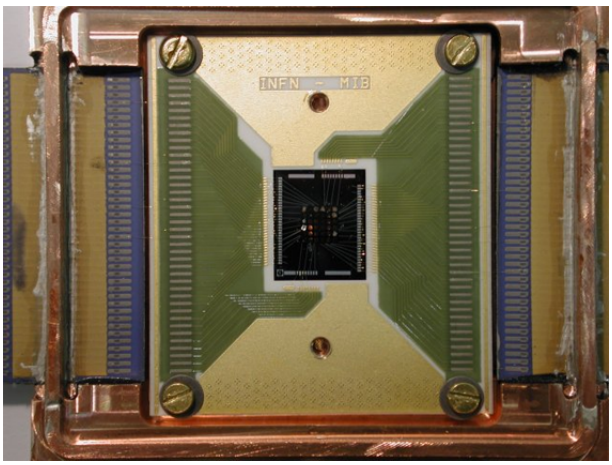


Figure 2.13: *Micro-calorimeter from the MARE-1 experiment.*

### 2.2.3 Coherent neutrino-nucleus scattering

The neutrino-nucleus coherent scattering is a well-predicted Standard Model phenomenon but it has never been observed experimentally. Nuclear recoils with a typical energy of few tens of keV are expected. Current neutrino detection experiments are not able to detect such events, but large experiments like some of those using bolometric detectors for dark matter or double beta decay searches could accomplish the requirements to detect these recoils, as was already proposed almost 30 years ago by B. Cabrera et al. [125]. Proposals to define this kind of detection are now appearing from these experiments with large mass, extremely low background, excellent energy resolution and low energy threshold.

Since the coherent elastic neutrino-nucleus interaction is similar to the WIMP-nucleus one, studies about such neutrino detection with the next generation 1 ton dark matter experiments has been carried out, for instance, in [126], where detection rates from neutrinos arising from pion- and muon- decay-at-rest sources (maximum neutrino energy of ≈53 MeV) are calculated for the Germanium Observatory for Dark Matter (GEODM), the SuperCDMS evolution, with 1.5 ton of mass with Ge bolometers at 40 mK. A coherent neutrino interaction discovery in GEODM could be achieved with a 2 ton·year exposure. Nuclear recoils produced by solar neutrinos have been also considered as a possible background for dark matter searches because the neutrino coherent scattering cross sections can be larger than the coherent WIMP cross sections [127]. In [128] is outlined the possibility to study the existence of sterile neutrinos via coherent interactions using a Si bolometer array operated at 15 mK with expected threshold of only 10 eV.

Besides studying the neutrino-nucleus coherent scattering, the direct detection of neutrinos would allow to obtain information from neutrino sources as the Earth, the Sun, supernovae or another astrophysical sources, as well as study neutrino oscillations. The DBD experiment CUORE, has studied the possibility of detecting neutrinos coming from type II supernovae through the coherent scattering of heavy nuclei (Te in their case). Thanks to an online trigger algorithm that lowers the threshold, they estimate their sensitivity to supernova neutrinos as a function of the supernova distance [129].

## 2.3 Other nuclear and particle physics applications

### 2.3.1 Axion searches

There is a great interest in the search for axions because the Peccei-Quinn mechanism is probably the most credible scheme to preserve CP in QCD. Moreover, an axion with certain properties could fulfill the cold dark matter content of the Universe. Axion search experiments have tried to detect such a particle without success to date, and numerous theoretical axion models are still viable with a wide range of axion masses and axion-matter couplings. Astrophysical observations are the most used strategy, particularly solar axion searches.

Axions can interact with matter, and thus be detected, by mean of several mechanisms. Two of the most explored are the axion-photon coupling and the axiolectric coupling. By the first one, called Primakov effect, axions are converted into photons (and vice versa) in presence of strong magnetic fields. The axion-photon conversion in the laboratory can be induced with a transverse magnetic field (axion helioscope method [130]) or in the intense Coulomb field of nuclei in a crystal lattice of the detector (Bragg scattering technique [131]). The axioelectric interaction is analogous to a photoelectric effect with the absorption of an axion instead of a photon. In both cases, very low energy thresholds are needed.

The dark matter experiment CDMS, operating Ge hybrid bolometers with charge collection, performed a search for solar axions using the Bragg scattering technique, which involves a strong correlation between incident beam direction and conversion probability, providing a unique signature. An upper limit of the axion-photon coupling constant $g_{a\gamma}$ was set as $2.4{\cdot}10^{-9}$ GeV$^{-1}$ for an axion mass smaller than 0.1 keV/c$^2$, the first limit using accurate measures of crystal orientation [132]. In the same work, a search for galactic axions detected with the axioelectric effect is performed, looking for an excess of event rate above background. In absence of a positive signal, they gave an upper limit to the axioelectric coupling $g_{ae}$ of $1.4{\cdot}10^{-12}$ for an axion mass of 2.5 keV/c$^2$, being the best limit so far. The EDELWEISS-II dark matter experiment, with the same kind of detectors than CDMS, has also published an axion search study using the same two approaches. They give a 95% C.L. upper limit on $g_{a\gamma}$ of $2.13{\cdot}10^{-9}$ GeV$^{-1}$ and $g_{ae} < 2.56{\cdot}10^{-11}$ [133].

As another example, the CUORE experiment also carried out an analysis of

axions arising from the 14.4 keV M1 transition in $^{57}$Fe in the core of the sun. The searched signal was a peak at 14.4 keV produced by mean of the axioelectric effect. A low energy trigger was optimized to reduce the energy threshold in some of the crystals, using a total exposure of 43.65 kg·day. An upper limit of $\sim 10^{-12}$ for $g_{ae}$ was obtained for an axion mass of 10 keV/c$^2$ [134], at the level of other competitive searches as is shown in figure 2.14.

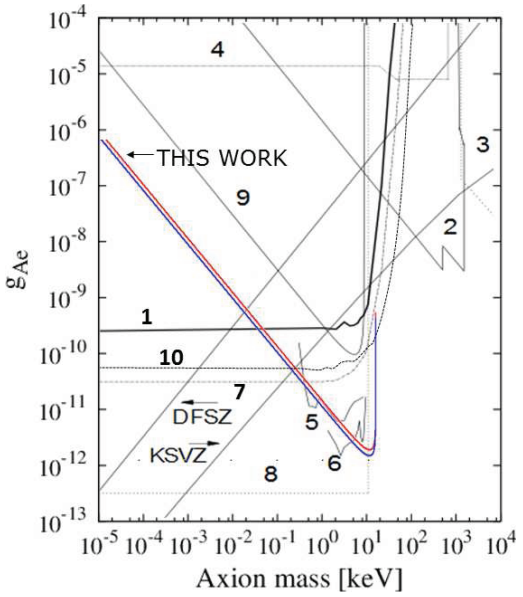


Figure 2.14: *Figure extracted from [134] comparing the bounds on $g_{ae}$ obtained with the CUORE crystals (labeled as "THIS WORK") given by two models (KSVZ, upper red line; and DFSZ, lower blue line) for the production of solar axions. Among the other shown results, the number (6) corresponds to the CDMS limit mentioned in the text. Lines labelled KSVZ and DFSZ represent the relationship between the axion mass and $g_{ae}$ in the corresponding models. For further details see reference [134].*

### 2.3.2 Measurements of nuclear decays

Scintillating bolometers offer the possibility to study individual decays of some isotopes due to their excellent energy resolution and discrimination capabilities, as well as detection efficiency. Measurements of nuclear physics parameters and nuclear decays have been performed obtaining some interesting results.

Scintillating bolometers were used to detect by the first time the $\alpha$ decay of $^{209}$Bi to the ground state of $^{205}$Tl (see scheme in figure 2.15a), an isotope commonly considered as the heaviest stable isotope [135]. They used two BGO ($Bi_4Ge_3O_{12}$)

crystals, one of 45.7 g also used by the ROSEBUD collaboration for dark matter searches and another one of 91.2 g. Their excellent discrimination properties at 20 mK allowed to reject cosmic ray induced events (see figure 2.15b); the $\alpha$ decay products were completely absorbed in the crystal due to their short ranges (8 $\mu$m the $\alpha$ particle and 170Å the nuclear recoil), guaranteeing practically 100% detection efficiency. The estimated half-life of $^{209}$Bi was $T_{1/2} = (1.9 \pm 0.2) \cdot 10^{19}$ yr. The decay to the first excited state is also advanced in the mentioned work, but its measurement including the branching ratio of the decay has been recently published in [136] by another group, using also a BGO scintillating bolometer. This decay is identified by the photon emitted (204 keV) in the deexcitation of $^{205}$Tl, that, for the detector, is simultaneous to the $\alpha$ decay products, producing the same amount of heat, but more light than the ground state transition. The measured branching ratio to the ground state is $(98.8 \pm 0.3)\%$. Other rare $\alpha$ decays have been also studied with scintillating bolometers as from lead isotopes using a $PbWO_4$ crystal [137], or tungsten isotopes using the $CaWO_4$ crystals from the ROSEBUD [138] and CRESST [139] collaborations.

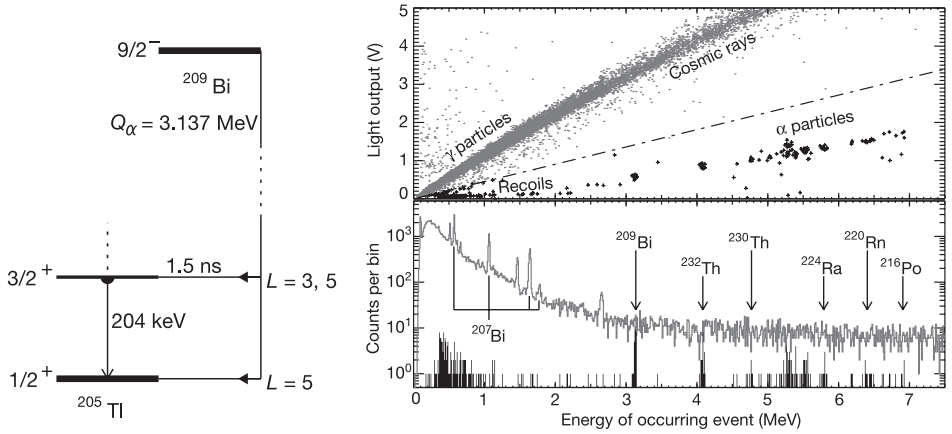


(a) (b)

Figure 2.15: *In (a) it is shown the decay scheme of $^{209}$Bi. In (b) they are shown the heat-light discrimination plot (top) and the spectra (bottom) of $\beta/\gamma$ events and $\alpha$ events in the BGO crystal, with the $^{209}$Bi $\alpha$ peak clearly visible. Both figures are extracted from [135].*

As an example of other nuclear studies carried out with scintillating bolometers, we can cite the first measurement of the L/K electron capture ratio of the $^{207}$Bi decay to the 1633 keV level of $^{207}$Pb with a BGO crystal [140] in the Canfranc Underground Laboratory, and the measurement of the L/K ratio of the electron capture in $^{7}$Be using a cryogenic micro-calorimeter [141].

### 2.3.3 Radiopurity assessment

Materials with high Z can be used as bolometers to perform good $\gamma$ ray spectroscopy, giving high efficiency and high energy resolution. Some of these crystals have reported resolution values comparable with that from HPGe detectors and have the advantage that, thanks to the wide absorber choice, frequently the source can be the detector itself. For this reason, these detectors are excellent options to carry out radiopurity tests of the absorber material, with the detection of internal $\alpha$, $\beta$ and $\gamma$ activities. Moreover, in the case of scintillating bolometers, the discrimination can offer extremely low backgrounds levels.

A direct application of bolometers for radiopurity assessment was performed in [142], where a roman lead bolometer was built to measure its radioactive contamination. They gave upper limits of $^{210}$Pb content of just few mBq/kg. In the chapter 5 of this thesis, $\alpha$ contaminations as low as a few tens of mBq/kg of Ra isotopes are reported in a scintillating bolometer of $SrF_2$.

Bolometers have been also proposed to perform environmental monitoring of alpha emitters, measuring activities and identifying the isotopes present in the surroundings, providing high-confidence detection and high-precision measurement of very faint signals. The measurement of the activities of actinides present in the environment could be used in nuclear security applications as, for example, nuclear waste management, nuclear power accidents or nuclear weapons testing (see for instance [143, 144]).

# Chapter 3

# Experimental setup

In this chapter it is described the equipment used for the characterization of scintillating bolometers (presented in chapter 5 of this thesis). It includes the cryogenic system of the dilution refrigerator (section 3.1), the data acquisition system to read the signals of the bolometers (section 3.2), and the radioactive and IR sources used to calibrate and monitor the bolometers response (sections 3.3 and 3.4). The characterization has been carried out in two different facilities: the bolometric laboratory of the Institut d'Astrophysique Spatiale of Orsay (IAS) and the Canfranc Underground Laboratory (LSC). Both installations are practically identical and even some devices are used in both of them, although there exist differences regarding mainly to the low radioactive background conditions of the LSC. These two laboratories are briefly described in sections 3.5 and 3.6.

## 3.1 The dilution refrigerator

As stated before, bolometers operate at very low temperatures, at approximately 10–30 mK. Such low temperatures can not be reached using cryogenic fluids even at very low pressures: $^4$He boils at 4.2 K and has a vapour pressure of $\sim 5 \cdot 10^{-2}$ mbar corresponding with 1.3 K of temperature; and $^3$He boils at 3.2 K and reaches 0.3 K at its vapour pressure of $3 \cdot 10^{-3}$ mbar. The $^3$He/$^4$He dilution refrigerator is the only continuous method for reaching temperatures lower than 0.3 K, getting down to 2 mK of temperature [145].

Dilution refrigerators use a liquid mixture of $^3$He and $^4$He whose phase diagram at saturated vapour pressure is shown in figure 3.1a. If a mixture with a $^3$He concentration, $x$, greater than 6.6% is cooled down, when the liquid temperature drops below 0.86 K it separates into two phases: one rich in $^4$He (we will mentioned it as dilute phase) and the other rich in $^3$He (concentrate phase). The phase rich in $^3$He floats on top because of its lower density. When temperature tends to zero, the concentrate phase becomes pure $^3$He; but in the dilute phase, the $^3$He concentration tends to a constant value of 6.6%, due to the quantum properties of these liquids. The cooling is produced by atoms of $^3$He continuously crossing the phase separation line from the $^3$He concentrated phase to the dilute one due to the enthalpy of the mixing, which is the difference of enthalpy $\Delta H$ between the two phases in adiabatic conditions. Because the specific heats of both phases are proportional to T at low enough temperatures, the resulting temperature dependence of the cooling power of the dilution process is

$$\dot{Q} \propto x \Delta H \propto T^2 \tag{3.1}$$

In an evaporating cryogenic liquid, where the number of atoms decreases exponentially with temperature, the temperature dependence of the cooling power results in:

$$\dot{Q} \propto P(T) \propto e^{-1/T} \tag{3.2}$$

Temperature dependence of cooling power for both cases is shown in figure 3.1b. Higher cooling powers can be achieved with dilution refrigerators at low enough temperatures.

But $^3$He atoms do not cross spontaneously from the concentrate to the dilute phase. In a dilution refrigerator (see scheme in figure 3.2), the vessel that contains the mixture in two phases is called the Mixing Chamber. The dilute phase of the Mixing Chamber is connected with the Still, a vessel kept at approximately 0.7 K, where almost pure $^3$He is evaporated since its vapour pressure is about 100

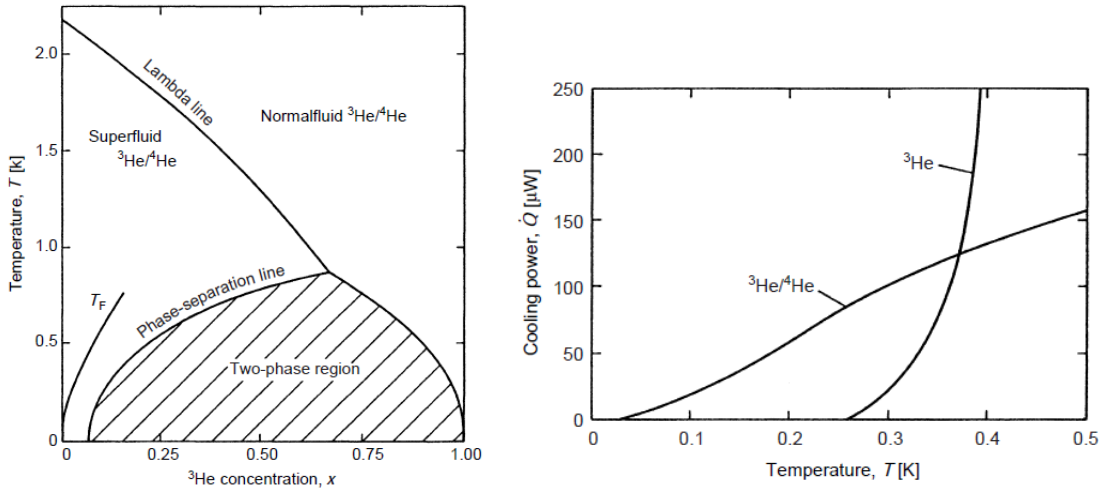


(a) (b)

Figure 3.1: *(a) Phase diagram of liquid $^3$He/$^4$He mixtures at saturated vapour pressure. (b) Cooling power of a $^3$He evaporation cryostat and of a $^3$He/$^4$He dilution refrigerator, assuming the same pumping ratio. Both figures are extracted from [145].*

times higher than that of $^4$He. As a result, the osmotic pressure developed between the Mixing Chamber and the Still drives $^3$He from the dilute phase of the Mixing Chamber to the Still, forcing the pass of $^3$He atoms from the concentrate to the dilute phase in the Mixing Chamber.

The $^3$He evaporated in the Still circulates through the pump and then it is precooled and condensed before entering the concentrated phase in the Mixing Chamber again. The pump is placed at room temperature, the returning $^3$He is first driven through cold traps (immersed in liquid nitrogen and/or helium, depending on the refrigerator) which purify and cool the gas and then it arrives at a condensation stage at 1.5 K. This stage usually consists of a $^4$He bath continuously pumped (called 1 K pot) followed by the so-called main flow impedance which establishes the needed pressure to assure the condensation, as in the case of the dilution refrigerator described in chapter 6. In some refrigerators, as the one used to cool the bolometers characterized in chapter 5 (which we will refer to as the French refrigerator), the reinserted $^3$He is condensed by Joule–Thompson expansion, being passed through an impedance provoking a high difference of pressure. The now liquid $^3$He flows through several heat exchangers in contact with the Still and with the dilute phase tube to reach the low enough temperature before entering into the Mixing Chamber.

The dilution unit is kept in a vacuum sealed vessel called Inner Vacuum Chamber (IVC) to avoid thermal leaks, and the IVC is immersed in a cryostat with LHe that helps to precool the tubes coming from room temperature.

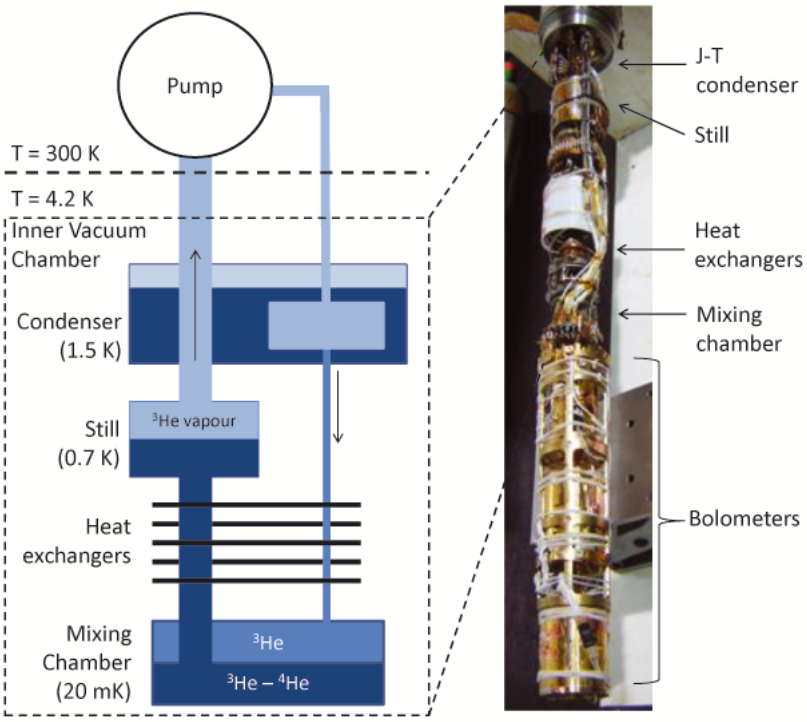


Figure 3.2: *Scheme of the most important parts of a dilution refrigerator and a picture of the French refrigerator used in the ROSEBUD experiments with a set of bolometers coupled to the Mixing Chamber.*

The French dilution refrigerator is a small and compact model of 6 cm of diameter and 100 cm length. Its base temperature is 20 mK. As mentioned above, this refrigerator uses a $LN_2$ cold trap and a Joule–Thompson (J–T) condensation stage to precool and condense the returning $^3$He. It has not only a helium bath, but also a liquid nitrogen one. The experimental volume that could be attached to the Mixing Chamber is about two liters, that means up to four scintillating bolometers of $\simeq$ 50 g each one. A slow control system enables to monitor and control some relevant parameters for the performance and safety, as the injection and aspiration pressures (typically about 0.7 bar and 0.7 mbar respectively). There are also some thermistors along the dilution unit to control the temperature of the Joule–Thompson stage, the Still and the Mixing Chamber.

## 3.2 Electronics and data acquisition system

The primary electric signal from the bolometer is obtained as the voltage difference in the Ge–NTD sensor, which is polarized through a load resistor $R_L$ of tens of M$\Omega$ following the circuit scheme of figure 3.3a. This resistor is attached to the copper

frame of the bolometer, kept at the same temperature to minimize the Johnson electronic noise. The polarization voltage $V_{polar}$ is provided by a commercial battery (of Hg 1.35 V or alkaline 1.5 V) installed in a metallic box with a potentiometer and a bell filter to provide a variable and stable voltage (usually from 50 mV to 1 V, in positive and negative values). A polarization box is shown in figure 3.3b. The resulting bias current applied to the Ge–NTD sensor is about units or tens of nA.

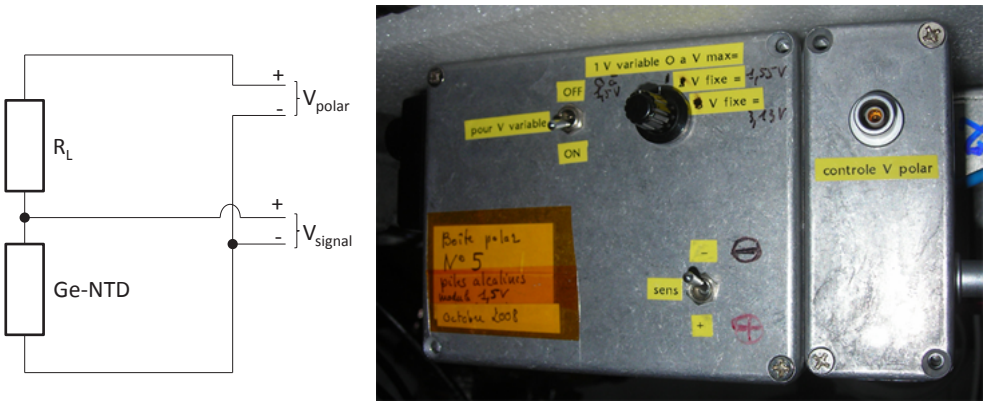


(a) (b)

Figure 3.3: *(a) Electric circuit of a Ge–NTD sensor attached to a bolometer. Polarization $V_{polar}$ is applied through a load resistor $R_L$. (b) Picture of a polarization box.*

Connections inside the bolometer frame are made with NbTi wires up to a cryogenic connector Malco fixed in the frame. The bolometers are connected to the top of the dilution unit with screened manganin wires, an alloy (Cu, Mn, Ni) of virtually zero temperature coefficient of resistance and low thermal conductivity.

Signals are very sensitive to noise and quite unstable. For this reason, the feeble signals arriving to the connectors in the top of the refrigerator are amplified and filtered in several stages before being digitized and registered. The first stages of electronics are enclosed in a Faraday cage and powered by batteries to reduce electromagnetic noise contributions. The signals are sent out of the Faraday cage by optical fiber to uncouple electronic noise components. We have used three different electronic chains indistinctly in the IAS laboratory and in the LSC (as an example, some components are shown in figure 3.4 which corresponds to a measurement carried out at LSC):

- In the oldest electronic chain (figure 3.5 top), the primary signal is sent to a FET (Field Effect Transistor) just at the top of the refrigerator, as close as possible to minimize parasitic noises. It is composed by 8 J-FET in parallel

and used to match impedances. The signal is then preamplified by a device with fixed gain ($G = 1000$) and after that it is sent to a low noise Stanford SR560 amplifier. This device has a double function: amplify the signal with variable gain (1–50000) and filter it through a band pass filter with selectable cutoff frequencies. In this stage of the chain, the band pass is usually wide, from $\sim 1$ Hz to $\sim 1$ kHz. The amplified electric signal is converted into a light signal by a Nicolet Isobe 3000 probe (variable gain 0.2–20) to be transmitted by optical fiber outside the Faraday cage where it is converted again into a voltage signal with another Nicolet Isobe 3000 probe. A second Stanford amplifier is usually used to filter the signal outside the Faraday cage (normally with a band pass of 10 Hz–300 Hz). The output signal of this amplifier is connected to a trigger module with up to 4 input channels (each with independent and adjustable threshold) with an OR logic output, or to a Nicolet 4094 scope with the same functionality, and in parallel to a digitizer card DAS 50 or DAS 58 (with 4 and 8 input channels respectively) that acquires the signals when it receives a TTL pulse from the trigger module. The digitizer cards have a resolution of 12 bits and a maximum sampling rate of 1 MHz.

- In the new electronic chains (figure 3.5 center) the primary signal is directly amplified by a Celians EPC1B amplifier with variable gain ($10^2$, $10^3$ or $10^4$), quasi-DC band width (low cutoff frequency lower than 0.05 Hz) and two modes of input coupling: High Impedance and High Pass Filter. The latter, which filters the signal continuous component, is the mode usually chosen. The amplified signal is directly digitized by a PXI 1036DC module from National Instruments with a digitized card of 32 bits of resolution and up to 100 kHz of sampling rate. This module can be powered by batteries and then installed inside the Faraday cage. The output digital signal is transferred by optical fiber directly to the PC. The problem of this configuration, is that the trigger has to be performed internally by the acquisition program, just in one channel instead of the logic OR of several ones. A solution already implemented for future runs is to power by batteries the trigger module mentioned in the paragraph above and connect it between the amplifiers and the PXI module providing an external source of trigger. Another drawback of this configuration is that there are no filters to the signal. To overcome this deficiency, we have used sometimes a third electronic configuration which is a mixture of the two electronic chains described above.

- In the third electronic configuration (figure 3.5 bottom), the primary signal is sent to the Celians amplifier and its output signal is converted into light

signal (Isobe probe), transmitted outside the Faraday cage through an optical fiber and converted into voltage signal (Isobe probe). Once reconverted, a Stanford amplifier is used to filter the signal, that is sent in parallel to the trigger module and the PXI digitizer card, allowing the logic OR trigger of several parallel signals.

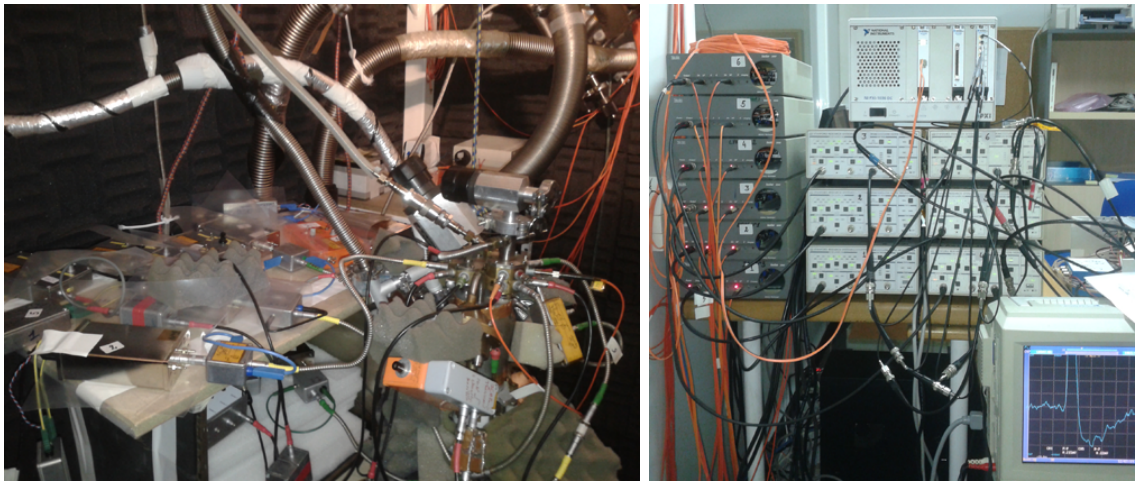

Figure 3.4: *In (a) they are shown the connections at the top of the dilution refrigerator in the LSC. There can be observed some Celians amplifiers and polarization boxes wrapped in plastic sheets to avoid ground loops. In (b) it is shown part of the electronics outside the Faraday cage, placed in the control cabin: the grey boxes are Isobe probes, the six white boxes are Stanford amplifiers and the PXI module is placed on top. Orange cables are optical fibers. The oscilloscope in the bottom right corner allows to visualize the signals.*

The shape of the digitized signal depends on the electronic components used in the chain, specially on those which apply a frequency filter. The second chain is the only one in which the signal is practically not filtered and the pulse is unipolar. It is always interesting to have the original signal from the bolometer, but in a DC acquisition the baseline must be very stable to perform a low threshold trigger; if the measurement conditions are not good enough, it is necessary to apply at least a high pass filter to remove the continuous component of the signal. By this reason, we usually use the Stanford amplifiers which can apply a band pass filter. The resulting signal is then a bipolar pulse with total area zero. In figure 3.6 are shown a typical non filtered pulse obtained with the second electronic chain and a pulse filtered by the Stanford amplifiers.

As mentioned above, several channels can be acquired simultaneously, two for

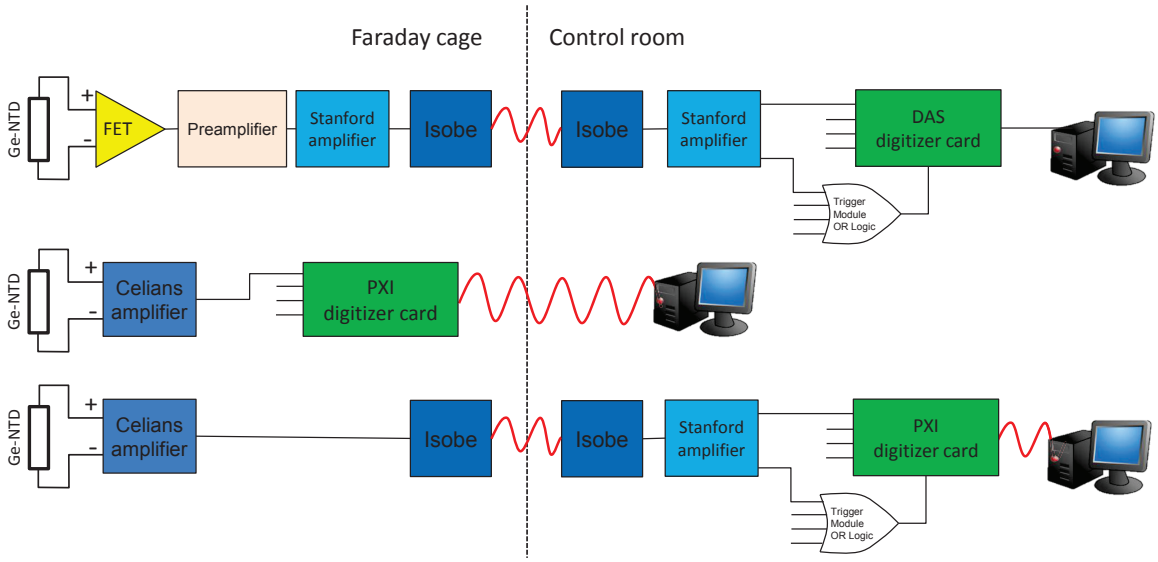


Figure 3.5: *Different electronic chains used for data acquisition indistinctly in the IAS laboratory and in the LSC. Red lines represent optical fibers.*

each scintillating bolometer (one for the heat signal and another for the light one). Parallel electronic chains are used for each channel up to the trigger module. When any of the channels produces a trigger, a trace of defined length is recorded for all the channels in binary files. A heading is attached to each trace file with additional information of the pulse as the trigger time, the trace length or the number of channels acquired.

The old acquisition software implemented in TurboBASIC and run in MS–DOS operative system, was replaced by a new data acquisition program implemented in LabWindows (C++) and dedicated to our experiment. In both programs, several parameters can be chosen by the user as the trace length (usually 4096 points per channel), the sampling rate (20–200 $\mu$s/point) or the number of points to be registered before the trigger (normally 1024 points). These programs allow to visualize online the acquired signals, the histogram of the different pulse parameters (amplitude, time constants, etc.) and scatter plots of two of them as for example, a heat amplitude versus light amplitude plot. The new acquisition software also offers the possibility to perform continuous acquisition, without trigger. In this mode, the signals are continuously registered. This option requires a big data storage, but allows to enhance the data treatment and reduces dead time with the off-line analysis.

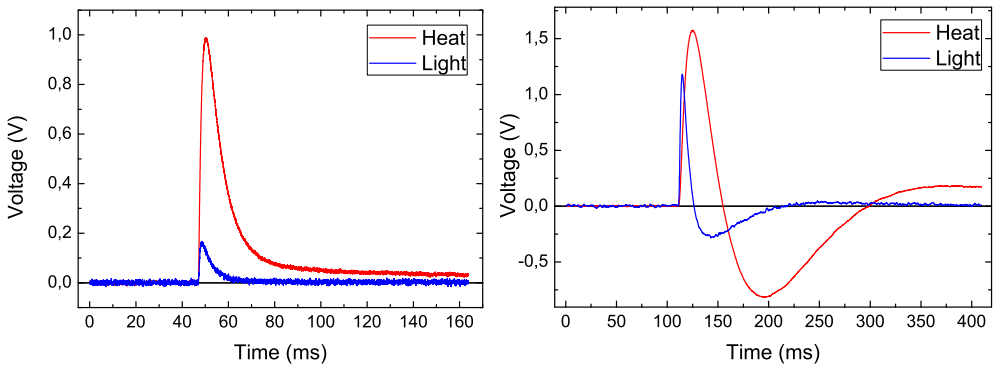


(a) (b)

Figure 3.6: *Examples of scintillating bolometer pulses from the heat and light channels obtained with an electronic chain without frequency filters (a) and with a band pass filter (b).*

## 3.3 Radioactive sources

Several radioactive sources with emission of photons, neutrons, $\alpha$ particles and recoiling nuclei, were used in this work to perform energy calibrations and to study the response of the detectors to the irradiation with different particles. In some bolometers, the radioactive contamination of the own crystal could be used to calibrate in energy, as is the case of the $SrF_2$ for the $\alpha$ particle band (see section 5.1.2) or the BGO for the $\gamma$ band (see section 5.3.1), but in most of the cases external sources are required.

The less penetrating sources are mounted inside the copper frame of the bolometer. In our scintillating bolometers, a $^{55}$Fe radioactive source is placed facing the Ge optical bolometers and avoiding the direct view of the scintillating crystals. $^{55}$Fe undergoes electronic capture to $^{55}$Mn with the emission of X–rays of $\simeq 6$ keV. These events are easily identified since they do not produce heat signal and the time constants of the light signal are faster than that from scintillating events. They are used to estimate the absolute response of the optical bolometers. Alpha sources are also installed close to the crystal in some measurements to assure that $\alpha$ particles reach the detector. We have used a $^{241}$Am source that undergoes $\alpha$ decay with a $Q_\alpha$ energy of 5637.81 keV, and the emission of $\alpha$ particles of 5442.80 keV (13.0%) and 5485.56 keV (84.5%), their corresponding recoiling nuclei of $^{237}$Np, and photons of 59.5 keV ($I_\gamma$=35.9%). A $^{210}$Po $\alpha$ source was also used, which has a $Q_\alpha$ value of 5407.46 keV and decays to $^{206}$Pb with the emission of an $\alpha$ particle of 5304.38 keV (100%).

Photon sources of $^{137}$Cs, $^{57}$Co and $^{109}$Cd were placed outside the cryostat in some measurements. Its main $\gamma$ lines are listed in table 3.1.

We used also a $^{252}$Cf source as neutrons emitter. This isotope is dominated by $\alpha$ decay but it has an appreciable spontaneous fission decay probability with the average emission of 3.7 neutrons per spontaneous fission; $2.3{\cdot}10^6$ n/s are produced per microgram of the sample [95]. Neutrons are emitted in a continuous energy spectrum with average energy of about 2 MeV. In some measurements, the $^{252}$Cf source was surrounded with paraffin to thermalize the fast neutrons.

| Isotope | $T_{1/2}$ | Emission | E (keV) | Intensity (%) |
|---|---|---|---|---|
| $^{55}$Fe | 2.73 y | X–ray Mn-$K_{\alpha 1}$ | 5.899 | 16.9 |
| | | X–ray Mn-$K_{\alpha 2}$ | 5.888 | 8.5 |
| $^{241}$Am | 432.2 y | $\alpha$ | 5485.56 | 84.5 |
| | | $\alpha$ | 5442.80 | 13.0 |
| | | $\gamma$ | 59.5 | 35.9 |
| $^{210}$Po | 138.376 d | $\alpha$ | 5304.38 | 100 |
| $^{137}$Cs | 30.07 y | $\gamma$ | 661.7 | 81.1 |
| $^{57}$Co | 271.79 d | $\gamma$ | 122.1 | 85.6 |
| | | $\gamma$ | 136.5 | 10.7 |
| $^{109}$Cd | 462.6 d | $\gamma$ | 88.0 | 3.61 |
| $^{252}$Cf | 2.645 y | n | 0–$10^4$ | 3.09* |

Table 3.1: *Radioactive sources used in this work and their relevant emissions [146]. (*)Intensity given for the $^{252}$Cf is the branching ratio for spontaneous fission.*

## 3.4 IR pulses generator

The response of the bolometer is highly dependent on its temperature, which is difficult to keep stable in long time periods, suffering noticeable drifts along a measurement. For this reason it is very important to monitor the stability of the bolometers response with a known signal of constant amplitude.

A wave generator connected to a LED diode produces infrared (IR) signals that can be controlled (intensity, length, frequency, etc.). These IR pulses are sent through an optical fiber to the bolometers inside the cryostat. They induce periodic signals in the bolometers with constant amplitude that are easily recognizable thanks

to its characteristic time constants. It is a useful tool to monitor the stability of the measurement and also to estimate its dead time just counting the fraction of IR events that are not registered in the measurement.

## 3.5 Installation at IAS

A bolometric facility has to meet certain requirements. Bolometers are very sensitive to noise contributions that disturb the signal, mainly electromagnetic and microphonic noise. The former are interferences from electronic devices or the electrical network, and the latter consist in mechanical vibrations that are eventually converted into electric signals.

The first measurements of the prototypes are performed in the facilities of the Insitut d'Astrophysique Spatiale[1] in Orsay. It is a ground laboratory equipped with a 2 x 2 x 3 $m^3$ Faraday cage in which the cryostat with the dilution refrigerator and the first stages of electronics are installed. It consists of an iron structure covered by copper plates and by an acoustic isolator to reduce microphonic noise inside the cabin. It is also electrically isolated from the network. The cryostat is placed inside a 1.5 x 1.5 x 1 $m^3$ hole dug in the ground and supported on an isolating base to avoid the transmission of vibrations from the ground. It is also surrounded by a lead shielding of 20 cm thickness to reduce the radioactive natural background. A scheme of the mounting and a picture of the inside of the Faraday cage are shown in figure 3.7. The vacuum tubes of the cryogenic system pass through lead filters before and after entering the Farady cage to uncouple vibrations from the pumps.

## 3.6 Installation at Hall B of the LSC

The most promising bolometers have been tested in low background conditions in the facilities of the Canfranc Underground Laboratory[2] (LSC). The LSC is an underground facility placed in the Pyrenees, specifically under the Monte Tobazo, between the Somport road tunnel and the old railway tunnel. It is covered by 850 m of rock (2450 m.w.e.) that provides a natural filter for muons arising from cosmic rays, resulting in an ultra-low background environment ideal to perform rare events searches. The ROSEBUD collaboration has operated in the old facilities

[1] http://www.ias.u-psud.fr

[2] http://www.lsc-canfranc.es

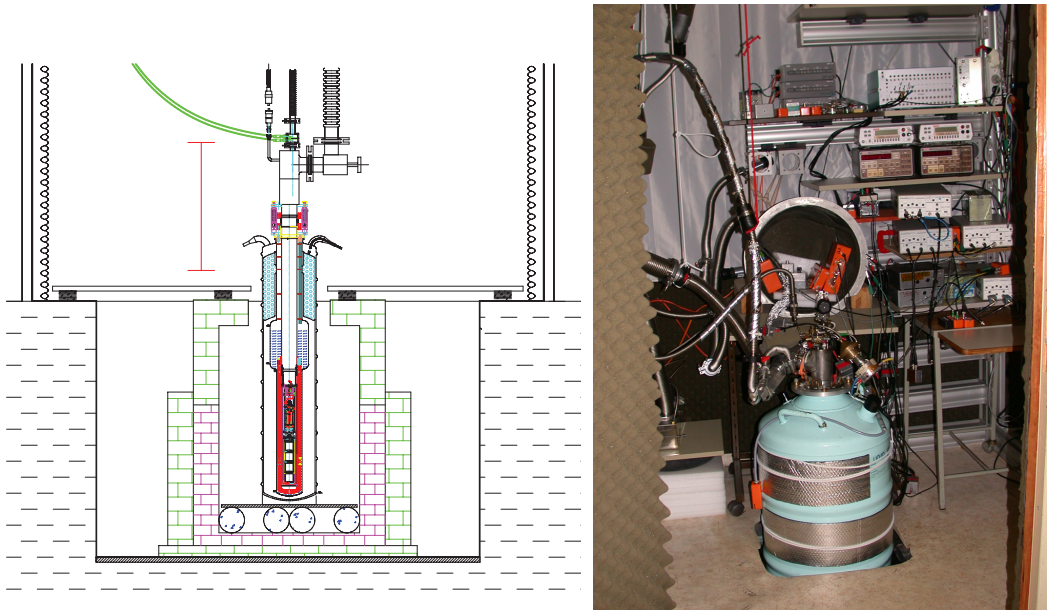

(a) (b)

Figure 3.7: *Section of the interior of the Faraday cage in the IAS laboratory (a). The lead shielding and the isolating base under the cryostat are also drawn. In (b) it is shown the cryostat with the dilution unit, and the first stages of electronics installed inside the Faraday cage in the IAS.*

(120 $m^2$) of the LSC since 1999. These facilities were run by the GIFNA group of the University of Zaragoza. The construction of the road tunnel, between Spain and France, provided a unique opportunity to build a new and larger laboratory. The new laboratory run by a consortium between the Spanish Ministerio de Economía y Competitividad, the Government of Aragón and the University of Zaragoza has been completed and delivered in June 2010. It has three experimental halls: the main hall or Hall A (40 x 15 x 12 $m^3$), the Hall B with 100 $m^2$ and 7 m height, and the smaller one, the Hall C with 50 $m^2$ and 7 m height, where it is installed a farm of HPGe detectors for radiopurity assessment. The ROSEBUD experiment was moved from the old facilities and installed in the Hall B, where a cryogenic installation was mounted next to the ANAIS[3] experiment of dark matter annual modulation search.

Since it was impossible to move the existing Faraday cage, a new one of 3 x 3 x 4.8 $m^3$ was built with the same estructure as in the IAS and old LSC facilities (iron covered with copper and acoustic isolator, as can be appreciated in figure 3.9). Some measurements of electromagnetic fields were performed to study the quality of the cabin. The frequency spectra of figure 3.10 show the attenuation

[3]http://gifna.unizar.es/anais

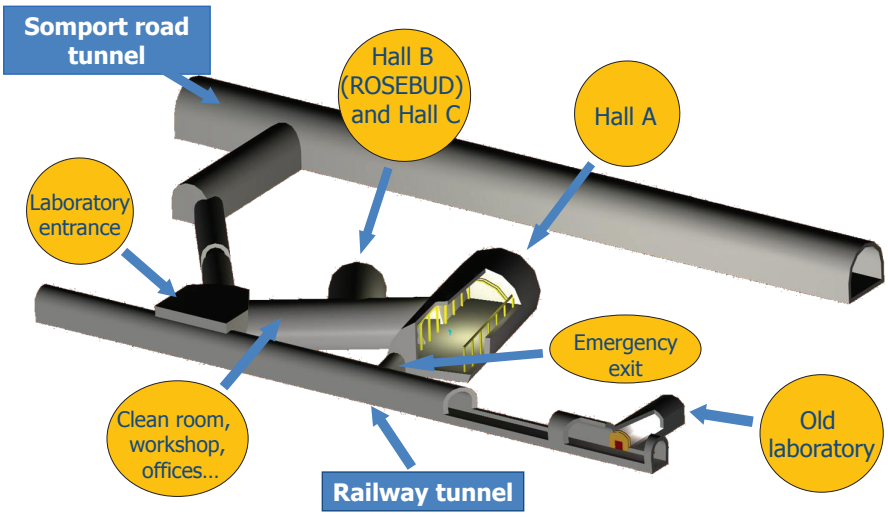


Figure 3.8: *Underground facilities of the LSC.*

of the field inside the Faraday cage (red lines) in relation with the field outside the cabin (grey lines). A metallic structure with a pulley was installed inside the cabin to lift the dilution unit (see figure 3.11a). The cryogenic system was moved from the old laboratory: cryostat, tubes, pumps, pneumatic bench, slow control system, etc. Anti–vibrational lead filters were also installed in the vacuum tubes between the cryostat and the pumping equipment, which was installed in a wooden box covered with acoustic insulator (see figure 3.11b).

In this installation more efforts were led to keep a low radioactivity and low noise environment, so that the cryostat had some improvements in this way. The liquid helium and liquid nitrogen baths are pumped and the nitrogen one is solidified to reduce the vibrations produced by the liquids boiling. The pumping lines pass through anti–vibrational filters made with foam filled barrels (see figure 3.11b). An external lead shielding of 25 cm thickness was built around the bottom half of the cryostat, where the bolometers are placed during a measurement. A base of 40 cm of polyethylene was also installed as part of a possible neutron shielding (see figure 3.9c). The external shielding is enclosed in a plastic box that could be sealed to introduce nitrogen gas from evaporation, free of the radioactive radon present in the air of the laboratory.

The electronic components outside the Faraday cage and the control computers were installed in the control room, over the ANAIS cabin.

(a) (b) (c)

Figure 3.9: *Faraday cage installed in the LSC. In (a) it is shown the iron cabin, that was internally covered with copper plates and acoustic insulator (b). In (c) it is shown the interior of the cabin, with the cryostat placed inside the lead shielding with a polyethylene basement.*

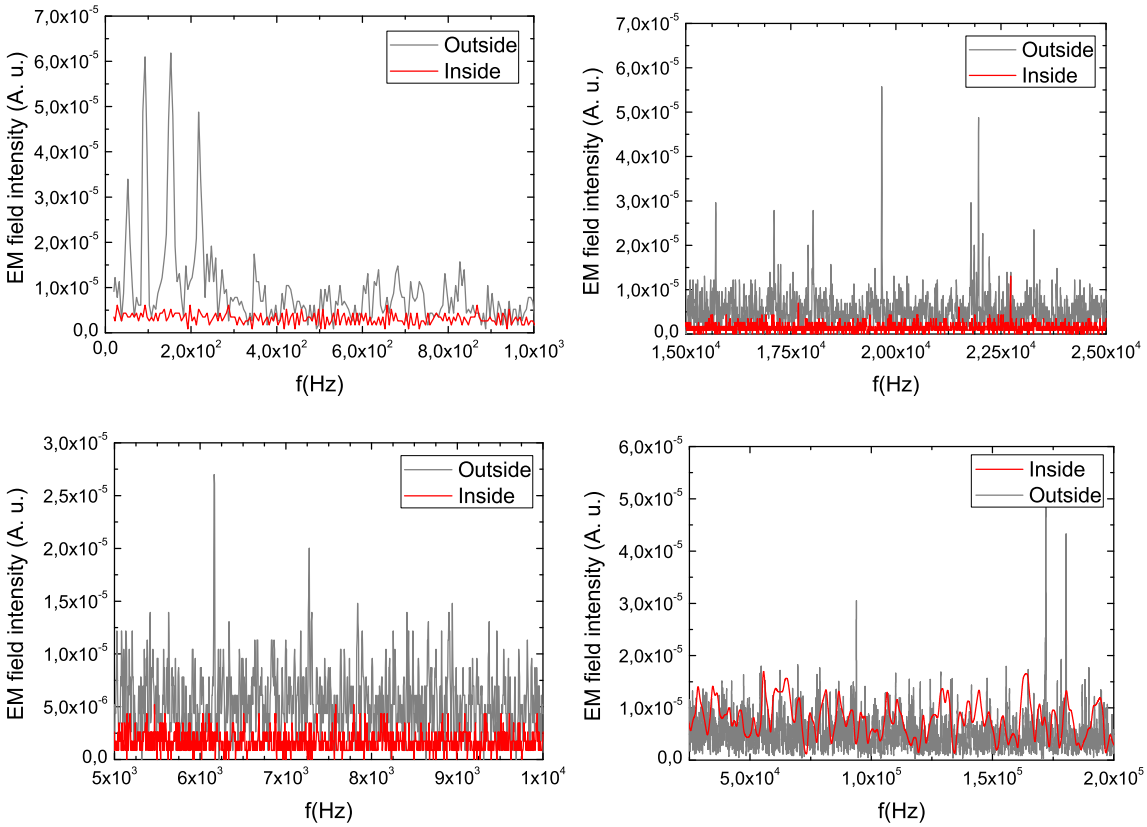


Figure 3.10: *Measurements of electromagnetic field inside (red line) and outside (grey line) the Faraday cage of ROSEBUD at the LSC at several frequency bands. Units of field intensity are arbitrary.*

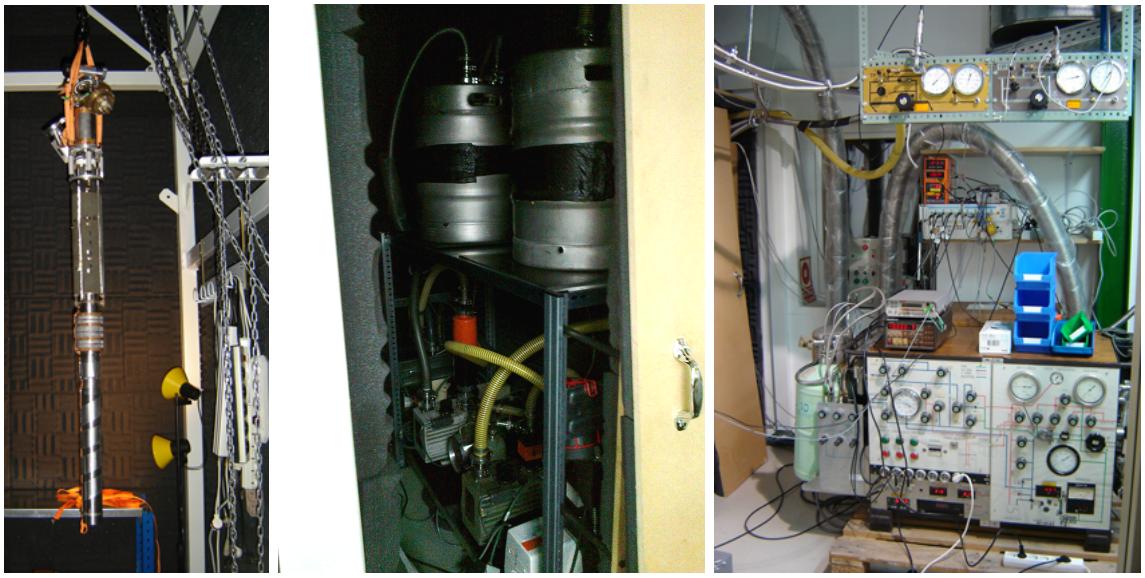

(a) (b) (c)

Figure 3.11: *In (a) it is shown the dilution refrigerator hanging from the pulley to be installed in the cryostat. In (b) they are shown some pumps and the vibrations filters made with foam filled barrels. The vacuum system control is shown in (c).*

# Chapter 4

# Pulse analysis

The signals digitized and acquired from each Ge-NTD sensor must be properly treated to obtain relevant information. In this chapter it is described this preliminary analysis. It starts with the process in which these signals are reduced to a few significant parameters organized in N-tuples (section 4.1). These N-tuples allow to control and correct measurement problems as long term instabilities (section 4.2) and the dead time (section 4.3). They also allow to reject spurious events (section 4.4).

## 4.1 N-tuples

Once the triggered pulses are acquired as was described in the previous chapter, a subsequent off-line analysis is required to obtain relevant information from each pulse. The recorded pulses are processed one by one with a program implemented in MATLAB® [147] to reduce the information from 4096 points (from now on, trace) to a N-tuple with the 10–20 most relevant parameters of the pulse. An example of original signal acquired with a $SrF_2$ scintillating bolometer is shown in figure 4.1, with the heat and light traces acquired simultaneously. The most common parameters extracted from a trace are described below and some of them are represented in a typical pulse in figure 4.2:

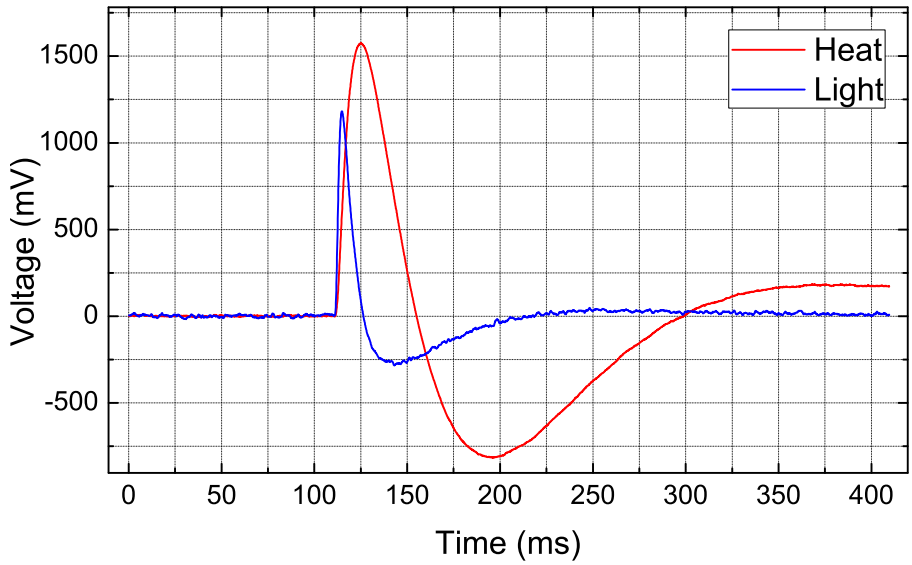


Figure 4.1: *Event acquired with a $SrF_2$ scintillating bolometer composed of two pulses: the heat signal (red) and the light signal (blue). The horizontal axis represents the time, that can be calculated with the sampling rate, in this case 10 kHz.*

- **Trigger flag.** It indicates whether the pulse reaches (value 1) or not (value 0) an established threshold level.
- **Trigger position.** Relative time (with origin in the onset of the trace) at which the pulse exceeds the threshold, if it does; in the other case, the value is set to zero.
- **Baseline and root mean square.** Mean value and standard deviation of the points before the trigger, usually the first 1000 points. The latter, the root mean square (RMS), is a estimator of the noise.

- **Pulse amplitude.** Maximum of the pulse with reference to the baseline. Several methods to estimate this parameter have been used and are explained in section 4.1.1.

- **Maximum position.** Relative time at which the pulse reaches its maximum.

- **Rise time.** Time interval in which the signal passes from the 10% to the 90% of the pulse amplitude.

- **Decay time.** Time interval in which the signal returns from the 90% to the 10% of the pulse amplitude. Other intervals are also commonly used as the decay time between the 90% and the 50% of the pulse amplitude, specially relevant for very long pulses.

- **Pulse area.** It is calculated as the addition of the points of a particular region, subtracting the baseline contribution. The region can be all the pulse (this area tends to zero in filtered signals), the positive part of the pulse (where the signal is above the 10% of the pulse amplitude), or regions corresponding with the rise time or decay time.

- **Absolute time.** Time (usually in seconds) corresponding with the onset of the pulse with regard to the beginning of the measurement. It is obtained from the heading of the event.

- **Time interval.** Time interval between the onset of the event and that of the previous one.

- **Event ID.** Correlative identification number given to each registered event.

Representation of these parameters are usually made in two kinds of graphs: a scatter plot showing two different parameters (one in each axis) or the same parameter in two different bolometers (usually heat and light of the same absorber), or a histogram showing the distribution of one parameter. For instance, the light versus heat pulse amplitude scatter plot of an absorber allows to identify the kind of particle that has interacted in the absorber: due to the different scintillation yield of different particles ($\beta/\gamma$ particles, $\alpha$ particles and other recoiling nuclei) they appear in well separated bands (see figure 4.3).

Other scatter plots as rise time versus pulse amplitude or baseline versus absolute time are very useful for the off-line analysis (instability correction, dead time estimation, spurious events rejection, etc) as will be shown in the next sections.

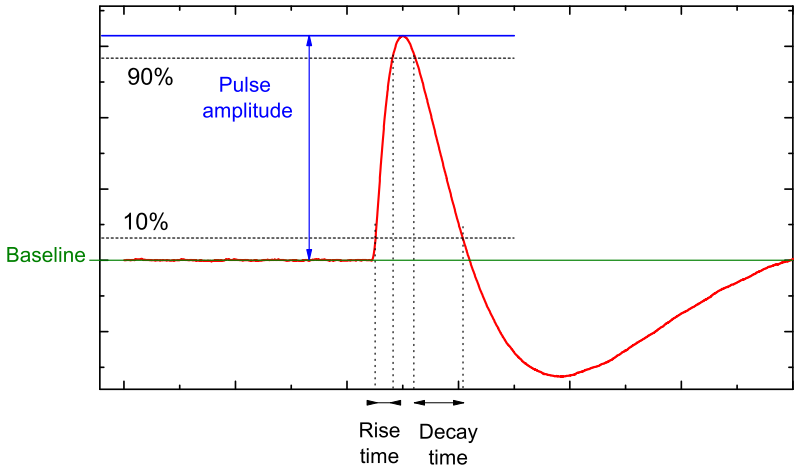


Figure 4.2: *Some of the most relevant parameters included in the N-tuples calculated from the trace of a pulse.*

### 4.1.1 Pulse amplitude estimators

The pulse amplitude is a parameter that gives information about the amount of energy deposited in the crystal by an interacting particle, either in the heat channel or in the light one. In the case of the heat channel it is used to estimate the energy of the particle and in the case of the light channel to identify its type. Since data are not ideal and are subject to statistical fluctuations, it is important to obtain a good estimator of the pulse amplitude of our signals which describes as precise as possible the response of the detector to the incident particles. By definition, a good estimator should be consistent, unbiased and efficient [148]. Several estimators of the pulse amplitude have been considered and tested. A description and evaluation of each of them is presented below:

- **Maximum.** This is the simplest method, it consist in taking directly the maximum value of the trace (subtracting the baseline). It is highly dependent on the noise and it is biased since it gives always a value higher than the real one, which is specially noticeable at very low energy since at the level of noise, the value is never zero as can be observed in figure 4.4.

- **Fit to average pulse.** In this method, each trace is fitted to a normalized average pulse (previously constructed by averaging pulses from the data) with two degrees of freedom, the temporal position of the pulse and its amplitude (that is allowed to be negative). The fitting procedure is carried out in a reduced region of the trace. It is a good method if the pulse shape is the same for all the signals of interest and independent of the energy, but in some cases

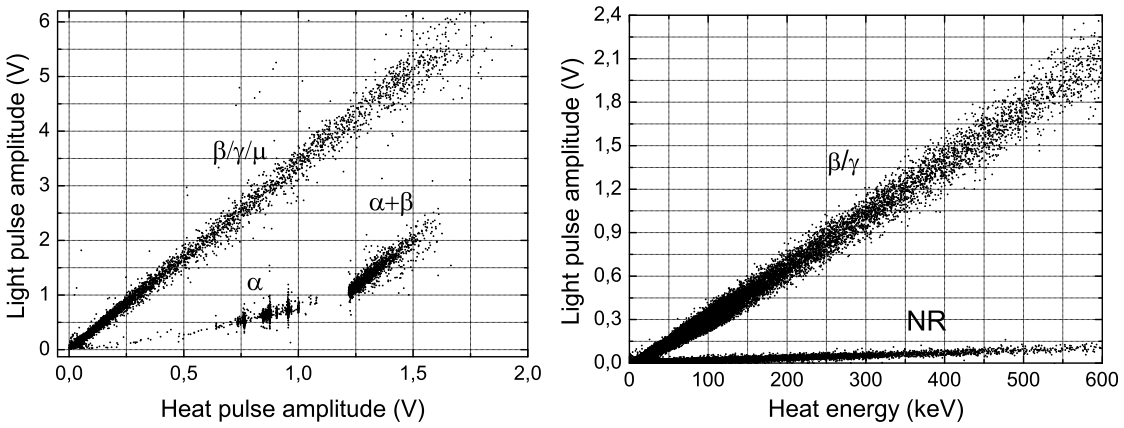


(a) (b)

Figure 4.3: *In (a) it is represented the heat versus light pulse amplitude of the events detected with a $SrF_2$ scintillating bolometer in a high energy measurement. Events due to $\alpha$ particle interactions are well separated from those due to $\beta/\gamma/\mu$ particles. In (b) it is shown the heat pulse amplitude (calibrated in energy) versus light pulse amplitude of the events registered in a sapphire scintillating bolometer in a low energy measurement with a $^{252}Cf$ neutron source. The $\beta/\gamma$ events are discriminated from nuclear recoils (NR) from neutron irradiation.*

you are interested in different kinds of particles or different ranges of energy, which induce slightly different pulse shapes, and then the estimations could not be as good as expected.

- **Smoothing.** In this case, a smooth filter is applied to the original pulse, resulting in a filtered pulse in which each channel is an average of its $n$ neighbor channels in the original trace (see figure 4.5). The number of neighbors used is optimized to each particular measurement according to the signal-to-noise ratio (pulse amplitude-RMS ratio). The pulse amplitude value is obtained as the maximum of the filtered pulse. With this method, noise or other fine–scale structures are removed, remaining the fundamental shape of the pulse. It is specially effective to reduce periodical noises as those arising from the electrical network.

- **Optimal filtering.** For this method it is considered that the pulse shape is independent of its amplitude $a$ and it exists a normalized template $s(t_n)$ for all the pulses, describing the acquired signal $v(t_n)$ as

$$v(t_n) = a \cdot s(t_n) + \sigma, \tag{4.1}$$

where $\sigma$ is the random noise. We obtain the template by averaging normalized

pulses as in the second method, and the noise contribution by averaging noise traces (free of pulses, i.e. traces with trigger flag of value 0). The aim of this procedure is to estimate $a$ by minimizing the chi-square function of $v(t_n)$. This can be done either in the temporal domain (specially if we had a flat noise in the frequency domain) or in the frequency domain, using the discrete Fourier transform. The pulse amplitude $a$ that minimizes this function in each domain is

$$a = \frac{\sum_n v(t_n)s(t_n)}{\sum_n s^2(t_n)} \tag{4.2}$$

$$a = \frac{\sum_n \frac{Re\left(v(f_n)\right) Re\left(s(f_n)\right) + Im\left(v(f_n)\right) Im\left(s(f_n)\right)}{\sigma^2(f_n)}}{\sum_n \frac{|s^2(f_n)|}{\sigma^2(f_n)}}. \tag{4.3}$$

In the frequency domain the frequency range can be restricted to an interval in which the signal-to-noise ratio has higher values, incorporating minimum and maximum cutoff frequencies. This method is widely explained in reference [149]. The problem of this procedure is that the optimum filter works properly with clean traces, but if there are any pile-up or other structure that distorts the pulse, the estimated amplitude is miscalculated.

Every estimator of the pulse amplitude has its advantages and drawbacks and it can suit well for certain measurements.

One parameter used to compare the different methods has been the energy resolution of the spectral peaks obtained with them, which is related with the efficiency of the estimator. The best full-width at half maximum (FWHM) resolution values obtained for a specific measurement, with each method, for an $\alpha$ peak of $^{226}$Ra (4870.63 keV) in a heat spectrum of a $SrF_2$ scintillating bolometer are summarized in table 4.1. Clearly, in this case the maximum method is the less efficient estimator; smoothing (with the adequate number of neighbors channels $n$) produces a slight improvement; and the methods that use a template pulse (fit to average and optimal filtering) are the most efficient ones, but they tend to lose an important number of pulses due to pile-up.

Other noticeable difference between methods is shown in figure 4.4, which displays the low energy region of a light versus heat pulse amplitude scatter plot using the pulse amplitude from two different estimators: the maximum and the fitting to average. In the first case, the cluster of noise events is centered at 27 mV

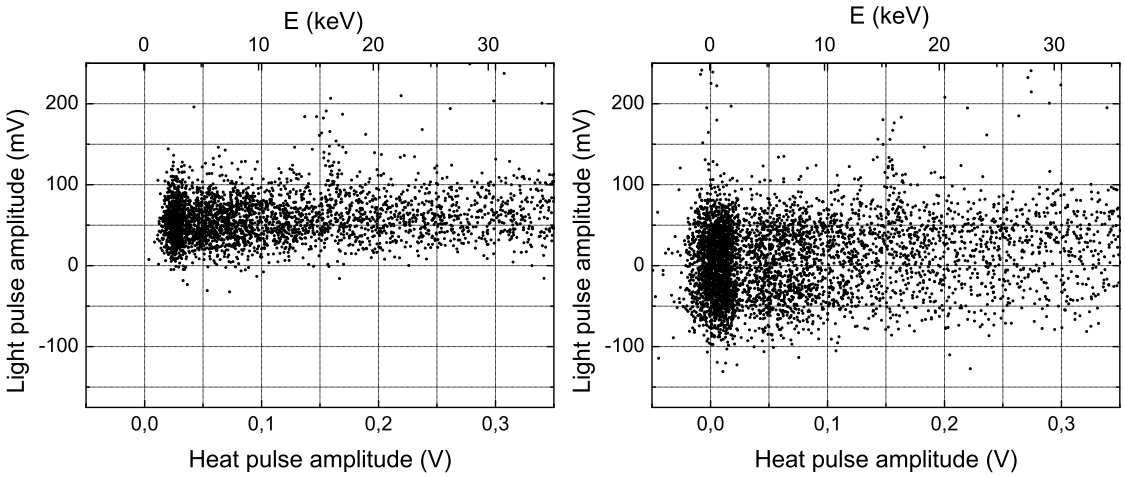


(a) (b)

Figure 4.4: *Heat versus light pulse amplitude of a low energy measurement with a BGO scintillating bolometer. In (a) the pulse amplitude was estimated using the maximum of the traces and in (b) was used the fitting to average method. In the first case the noise distribution is clearly more biased (shifted to positive values due to the RMS of the heat and light channels).*

heat and 52 mV light, while in the second one it is centered at 7 mV heat and 0 mV light, lowering the detection threshold. In the light channel, the second distribution is wider than the first one, so that the discrimination threshold improvement is less noticeable.

The results obtained with each estimator slightly depend on the experimental conditions, and consequently the best estimator has to be determined for each specific measurement. As a rule of thumb, smoothing provides great improvements in measurements with noisy baselines, fitting to average pulse or optimal filtering are strongly recommended to study low energy measurements due to the improvements in energy resolution and for high energy measurements the method of the maximum works well enough and it is the fastest regarding to computing time (and can be easily implemented in the on-line acquisition). In the different measurements analyzed in this thesis, we have used the estimator that better works in each case.

### 4.1.2 Off-line trigger in continuous acquisitions

In continuous acquisition, an off-line analysis is needed to search for pulses along the continuous trace and extract its parameters to construct the N-tuples. We have

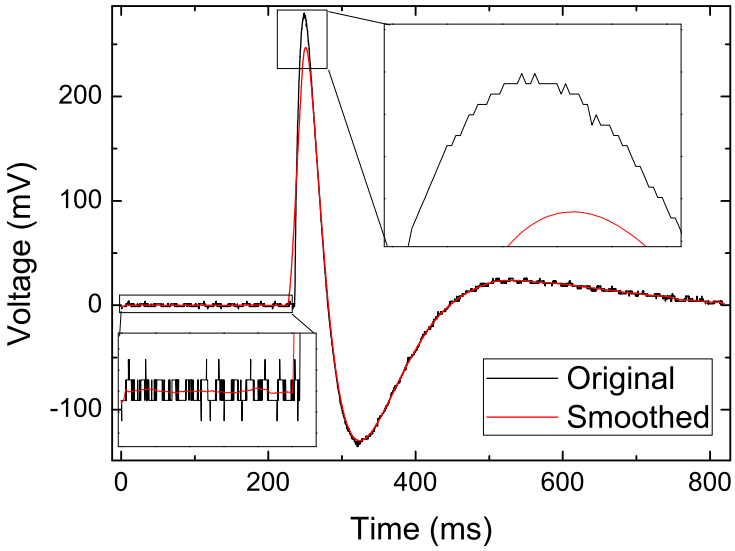


Figure 4.5: *Heat pulse before (black) and after (red) applying a smoothing filter (some regions are zoomed). The pulse shape suffers some changes, but the signal-to-noise ratio is optimized.*

| Method | FWHM (keV) |
|---|---|
| Maximum | $22.6 \pm 0.5$ |
| Fit to average | $9.8 \pm 0.2$ |
| Smoothing | $17.2 \pm 0.2$ |
| Optimal filtering | $7.9 \pm 0.2$ |

Table 4.1: *Values of FWHM energy resolution obtained with different estimators of the pulse amplitude for the $\alpha$ peak of $^{226}Ra$ in a heat spectrum of a $SrF_2$ scintillating bolometer.*

implemented a trigger algorithm to find the pulses. It compares the voltage values between two points spaced a certain time interval $\delta$; if the difference V(t)-V(t-$\delta$) exceeds a threshold $h$, the algorithm gives a trigger flag (see figure 4.6a) and starts searching again after a dead window (as short as possible to minimize the dead time). The values of $\delta$, $h$ and dead window have to be properly chosen for each measurement. Once a pulse is found, the N-tuples creation program processes it in a window around the trigger position, wide enough to encompass the pulse and its pre-trigger region. Figure 4.6b shows the trigger flags (black triangles) found in a long trace.

An advantage of continuous traces in multichannel acquisitions, as in scintillating bolometers, is that a logic trigger can be included to be performed off-line avoiding

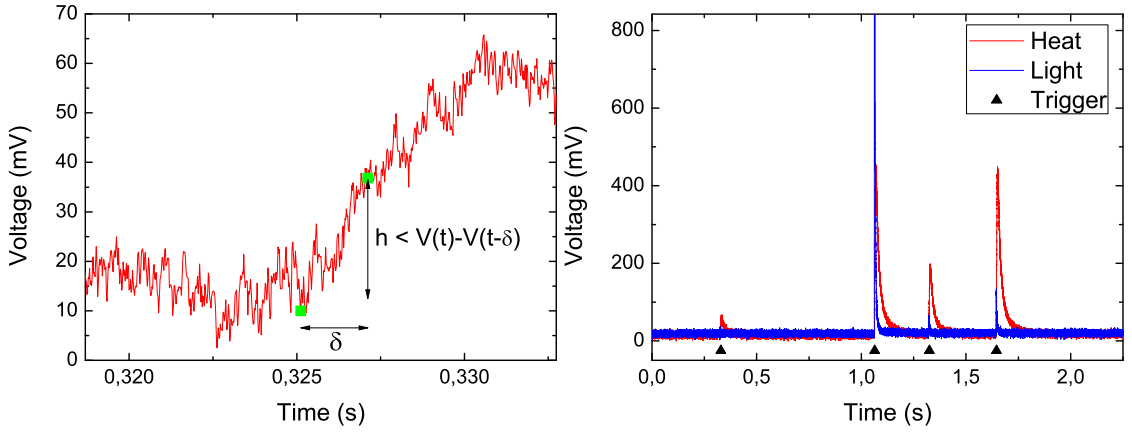


(a) (b)

Figure 4.6: *In (a) it is shown the trigger algorithm concept. In this specific trace, the second green point gives a trigger flag when its voltage is compared with the one of the first green point and the difference exceeds the threshold h. In (b) it is shown a long trace of a scintillating bolometer of $CaF_2$ (heat and light channels) and the trigger flags (black triangles) obtained with the algorithm.*

the use of a external trigger module.

## 4.2 Instability correction

As stated in section 3.4, the constant IR pulses periodically sent to the scintillating crystals allow to monitor the stability of the measurement and detect variations of the gain caused by changes in the temperature or in the behavior of the electronic devices. The scintillating crystals used in this work are almost transparent to IR light, and the IR photons are directly collected in the Ge optical bolometer producing a light signal of constant amplitude easily identified since their time constants are different from that of real events (particles interacting in the crystal scintillator). This fact can be noticed in figure 4.7a.

The IR pulses practically do not produce a heat signal (see figure 4.7b) and, consequently, to monitor and stabilize the heat channel one has to resort ro intense spectral lines (from internal contaminations of the crystals or from external sources).

The time evolution of the pulse amplitude of the reference signals (IR pulses in the light channel and spectral lines in the heat channel) shows the gain changes during the measurement. Figure 4.8 shows, as and example, these variations in two measurements: one that practically can not be corrected and another one that can

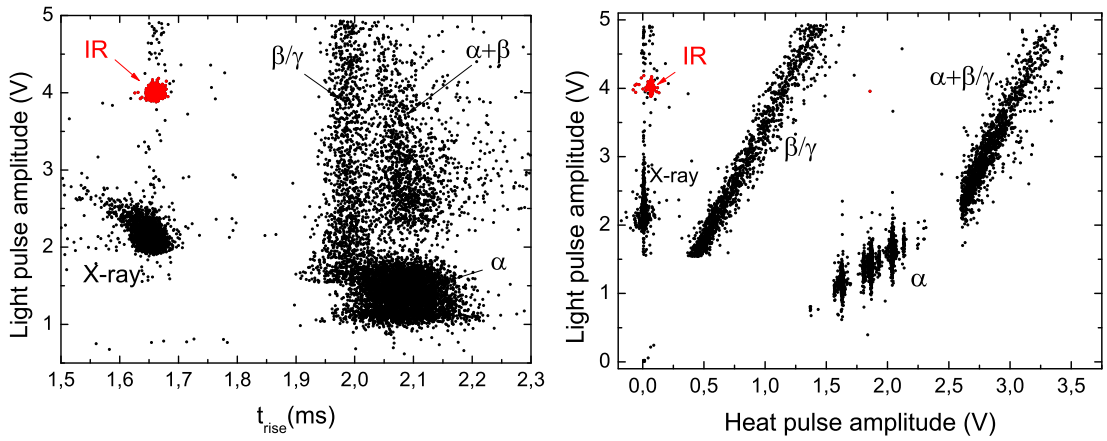


(a) (b)

Figure 4.7: *(a) Scatter plot of pulse amplitude versus rise time in the light channel of a $SrF_2$ scintillating bolometer. Events that interact directly in the optical bolometer (IR and X–rays from the $^{55}Fe$ source) are faster than those producing scintillation in the crystal; and among these, $\beta/\gamma$ events are faster than $\alpha$ interactions and $\alpha + \beta$ coincidences. (b) Heat versus light pulse amplitude of the events of the same measurement. IR and X–rays only produce a heat signal.*

be corrected. The first case (figure 4.8a) shows the IR pulses in the light channel of a BGO scintillating bolometer; the measurement was highly unstable and it is quite hard to obtain quality data. Similar instabilities were observed for the $\alpha$ lines in the heat channel. In the second case (figure 4.8b), the most intense $\alpha$ lines arising from internal contamination of the $SrF_2$ crystal are used to monitor the stability in the heat channel; the gain variation is smooth and continuous (probably the dilution refrigerator was cooling down slowly during the measurement; in fact a similar behavior was observed for the IR pulses in the light channel) and data can be corrected or stabilized.

If the gain as function of time can be parameterized (usually with a first or second degree polynomial function), the pulse amplitude of every pulse can be corrected by applying a factor whose value depends on the pulse absolute time (see figure 4.8b).

## 4.3 Dead time estimation

The dead time of a measurement is the time in which the detector is not sensitive. It is related with the duration of the pulse signals and with the electronic data processing. It affects specially in measurements with high detection rate.

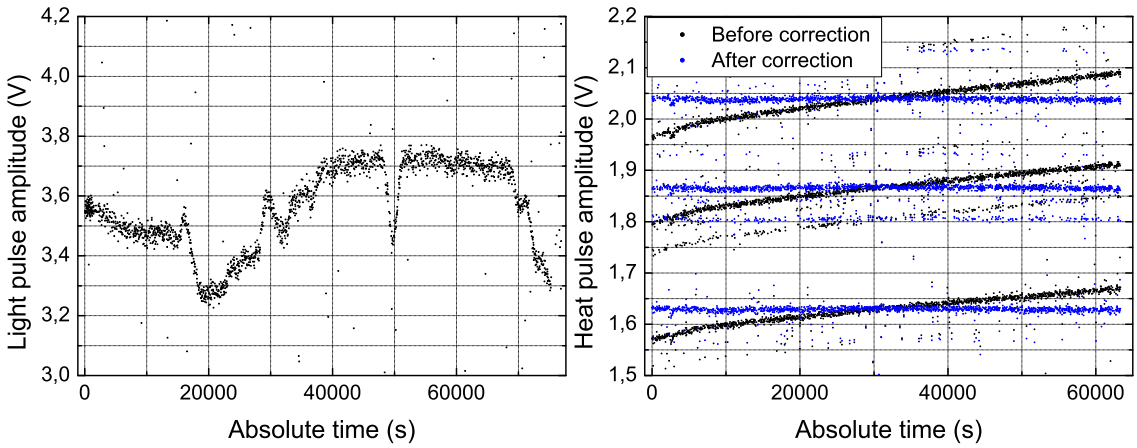


(a) (b)

Figure 4.8: *In (a) it is shown the pulse amplitude as function of time for IR pulses in the Ge optical bolometer mounted in a BGO scintillating bolometer. It was a highly unstable measurement. In (b) it is shown the pulse amplitude as function of time for $\alpha$ spectral lines in a $SrF_2$ scintillating bolometer before (black) and after (blue) applying the method for stability correction. Stabilization was done with the $\alpha$ line at around 2.05 V and using as correction factor the ratio between its mean value and the value estimated from the polynomial fit as a function of the time.*

IR pulses are also used to estimate the dead time. Since they are sent with a known frequency, we know how many pulses have been sent in a whole measurement of duration $t$. Identifying the IR pulses detected in the bolometer, we can estimate the dead time of the measurement as

$$t_{dead} = \frac{Sent - Detected}{Sent} t \tag{4.4}$$

## 4.4 Spurious events rejection

Some filters must be applied to the data to efficiently reject events that are not due to particle interactions in the scintillating crystal or events in which the N-tuple parameters could have been miscalculated.

When a scintillating bolometer is exposed to radiation, incident particles can deposit energy not only in the scintillating crystal, but also in other pieces of the detector. This amount of energy can reach the Ge–NTD sensor inducing a signal that could mimic a crystal signal. The detector parts that more contribute with this

kind of events are those which are closer to the Ge–NTD or the crystal; these are, for instance, the Ge–NTD itself and some coupling and thermalization pieces between the Ge–NTD and the crystal. Usually, these events can be identified because of their different time constants or scintillation properties. Particles interacting in the Ge–NTD are faster than those interacting in the crystal, since they avoid the thermal boundary resistance (Kapitza resistance) between the crystal and the Ge–NTD. To reject these events, cuts are performed in the parameter space of pulse amplitude versus rise time (or decay time) as can be seen in figure 4.9. The distribution of rise (decay) time spreads for very low amplitude signals, so the cut efficiency is very limited below a pulse amplitude threshold.

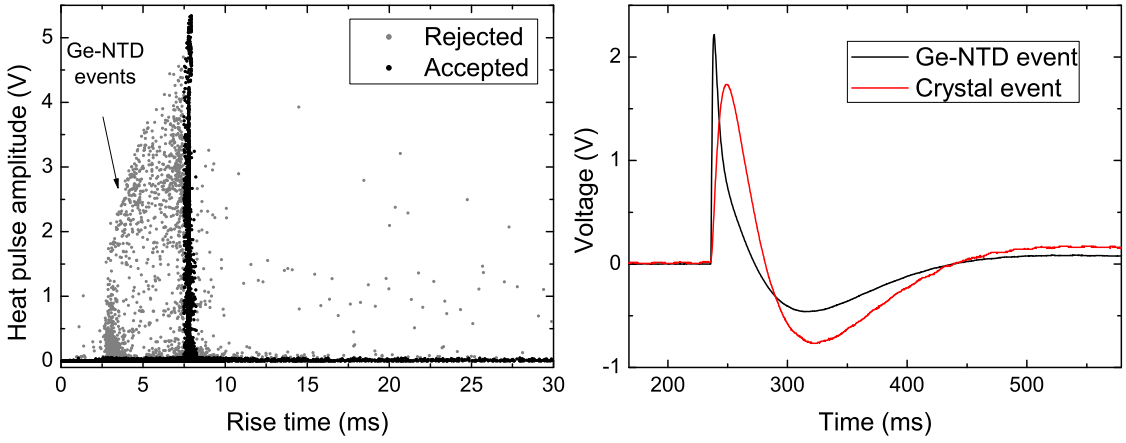


(a) (b)

Figure 4.9: *(a) Scatter plot of pulse amplitude versus rise time in the heat channel for a $SrF_2$ scintillating bolometer. Gray events are probably interactions in the Ge–NTD sensor and are rejected by the rise time cuts. In (b) it is shown the comparison of one of these events with an event interacting in the $SrF_2$ crystal (both are heat pulses).*

The digitized signal of some events can be deformed due to several reasons. For instance, particles with energies out of the range of some electronic devices induce saturated and deformed electric signals (see figure 4.10), some drifts in the baseline can surpass the threshold level and trigger false pulses, and overlapped events cause a bad estimation of the N-tuple parameters. All these events can be identified studying certain parameters as the ratio between pulse amplitude and pulse area, the baseline level or the time constants. Along a measurement, there could be some periods of large electronic noise. Events acquired in these periods worsen the quality of the measurement, so they are rejected using the root mean square (RMS) of the baseline (an example is shown in figure 4.11).

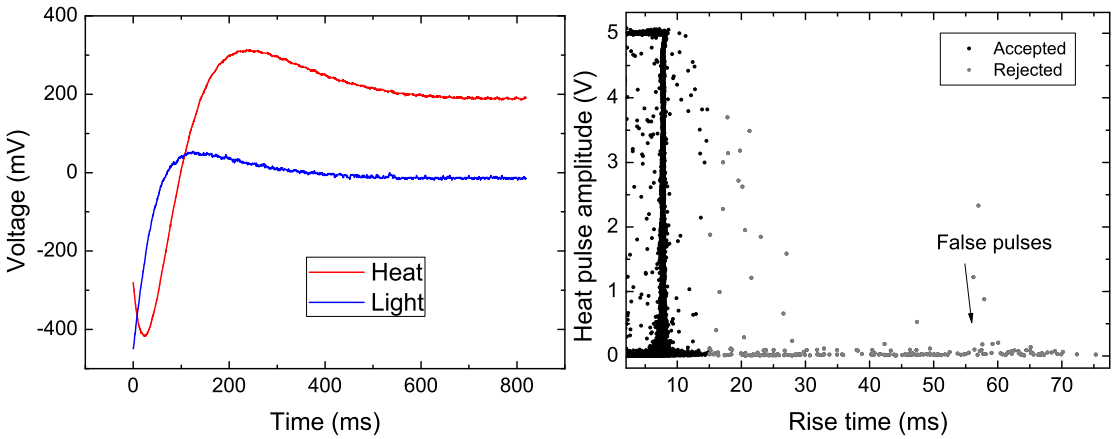


(a) (b)

Figure 4.10: *In (a) it is shown a false pulse due to the distortion produced by a previous energetic event that triggers the acquisition. In (b) it is shown the cut performed in rise time to avoid these false events.*

Another criterion to reject events is the comparison of their maximum positions in the traces of heat and light. Sometimes, a second event is registered in a trace after the event that caused the trigger and then the algorithm that estimates the pulse amplitude could assign to one event different pulses in heat and light (see figure 4.12a). To avoid that, it is required that the temporal positions of the heat and light maxima have the adequate separation (light pulses are faster than heat pulses) as can be observed in figure 4.12b. Since in noise traces (without pulses) the maximum position can be found all along the trace, with this method, events that induce a signal only in one of the channels (heat or light) are rejected. Another option is to restrict the pulse amplitude estimation to a narrow temporal window just after the trigger instead of the whole trace, assuring that events with only one signal (heat or light) are not rejected.

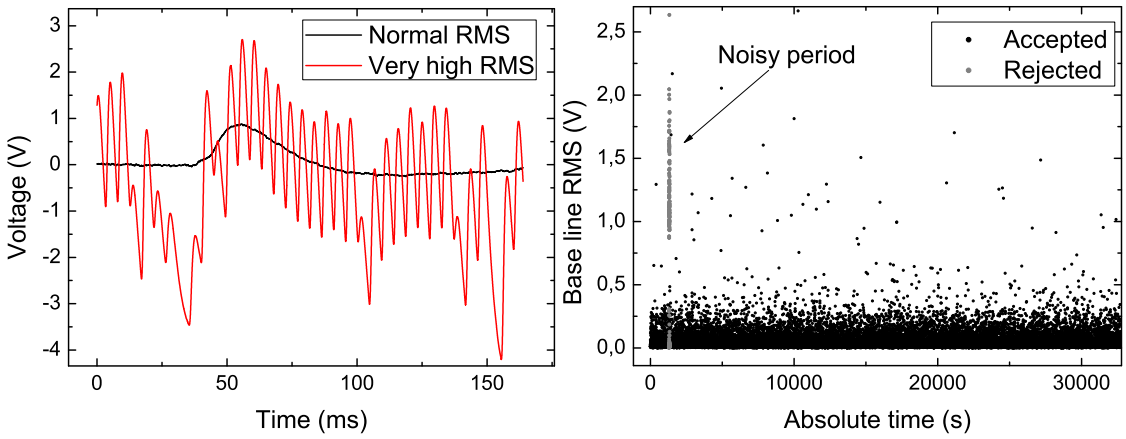


(a) (b)

Figure 4.11: *In (a) they are shown two independent heat events of the same measurement. The one plotted in red was taken during a noisy period. In (b) it is shown the RMS of the base line versus the events absolute time, a period of high RMS is rejected.*

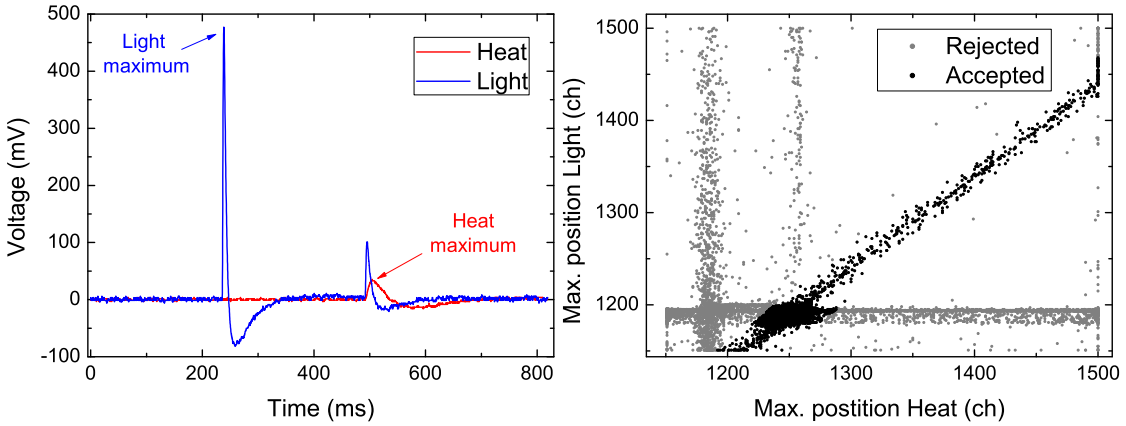


(a) (b)

Figure 4.12: *(a) A double trace of heat and light in which the maximum of each channel corresponds to different pulses. (b) A scatter plot of the pulse maximum position in the light channel versus the same parameter in the heat channel. Rejected events are plotted in grey and the accepted ones in black.*

# Chapter 5

# Characterization and applications of scintillating bolometers

The characterization of scintillating bolometers for several purposes is presented in this chapter. First, in section 5.1 it is shown the study of a $SrF_2$ scintillating bolometer, including the characterization of its heat and light responses to different particle interactions, the measurements of its fluorescence spectrum at different temperatures and the application and prospects of this material for double beta decay searches. Bolometers devoted to neutron detection and spectroscopy, based on nuclear reactions induced by neutrons in Li-based materials, are tested and studied in section 5.2. In the last section of this chapter, section 5.3, the discrimination properties of scintillating bolometers of BGO and sapphire and their application for dark matter searches are analyzed.

## 5.1 A $SrF_2$ scintillating bolometer

A $SrF_2$ crystal was tested as scintillating bolometer at around 20 mK of temperature in the facilities of the IAS in Orsay. We have analyzed its response in both channels, heat and light, its particle discrimination capability and its potentiality for the study of double beta decay of $^{84}$Sr nuclei.

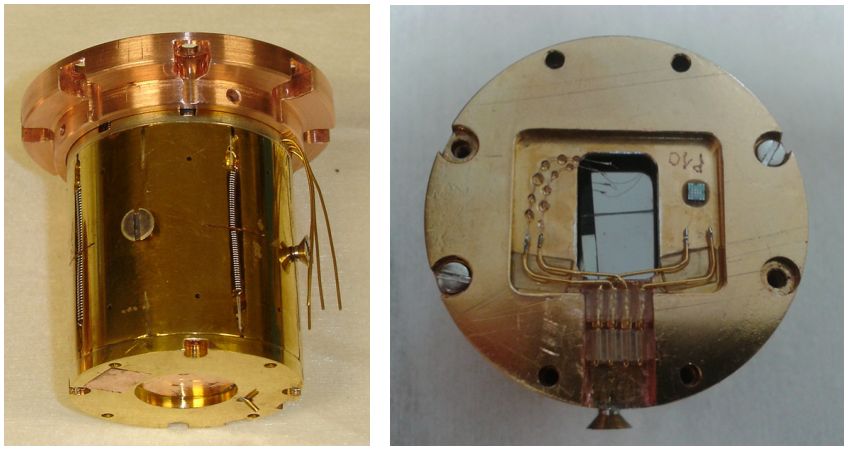

(a) (b)

Figure 5.1: *$SrF_2$ scintillating bolometer used in this work: (a) side view; the protruding screw in the right side is used to introduce in its tip internal radioactive sources, and the upper piece to couple the bolometer to a dilution refrigerator. (b) top view; it shows the polarization circuit for the Ge–NTD sensor glued to the crystal. Thermalization of the wires can be appreciated with glue drops.*

### 5.1.1 General features

Strontium fluoride is an inorganic material with cubic crystal structure. It is transparent to light in the wavelengths from vacuum ultraviolet (∼150 nm) to infrared (∼11 $\mu$m). It is a dielectric and diamagnetic crystal with a Debye temperature $\Theta_D = 381.7$ K [150]. At very low temperatures, its molar heat capacity can be written as

$$C(T) = \frac{12}{5}\pi^4 n N_A k_B \left(\frac{T}{\Theta_D}\right)^3 = 1.048 \cdot 10^{-4} T^3 J/(mol \cdot K), \qquad (5.1)$$

being $n$ the number of atoms per molecule, $N_A$ the Avogadro number, $k_B$ the Boltzmann constant and $T$ the temperature in Kelvin. The heat capacity per unit volume of the Ge–NTD sensor attached to the $SrF_2$, mainly due to free electrons,

can be expressed at low temeperatures as

$$C(T) = \gamma T = 5 \cdot 10^{-7} T J/(cm^3 \cdot K), \tag{5.2}$$

where the value of $\gamma$, dependent on the dopant concentration, was provided by N. Coron [151] for our sensor.

The crystal used in this work weights 53.6 g and is cylindrical shaped (25 mm high and 25 mm diameter). Its heat capacity is $4.5 \cdot 10^{-5} T^3$ J/K, that at 20 mK is $3.6 \cdot 10^{-10}$ J/K. A rectangular prism shaped Ge–NTD sensor, with dimensions $9.04 \times 6.68 \times 0.451$ mm$^3$, was glued to its surface. Its heat capacity is $1.4 \cdot 10^{-8} T$ J/K which results in $2.8 \cdot 10^{-10}$ J/K at 20 mK (slightly smaller than that of the $SrF_2$ crystal). Adding both contributions, we estimate a total heat capacity at 20 mK of temperature of about $6.4 \cdot 10^{-10}$ J/K. In the figure 5.1 is shown the copper frame that enclosed the crystal (internally coated with silver) and the Ge–NTD polarization circuit. In most of the measurements it was mounted in a double bolometer configuration with a 45 $\mu$m thick and 25 mm diameter Ge wafer as light detector. For details of the optical bolometer see [43]. Some preliminary results with this bolometer were already presented and published [152].

A $^{55}$Fe source was installed inside the copper frame facing the Ge bolometer for its absolute calibration. Some measurements with the $SrF_2$ scintillating bolometer were performed using also a $^{241}$Am alpha source placed inside the bolometer copper frame. Sometimes, an external $^{252}$Cf neutron source was used to induce Sr and F nuclear recoils and an external $^{137}$Cs source to allow gamma energy calibration. For the characterization of the $SrF_2$ response we can also profit from the internal contamination in radium of the $SrF_2$ crystal (see below).

### 5.1.2 Heat response

The heat–light scatter plot of figure 5.2 allows to discriminate the $\beta/\gamma/\mu$ band, the $\alpha$ lines and the $\alpha+\beta$ events band, and to build their corresponding heat spectra (figure 5.3) . The $SrF_2$ crystal characterized in this work has an inner contamination arising from the natural radioactive chains (figure 5.4) whose most intense alpha lines are labeled in figure 5.3a and shown in table 5.1. We identified alpha emissions coming from $^{226}$Ra and its daughters $^{222}$Rn, $^{218}$Po and $^{210}$Po, and also from $^{224}$Ra and its daughter $^{220}$Rn. Other elements from these chains are harder to identify: $^{214}$Po and $^{212}$Po have very short half-lives (160 $\mu$s and 0.3 $\mu$s, respectively) in comparison with the bolometer response (tens of ms) and their alpha particles are, in practice, detected simultaneously with the electron arising from their parents $^{214}$Bi and $^{212}$Bi,

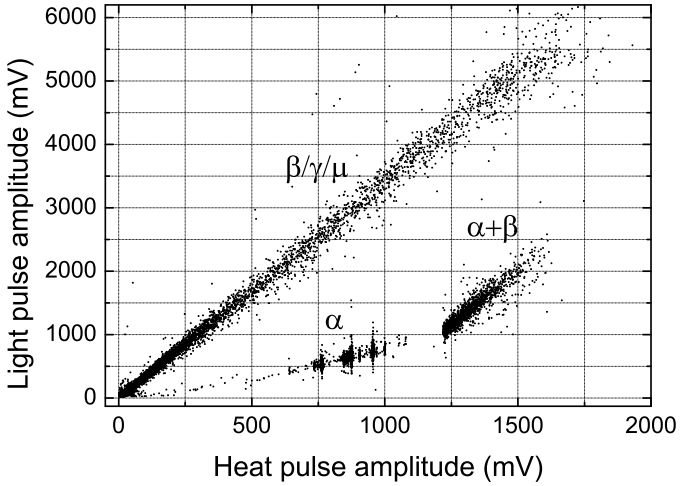


Figure 5.2: *Scatter plot showing the heat and light pulse amplitude for each event obtained in a measurement of 14 h of live time. The discrimination capability of scintillating bolometers is evident, identifying, in this case, electron recoiling events (from electrons, photons and muons), alpha particles ($\alpha$) and coincidences of $\alpha + \beta$ events.*

resulting an event with the energy equal to the sum of the alpha and beta particles (tagged as $\alpha + \beta$ in figure 5.2 and also shown in figure 5.3b); $^{216}$Po has a half-life of 0.15 s, lying nearly always in the trace of the previous event from $^{220}$Rn (trace length was 0.82 s) and consequently being lost in our analyses. The two peaks coming from a $^{241}$Am $\alpha$ source are also labeled in the spectrum 5.3a. There is a small peak in the right wing of the most intense one, hard to discriminate, that could arise from $^{228}$Th (parent nuclei of $^{224}$Ra, with $Q_\alpha = 5520$ keV) but we can not claim the presence of $^{228}$Th. Some events placed at around 642 mV (not shown in figure 5.3a) may also indicate the presence of $^{232}$Th ($Q_\alpha = 4083$ keV) with an activity of approximately 3 mBq/kg.

The activity was calculated from the areas of the peaks (shown in table 5.1) taking into account the dead time of the measurement. It seems that the chain from $^{226}$Ra is broken, probably because of the long half-life of $^{210}$Pb (22 yr). We estimated an activity of $496 \pm 2$ mBq/kg of $^{226}$Ra, $72 \pm 6$ mBq/kg of $^{210}$Po and $21 \pm 1$ mBq/kg of $^{224}$Ra. These numbers show that scintillating bolometers can be used for radiopurity assessing of crystals. Thanks to the discrimination capabilities they can reach sensitivity levels of the order of mBq/kg or even lower.

The detector showed a good linearity in the heat response as can be seen in figure 5.5a. FWHM energy resolution less than 0.2 % was reached for alphas. We assume that in an alpha decay both, the alpha particle and the nuclear recoil, produce

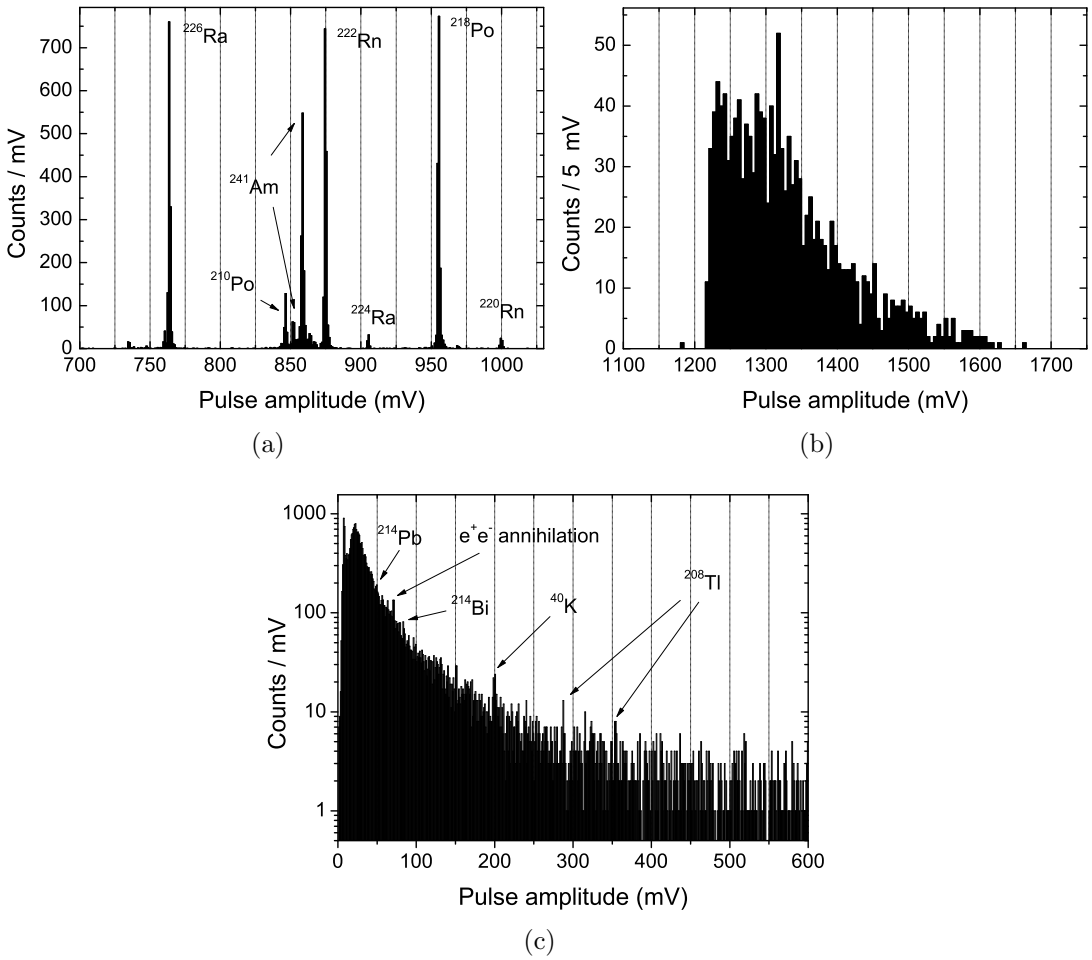


Figure 5.3: *Heat amplitude spectra of the $\alpha$ (a), $\alpha + \beta$ (b) and $\beta/\gamma/\mu$ (c) regions observed in the measurement previously shown in figure 5.2. Main identified lines are labeled.*

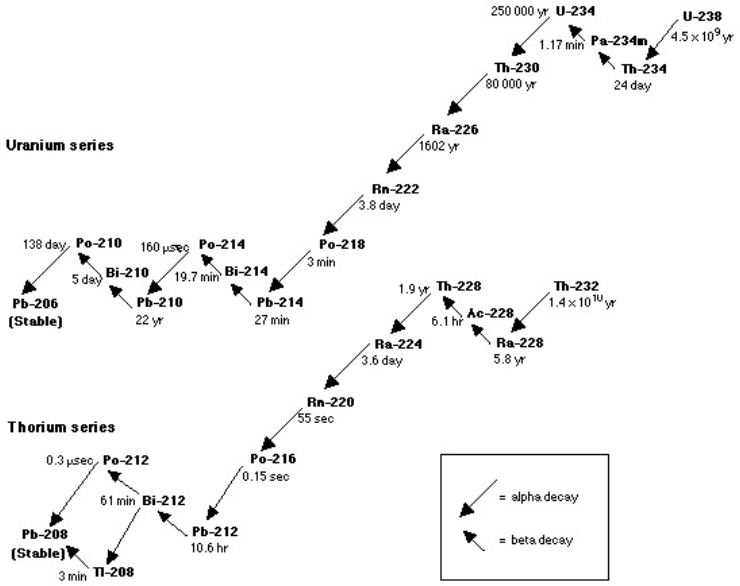


Figure 5.4: *Natural radioactive decay series of* $^{238}U$ *and* $^{232}Th$*. The half–life of each isotope is indicated. Taken from [153].*

a similar heat response in the bolometer, consequently, we assigned the $Q_\alpha$ energy value of the decay to each peak. This approach was proved with a simple calculation: the difference between the heat response of the coincidence "$\alpha$ + nuclear recoil" measured in the crystal and the estimated response to only the $\alpha$ particle using the $\alpha$ events from the $^{241}$Am source, differs only in 2% from the expected energy of the nuclear recoil.

In the $\beta/\gamma/\mu$ band spectrum, we identified gamma emitters coming probably from the natural radioactive background, as we can see in figure 5.3c and table 5.2; a good linearity is also observed (see figure 5.5b).

The alpha and gamma energy calibration fitted functions are, respectively,

$$A_h^\alpha(E) = E(keV)(15.31 \pm 0.03) \cdot 10^{-2} mV/keV + (18 \pm 2)mV \tag{5.3}$$

$$A_h^\gamma(E) = E(keV)(13.50 \pm 0.02) \cdot 10^{-2} mV/keV + (1.5 \pm 0.1)mV \tag{5.4}$$

### Heat Relative Efficiency Factor

The detector response to a particle interaction depends on the type of particle and also on the energy and temperature. The dependence on the type of particle is

| Isotope | Heat amplitude (mV) | $Q_\alpha$ energy (keV) | FWHM (keV) | Area (counts) |
|---|---|---|---|---|
| $^{226}$Ra | 763.397±0.008 | 4870.63(25) | 8.0±0.1 | 1194±18 |
| $^{222}$Rn | 874.814±0.006 | 5590.3(3) | 8.8±0.1 | 1329±14 |
| $^{218}$Po | 955.287±0.004 | 6119.68(9) | 9.6±0.1 | 1412±9 |
| $^{210}$Po | 846.442±0.032 | 5407.46(7) | 7.9±0.5 | 196±13 |
| $^{224}$Ra | 905.314±0.051 | 5788.87(15) | 10.1±0.8 | 59±5 |
| $^{220}$Rn | 999.855±0.057 | 6404.67(10) | 12.1±0.9 | 55±4 |
| $^{241}$Am | 858.409±0.015 | 5485.56(12)* | 10.0±0.2 | 958±22 |
| $^{241}$Am | 852.024±0.026 | 5442.80(13)* | – | 50±8 |

Table 5.1: *Gaussian parameters of the $\alpha$ peaks with their identification and corresponding energies [146]. The (*) indicates that in the peaks arising from the external $^{241}$Am source only the energy of the $\alpha$ particle has been considered, and consequently, those are the values written in the table instead of the $Q_\alpha$. The 5442.8 keV peak was not well resolved to estimate its FWHM energy resolution.*

specially strong in the scintillation signal, as we will see in the next section, but some differences are also observed in the heat signal. The heat Relative Efficiency Factor between two kind of particles, say $a$ and $b$, denoted in the following by $\mathrm{REF}_h(a{:}b)$, is defined as the ratio between the heat signal produced by a particle $a$ depositing an energy in the crystal and that produced by a particle $b$ depositing the same energy. This factor also depends on the definition of the energy estimator (pulse area, pulse amplitude, etc.) and other experimental conditions, besides the temperature, like the bias and signal processing. We have estimated the $\mathrm{REF}_h(\alpha{:}\gamma)$, as a function of the energy, profiting from the $\alpha$ and $\gamma$ energy calibrations, using the following expression:

$$REF_h(\alpha:\gamma) = \frac{A_h^\alpha(E)}{A_h^\gamma(E)_\gamma}. \tag{5.5}$$

We estimate the $\mathrm{REF}_h(\alpha{:}\gamma)$ dividing the energy calibration fitted functions of each band (equations 5.3 and 5.4). The obtained values are shown in figure 5.6. The error bands represent the $1\sigma$ confidence level and they were the result of propagating statistical errors from the linear fits. According to our calculations, $\alpha$ particles produce a 15–30% more heat than $\beta/\gamma$ particles depositing the same energy. Notice that systematic errors have not been considered and that we are comparing two data sets with very different energy ranges, up to 2 MeV in the case of the gammas and

| Emitter | Heat amplitude (mV) | Energy (keV) | FWHM (keV) |
|---|---|---|---|
| $^{214}$Pb | 48.92±0.47 | 351.932(2) | – |
| $e^-e^+$ annihilation | 70.52±0.09 | 511.00 | 9±8 |
| $^{214}$Bi | 83.43±0.26 | 609.312(7) | – |
| $^{40}$K | 199.45±0.37 | 1460.83 | 32±6 |
| $^{208}$Tl (simple escape) | 287.38±0.83 | 2103.53(1) | 6±19 |
| $^{208}$Tl | 353.87±0.39 | 2614.53(1) | 17±6 |

Table 5.2: *Gaussian parameters of the $\gamma$ peaks with their identification and corresponding energies [146]. The peaks were hardly resolved and the resolution of some of them could not be estimated.*

around 5–6 MeV for the alphas.

### 5.1.3 Light response

As shown in figure 5.2, the light channel allows to discriminate the interacting particle but other properties as the energy resolution are not as good as in the heat channel due to the lower number of carriers produced and collected. Efforts are being carried out to improve the resolution and characteristics of bolometers as light detectors (see section 1.3.2). Although in a light spectrum we could not resolve the alpha peaks, we used the excellent resolution of the heat channel to select them and then estimate their characteristic gaussian parameters. They are summarized in table 5.3. We assumed that the amount of light produced by the nuclear recoil in the alpha disintegration is negligible compared to the light produced by the alpha particle (see next pages for justification of this approach), consequently, we calibrated the light channel using the $\alpha$ particles kinetic energies ($E_\alpha$). In the case of the gamma band, it was not possible to isolate the peaks from the background, so we could not study them.

A good linearity was also observed in the light channel (figure 5.7). The worse energy resolution of the internal contamination peaks (around 11%) with regard to those of the external $^{241}$Am source (around 6%), could be explained as the accumulation of several factors. The light from internal contamination is produced in the bulk of the crystal and could have inhomogeneities in the scintillation; photons arising from the interactions can take very different paths before reaching the optical bolometer, with different number of reflections on the walls of the bolometer cavity,

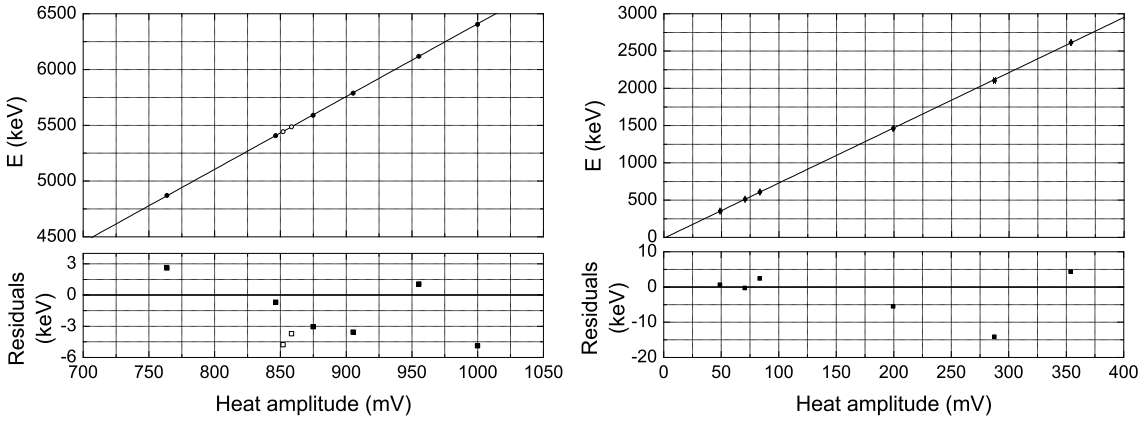


(a) (b)

Figure 5.5: *Energy calibration of the alpha (a) and gamma (b) peaks in the heat channel. The $^{241}Am$ peaks (empty markers in (a)) were not used for energy calibration.*

absorbtion in the own crystal and other non-specified sources, and these differences spread the signal.

With the events from the $^{55}$Fe X-ray source, directly faced to the optical bolometer, we could estimate its absolute response or light yield, that is, the fraction of energy of the incoming particle that is collected into the light detector. If we assume that the 5.9 keV X-ray emitted by the $^{55}$Fe source is completely absorbed in the Ge detector (note that thermalization in semiconductors can be limited by energy lost to trapping as reported in [154] for doped Ge thermistors), we could compare the response to this direct source with the response to a source that produces scintillation in the heat bolometer (for that we used the $^{218}$Po alpha line from inner contamination). For the X-ray source the response was $164.6 \pm 0.2$ mV/keV and for the $^{218}$Po alpha particle $122.4 \pm 0.2$ mV/MeV. With these data we estimated an equivalent light energy of $0.743 \pm 0.002$ keV/MeV for alpha particles.

We have also measured at IAS the scintillation spectra of the $SrF_2$ crystal under X-ray irradiation at different temperatures (300, 77 and 4 K). To do this, we used a small L$^4$He cryostat that allowed cooling down to 4 K. The sample cooled was a $SrF_2$ disk ($\varnothing = 19.9$ mm, $h = 2.08$ mm) cut from the same batch as the scintillating bolometer crystal. The experimental set-up is shown in figure 5.8. The sample was mounted inside a reflecting copper cavity internally coated with silver and with an aluminium window for the X-ray irradiation. The cavity was installed inside the cryostat which has a Be window to allow the pass of X-rays from the tube (40 kV and 98 $\mu$A). The collected light was transmitted by an optical fiber to an Avantes Fiber

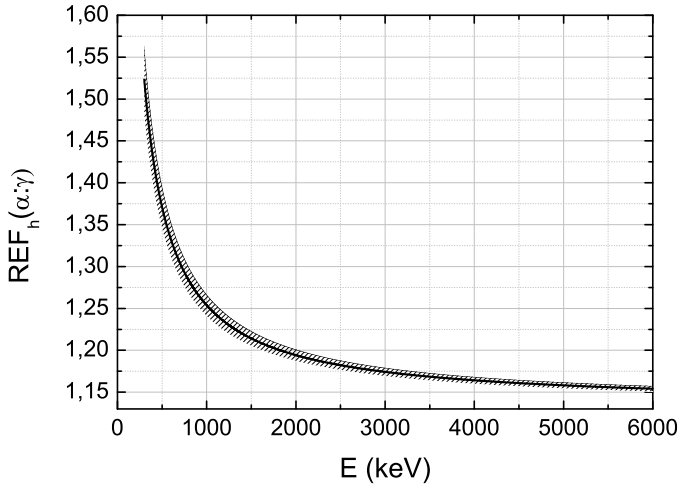


Figure 5.6: *Heat Relative Efficiency Factor between $\gamma$ and $\alpha$ interactions as a function of the energy. The shadow region represents the statistical error bands at $1\sigma$ confidence level.*

Spectrometer with diffraction grating and registered with a CCD detector. Details of the mounting are widely explained in references [12, 32] where it was used with other materials. Measurements were made with a integration time of 10 minutes. To estimate the relative intensity of scintillation photons emitted $\eta(\lambda)$ at a given temperature, the measured spectrum $I_m(\lambda)$ must be corrected by several factors which depend on the wavelength $\lambda$

$$\eta(\lambda) = \frac{I_m(\lambda)}{\eta_C(\lambda) \cdot \eta_f(\lambda) \cdot \eta_g(\lambda) \cdot S_S(\lambda)} \tag{5.6}$$

being $\eta_C(\lambda)$, $\eta_f(\lambda)$ and $\eta_g(\lambda)$ the transmission efficiency of the crystal cavity, the optical fiber and the diffraction grating, respectively, and $S_S(\lambda)$ the spectral relative sensitivity of the spectrometer. The efficiency of the cavity, defined as the ratio between the light collected by the optical fiber and that emitted by the crystal, was estimated using a simple model involving the geometry and the reflectivity of the cavity, but neglecting the absorption of photons in the own crystal (see [12] for details), as

$$\eta_C(\lambda) = x + \frac{R(\lambda) \cdot \varphi}{1 - R(\lambda) \cdot (1 - \varphi)} \cdot (1 - x) \tag{5.7}$$

standing $x$ for the fraction of light directly collected by the optical fiber, and the second term, for the light collected after successive reflections in the cavity. $R(\lambda)$ is the reflectivity of the cavity coating [155] and $\varphi$ the probability that a photon reaches the fiber with a correct angle for its transmission. With our geometry we have $x = \frac{S_f}{S_c}\frac{\Omega_f}{\Omega_c}$ and $\varphi = \frac{S_f}{S_c}\frac{\Omega_f}{2\pi}$, where $S_f$ is the cross section of the optical fiber, $S_c$ is the cavity total area, $\Omega_f$ is the solid angle for transmission of photons

| Isotope | Light amplitude (mV) | $E_\alpha$ (keV) | FWHM (keV) |
|---|---|---|---|
| $^{226}$Ra | 426.5±0.4 | 4784.34(25) | 474±8 |
| $^{222}$Rn | 519.5±0.3 | 5489.52(30) | 589±5 |
| $^{218}$Po | 592.2±0.3 | 6002.35(9) | 632±6 |
| $^{210}$Po | 495.9±0.4 | 5304.38(7) | 487±7 |
| $^{224}$Ra | 538.6±1.9 | 5685.37(15) | 666±33 |
| $^{220}$Rn | 624.6±0.9 | 6288.08(10) | 479±15 |
| $^{241}$Am | 516.2±0.2 | 5485.56(12) | 322±7 |
| $^{241}$Am | 511.0±0.3 | 5442.80(13) | 320±4 |

Table 5.3: *Amplitude and energy resolution (FWHM) of each alpha peak associated with its corresponding energy [146]. We assumed that the light produced by the recoiling daughter nucleus is negligible (see text), and therefore we indicate the $\alpha$ particle kinetic energy $E_\alpha$ instead of the $Q_\alpha$ value.*

by the fiber (extracted from the fiber documentation) and $\Omega_c$ is the solid angle subtended by the crystal at the optical fiber position ($\simeq 2\pi$ in this measurement). The transmission efficiency from the fiber, encompassing $\eta_f(\lambda)$, $\eta_g(\lambda)$ and $S_S(\lambda)$, was measured experimentally in [32]. Figure 5.9a plots both correction factors as function of the wavelength and figure 5.9b shows the corrected scintillating spectra obtained at three different temperatures, 300 K, 77 K and 4 K. Efficiencies of the mounting are not optimal for UV emissions, as is the case for $SrF_2$ scintillation which has the main emission in the region from 300 to 450 nm. This fact reveals that silver is not a good coating for this scintillating bolometer; other materials as, for example, aluminium, could be considered in future. We integrated the whole spectra (275 to 825 nm) to compare the global amount of light produced at each temperature: the light produced at 77 K was a 35% larger than that at room temperature, and at 4 K the $SrF_2$ produced a 45% more light than at 300 K. In reference [156], scintillation spectra of pure and $Ce^{3+}$-doped $SrF_2$ crystals are shown attributing emission bands at 310 and 325 nm to the 5d-4f emission of $Ce^{3+}$ ions. The most intense line of our spectra, at 325 nm, would match with their second band.

### Particle discrimination in the light channel

The scintillation yield strongly depends on the type of incident particle. We define the light Relative Efficiency Factor between two kinds of particle $a$ and $b$, $\mathrm{REF}_l(a{:}b)$,

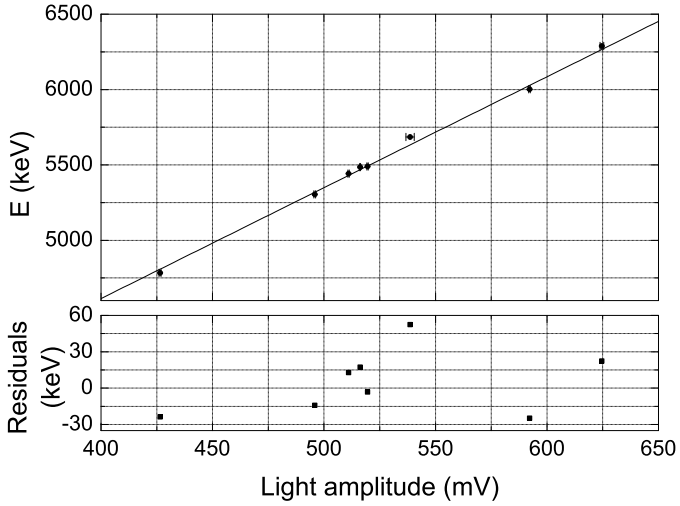


Figure 5.7: *Alpha energy calibration of light signals. Unlike the heat channel, the* $^{241}$*Am peaks were also used for the calibration.*

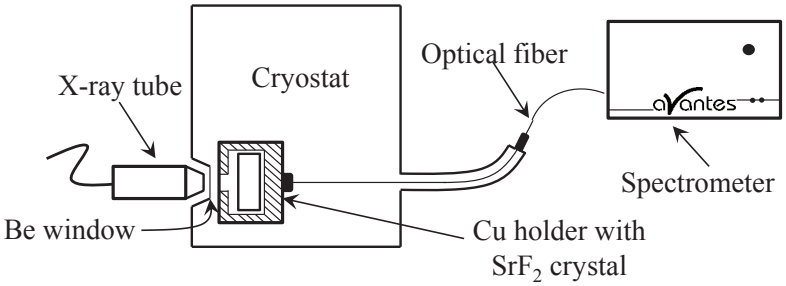


Figure 5.8: *Experimental set-up used to measure the* $SrF_2$ *scintillation spectra at different temperatures.*

following the previous definition of the $\mathrm{REF}_h$ (equation 5.5), but comparing the scintillation responses in this case. An accurate measurement of this magnitude is essential in some experiments to allow discrimination of the searched signal from some background events.

We studied the $SrF_2$ light response to different particles exposing the scintillating bolometers to neutrons from a $^{252}$Cf source, to photons from a $^{137}$Cs source and profiting from the internal contamination of the crystal in $^{226}$Ra and $^{224}$Ra chains. Figure 5.10a shows the light versus heat scatter plot obtained in a dedicated measurement at high energy (up to 12 MeV). Events of the upper band (labeled $\beta/\gamma/\mu$) are due to electrons, photons and muons, and were fitted to a straight line to describe the $\beta/\gamma$ light response of the detector (equation 5.8 and red line in figure 5.10a). To calculate the $\mathrm{REF}_l(\beta/\gamma{:}\alpha)$ at given energies, we estimated the mean

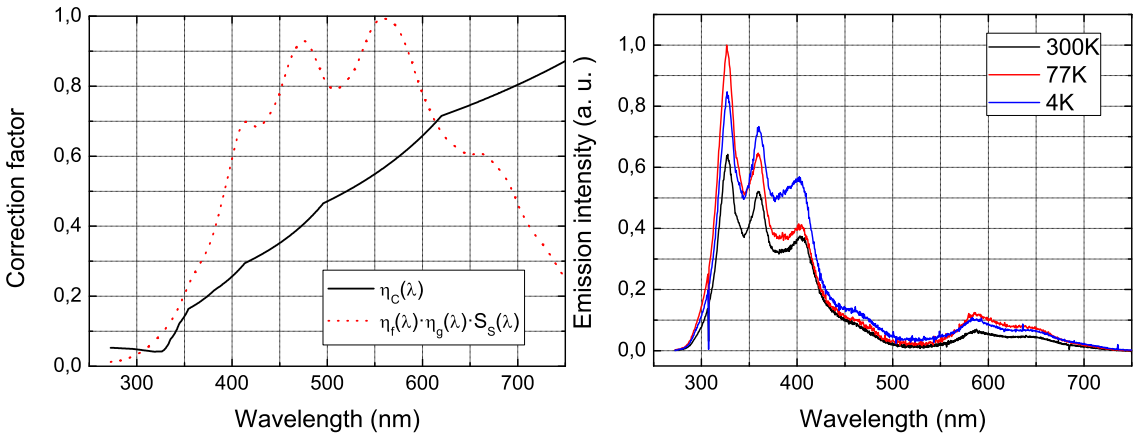


(a) (b)

Figure 5.9: *(a) Transmission efficiencies of the crystal cavity ($\eta_C$), estimated with the equation 5.7, and of the rest of the mounting (measured experimentally) englobing the optical fiber ($\eta_f$), the diffraction grating ($\eta_g$) and the spectral sensitivity of the spectrometer ($S_S$). In (b) it is displayed the corrected scintillation spectra measured at different temperatures with an X–ray excitation source. These curves have been normalized to the maximum of the 77 K curve, keeping their relative ratio.*

value of the distributions of light amplitudes obtained for the most intense $\alpha$ peaks and directly compared them with the $\beta/\gamma$ light responses calculated from equation 5.8 and the corresponding $\gamma$ calibration (see table 5.4 and points in figure 5.11a).

$$A_l^{\gamma}(mV) = A_h^{\gamma}(mV)(3.380 \pm 0.002) + (2.6 \pm 0.5) \tag{5.8}$$

We also parameterized the light response of the $\alpha$ band by fitting the points that represent the six peaks shown in table 5.4 and the average heat and light responses of seven energy windows containing $\alpha$ events with less energy than the peaks. The 0–8 MeV region of the $\alpha$ band was best described by a second order polynomial function, obtaining the following result

$$A_l^{\alpha}(mV) = (A_h^{\alpha})^2(mV^2)(4.2 \pm 0.3)10^{-4} + A_h^{\alpha}(mV)(0.34 \pm 0.03) + (27 \pm 11) \tag{5.9}$$

Figure 5.10a shows this fit (bottom red line) and the points used from the peaks and windows (in blue).

From the ratio between the two fitted light responses (equations 5.8 and 5.9) and using their respective heat energy calibrations, we did a continuous estimate of the $\mathrm{REF}_l(\beta/\gamma{:}\alpha)$ as a function of the energy. The result is shown as a solid line in figure 5.11a. The light gray region represents the one standard deviation ($1\sigma$)

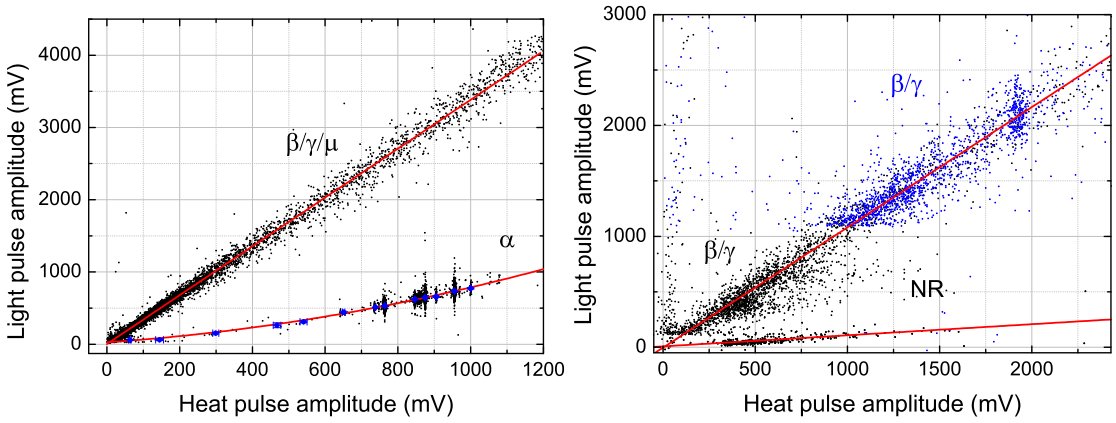


Figure 5.10: *Light versus heat discrimination plots used for the light REF estimations between $\beta/\gamma$ and $\alpha$ particles (a) and between $\beta/\gamma$ and Nuclear Recoils (b). Fitting functions for each distribution are also plotted. Blue points in (a) represent the points used to perform the $\alpha$ band fit (see text). In (b) it is shown the composite plot of two different measurements with the same experimental conditions: one in black with a $^{252}Cf$ neutron source and low threshold, and another one in blue with a $^{137}Cs$ $\gamma$ source and high threshold ($\simeq$1 V in light).*

uncertainty: it includes statistical errors from uncertainties in the fitting parameters and a systematic error obtained forcing one or both of the heat versus light fitted curves to pass through the (0,0) point (it was estimated as half the difference between the maximum and minimum values obtained in the various fits). It can be observed that points lie in the error band of the estimation but shifted downwards, suggesting that the second degree polynomial function does not accurately reproduce the $\alpha$ light response in the full energy range.

To estimate the light REF between $\beta/\gamma$ and nuclear recoils we used two different measurements (identified with two different colors, black and blue, in figure 5.10b) carried out in the same experimental conditions. The measure in blue had a $^{137}$Cs gamma source (it emits photons of 662 keV, being the full–absorption peak placed at $\simeq$1.9 V of heat amplitude), and the measure in black had a $^{252}$Cf neutron source that induces Sr and F nuclear recoils (NR). The heat channel was calibrated with the gamma line and, consequently, energies are electron equivalent ones. The nuclear recoil band was parameterized fitting all the points, properly selected, to a straight line obtaining the equation 5.10. For the $\beta/\gamma$ band we selected five heat windows of events along the band and took the average heat amplitude and the center of the gaussian fitted to the light amplitude of the events in each window. With this values

| Energy (MeV) | $\beta/\gamma$ light response (mV) | $\alpha$ light response (mV) | $\mathrm{REF}_l(\beta/\gamma:\alpha)$ |
|---|---|---|---|
| 4.78 | 2191±3 | 531±1 | 4.13±0.01 |
| 5.30 | 2428±3 | 621±2 | 3.91±0.01 |
| 5.49 | 2513±4 | 647±1 | 3.88±0.01 |
| 5.69 | 2602±4 | 656±9 | 3.96±0.05 |
| 6.00 | 2747±4 | 735±1 | 3.74±0.01 |
| 6.29 | 2877±4 | 773±7 | 3.72±0.04 |

Table 5.4: *Light responses to different energies corresponding with the main $\alpha$ lines and their respective light REF estimations. Statistical errors from the fitted functions have been propagated.*

and the gaussian center in heat and light of the 662 keV peak we performed a linear fit deriving the equation 5.11. Assuming that the heat response to photons and NR is the same, we estimated the energy dependent light REF between $\beta/\gamma$ and nuclear recoils dividing 5.11 by 5.10. The result obtained is shown in figure 5.11b where the error band (in light gray) includes the statistical error and a systematic error estimated as previously, assuming the possibility that one or both of the light vs. heat functions pass through the (0,0) point.

$$A_l^{NR}(mV) = A_h(mV)(0.100 \pm 0.006) + (8 \pm 4) \tag{5.10}$$

$$A_l^{\gamma}(mV) = A_h(mV)(1.085 \pm 0.011) + (4 \pm 16) \tag{5.11}$$

### Semi-empirical estimates of light REF

In reference [157] Tretyak proposed a simple semi-empirical approach (based on the model of Birks [158]) to estimate the quenching factor (inverse of the $\mathrm{REF}_l(\beta/\gamma:i)$) for ions against electrons, with only one free parameter. In this approach the light REF between electrons ($\beta/\gamma$) and ions ($i$) can be written as

$$REF_l(\beta/\gamma:i)(E) = \frac{\displaystyle\int_0^E \frac{dE}{1+kB\cdot\left(\frac{dE}{dr}\right)_e}}{\displaystyle\int_0^E \frac{dE}{1+kB\cdot\left(\frac{dE}{dr}\right)_i}} \tag{5.12}$$

where $E$ is the deposited energy, $(dE/dr)_e$ and $(dE/dr)_i$ are the electron and ion stopping powers, respectively, and $kB$ is the Birks factor, the only free parameter

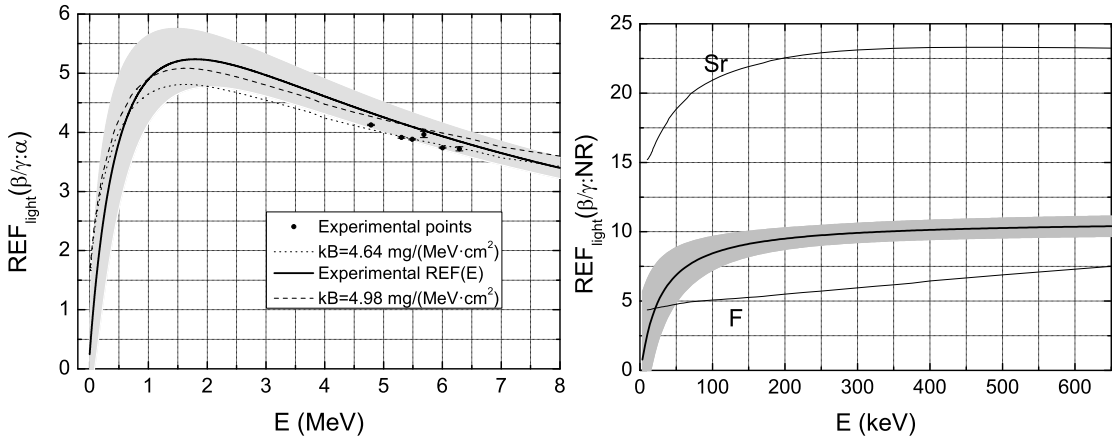


(a) (b)

Figure 5.11: *$REF_l(\beta/\gamma{:}\alpha)$ (a) and $REF_l(\beta/\gamma{:}NR)$ (b) in the $SrF_2$ scintillating bolometer. The solid lines (and light-gray regions for the $1\sigma$ error bands) were estimated as the ratio between the two light responses. The points shown in (a) correspond to discrete estimates at the energies of the $\alpha$ peaks. The dotted and dashed lines in (a) are the $REF_l(\beta/\gamma{:}\alpha)$ obtained from the fits explained in the text that give Birks factors of $kB = 4.64$ mg/(MeV· cm$^2$) and $kB = 4.98$ mg/(MeV· cm$^2$) respectively. The lines labeled with Sr and F in (b) are $REF_l(\beta/\gamma{:}NR)$ estimated with the Birks factor of 4.98 mg/(MeV· cm$^2$) for Sr and F nuclear recoils.*

in the expression. Mass thickness units are used in the following for $(dE/dr)$ and $kB$. If one knows the value of $kB$, one can calculate the light REF from the data available about stopping powers for the considered target. As explained in [157], in a given material, for the same experimental conditions and data treatment procedure, $kB$ will be the same for all particles and can be considered a constant. Then one can estimate $kB$ from the measurement of, for instance, the light REF$(\beta/\gamma : \alpha)$, and use this value to estimate the light REF for other particles and energies. A detailed description of the model is given in section 2 of reference [157].

We could estimate the Birks factor $kB$ for $SrF_2$, at the conditions of our data taking, fitting the equation 5.12 to our experimental data of the light REF obtained, both from the alpha points and from the continuous energy dependent estimation (we used the energy range between 0 to 8 MeV). The values obtained for $kB$ were 4.64 mg/(MeV·cm$^2$) with a goodness of fit $\chi^2/n.d.f. = 30.4$ for the six $\alpha$ points (see table 5.4) and 4.98 mg/(MeV·cm$^2$) with a goodness of fit $\chi^2/n.d.f. = 0.19$ for the continuous estimate. The stopping power for electrons was estimated with the ESTAR program [159] whereas for the $\alpha$ particles the SRIM program [160] was used. Calculations of the model are shown in figure 5.11a: the dotted line

corresponds to the six points $kB$ fit and the dashed one to the fit to the continuous experimental light REF. It can be observed that the calculations of the model are in good agreement with our experimental light REF for $\alpha$ particles, although the model tends to underestimate the variation with energy, as was already stated in [157]. Obviously, the continuous estimation describes better the full energy range of the light REF, whereas the local alpha peak region (from 4.5 to 6.5 MeV) is better explained with the discrete point estimation. To use the Tretyak approach to estimate the light REF in $SrF_2$ for other ions in the full energy range, we decided to use the value of kB=4.98 mg/(MeV$\cdot$ cm$^2$) of the continuous estimate.

We calculated the light REF for nuclei of F and Sr, that are the recoiling nuclei in our crystal, using the Birks factor obtained before. The results are compared with the experimental light REF for nuclear recoils in figure 5.11b. The experimental data lie between the model estimations for F and Sr as could be expected if the nuclear recoils induced by neutrons were an average of recoils of both elements, but effectively, recoils induced by neutrons at energies above $\simeq$50 keV are practically all F nuclei due to kinematical reasons. The model seems to underestimate the light REF for F ions, but we must also take into account that we are using a $kB$ value derived from a measurement (that shown in figure 5.10a) with slightly different conditions (bias, gain).

We used also the Tretyak approach to have an estimation of the light REF for heavy recoiling nuclei, as it is the case, for instance, of the daughter nuclei in $\alpha$ decays. Calculations from equation 5.12 showed that a Pb nucleus of 100 keV of kinetic energy, which is a representative case of the alpha decays present in our $SrF_2$ crystal, has a REF$_l(\beta/\gamma$:Pb) of 37. An $\alpha$ particle of 5.5 MeV gives a light signal of 650 mV according to its energy calibration, and a $\beta/\gamma$ event of 100 keV, according to the equation 5.8 and its energy calibration has a light signal of 53 mV. Using the REF$_l$ value, a Pb recoiling nucleus of the same energy would produce a light signal of 1.4 mV. This means that in alpha decays, the recoiling nucleus produces a 0.2% of the light produced by the $\alpha$ particle, which supports the approximation used before of considering that the light produced in alpha decays is only due to the $\alpha$ particle.

**Spatial inhomogeneity in the light output**

Understanding the factors which contribute to worsen the energy resolution of the light channel is important to improve the discrimination capability of scintillating bolometers. The properties of the radioactive chains present in the $SrF_2$ crystal and described in section 5.1.2 allow to study inhomogeneities in the light output, as it

was preliminarily suggested in [161].

Nuclear recoils arising from alpha decays have ranges of some tens of Å in the crystal. Consequently, we can suppose that in a cascade two consecutive decays in the chain emit light from the same point (crystal dimensions are of the order of cm). We studied the $\alpha$ triplet of delayed coincidences between successive nuclei in the $^{224}$Ra (18±3 mBq/kg) radioactive chain:

$$^{224}\mathrm{Ra} \rightarrow {}^{220}\mathrm{Rn} \rightarrow {}^{216}\mathrm{Po} \rightarrow {}^{212}\mathrm{Bi} \tag{5.13}$$

These alpha events were easily identified because the time constants of the bolometer (at most a few tens of ms) are much faster than the interval between two successive decays, being $T_{1/2}(^{220}\mathrm{Rn}) = 55$ s and $T_{1/2}(^{216}\mathrm{Po}) = 0.15$ s, and the activity of this chain is low enough (1 decay every 17 minutes) to find the coincidences. Thanks to the heat spectrum, it was easy to identify the alpha particles coming from $^{224}$Ra and $^{220}$Rn and identify 63 $\alpha - \alpha$ pairs. They are shown in figure 5.12a normalized with the mean value and standard deviation of their corresponding measurements because in order to have more statistics we have used two measurements: in one we identified 33 pairs and in the other one 30 pairs. Identifying the $^{216}$Po events was more complicated owing to the fact that their signal appears in the same trace of the corresponding $^{220}$Rn event as a pile-up. To estimate the parameters of the second peak in the trace we subtracted a template pulse fitted to the first one, leaving a flat baseline. The resolution of this new $^{216}$Po peak was not as good as the previous ones as it was expected due to the method itself, but it does not compromise the identification of $\alpha - \alpha$ pairs. In this way 38 $\alpha - \alpha$ pairs were identified (see figure 5.12a).

We can observe in figure 5.12a that clearly exists a positive correlation between the light output of the three $\alpha$ emitters. In the table 5.5 we show the correlation coefficients ($\rho$) for the three possible combinations.

| Isotopes pair | N | $\rho$ | Significance |
|---|---|---|---|
| $^{224}$Ra – $^{220}$Rn | 63 | 0.71±0.06 | $6.9\sigma$ |
| $^{220}$Rn – $^{216}$Po | 38 | 0.76±0.07 | $5.9\sigma$ |
| $^{224}$Ra – $^{216}$Po | 38 | 0.58±0.11 | $3.9\sigma$ |

Table 5.5: *Number of pairs N identified for each coincidence with the correlation coefficient $\rho$ of their light amplitude and the significance of these values (see text for explanations).*

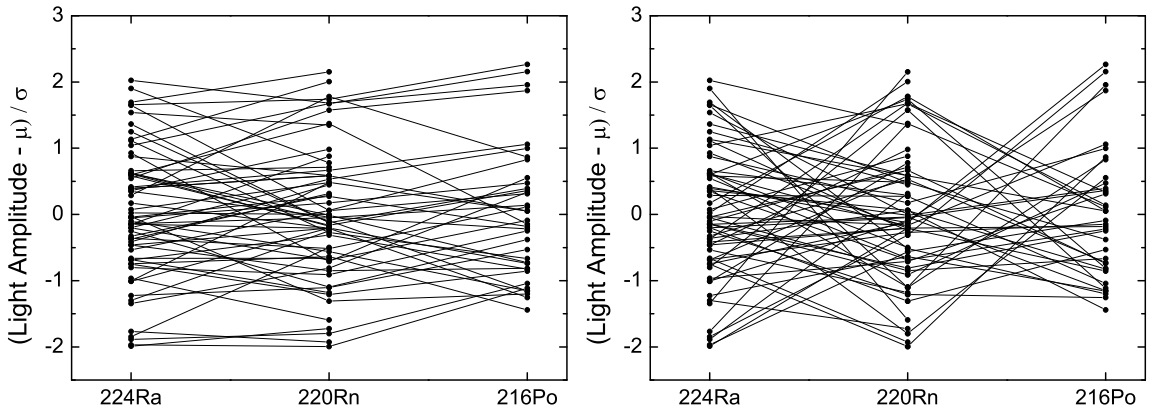


(a) (b)

Figure 5.12: *Light output analysis of delayed coincidences α–α–α. The vertical axis represent the light amplitude of each event normalized with the mean value (μ) and standard deviation (σ) of its distribution. The identified coincidences are matched by lines in (a), while in (b) the associations were done randomly.*

We wanted to assure that our events from $^{224}$Ra and $^{220}$Rn were correctly related. The frequency distribution of the elapsed time between paired events should follow the exponential law of radioactive decay,

$$\frac{\Delta N}{\Delta t} = N_0 \left(\frac{\ln 2}{T_{1/2}}\right) \exp(-\frac{\ln 2}{T_{1/2}} t). \tag{5.14}$$

Both experimental and theoretical distributions are plotted in the figure 5.13a. Excluding the first bin (where some events are lost due to the dead time of the experiment) the experimental distribution is compatible with the expected one. Despite the poor statistics we observed approximately half the pairs separated by less than 55 s (30.5 pairs) and half the pairs separated by more time (34.5 pairs).

The second test consisted in calculating the correlation coefficient for several random pairings of the events (see figure 5.12b), and studying their distribution. Figure 5.13b shows the correlations coefficient distribution obtained when the 33 pairs of $^{224}$Ra and $^{220}$Rn delayed coincidence of one of the measurements used, are selected randomly 10000 times. We obtain a Gaussian distribution with mean $(0.7 \pm 2.0) \cdot 10^{-4}$ and standard deviation $0.180 \pm 0.002$, in excellent agreement with the expected values (mean zero and standard deviation $1/\sqrt{33}$).

If we consider that our random pairs are not correlated, the resulting distribution must have an expected value of zero and variance $V = N^{-1}$ (being N the number of data pairs), and tends to a Gaussian distribution in the large sample limit (N≥500). As our N is 63, we will use the Fisher transformation of $\rho$, $z = tanh^{-1}(\rho)$ with

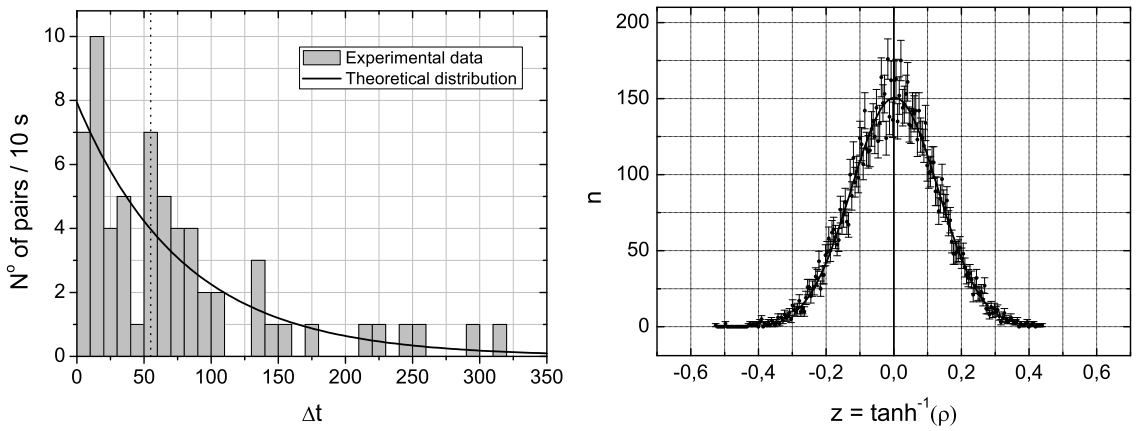


(a) (b)

Figure 5.13: *Figure (a) shows the theoretical and experimental distribution of the elapsed time between paired events of the $^{224}Ra$-$^{220}Rn$ $\alpha - \alpha$ delayed coincidence. The vertical dotted line indicates the half–life of $^{220}Rn$. In (b) it is shown the distribution of the z–transformation (see text) of the correlation coefficients obtained for 10000 random pairings of the events, centered at zero and with the expected variance $(N-3)^{-1}$. Only one measurement (that with 33 pairs) has been used for this plot).*

expected value zero and $V = (N-3)^{-1}$, that approaches Gaussian limit much more quickly as a function of N (see chapters 5 and 9 of [162]) to determine the significance. We followed this method to give the significance of our correlation coefficients in the table 5.5. We concluded that our correlation coefficients have statistical significances of $6.9\sigma$, $5.9\sigma$ and $3.9\sigma$.

The confirmation of this correlation effect indicates the existence of a position dependence of the light signal that can be attributed to variations in the light yield (inhomogeneities in the crystal) and/or light collection. This interpretation is also supported by the fact before-mentioned that the energy resolution of $\alpha$ events not produced in the bulk of the crystal (which is the case of $\alpha$ events from the external $^{241}$Am source) is better than that of the internal contamination peaks, as can be noticed in the table 5.3. We quantified this effect comparing the average FWHM of the inner contamination peaks, that is $\Gamma_{bulk} = (10.61 \pm 0.55)\%$, with the average of the two $^{241}$Am peaks, $\Gamma_{surface} = (5.86 \pm 0.72)\%$. The difference can be appreciated in figure 5.14. It seems that this positional effect contributes to the resolution with a quantity $\Gamma_{effect}$ that, assuming independent contributions, can be estimated from:

$$\begin{aligned} \Gamma^2_{bulk} &= \Gamma^2_{surface} + \Gamma^2_{effect} \\ \Gamma_{effect} &= (8.84 \pm 0.81)\% \end{aligned} \tag{5.15}$$

This value, larger than the resolution for surface interactions, is an important contribution that worsens the energy resolution.

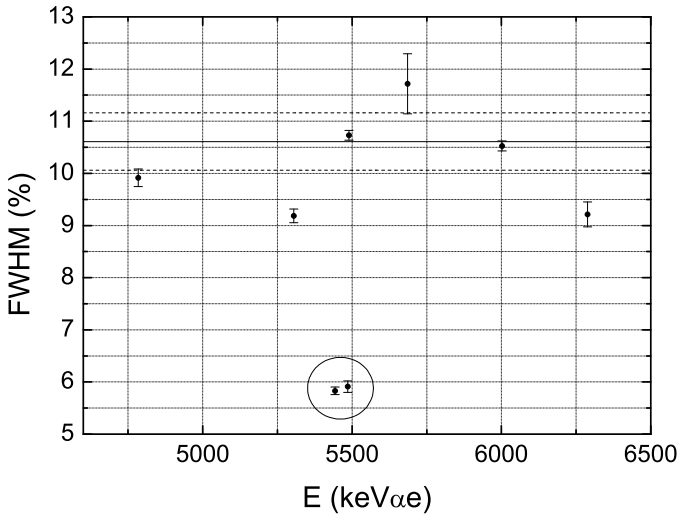


Figure 5.14: *Energy resolution of the $\alpha$ peaks arising from inner contamination, which average is plotted with a horizontal solid line (statistical errors in dotted lines), and of the $\alpha$ peaks from the $^{241}Am$ source (points inside the circle), which is clearly better.*

### 5.1.4 Pulse shape discrimination

A series of measurements were carried out to analyze the thermal response of the $SrF_2$ crystal to different particles. We realized that not only the light response but also the thermal pulse shape depends on the type of incident particle. This difference would allow particle discrimination in bolometers without the need of measuring the crystal scintillation, simplifying remarkably the detector structure and the read-out (specially in multi–target experiments). The heat response to $\alpha$ particles is faster than the response to electron recoils (see figure 5.15), while there is not a noticeable difference between the responses to nuclear recoils and to electron recoils.

Following [163], we quantified the discrimination power D between $\alpha$ particles and electron recoils ($\beta$, $\gamma$ and $\mu$ particles) at a given energy for our two time parameters of the pulses, rise time and decay time ($\tau_r$ and $\tau_d$), using the equation

$$D_\tau(\beta/\gamma : \alpha) = \frac{\mu_\tau^{\beta/\gamma} - \mu_\tau^{\alpha}}{\sqrt{(\sigma_\tau^{\beta/\gamma})^2 + (\sigma_\tau^{\alpha})^2}} \tag{5.16}$$

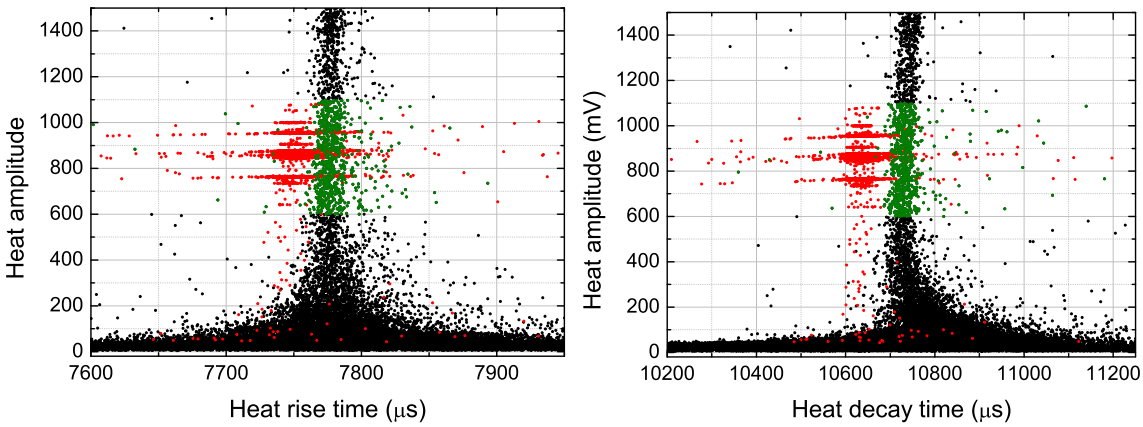


(a) (b)

Figure 5.15: *Scatter plot of heat amplitude vs. rise time (a) and decay time (b). Alphas are plotted in red and $\beta/\gamma$ events in black. Events in the $\beta/\gamma$ band with energies in the range of the $\alpha$ particles (used in the analysis to compare with them) are plotted in green.*

being $\mu$ and $\sigma$ the mean value and standard deviation of the distributions of $\tau_r$ and $\tau_d$, respectively, and with the superscript indicating the type of particle.

This discrimination power depends on the energy of the particles mainly due to the increasing width of the distributions for low energies that can be appreciated in figure 5.15. We estimated this value in the region of alpha interactions, selecting events in the $\beta/\gamma$ band approximately from 4.5 to 6.5 MeV. The distributions of rise time and decay time for both populations are plotted in figure 5.16. A gaussian fit to each peak reveals an average rise time of $7749.42 \pm 0.01$ $\mu$s for $\alpha$ events and $7776.31 \pm 0.11$ $\mu$s for $\beta/\gamma$ particles; and an average decay time of $10635.31 \pm 0.12$ $\mu$s for $\alpha$ and $10730.63 \pm 0.16$ $\mu$s for $\beta/\gamma$ events. The D value results equal to $2.98 \pm 0.03$ sigmas for the rise time and $3.87 \pm 0.02$ sigmas for decay time.

Although our discrimination could not be enough to avoid the use of the scintillation light, efforts can be made in this way, looking for parameters which combine different shape indicators and optimize the discrimination power, as was made in [35, 163]. In the first of these references is also given a possible explanation of this differences in the pulse shape, relating them with the dependence of light yield on the nature of the interacting particle. The different fraction of energy that flows into heat and light for each particle would lead to a different time evolution of the signals.

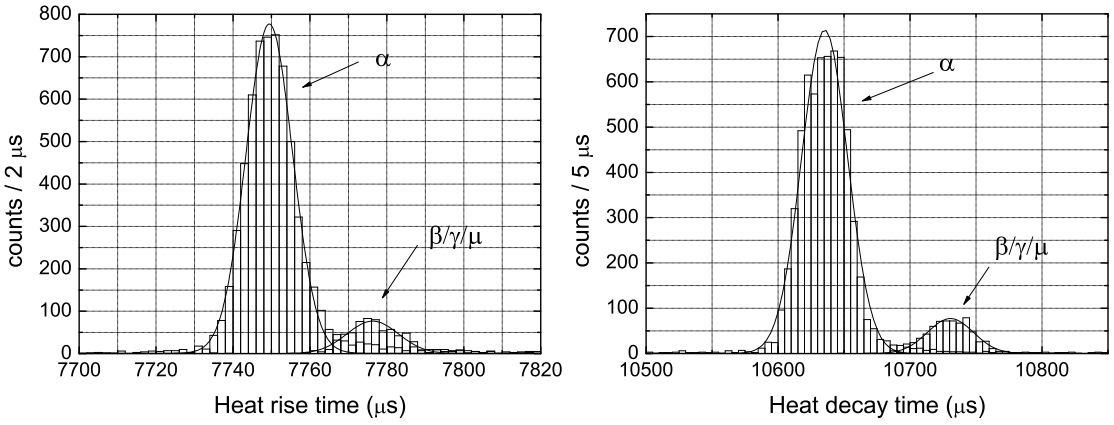


(a) (b)

Figure 5.16: *Rise time (a) and decay time (b) distributions of the heat signal for events from the $\alpha$ band and the $\beta/\gamma$ band in $SrF_2$.*

### 5.1.5 Double beta decay of $^{84}$Sr

Natural strontium consists mainly of $^{84}$Sr (0.56%), $^{86}$Sr (9.86%), $^{87}$Sr (7.00%) and $^{88}$Sr (82.58%). $^{84}$Sr is one of the natural occurring isotopes that can undergo double beta decay (DBD), particularly in the so–called positron decay modes. Figure 5.17 shows the expected decay scheme of $^{84}$Sr to $^{84}$Kr. We are interested in the transitions that occur between the $0^+$ ground states of the parent and daughter nuclei and in transitions to low-lying excited states, in particular to the first excited state of 881.6 keV (this is a $2^+$ state that has the distinctive feature that, in contrast to the $0^+ \rightarrow 0^+$ decay, can only be generated by right-handed currents).

In contrast with the $2\beta^-2\nu$ decay process, the positron decay modes have not been observed experimentally (except $^{130}$Ba decay derived from geochemical methods [164]), but there are several experiments in the last few years trying to measure half–lives for this modes in many nuclei from $^{64}$Zn to $^{132}$Ba (see [165] and references therein), and particularly in $^{84}$Sr [166, 167].

For this kind of isotopes, decaying to an isobar with atomic number two units lower, there exist three possible double beta decay modes, each one with or without emission of two neutrinos: double $\beta^+$ decay ($2\beta^+$), $\beta^+$ decay and electron-capture ($\varepsilon\beta^+$), or double electron-capture ($2\varepsilon$):

$$2\beta^+ : {}^{84}\mathrm{Sr} \rightarrow {}^{84}\mathrm{Kr} + 2e^+ \ (+\ 2\nu_e) \tag{5.17}$$

$$\varepsilon\beta^+ : {}^{84}\mathrm{Sr} + e^- \rightarrow {}^{84}\mathrm{Kr} + e^+ \ (+\ 2\nu_e) \tag{5.18}$$

$$2\varepsilon : {}^{84}\mathrm{Sr} + 2e^- \rightarrow {}^{84}\mathrm{Kr} \ (+\ 2\nu_e) \tag{5.19}$$

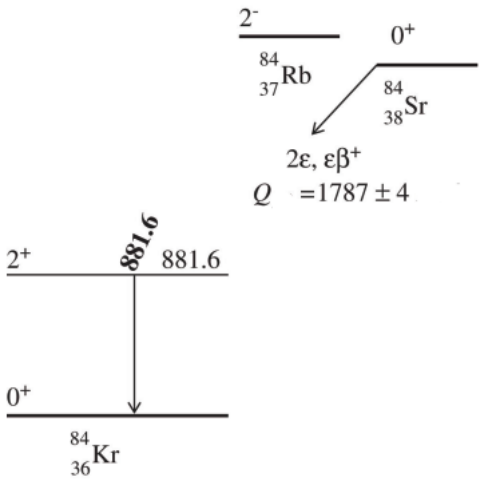


Figure 5.17: *Decay scheme of* $^{84}Sr$ *[168]. Energies are in keV.*

As is quoted in figure 5.17, the Q-value for this process, that is, the difference between the neutral atomic masses of the parent and daughter is $Q = (1787 \pm 4)$ keV. The available energy T for the particles in the final state for each mode in the $0^+ \rightarrow 0^+$ transition can be written as:

$$2\beta^+ : T = Q + \Delta B - 4m_e \simeq -257 \text{ keV} < 0 \text{ (forbidden)} \tag{5.20}$$

$$\varepsilon\beta^+ : T = Q + \Delta B - 2m_e - b_e \simeq 765 \text{ keV} \tag{5.21}$$

$$2\varepsilon : T = Q + \Delta B - b_{e1} - b_{e2} \simeq 1787 \text{ keV} \tag{5.22}$$

where $\Delta B$ is the difference between the binding energy of the atomic electrons of the parent and daughter nuclei and $b_e$ is the captured electron binding energy. The first contribution is, for many purposes, negligible in comparison with the Q value, and the value of $b_e$ depends on the electron that is captured: the higher probability corresponds to electrons of K shell ($b_{eK} = 14.3$ keV), followed by L shell electrons ($b_{eL1} = 1.9$ keV, $b_{eL2} \approx b_{eL3} = 1.7$ keV) [168]. Equation 5.20 shows that the $2\beta^+$ decay is energetically forbidden.

The decay from the ground state of $^{84}$Sr to the first excited level of $^{84}$Kr could be only possible in the $2\varepsilon$ mode, because the energy available for this process is $Q - E_{exc} = 1787$ keV$-881.6$ keV $= 905.4$ keV:

$$2\beta^+ : T = Q - E_{exc} + \Delta B - 4m_e \simeq -1138.6 \text{ keV} < 0 \text{ (forbidden)} \tag{5.23}$$

$$\varepsilon\beta^+ : T = Q - E_{exc} + \Delta B - 2m_e - b_e \simeq -116.6 \text{ keV} < 0 \text{ (forbidden)} \tag{5.24}$$

$$2\varepsilon : T = Q - E_{exc} + \Delta B - b_{e1} - b_{e2} \simeq 905.4 \text{ keV} \tag{5.25}$$

Next, we will analyze how we could detect the different allowed DBD processes

with our detector. For the approximated energies given above the $\Delta B$ and $b_e$ values have been neglected, but we will use $b_e$ in the following.

### Two neutrinos DBD modes

Following the order in which they have been described previously, the first decay mode allowed is the $\varepsilon\beta^+2\nu$ from ground state to ground state. According to the expression 5.18, the available energy is shared among the positron $e^+$ and the two neutrinos $\nu_e$ (kinetic energy of the $^{84}$Kr recoiling nucleus is negligible), producing for each particle a continuous energy spectrum from zero up to $T$. Since neutrinos are undetectable by our detector, we focus on the detection of the positron. This particle will lost their energy in the crystal and finally it will annihilate with an electron, producing a pair of 511 keV photons. Besides, after the electron capture, Kr characteristic X–rays or Auger electrons will be emitted . All this processes can be considered simultaneous in our detector, therefore the resulting signal will be the addition of the X–rays or Auger electrons energy, the positron energy (from 0 to $T$) and the energy deposited in the crystal by the two 511 keV photons: this produces a continuous energy spectrum from zero up to 1787 keV (765+511+511) without distinctive peaks and difficult to disentangle from the background.

The other allowed decay between ground states is the $2\varepsilon2\nu$. In this case, reported in the expression 5.19, practically the whole energy available in the final state is taken away by the two neutrinos. The only detectable signal are the X–rays or Auger electrons produced in the atomic deexcitation following the double electron capture. This decay mode would produce decay signals, but unfortunately the higher possible energy is 28.6 keV, well below our threshold detection.

The last possible decay mode is the $2\varepsilon2\nu$ to the first excited level of $^{84}$Kr. The only difference with the process between ground states explained in the last paragraph is that the $^{84}$Kr excited nucleus decays to the ground level by emitting a 881.6 keV photon. It is possible to search the peak signal for the particular case when this photon is completely absorbed. Since the photon is accompanied by the X–rays or Auger electrons, the signal is searched between 881 and 881+28.6 keV depending on the electrons captured (see table 5.6 for details).

Since the first process does not produce a distinctive signal and the second one is not detectable due to the threshold energy, we will focus on the third one: the $2\varepsilon2\nu$ decay to the $2^+$ excited level.

### Neutrinoless DBD modes

In the neutrinoless modes, the energy distribution of the final state is easier because there are two particles less than in the two neutrinos respective modes. In the case of the $\varepsilon\beta^+0\nu$ decay, the whole energy of final state is practically taken by the positron, consequently the expected signal of the process will be the sum of the electron capture X–rays (or Auger electrons), the positron energy T, and the fraction of the energy from the two 511 keV annihilation photons absorbed by the crystal. For instance, in the case of the most likely electron capture (K–shell), the total energy detected will be 765 keV plus the energy deposited by the two annihilation photons. Three distinctive signals can be produced: both annhilation photons are completely absorbed (peak signal energy of 1787 keV), one photon escapes without any interaction in the crystal and the other is fully absorbed (signal at 1276 keV), and both photons escape without depositing energy in the detector (signal at 765 keV).

The $2\varepsilon0\nu$ disintegration, both to ground or excited level, can be considered at the same time due to its peculiarities. In those cases, there is just one particle in the final state, the $^{84}$Kr nucleus, but the conservation laws of energy and momentum in the process require the emission of one or more additional particles (also needed in the transition to the excited level, because the nuclear deexcitation photon is a subsequent process). The main possibilities (see [169] for details) are the emission of a photon, the emission of two photons, the emission of an internal conversion electron and the emission of an electron–positron pair produced by a virtual photon. The later mode is the most probable of the four mentioned above, but its decay rate is smaller by four orders of magnitude than the one in the $\varepsilon\beta^+$ mode [169]. Consequently, we will focus only on the $\varepsilon\beta^+0\nu$ decay.

### Limits on the half-life

Once discussed the double beta decay processes that could be searched efficiently with our $SrF_2$ bolometer, we tried to estimate the half-life $T_{1/2}$ of these disintegration modes from our data, which, for rare event searches where $T_{1/2}$ is very long, can be expressed as

$$T_{1/2} = \ln 2 \left( \frac{Nt\varepsilon}{S} \right) \tag{5.26}$$

where $N$ is the number of atoms candidates to double beta decay, $t$ is the measuring time ($t \ll T_{1/2}$), $\varepsilon$ is the detection efficiency and $S$ is the number of events that can be attributed to the process. The sensitivity of an experiment $S_{1/2}$ can be estimated, based on the square root criterion, assuming that an experiment is sensitive to signals

of the order of the statistical fluctuation of the experimental background. Then, the signal can be expressed as

$$S = \sqrt{b\,(\Delta E)\,Mt} \tag{5.27}$$

where $\Delta E$ is the energy resolution of the detector, $M$ the source mass and $b$ the experimental background in units of events/(energy mass time). Including this equation in 5.26, the sensitivity can be written as

$$S_{1/2} = (\ln 2)\, N_A \left(\frac{f_A x \varepsilon}{W}\right) \sqrt{\frac{Mt}{b\Delta E}}, \tag{5.28}$$

being $N_A$ the Avogadro constant, $W$ the molecular weight, $f_A$ the isotopic abundance of the candidate nucleus and $x$ the number of candidate nuclei per molecule. This expression is usually used to compare different experiments. If the number of total events is very low ($< 15$), $S$ is not evaluated with equation 5.27 but as the upper limit of a Poisson process with background [170].

Efficiencies of our detector for the different possible signals have been simulated by Monte Carlo with the software PENELOPE [171]. As an example, figure 5.18 shows the spectrum simulated for the $\varepsilon\beta^+0\nu$ decay mode.

We have summarized in the table 5.6 the possible peak signals that could be detected from the doble beta decay modes (two neutrinos and neutrinoless) mentioned above. We have highlighted in bold those that have more detection probabilities with our bolometer for each decay mode. Although the $2\varepsilon2\nu$ 28.6 keV signal is lower than our detection threshold, we have included it foreseeing the possible future development of a $SrF_2$ bolometer with lower energy threshold. As stated before we will finally search for the $2\varepsilon2\nu$ decay to the $2^+$ excited state looking for a peak at 910.2 keV and for the $\varepsilon\beta^+0\nu$ decay to the ground state looking for a peak at 765.0 keV.

As can be seen in figure 5.19 there were no evidence of a DBD signal neither at 765 keV nor 910 keV. Then, in absence of a signal, we derive a limit $\lim S$ to the half-lives of the processes at 90% C.L. (this value of C.L. will be used from this point for remaining calculations) as

$$\lim S = n + 1.28\sqrt{n} - B \tag{5.29}$$

being $n$ the number of events detected in the energy window where the DBD signal is searched and $B$ is the expected number of events due to background. The former is estimated from the background measured in the spectrum below and above next to the region of interest.

| Decay mode | Detection | Peak energy | $\varepsilon_T$ |
|---|---|---|---|
| $2\varepsilon 2\nu$ | 2 X–ray (KK) | **28.6 keV** | **0.983** |
| (g.s. $\rightarrow$ g.s.) | 2 X–ray (KL) | 16.0 keV | 0.991 |
| | 2 X–ray (LL) | 3.4 keV | $\approx$1 |
| $2\varepsilon 2\nu$ | 2 X–ray (KK) + $\gamma$(881.6 keV) | **910.2 keV** | **0.0271** |
| (g.s. $\rightarrow$ 881.6 keV) | 2 X–ray (KL) + $\gamma$(881.6 keV) | 897.6 keV | 0.0274 |
| | 2 X–ray (LL) + $\gamma$(881.6 keV) | 885.0 keV | 0.0276 |
| $\varepsilon\beta^+ 0\nu$ | X–ray(K)+e$^+$+ 2$\gamma$(511 keV) | 1787 keV | 0.0029 |
| (g.s. $\rightarrow$ g.s.) | X–ray(K)+e$^+$+ $\gamma$(511 keV) | 1276 keV | 0.0877 |
| | X–ray(K)+e$^+$ | **765 keV** | **0.452** |

Table 5.6: *Most plausible double beta decay modes and signals that could be studied with a $SrF_2$ bolometer. The energy of the searched peak signal [168] and its total detection efficiency $\varepsilon_T$ are indicated. The most probable signal for each mode is highlighted in bold.*

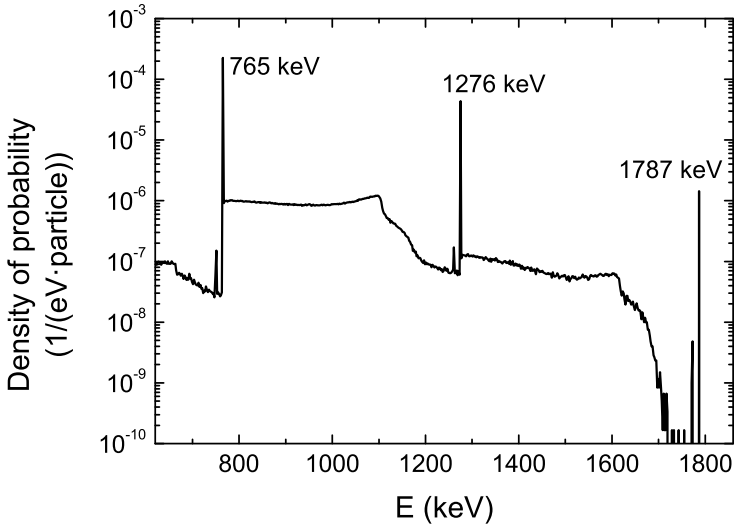


Figure 5.18: *Spectrum produced by the emission of 765 keV positrons in the bulk of our $SrF_2$ crystal simulated by Monte Carlo with PENELOPE [171]. The higher energy peak corresponds with the complete absorption of the positron and the two 511 keV photons produced by the annihilation. Peaks at 1276 keV and 765 keV correspond with, respectively, the single and double escape of the full energy peak. Small peaks at the left of the main ones come from the escape of a K–shell X–ray. It is clear that the signal with the higher efficiency is the 765 keV peak.*

We assumed an energy resolution for our detector of 1.8% for the $\beta/\gamma$ peaks, according to the resolution obtained at the 662 keV peak in a calibration with a $^{137}$Cs

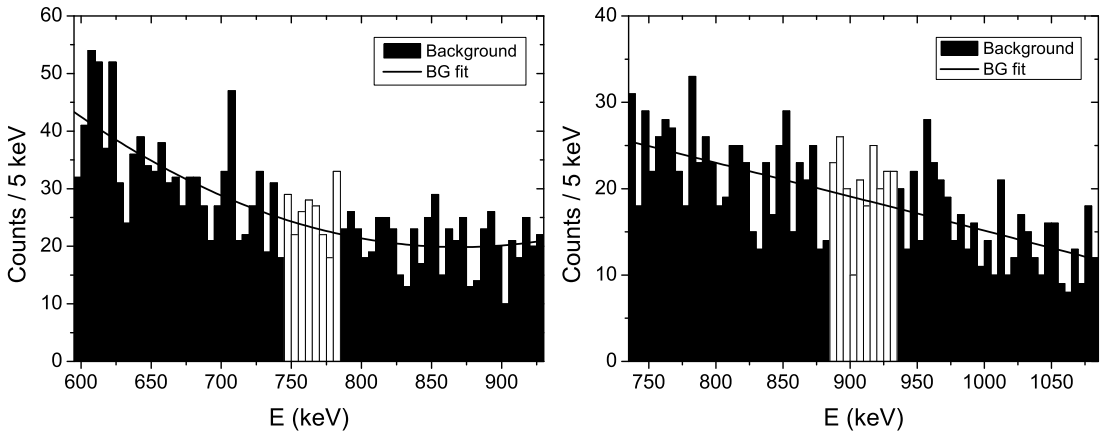


(a) (b)

Figure 5.19: *Energy regions around the searched signals of 765.0 keV and 910.1 keV in the spectrum measured in 14.1 h with the $SrF_2$ bolometer. Black filled columns indicate the regions used to parameterize the background. Fitted functions are also plotted.*

gamma source. We defined the energy window where the DBD peak is searched as $E \pm 1.4\sigma$ which covers the 83.85% of the total area in a gaussian peak. The number of events enclosed in this region is $n$. To obtain the expected background, we fitted the spectrum in an energy window of $\simeq 300$ keV centered in the energy of the searched signal to a parabolic function. To avoid the influence of the possible DBD signal, the region $E \pm 3\sigma$ was not included in the background fit. In the figure 5.19, the regions used to parameterize the background are plotted in black filled columns and the black line corresponds with the fitted function. Finally, to estimate the parameter $B$, we integrated the background function between $E - 1.4\sigma$ and $E + 1.4\sigma$. Values obtained for $n$ and $b$ are shown in the table 5.7.

| E (keV) | $\sigma$ (keV) | Expected background ($B$) | Peak events ($n$) | $\lim S$ |
|---|---|---|---|---|
| 765 | 5.86 | 76.3 | 85.7 | 21.2 |
| 910.1 | 6.97 | 73.0 | 72.6 | 14.1 |

Table 5.7: *Summary of the parameters and data used to estimate the upper limit to a DBD signal in our 14.1 h measurement shown in figure 5.19.*

To calculate the upper limit of our signal we required it to be within the allowed physical range (it can not be negative) [170]. To estimate the half-life limit from $\lim S$ we have to introduce an additional factor in the right–hand side of the formula 5.26, the gaussian correction factor 0.8385 associated with the region selected of the peak

($E \pm 1.4\sigma$). The remaining factors are related with the experimental configuration: the number of candidate nuclei $N$ can be calculated from the mass of the bolometer (53.6 g) and the isotopic abundance of $^{84}$Sr (0.54% of natural strontium); the live time was 14.1 h. With all this data we estimated the following limits (at 90% C.L.) on the half-life of the two double beta decay processes of the $^{84}$Sr studied:

$$T_{1/2}^{\varepsilon\beta^+0\nu}(\text{g.s.} \rightarrow \text{g.s.}) \geq 4.2 \cdot 10^{16} \text{ yr} \tag{5.30}$$

$$T_{1/2}^{2\varepsilon2\nu}(\text{g.s.} \rightarrow 882.6 \text{ keV}) \geq 3.7 \cdot 10^{15} \text{ yr} \tag{5.31}$$

Although our experiment was not optimized to study these decays, our limit on the half–life for the mode $\varepsilon\beta^+0\nu$ to the ground state of the daughter nucleus in $^{84}$Sr is better than the best published limit so far, estimated by P. Belli et al. [166] ($6.9{\cdot}10^{15}$ yr) with a $SrI_2$(Eu) scintillator, and close to the limit advanced by H. J. Kim in [167] but not yet published ($4.6 \cdot 10^{17}$ yr) with a $SrCl_2$ scintillating crystal. For the mode $2\varepsilon2\nu$, our result is one order of magnitude below the limit reached in [166] ($3.1 \cdot 10^{16}$ yr). Anyway, all these limits are far from the theoretical calculations. For instance, in [172] using a deformed shell model, there is an estimate of $\sim 10^{26}$ and $\sim 10^{24}$ years for the double decay modes $\varepsilon\beta^+2\nu$ and $2\varepsilon2\nu$ (and for the neutrinoless modes higher values can be expected).

### Sensitivity for $\varepsilon\beta^+0\nu$ decay

Some improvements in our experiment could enhance its sensitivity to DBD processes. We studied the effect in the $\varepsilon\beta^+0\nu$ mode for which we obtained a half-life limit competitive with current experimental results. We assumed some possible values for the background (from 0 up to $10^5$ counts/(keV kg yr)) and for the live time of the measurement (from $10^{-2}$ to 1 yr). The values of sensitivity obtained are shown in the table 5.8. The higher sensitivity, that estimated for the case with longest $t$ and lowest background, reaches a value of $1.9 \cdot 10^{20}$ yr. For a given measuring time, the sensitivity not always enhance by diminishing the background; it has an asymptotic behavior due to the fact that, from a given experimental point, the detected events are practically zero and thereafter $S_{1/2}$ does not scale with $b^{1/2}$. Consequently, one must upgrade other parameters to raise the limit.

The sensitivity is directly proportional to the isotopic abundance of the $^{84}$Sr (equation 5.28). Enrichments of 99% could be achieved [173] (against the 0.54% of natural abundance), increasing the limits on the half–lives by two orders of magnitude. Sensitivities of the order of $10^{21}$–$10^{22}$ yr could be reached.

| $b$ $(c/(keV\ kg\ yr))$ \ $t(yr)$ | 0.01 | 0.1 | 1 |
|---|---|---|---|
| 0 | $1.9{\cdot}10^{18}$ (*) | $1.9{\cdot}10^{19}$ (*) | $1.9{\cdot}10^{20}$ (*) |
| $10^0$ | $1.9{\cdot}10^{18}$ (*) | $1.9{\cdot}10^{19}$ (*) | $1.0{\cdot}10^{20}$ (*) |
| $10^1$ | $1.9{\cdot}10^{18}$ (*) | $1.0{\cdot}10^{19}$ (*) | $6.2{\cdot}10^{19}$ (*) |
| $10^2$ | $1.0{\cdot}10^{18}$ (*) | $6.2{\cdot}10^{18}$ (*) | $4.0{\cdot}10^{19}$ |
| $10^3$ | $6.2{\cdot}10^{17}$ (*) | $4.0{\cdot}10^{18}$ | $1.3{\cdot}10^{19}$ |
| $10^4$ | $4.0{\cdot}10^{17}$ | $1.3{\cdot}10^{18}$ | $4.0{\cdot}10^{18}$ |
| $10^5$ | $1.3{\cdot}10^{17}$ | $4.0{\cdot}10^{17}$ | $1.3{\cdot}10^{18}$ |

Table 5.8: *Sensitivity (in years) to the half–life of the process $\varepsilon\beta^+0\nu$ using different values of the background (b, in units of counts/(keV kg yr)) and the measuring time (t, in years). Results had been calculated using the equation 5.28, with the exception of those scenarios marked with (*) where the number of events is not enough to use the gaussian approximation and the limits to the signal were calculated as Poisson processes with background [170].*

The other parameters that can be changed are the detector mass and its efficiency, but they are correlated in the sense that a change in the mass leads to a modification in the detector size and efficiency. Following the same method than before to calculate the efficiency, we simulated three $SrF_2$ cylindrical crystals with masses of 200 g (heigh = diameter = 3.917 cm), 500 g ($h = \varnothing = 5.316$ cm ) and 2 kg ($h = \varnothing = 8.438$ cm). In this case, estimations of the efficiency were done not only searching the 765 keV signal of the $\varepsilon\beta^+0\nu$ decay, but also the signals of 1276 and 1787 keV which assume the absorbtion of either one or both 511 keV photons. In table 5.9 it can be observed how the efficiency for the double escape peak decreases as the bolometer becomes larger, whereas the efficiencies for the single escape and full absorption peaks increase with the mass. The sensitivity $S_{1/2}$ in each case is also given in the table 5.9 and plotted in figure 5.20. This value tends to an asymptote by increasing the bolometer size, and an optimal mass and size could be achieved for each searched signal. In our case, the better limits could be attained by searching the 1276 keV signal in bolometers of 2 kg.

| Energy (keV) | Bolometer mass (kg) | $\varepsilon$ | $S_{1/2}$ (y) |
|---|---|---|---|
| 765 | 0.0536 | 0.453 | $5.4{\cdot}10^{16}$ |
| | 0.2 | 0.321 | $7.4{\cdot}10^{16}$ |
| | 0.5 | 0.228 | $8.3{\cdot}10^{16}$ |
| | 2.0 | 0.116 | $8.5{\cdot}10^{16}$ |
| 1276 | 0.0536 | 0.0877 | $1.3{\cdot}10^{16}$ |
| | 0.2 | 0.152 | $4.2{\cdot}10^{16}$ |
| | 0.5 | 0.207 | $9.0{\cdot}10^{16}$ |
| | 2.0 | 0.275 | $2.4{\cdot}10^{17}$ |
| 1787 | 0.0536 | 0.0029 | $4.8{\cdot}10^{14}$ |
| | 0.2 | 0.0114 | $3.7{\cdot}10^{15}$ |
| | 0.5 | 0.0274 | $1.4{\cdot}10^{16}$ |
| | 2.0 | 0.0834 | $8.5{\cdot}10^{16}$ |

Table 5.9: *Efficiency $\varepsilon$ and sensitivity $S_{1/2}$ to the $\varepsilon\beta^+0\nu$ process for different $SrF_2$ bolometer masses and searched signals.*

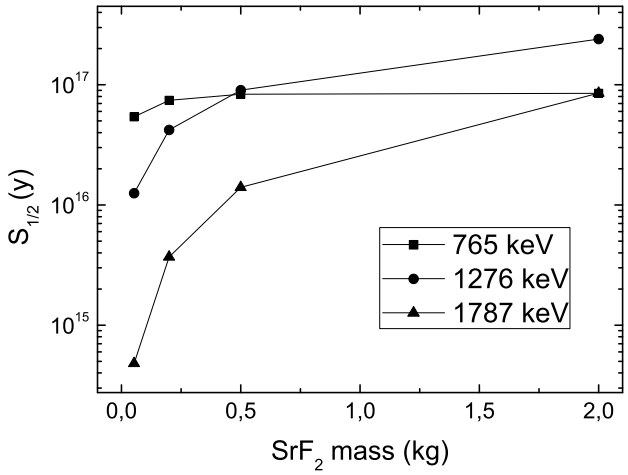


Figure 5.20: *Detection sensitivity to $\varepsilon\beta^+0\nu$ as a function of the crystal mass through three possible signals described in the table 5.6, detecting both 511 keV photons (signal at 1787 keV), one 511 keV photon (signal at 1276 keV) or neither of them (signal at 765 keV).*

## 5.2 Bolometers for neutron spectroscopy

One of the most practical techniques for very low background neutron spectroscopy are those based on neutron–induced nuclear reactions. The incoming neutron energy

is shared between the reaction products, and the energy deposited by these heavy charged particles, after subtracting the Q value of the reaction, gives directly the incident neutron energy. In this section we have studied different scintillating bolometers made of targets containing $^{6}$Li and/or $^{10}$B, some of the preferred isotopes due to their relatively high cross–section for neutron captures.

### 5.2.1 LiF scintillating bolometers

LiF is an interesting material for bolometric neutron detection: its low heat capacity (with a Debye temperature of 734 K [174]) makes it suitable as bolometer and, although its scintillation is negligible at room temperature, the light emission increases as temperature goes down. Several LiF bolometers and scintillating bolometers have been built by the IAS group [175,176] and some of them were tested within the ROSEBUD collaboration at the Canfranc Underground Laboratory due to its promising features as both dark matter target (two light nuclei with non zero nuclear spin, sensitive to light WIMPs and spin–dependent interactions) and neutron detector [8, 97].

Previous works [176] showed that LiF has a feeble light yield compared with other scintillating bolometers (6.8 times lower than $SrF_2$ in $\alpha$ response) but it is enough to discriminate the neutron capture reaction $^{6}$Li(n,t)$\alpha$ (with Q–value = 4.78 MeV) from the $\gamma$ background. This allows to make fast neutron spectroscopy at virtually zero background [177]. In the J. Gironnet Ph.D. thesis [178], it is described the development of LiF neutron spectrometers at IAS, including the characterization in the monoenergetic neutron source AMANDE at the French Institute for Radiological Protection and Nuclear Safety (IRSN) of a semi-portable prototype with a $^{6}$Li enriched LiF bolometer of 0.5 g. Efforts have been also directed to the measurement of the differential neutron flux inside a bolometric experiment with the simultaneous use of LiF and $Al_2O_3$ detectors, showing the feasibility of monitoring the fast neutron flux inside the shielding of future dark matter searches with scintillating bolometers [97]. This idea has been developed in the Ph.D. thesis of T. Rolón [98].

In this work, we have estimated the light REF of a 33 g LiF scintillating bolometer irradiated at IAS with $\alpha$ particles from a $^{241}$Am source and $\beta/\gamma/\mu$ particles and neutrons from the natural radioactive background. To obtain the REF$_l(\beta/\gamma{:}\alpha)$ we used a measurement with the $^{241}$Am source partially covered with mylar foils (one third of the source area was covered with 6 $\mu$m and another third with 12 $\mu$m). In this way, we observed the $\alpha$ line from $^{241}$Am at 5.48 MeV and two $\alpha$ energy degraded lines at 4.00 and 4.76 MeV (see figure 5.21a). The energy of degraded $\alpha$ particles was

estimated with SRIM [160]. Measurements were performed at surface level (at IAS) instead of underground (at LSC) in order to have a high flux of cosmic ray muons and, consequently, extend the $\beta/\gamma$ band to the energies of the $\alpha$ particles. The energy calibration was performed with the three $\alpha$ lines considering a $\mathrm{REF}_h(\beta/\gamma{:}\alpha) = 1$. Responses to $\beta/\gamma$ and $\alpha$ particles where divided into energy windows and fitted to parabolic functions (the energy range selected for the $\alpha$ band was from 3 to 7 MeV, to ensure good statistics). The light REF was calculated as the quotient between the two fitted functions as done in section 5.1.3. The obtained values are displayed as a solid line with gray error band in figure 5.22a. Values were also estimated at the energy of the three $\alpha$ lines (filled dots), assuming an energy window for each line that includes the $\alpha$ peak (horizontal error bars in 5.22a represent the window width) and estimating the center of their light distributions. These discrete values are also given in table 5.10.

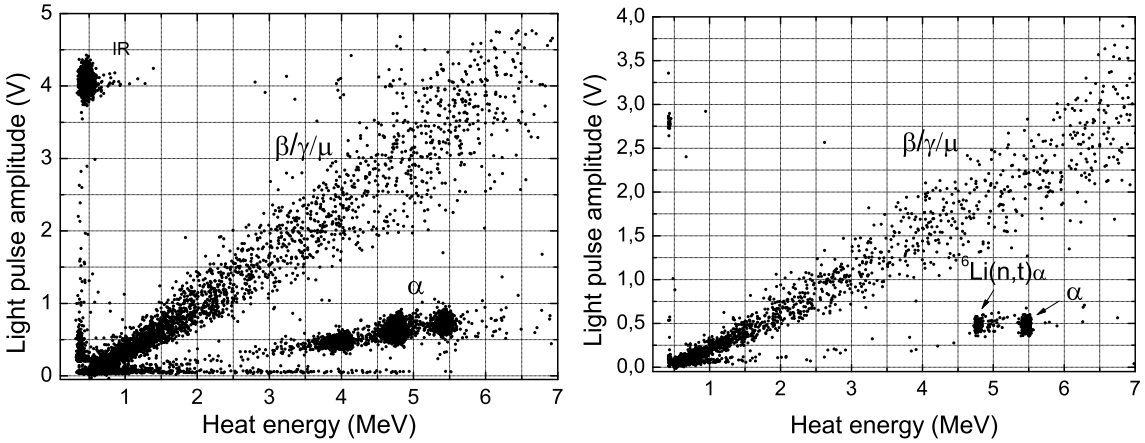


(a) (b)

Figure 5.21: *Heat versus light scatter plots of the LiF scintillating bolometer. In (a) the detector was exposed to a $^{241}Am$ $\alpha$ source partially covered with mylar foils of different thicknesses (6 and 12 $\mu m$) allowing to have $\alpha$ particles at three different energies (5.48, 4.76 and 4.00 MeV). Heat energy calibration was performed with the $\alpha$ band. In (b) the $^{241}Am$ source is uncovered. We can distinguish $\alpha$ particles from $^{241}Am$ (labeled $\alpha$), the thermal neutron capture $^{6}Li(n,t)\alpha$ and some fast neutrons events (placed between the two mentioned peaks). Neutrons and $\beta/\gamma$ events come from the natural radioactive background.*

The light REF between $\beta/\gamma$ events and the products of the $^{6}$Li(n,t)$\alpha$ neutron capture reaction was estimated from natural background, in a measurement in which the $^{241}$Am source was uncovered (figure 5.21b). In the quoted capture, thermal neutrons of the background are absorbed by $^{6}$Li nuclei with an available energy of $Q = 4.78$ MeV, resulting in the emission of an $\alpha$ particle (with 2.05 MeV kinetic

energy) and a tritium nucleus (with 2.73 MeV kinetic energy). If the captured neutron is not thermalized, the available energy in the capture reaction is the sum of $Q$ and the neutron kinetic energy. The peak labeled as $^6$Li(n,t)$\alpha$ in figure 5.21b at 4.78 MeV corresponds to the combined absorbtion of the $\alpha$ and tritium particles produced by thermal neutrons. It presents a FWHM energy resolution of 53 keV. The few events placed at its right, between the neutron capture reaction and the $\alpha$ peak (5.5 MeV) come from the capture of fast neutrons, mainly from the $^6$Li(n,t)$\alpha$ resonance at about 240 keV (signal at $\simeq$ 5.02 MeV). The light REF($\beta/\gamma$:$^6$Li(n,t)$\alpha$) at 4.78 MeV was obtained as the quotient between the center of the light distributions of $\beta/\gamma$ events and that of the neutron capture peak, in an energy window for both bands centered in the $Q$ value and wide enough to cover the whole capture peak. The estimated value was $4.3 \pm 0.2$ and it is represented as an empty dot in the figure 5.22a.

| Energy (MeV) | $REF_l$ |
|---|---|
| 4.00 | $4.79 \pm 0.06$ |
| 4.76 | $4.7 \pm 0.1$ |
| 5.47 | $4.63 \pm 0.7$ |
| 4.78(*) | $4.3 \pm 0.2$ |

Table 5.10: *Estimated discrete values of $REF_l(\beta/\gamma{:}\alpha)$ (first three values) and $REF_l(\beta/\gamma{:}^6Li(n,t)\alpha)$ (marked with *).*

We applied the semi–empirical model proposed by Tretyak, already used with the $SrF_2$ scintillating bolometer, to estimate the light response of LiF to different particles. The Birks factor was estimated by fitting the continuous $REF_l(\beta/\gamma{:}\alpha)$ of figure 5.22a to equation 5.12 in the region from 3.5 to 6 MeV where most of the $\alpha$ events are concentrated. The calculated $kB$ value was 3.48 mg/(MeV·cm$^2$) with a goodness of fit $\chi^2/n.d.f. = 2.1$. The fitted value of light REF for $\alpha$ particles is represented in the same figure with a dashed line. Values obtained with this Birks factor for F, Li and tritium nuclei are also plotted in the figure 5.22b.

To test the Tretyak model, we could obtain the theoretical light response for the $\alpha$ and tritium particles emitted in the thermal neutron capture reaction based on the estimations of their respective light REFs. This calculations are summarized in table 5.11. The theoretical estimation of the light response for the coincidence $\alpha$ and tritium would be $579 \pm 11$ mV and the experimental peak is centered at $486 \pm 3$ mV. It can be concluded that the model underestimates at least one of the light REFs ($\alpha$ particles or tritium).

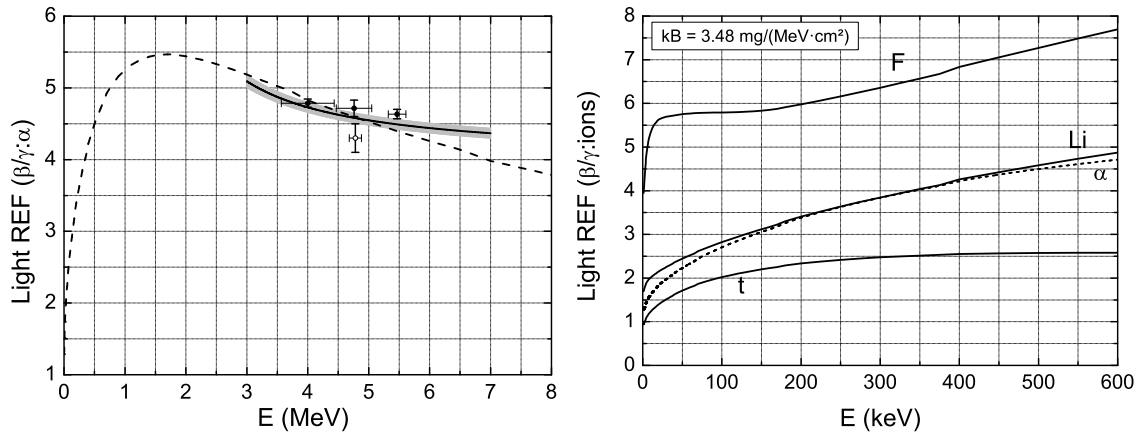


(a) (b)

Figure 5.22: *In (a) they are shown the experimental $REF_l(\beta/\gamma{:}\alpha)$ (solid line with error band for the continuous estimation and black dots for the discrete ones) and $REF_l(\beta/\gamma{:}^6Li(n,t)\alpha)$ at the $^6Li(n,t)\alpha$ energy (white dot). The dashed line in (a) is the $REF_l(\beta/\gamma{:}\alpha)$ obtained from the fit explained in the text following the Tretyak approach, that gives a Birks factor $kB = 3.48$ mg/(MeV·cm$^2$). In (b) they are shown the $REF_l$ estimations obtained with the same Birks factor for $\alpha$ particles (dashed line, already shown in (a)), tritium recoils and Li and F nuclear recoils.*

### 5.2.2 Enriched $^6$LiF scintillating bolometer

Natural lithium consists of $^6$Li (7.5%) and $^7$Li (92.5%), and natural fluorine consists of $^{19}$F (100%). The isotope of LiF that dominates the thermal neutron capture is $^6$Li (see figure 5.23a), but its isotopic abundance in natural lithium is rather low. LiF crystals enriched in $^6$Li have been built and tested in order to increase the neutron detection efficiency. Apart from the transportable 0.5 g $^6$LiF neutron detector developed at IAS and mentioned above (enriched at 95% in $^6$Li, 32 keV energy resolution for the thermal neutron capture peak [177]), other small enriched $^6$LiF crystals (no larger than 0.5 g) reported good features detecting the $^6$Li(n,t)$\alpha$ neutron capture reaction operating as bolometers at temperatures $\sim 0.1$ K, reaching FWHM energy resolutions of 39 keV at 5.3 MeV [179] and 52 keV at 4.8 MeV [180].

A prototype $^6$LiF (enriched at 95% in $^6$Li) cylindrical cristal ($\o$ = 25.1 mm, $h$ = 25.2 mm) of 32 g mass was tested as scintillating bolometer at 20 mK first at IAS and then in an ultralow background environment at the LSC. Figure 5.24a shows a measurement carried out at IAS with irradiation of $\alpha$ particles from $^{241}$Am and neutrons thermalized with paraffin from a $^{252}$Cf source. The peaks of neutron capture and $\alpha$ particles are easily identified. The heat energy spectrum of this measurement

| Energy (MeV) | Light response $\beta/\gamma$ (mV) | REF$_l(\beta/\gamma$:ion) | Light response ion (mV) | Summ (mV) |
|---|---|---|---|---|
| 2.05 ($\alpha$) | 648±11 | 5.43 | 119±2 | 579±11 |
| 2.73 (t) | 956±22 | 2.08 | 460±10 | |

Table 5.11: *Calculations of the light response for the coincidence $\alpha$ and tritium from the thermal neutron capture in $^6$Li, based on their respective REF$_l$ estimations with the Tretyak model.*

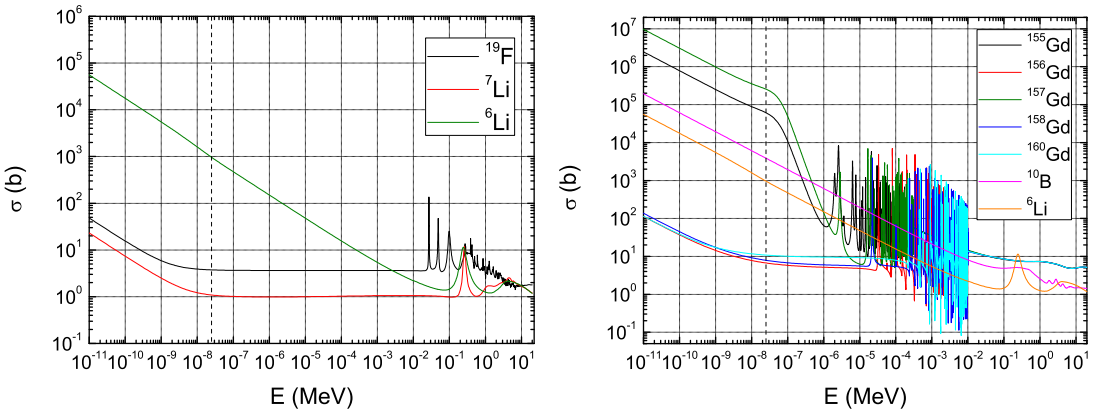


(a) (b)

Figure 5.23: *Total neutron capture cross section for the main isotopes present in LiF (a) and LGBO (b) [96]. The vertical dashed line indicates the thermal neutron energy.*

is displayed in figure 5.24b superimposed to the spectrum of a measurement with fast neutrons (where the neutrons from the $^{252}$Cf source were not thermalized). Fast neutrons captured at the $^6$Li resonance appear mostly 240 keV above the thermal neutrons capture (see in figure 5.23a the resonance in the neutron capture cross section of $^6$Li at this energy). The achieved energy resolution was 32 keV FWHM both for the thermal neutron capture and for the $\alpha$ peak. The tail of events in the left of the thermal neutron peak corresponds with surface captures of neutrons where one of the products, $\alpha$ or tritium nucleus, escapes without being fully absorbed.

These first tests showed that about 40% of the neutron captures occur near to the surface of the crystal producing losses in the energy detected; note that the mean free path of thermal neutrons in $^6$LiF(95%) has been estimated in 170 $\mu$m, and that of $\alpha$ particles and tritium ions are 6 $\mu$m and 35 $\mu$m, respectively. An optimal design of the size of the crystal could be used in the development of future $^6$LiF detectors.

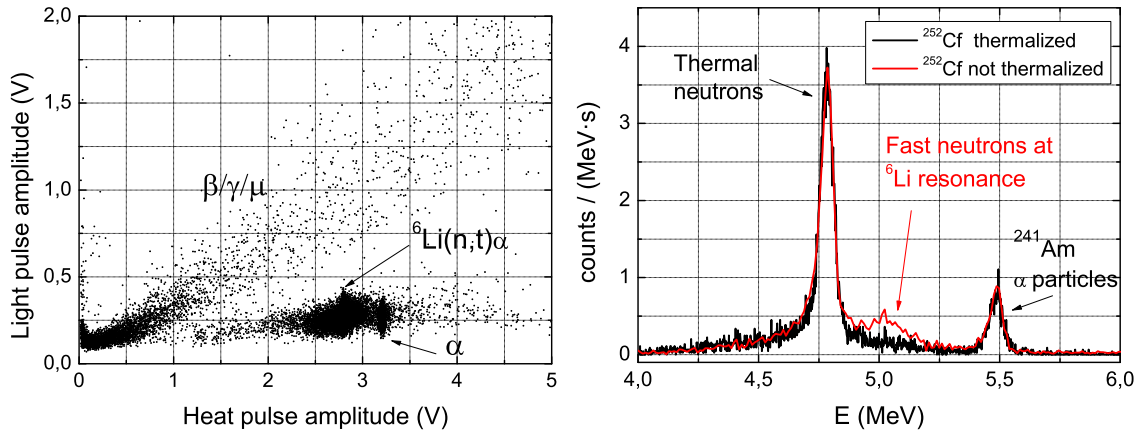


(a) (b)

Figure 5.24: *In (a) it is shown a light vs heat scatter plot of the 32 g $^{6}$LiF scintillating bolometer irradiated at IAS with thermal neutrons from a $^{252}$Cf source covered with paraffine and with α particles from a $^{241}$Am source. Events in the β/γ/μ band come from the natural radioactive background. In (b) it is represented (black line) the heat spectrum of the neutron capture reaction and α particles from the measurement shown in (a) and that of a measurement with fast neutrons, using the $^{252}$Cf neutron source without paraffin (red line).*

The measured light yield was twice lower than that of other not enriched LiF crystals [176], obtaining values of 0.21 keV/MeV for gammas, 0.06 keV/MeV for the neutron capture and 0.05 keV/MeV for $\alpha$ particles. In spite of this low scintillation yield, the neutron band is well separated from the $\beta/\gamma$ band down to 2 MeV, with a discrimination power defined as in equation 5.16 but for this magnitude $D = 2.7 \pm 0.4$ sigma at this energy. Light discrimination between neutron captures and $\alpha$ particles is not possible because the two bands are overlapped (see figure 5.24a). To estimate light REFs, heat energy windows of $2.4\sigma$ around the peak centers where selected, estimating the light responses as the center of the light distributions for each band and window. Results were a $\mathrm{REF}_l(\beta/\gamma{:}\alpha)$ of $4.7 \pm 0.5$ at 5.48 MeV and a $\mathrm{REF}_l(\beta/\gamma{:}^{6}\mathrm{Li(n,t)}\alpha)$ of $3.48 \pm 0.05$ at 4.78 MeV. The former is very similar to that obtained for natural LiF whereas the latter is a 20% lower.

The enriched $^{6}$LiF scintillating bolometer was measured underground in the Hall B of the LSC. A light vs heat scatter plot is shown in figure 5.25. A $^{241}$Am $\alpha$ source covered with a 23.5 $\mu$m mylar foil was installed in the bolometer, producing energy degraded alpha particles ($E_\alpha = 2133$ keV) to avoid its overlapping with the thermal neutron peak. There was also a small silver disk ($\phi = 1.6$ mm, thickness = 30 $\mu$m) glued to the crystal and facing the $^{241}$Am source, installed for other purposes (it

is being used by the IAS group to study the absolute energy thermalized in the bolometer after a particle interaction). Approximately one half of the $\alpha$ particles coming from the source interact with the silver disk (green events in figure 5.25, are easily identified due to their fast time constants) and the other half with the $^{6}$LiF crystal (red events). There was a group of events (displayed in blue) in the region where the neutron capture was expected, between 4 and 6 MeV, whose origin could be attributed to $\alpha$ particles from inner contamination, although peaks are not well resolved in the heat spectrum due to the poor energy resolution. The number of events in this group, 328, is in agreement with the radioactive contamination levels measured by M. De Jésus (Institut de Physique Nucléaire de Lyon) in the powder used to build the crystal, mainly from the $^{238}$U natural chain. These measurements showed activity levels of $125 \pm 13$ mBq/kg of $^{234}$Th, $10 \pm 3$ mBq/kg of $^{214}$Pb and $74 \pm 14$ mBq/kg of $^{210}$Pb.

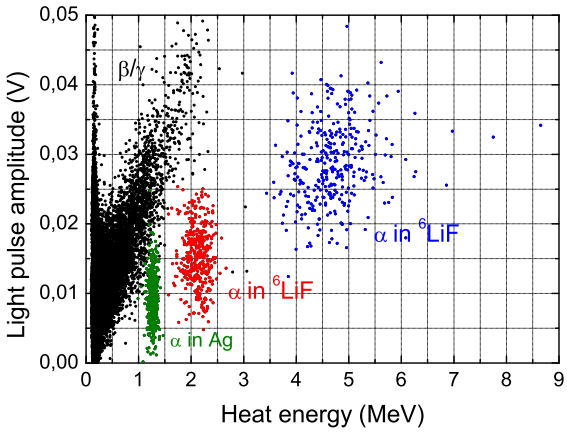


Figure 5.25: *Light vs heat scatter plot of the 32 g $^{6}$LiF scintillating bolometer in a background measurement of 9.45 h at LSC.*

### 5.2.3 Others $^{6}$Li/$^{10}$B based materials

Other scintillators based on neutron captures in $^{6}$Li and $^{10}$B are being investigated at IAS for neutron detection purposes. Two small lithium borates (5 x 5 x 5 mm$^3$), LGBO ($Li_6Gd(BO_3)_3$, enriched at 95% in both isotopes $^{6}$Li and $^{10}$B) and $Li_6Eu(BO_3)_3$, were built and preliminarily tested as scintillating bolometers.

In this case also the $^{10}$B(n,$\alpha$) reaction can be used to detect neutrons, specially thermal neutrons. The natural isotopic abundance of $^{10}$B is 19.8%. The reaction, whose cross section is shown in figure 5.23b, can lead to an excited state of $^{7}$Li (94%, with Q–value = 2.310 MeV) or to the ground state of $^{7}$Li (6%, with Q–value = 2.792 MeV).

The $Li_6Eu(BO_3)_3$ detector has been preliminarily studied in the J. Gironnet Ph.D. thesis [178] and in [181]. Promising results were found, obtaining a collected light yield 10 times better than that from our $^6$LiF with excellent FWHM energy resolution (13 keV on the $^{10}$B thermal neutron capture peak at 2.310 MeV).

Our work has focused on the characterization of the LGBO crystal. This material has several nuclei with high cross section for thermal neutron capture ($^6$Li, $^{10}$B and several Gd isotopes, see figure 5.23b), which could be a disadvantage for thermal neutron detection since Gd has the higher cross sections (specially $^{155}$Gd and $^{157}$Gd, with natural isotopic abundance of 14.8% and 15.7%, respectively) and its products are difficult to detect, but an advantage if your purpose is to detect fast neutrons because the thermal peak becomes lower. In figure 5.26 it can be observed a measurement of LGBO exposed to a $^{241}$Am source and to thermalized neutrons from the $^{252}$Cf source. The $^{241}$Am source was not well collimated and its 60 keV photons are sometimes detected together with the $\alpha$ particles. Some of these photons interact in the optical bolometer in coincidence with the absorbtion of 5.48 MeV $\alpha$ particles in the LGBO crystal; these events form the tail at higher light amplitude of the $\alpha$ peak (red dots). The neutron capture $^6$Li(n,t)$\alpha$ is displayed in blue. Green events are due to captures in $^{10}$B.

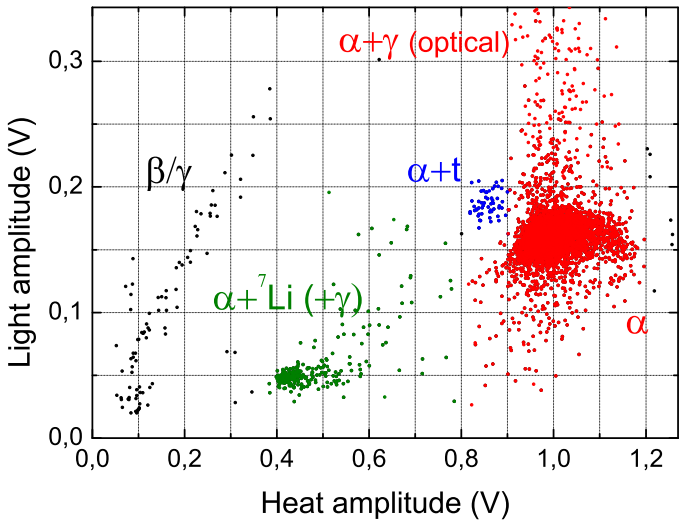


Figure 5.26: *Light versus heat scatter plot of the LGBO scintillating bolometer irradiated with $\alpha$ particles from $^{241}$Am and thermalized neutrons from a $^{252}$Cf source. Neutron captures in $^6$Li (blue) and $^{10}$B (green) can be observed.*

Poor energy resolution was observed in LGBO, being the FWHM for the $\alpha$ peak of $\simeq 9\%$. The collected light yield estimated was 0.08 keV/MeV for $\alpha + t$ events at 4.8 MeV, 0.04 keV/MeV for $\alpha$+$^7$Li at 2.3 MeV and 0.06 keV/MeV for $\alpha$ particles at 5.5 MeV. The average light yield of $\beta/\gamma$ events, extrapolating the $\beta/\gamma$ band to the

energy of the three peaks, was estimated as 0.26 keV/MeV. The light REF for the three peaks with regard to the $\beta/\gamma$ band was also obtained by fitting to a straight line the $\beta/\gamma$ band and extrapolating the fitted function up to the energies of the peaks (it was considered heat REF = 1). Estimations are $REF_l(\beta/\gamma{:}^6Li(n,t)\alpha) = 3.3$, $REF_l(\beta/\gamma{:}^{10}B(n,\alpha)^7Li) = 6.1$ and $REF_l(\beta/\gamma{:}\alpha) = 4.3$. Table 5.12 summarizes the main features of neutron detectors studied in this section.

| Target | Light Yield (keV/MeV) | | | | $REF_l$ | | |
|---|---|---|---|---|---|---|---|
| | $\beta/\gamma$ | $\alpha$ | $^6Li(n,t)\alpha$ | $^{10}B(n,\alpha)^7Li$ | $(\beta/\gamma{:}\alpha)$ | $(\beta/\gamma{:}\alpha+t)$ | $(\beta/\gamma{:}\alpha{+}^7Li)$ |
| LiF | 0.38 | 0.11 | - | - | 4.7 | 4.3 | - |
| $^6$LiF | 0.21 | 0.05 | 0.06 | - | 4.7 | 3.5 | - |
| LGBO | 0.26 | 0.06 | 0.08 | 0.04 | 4.3 | 3.3 | 6.1 |

Table 5.12: *Summary of the response to different particles and the discrimination properties of the crystals studied in this work. The light yield for the not enriched LiF was extracted from [176]. Light REF($\beta/\gamma{:}\alpha$) was estimated at 5.5 MeV (the energy of the $^{241}Am$ $\alpha$ particles).*

## 5.3 Bolometers for dark matter searches

Accurate knowledge of light REF between electron and nuclear recoils is required by some dark matter direct search experiments to estimate the energy of the recoiling nuclei from the scintillation signal or to implement an effective background rejection based on the comparison of the scintillation with ionization or heat signals. In this section we present measurements of $REF_l(\beta/\gamma{:}\alpha)$ and $REF_l(\beta/\gamma{:}NR)$ estimated in two scintillating bolometers of BGO and $Al_2O_3$ operated at 20 mK. Measurements were carried out irradiating these detectors with fast neutrons, monoenergetic photons, $\alpha$ particles and recoiling nuclei arising from different radioactive sources.

Both detectors, BGO and $Al_2O_3$, have been widely studied in previous works of the IAS group [135,176] and in the ROSEBUD collaboration [8,24,36,140,182–185], and also values for light REFs were presented. In this work [37], we present a more detailed study which, besides the dependence on the energy, includes the dependence of the light response on the masses of the recoiling nuclei. Moreover, we performed a reanalysis of the pulses using a pulse template (allowing negative amplitudes) to estimate the heat and light amplitudes of the events (methods to estimate the pulse amplitude were explained in chapter 4) to avoid noise bias that could distort

estimates at very low energies. Results obtained for the different light REFs were compared with the calculations based on the Tretyak semi–empirical approach as was previously done for the $SrF_2$ and LiF bolometers. The discrimination capabilities of these detectors are also presented.

In collaboration with the *Instituto de Física Teórica* (IFT) and the *Universidad Autónoma de Madrid* (UAM) we have analyzed the role of different bolometric targets in the determination of the phenomenological properties of WIMP dark matter. We have investigated targets that have been used as scintillating bolometers and analyzed the conditions under which the DM properties can be reconstructed when combining data from these targets and those used by other experiments (in particular Ge and Xe). In this context, $Al_2O_3$ and LiF are the most promising targets (see [186] for details).

### 5.3.1 Particle discrimination in BGO

The BGO ($Bi_4Ge_3O_{12}$) scintillating crystal used in this section was a 46 g cylinder and measurements were performed in the IAS cryogenic facility. We studied its response to different particles exposing the scintillating bolometer to $\alpha$ particles from a $^{241}$Am source mounted inside the copper cavity, and to a $^{252}$Cf neutron source to induce recoils of the target nuclei. Scatter plots of light versus heat (energy calibrated) responses are shown in figure 5.27 for a high energy measurement with the $\alpha$ source (a) and for a low energy measurement with neutron induced nuclear recoils (b). The so–called $\beta/\gamma$ band was populated by cosmic muons, and by photons coming from the natural radioactive background and from the own crystal which was contaminated in $^{207}$Bi ($\simeq$ 3 Bq/kg of bismuth [140, 184]). In the $\alpha$ band there were also $\alpha$ particles arising from the natural radioactive series ($^{238}$U, $^{232}$Th and daughters) present in the crystal, and from the $^{209}$Bi $\alpha$ decay. The energy calibrations of the heat channel in both figures were obtained using $\gamma$ lines from $^{207}$Bi.

In the following we will assume that the heat response to different particles ($\alpha$, $\beta/\gamma$ and NR) is the same. This is a reasonable assumption for these bolometers (BGO and $Al_2O_3$) since heat REFs are expected to be close to unity although variations of a few percents have been reported [24, 36, 187, 188].

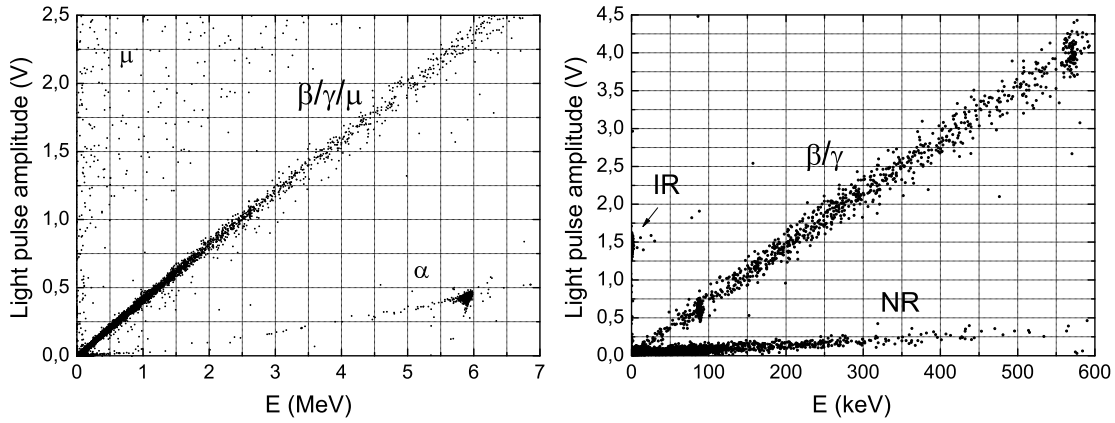


(a) (b)

Figure 5.27: *Light versus heat scatter plot obtained with the BGO scintillating bolometer; the heat channel was calibrated with $\gamma$ lines. In (a) the bolometer was irradiated with $\alpha$ particles from a $^{241}Am$ source (peaks in $\simeq 5.9$ MeV, indicating a 7% higher response for $\alpha$ particles than for $\beta/\gamma$ ones); events in the upper-left corner are due to muons depositing energy in both bolometers, the Ge light detector and the scintillating one. The Nuclear Recoil events in (b) were induced by neutrons from a $^{252}Cf$ source. IR pulses sent from a LED to the light detector are also indicated.*

### Light REF for $\alpha$ particles and NR events

Some of the bands in the plots of figure 5.27 show a slight deviation from linearity. We carried out F–tests for each band in order to decide wether a quadratic function gives a significantly better fit to the data than a straight line. We used linear fits for the bands unless the results of the F–test indicated that the second degree polynomial fit was more likely to be correct with a 5% significance level.

The $\beta/\gamma$ band of the figure 5.27a was parameterized by fitting their events to a straight line that describes the light response of the detector to electronic recoils as a function of the energy deposited in the crystal. The region from 3 to 7 MeV of the $\alpha$ band was best described by a quadratic function, consequently, the $\alpha$ light response was fitted to a parabolic function. The $\mathrm{REF}_l(\beta/\gamma{:}\alpha)$ was estimated from the ratio between the two fitted light responses, and it is shown in figure 5.28a with its $1\sigma$ error band. These uncertainties include statistical errors from the fitting parameters and a systematic error considering several fitting functions and fitting energy ranges (systematic error was estimated as half the difference between the maximum and minimum values obtained in the several considered fits). We have not estimated the $\alpha$ particles light response below 3 MeV because of the scarce number of events at

such low energies.

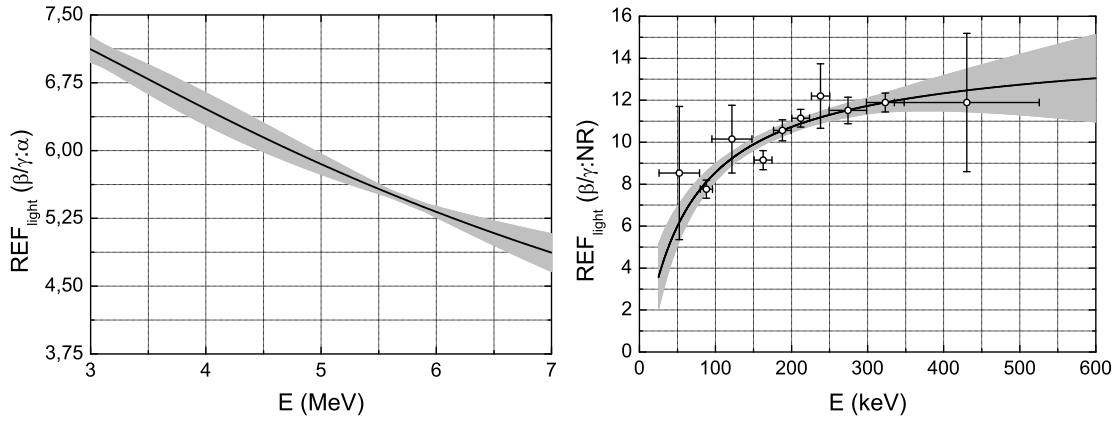


(a) (b)

Figure 5.28: *Light REF ($\beta/\gamma$:$\alpha$) (a) and light REF ($\beta/\gamma$:NR) for the BGO scintillating bolometer. Grey areas represent the $1\sigma$ error bands. The white dots in (b) correspond to discrete estimates with energy windows.*

The events of the $\beta/\gamma$ and neutron induced nuclear recoils bands shown in figure 5.27b were fitted both to second degree polynomial functions to describe the two light responses. The $\mathrm{REF}_l(\beta/\gamma\text{:NR})$, obtained by dividing the two fitted functions, is shown in figure 5.28b. Uncertainties at one standard deviation are included considering statistical and systematic errors as in the case of the figure 5.28a. The estimated light REF is an effective value resulting of combining Bi, Ge and O recoil events, although, for kinematic reasons, at energies above 20–25 keV the contribution of Bi recoiling nuclei is negligible and above 70–80 keV also that of Ge nuclei. We also estimated the $\mathrm{REF}_l(\beta/\gamma\text{:NR})$ at particular energy windows by dividing the mean light responses to $\beta/\gamma$ events with that to NR events for each energy window. Results are shown as white dots in the figure 5.28b.

We defined in the equation 5.16 the discrimination power for the time constants of pulses, but as in section 5.2.2 any other magnitude can be used instead, as for example the light response. With this expression, we take into account not only the mean values $\mu$, but also the dispersion, represented by the standard deviation $\sigma$, since it is a fundamental parameter to discriminate between two different populations. When focusing on the rejection of events of one of the populations, as it is the case of $\gamma$ background rejection in dark matter experiments, we can define the rejection power $R$ of $\beta/\gamma$ background from the nuclear recoil region of interest as

$$R(\beta/\gamma : NR) = \frac{\mu^{\beta/\gamma} - \mu^{NR}}{\sigma^{\beta/\gamma}}. \tag{5.32}$$

This magnitude gives a direct estimate of the fraction of gamma events that enter in a 50% C.L. nuclear recoils acceptance region. With these definitions, we estimated the energy dependent values of discrimination power $D$ and rejection power $R$ in BGO. Figure 5.29 shows the results obtained with the continuous and discrete methods previously described. Good discrimination and rejection power are obtained down to energies of about 25–30 keV.

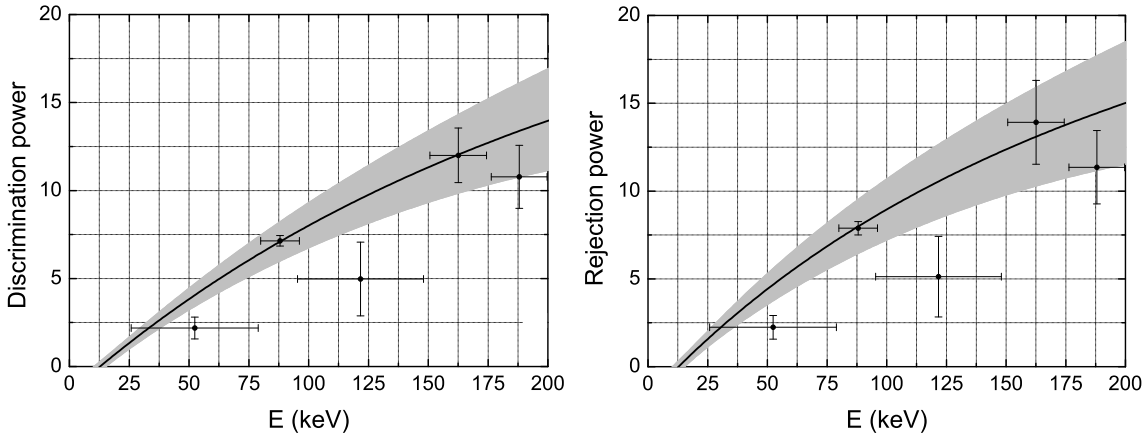


(a) (b)

Figure 5.29: *Light discrimination power D (a) and rejection power R (b) between $\beta/\gamma$ and neutron induced nuclear recoils in the BGO scintillating bolometer. The two methods used (continuous and discrete) are described in the text.*

### Light REF for O and Np ions

To study the $\mathrm{REF}_l(\beta/\gamma{:}\mathrm{NR})$ dependence on the recoiling nuclei masses, the BGO was irradiated simultaneously with neutrons from the $^{252}$Cf source and with $^{237}$Np recoiling nuclei (kinetic energy 92.4 keV) from the $\alpha$ decay of the $^{241}$Am internal source. The study was performed in a heat energy window of $\simeq$ 8 keV width centered at 88 keV, containing the Pb K–shell binding energy peak from $^{207}$Bi decay (FWHM=2.0 keV) in the $\beta/\gamma$ band and the $^{237}$Np recoils with the highest energies in the nuclear recoils band (see figures 5.30a). Since $^{237}$Np recoils produce a low-energy tailing peal (see figure 5.31), the high the energy, the higher the number of NR events. The figure 5.30b shows the light pulse amplitude distribution of the selected nuclear recoils (blue events in figure 5.30a) and that of NR events when the $^{252}$Cf source is removed (cross–shaded bars). It can be interpreted as two peaks: the peak with higher light response (mean of $185.1 \pm 3.5$ mV) would correspond with neutron induced nuclear recoils, at these energies mostly of O nuclei, because

it disappeared when the neutron source was removed; the second peak, with lower energy (mean of $38.9 \pm 4.4$ mV), can be ascribed to $^{237}$Np recoiling nuclei (it remains present, with the same counting rate, in measurements without the $^{252}$Cf source).

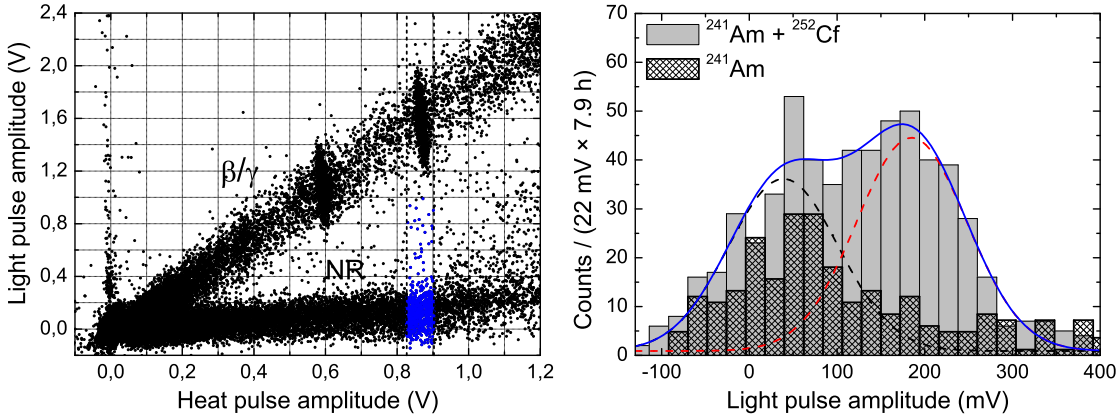


(a) (b)

Figure 5.30: *In figure (a) it is presented the light vs heat scatter plot of BGO at low energies under simultaneous irradiation with neutrons and $^{237}$Np recoiling nuclei. Gamma peaks at $\simeq 0.6$ V of heat (59.5 keV from $^{241}$Am) and at $\simeq 0.85$ V (88.0 keV from Pb K–shell X–rays) are clearly identified. The energy window selected for the analysis is indicated by the vertical dashed lines. In (b) it is shown the histogram of light pulse amplitude of the selected nuclear recoils (those in blue in figure (a)) in grey bars. A double–peak fit (blue line) reveals two peaks due to the $^{237}$Np recoils (black dashed line) and to neutron induced recoils (red dashed line). The histogram of NR events obtained in the same heat window and the same experimental conditions when the $^{252}$Cf source was removed, normalized in exposition time, is also shown with cross–shaded bars.*

We fitted the light distribution of nuclear recoils shown in figure 5.30b to a double–peak gaussian function with the same standard deviation. A systematic error was estimated by considering two other fitting functions: a double–peak gaussian with different standard deviations and also an independent gaussian peak fit for each peak (using half the histogram). The systematic uncertainty was quoted as half the difference between the extreme values obtained. The distribution of light response for $\beta/\gamma$ events, in the same heat energy window as NR, was fitted to a gaussian peak, resulting a mean response of $1568.3 \pm 3.6$ mV. The ratio between the main values of the light responses for $\beta/\gamma$ and NR events gives us the REF$_l(\beta/\gamma$:NR), obtaining two values in this case: a REF$_l(\beta/\gamma$:O) of $8.5 \pm 0.2_{stat} \pm 2.1_{sys}$ and a REF$_l(\beta/\gamma$:$^{237}$Np) of $40.3 \pm 4.5_{stat} \pm 7.8_{sys}$. The high uncertainty of the second estimate is caused by the low scintillation produced by Np nuclei. Note that this low scintillation could be

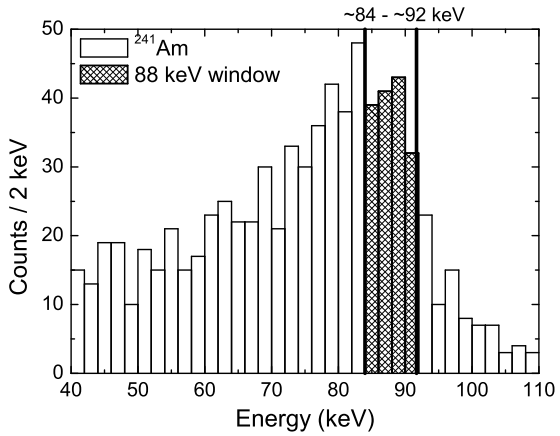


Figure 5.31: $^{237}Np$ *heat nuclear recoil spectrum obtained in the BGO when the* $^{252}Cf$ *source was removed. Events selected for the analysis of the* $REF_l$ *for Np ions are cross-shaded.*

partially attributed to surface effects affecting the light yield or light collection (Np nuclei always interact in the same small volume in the very surface of the crystal). Nevertheless, this surface effect has not been observed with $\alpha$ particles (although they have a larger range than Np recoils) in tested scintillating bolometers (see for instance reference [152] and figure 5.7). If surface effects are discarded, this second value can be considered as a rough estimation of the light REF for heavy nuclei, particularly for Bi nuclei, in BGO.

These light REF estimates (assumed energy independent) could allow to construct two separate nuclear recoils acceptance regions (one for light and another for heavy recoiling nuclei) that could improve sensitivity of BGO as dark matter target as it is done by the CRESST collaboration with $CaWO_4$ [18]. This is a signature that could also provide information about WIMP properties profiting from a multi–target approach (see [186]).

### Semi–empirical estimations of light REF

We used the semi–empirical approach proposed by Tretyak to estimate the light REF in BGO for different particles. The Birks factor kB at 20 mK was obtained by fitting the $REF_l(\beta/\gamma{:}\alpha)$ of equation 5.12 to the experimental data in the energy range 3–7 MeV (line shown in figure 5.28a). A value of 10.7 mg/(MeV·cm$^2$) was obtained with a goodness of fit $\chi^2/n.d.f = 4.9$. The result obtained with the model for light REF between $\beta/\gamma$ and $\alpha$ particles is plotted in figure 5.32a (dashed line) in comparison with the experimental values previously shown in figure 5.28a (solid line

with error bands). The experimental results showed a steeper variation with energy than the calculations of the model, but, as previously stated, the model tends to underestimate the variation with energy of the light REF for $\alpha$ particles.

With the $kB$ value obtained we calculated the light REF for O, Ge, Bi and U ions in BGO (see figure 5.32b). The programme that calculates the Stopping Power does not include Np ions in its database, but the estimates of U must be similar to that of Np (very similar atomic number, 92 and 93, respectively). The light REF estimated for U is compatible with our experimental measurement for Np at 88.0 keV, but the systematic uncertainty is too large to be conclusive. The model underestimates by approximately 30% the light REF for O ions.

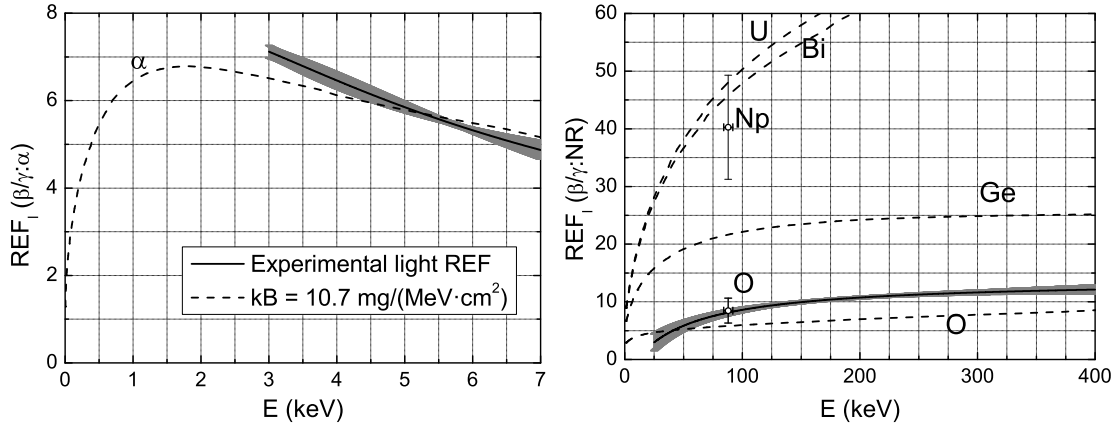


(a) (b)

Figure 5.32: *Light REF estimations in BGO for different ions using the Birks factor obtained by fitting equation 5.12 to the experimental values obtained for $\alpha$ particles (solid line in (a) with error bands), $kB = 10.7$ mg/(MeV·cm$^2$). The measured values for $^{237}$Np and O recoiling nuclei at 88.0 keV are also shown with their total error bars. The solid line with error bands in (b) is the continuous estimate of $REF_l(\beta/\gamma{:}NR)$, with recoils dominated by O nuclei, previously shown in figure 5.28b.*

### 5.3.2 Particle discrimination in $Al_2O_3$

A similar study of the light response to different particles was done for sapphire using a cylindrical 50 g $Al_2O_3$ scintillating bolometer. The crystal, although nominally pure [182], showed a Ti concentration of 6 ppm [189]. It was exposed to $\alpha$ particles and $^{206}$Pb recoiling nuclei from a $^{210}$Po source, to photons from sources of $^{241}$Am, $^{57}$Co and $^{109}$Cd, and to neutrons arising from a $^{252}$Cf source. In figure 5.33 are shown two light versus heat scatter plots. In (a) it is shown a high energy measurement in

which the crystal was exposed to the $^{210}$Po source; the heat channel was calibrated with $\alpha$ particles due to the poor photoelectric efficiency of the sapphire in the MeV energy region. In figure 5.33b it is shown a low energy measurement with the $^{252}$Cf neutron source; in this case, the energy calibration was done with $\gamma$ lines from the radioactive sources of $^{241}$Am (59.5 keV) and $^{57}$Co (122.1 keV).

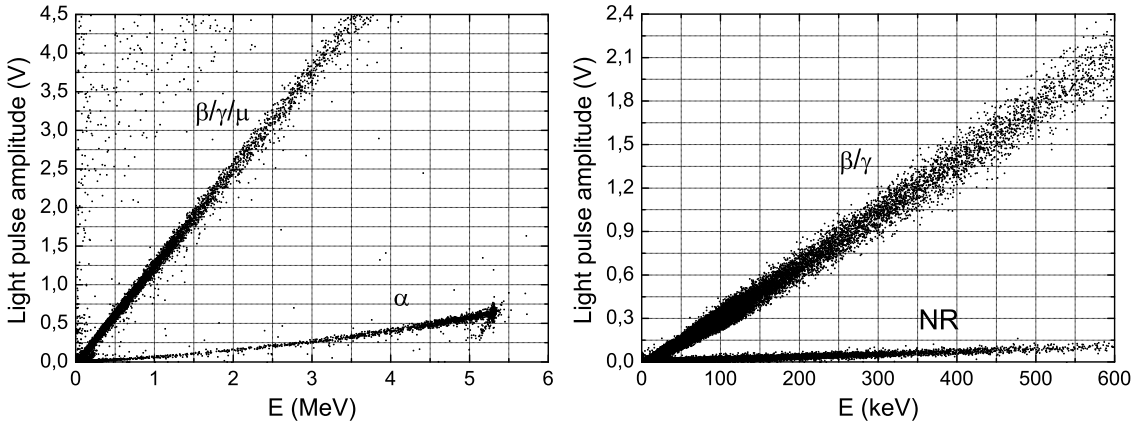


(a) (b)

Figure 5.33: *Light versus heat scatter plot of the $Al_2O_3$ scintillating bolometer irradiated with $\alpha$ particles from a $^{210}$Po source (5.3 MeV) (a), and exposed to neutrons from $^{252}$Cf and photons from $^{241}$Am and $^{57}$Co sources (b). The heat channel was calibrated in energy with $\alpha$ particles in (a) and with $\gamma$ lines in (b).*

### Light REF for $\alpha$ particles and NR events

The REF$_l(\beta/\gamma{:}\alpha)$ was estimated as the ratio between the two polynomial functions fitted to the light responses to $\beta/\gamma$ particles (linear fit) and to $\alpha$ particles (parabolic fit) of figure 5.33a. The energy range of events used to perform the fits was from 0.5 to 6 MeV. The result is shown in figure 5.34a as a solid line with grey error band. Values are only shown down to 1.5 MeV because at lower energies systematic error due to the choice of the fitting functions increases enormously. Both bands of figure 5.33b, $\beta/\gamma$ and NR, were fitted to second degree polynomial functions. The light REF($\beta/\gamma$:NR) resulting from their quotient is plotted in figure 5.34b. We also did a discrete estimate of this light REF separating the events of both bands in energy windows. These values are represented as circles in figure 5.34b.

Figure 5.35 displays the light discrimination power $D$ and rejection power $R$ between $\beta/\gamma$ and NR events, from equations 5.16 and 5.32, with the continuous and discrete methods already used for the BGO. Good discrimination was obtained down

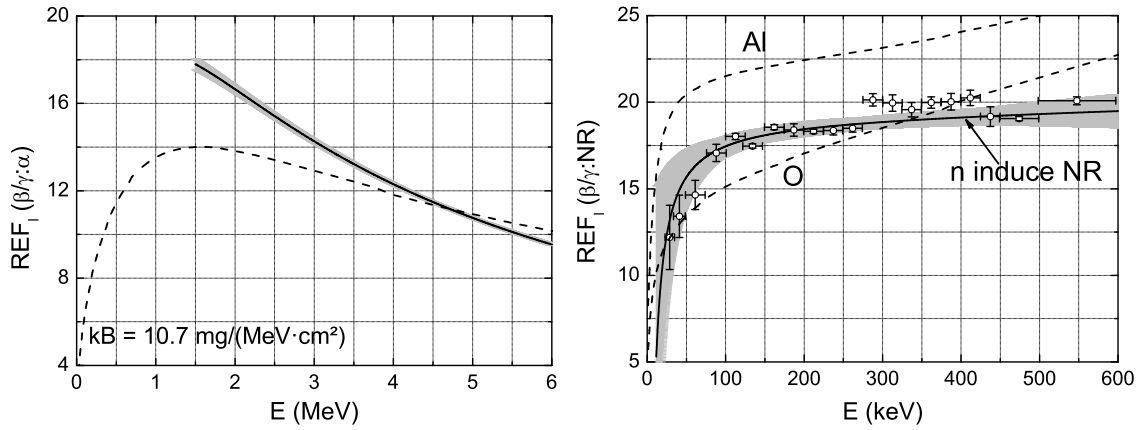


(a) (b)

Figure 5.34: *$REF_l(\beta/\gamma{:}\alpha)$ (a) and $REF_l(\beta/\gamma{:}NR)$ (b) in $Al_2O_3$ at 20 mK. The solid lines represent the experimental values with their error bands (in gray). The white circles are discrete estimations at some energy windows. The dashed lines are estimations of light REF obtained with the Tretyak model for $\alpha$ particles (a) and Al and O ions (b), with the Birks factor value indicated in (a) and obtained as it is explained in the text.*

to energies of 15–20 keV, showing the suitability of $Al_2O_3$ for dark matter searches.

### Light REF for Pb ions

We studied the dependence of the light REF($\beta/\gamma$:NR) of sapphire on the nuclear recoil mass by exposing the scintillating bolometer to $^{206}$Pb recoiling nuclei (from the $\alpha$ decay of the $^{210}$Po source) with 103.1 keV of kinetic energy. Figure 5.36a shows the light versus heat scatter plot obtained in a measurement in which, besides the $^{210}$Po source, a $^{252}$Cf source was present. The heat channel was calibrated with full–absorption $\gamma$ lines of $^{57}$Co and $^{109}$Cd and events in both bands were selected in a heat window centered at 103.3 keV with $\approx 7$ keV width (selected events are limited by dashed vertical lines in figure 5.36a). Figure 5.36b displays the histogram of light pulse amplitude of the NR events selected. Like in figure 5.30b of BGO, there were two peaks, and that of higher amplitude (mean of $56.0 \pm 0.9$ mV) disappeared when the $^{252}$Cf neutron source was removed. Consequently, this peak is attributable to Al and O recoiling nuclei (induced by neutrons) and the peak with lower light response (mean amplitude of $0.8 \pm 1.2$ mV) to $^{206}$Pb recoiling nuclei. $\beta/\gamma$ particles of the same energy had a mean light response of $953 \pm 11$ mV. We followed the same procedure explained before for BGO for the fitting of the distribution of light responses, for the

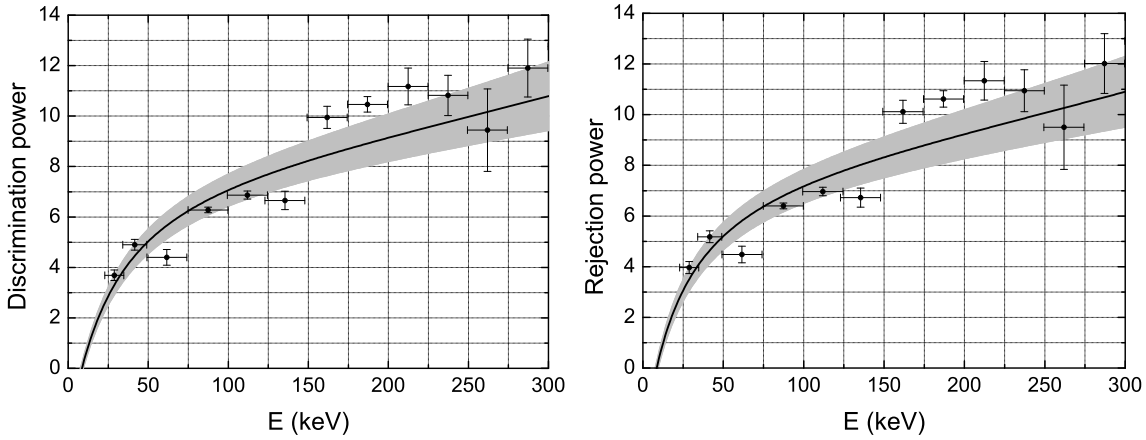


(a) (b)

Figure 5.35: *Light discrimination power D (a) and rejection power R (b) between $\beta/\gamma$ and neutron induced nuclear recoils of the $Al_2O_3$ scintillating bolometer. The two methods used (continuous and discrete) are described in the text.*

estimate of statistical and systematic uncertainties and for the estimate of the light REFs. We obtained a $\mathrm{REF}_l(\beta/\gamma{:}\mathrm{NR})$ of $17.0 \pm 0.3_{stat} \pm 1.1_{sys}$ for neutron induced NR (Al and O). The $\mathrm{REF}_l(\beta/\gamma{:}^{206}\mathrm{Pb})$ was not estimated because the scintillation produced by these nuclei is compatible with zero, so we derived a lower limit of 104.2 at 95% of confidence level.

### Semi–empirical estimates of light REF

We estimated the Birks factor $kB$ in sapphire at 20 mK fitting the $\mathrm{REF}_l(\beta/\gamma{:}\alpha)$ of equation 5.12 to the experimental values in the region 4–5.5 MeV, that is the $\alpha$ region with higher density of events. We obtained the value for $kB$ of 10.7 mg/(MeV·cm$^2$) with a goodness of fit $\chi^2/n.d.f. = 57.6$, and the resulting $\mathrm{REF}_l$ is plotted in the figure 5.34a with dashed line. The $\chi^2/n.d.f.$ high value probably reflects the fact that our measured values had a much stronger dependence on the energy than calculations of the semi–empirical model. That is the reason why we restricted the fitting region to that with higher statistics. With this $kB$ value we calculated the predictions of light REF for O and Al ions in $Al_2O_3$ (dashed lines in figure 5.34b). Although the experimental results for neutron induced NR in sapphire are between the values obtained with the model for Al and O in the 25–350 keV energy range, clearly, the semi–empirical model did not describe our experimental data.

After using the Birks model in several targets ($SrF_2$, LiF, BGO and $Al_2O_3$) and

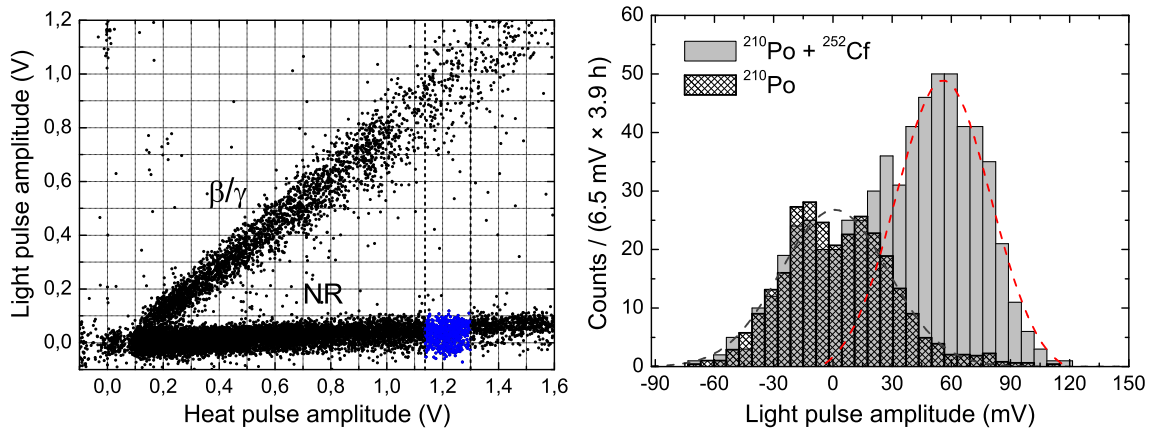


(a) (b)

Figure 5.36: *In figure (a) it is presented the light vs. heat scatter plot of $Al_2O_3$ at low energies under simultaneous irradiation with fast neutrons and $^{206}Pb$ recoiling nuclei. The energy window selected for the analysis is indicated by the vertical dashed lines. In (b) it is shown the histogram of light pulse amplitude of the selected nuclear recoils (those in blue in figure (a)) in grey bars. A double–peak fit reveals two peaks due to the $^{206}Pb$ recoils (black dashed line) and to neutron induced recoils (red dashed line). The histogram of NR events obtained in the same heat window and the same experimental conditions when the $^{252}Cf$ source was removed, normalized in exposition time, is also shown with cross–shaded bars.*

comparing their estimations of light REF with experimental values, we could say that the model produces acceptable qualitative results considering its simplicity but, experimental measurements of light REFs becomes not only advisable but in some experiments also unavoidable because up to date models are not satisfactory enough.

# Chapter 6

# Installation and tuning of a new bolometric facility

In this chapter we describe in detail the technical aspects of the mounting and tuning of a cryogenic laboratory to perform bolometric measurements in the University of Zaragoza. In section 6.1, it is exposed the context in which such a laboratory is installed and the available equipment. In section 6.2 we relate the repairs and tuning of the cryogenic system to reach the conditions needed to operate bolometers. Sections 6.3 and 6.4 include the systems to monitor and control temperatures and other relevant parameters of the cryogenic installation. The wiring and readout installed to measure with bolometers is described in section 6.5 and the improvements of the installation to optimize the bolometer operation by reducing noise contributions in section 6.6. Finally, the first bolometric tests with a $SrF_2$ crystal in the new laboratory are presented in section 6.7, and the physics goals and prospects are explained in section 6.8.

## 6.1 Introduction

Our Nuclear and Astroparticle Physics Research Group (GIFNA) of the University of Zaragoza has a collaboration with the Advanced Detectors Group (ADG) of the Lisbon University for the loan and operation of a dilution refrigerator (DR) to be used for the research, development and testing of new bolometers at the Zaragoza University laboratory for the pursuit of a collaborative cryogenic dark matter search project at LSC. The equipment, from Oxford Instruments[1], included a Kelvinox–100 dilution refrigerator, a LHe cryostat, pumps and vacuum systems, a dump with $^3$He/$^4$He mixture, cold traps and the gas handling system, and it is property of the Lisbon University. A low temperature laboratory was equipped in Zaragoza including a concrete square hole of 1.2 x 1.2 m$^2$ and 1.8 m depth (to lodge the cryostat and allow mounting/dismounting of the dilution unit and the possibility of a lead shielding), separation and isolation of the 2 x 2 m$^2$ floor surrounding the hole from that of the rest of the room, a metallic structure with a pulley, an electric box, air compressed supply and a gas outlet for the pumps (see figures 6.1 and 6.2). The dilution refrigerator had been out of operation for several years before its transportation from Lisbon to Zaragoza. First tests of vacuum and circulation at room and liquid nitrogen temperature were successfully performed, and after some rudimentary repairs and upgrades (mainly covering all the holes in the plates and, in particular, those aligned with the experimental access port) a base temperature of $\simeq$ 28 mK was reached at full operation. Note that according to the specifications from Oxford Instruments, the guaranteed base temperature of this dilution refrigerator is 15 mK with a cooling power of 100 $\mu$W at 100 mK.

Unlike the IAS DR described in chapter 3, the Kelvinox–100 has a 1 K pot stage to condense the mixture in the dilution unit, and a liquid helium cold trap, besides the liquid nitrogen one, to precool it. The refrigerator is operated from the Kelvinox Intelligent Gas Handling system (IGH, see figure 6.2b) that also allows its remote control from a PC through the standard interface RS232, with the software provided by the manufacturer. This software is developed in the National Instruments LabView[2] environment and includes several sophisticated automatic routines. The IGH consists of two different parts: one is dedicated to the circulation and handling of the mixture and the other to auxiliary pumping operations. Both systems are connected to their relevant components (cryostat, refrigerator insert, dump, pumps, etc.) by flexible pumping lines.

[1] http://www.oxford-instruments.com
[2] http://www.ni.com/labview/

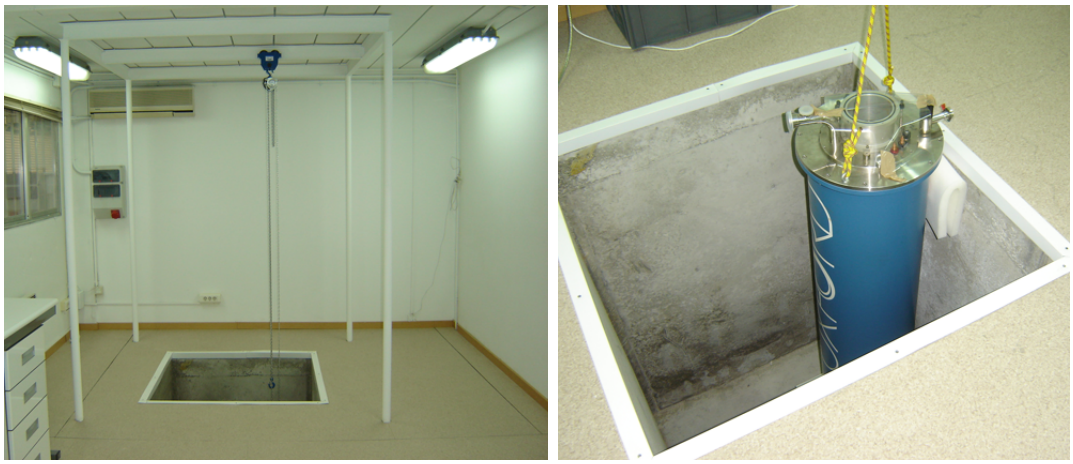

(a) (b)

(c) (d)

Figure 6.1: *(a) New laboratory ready to lodge the Lisbon cryogenic system; with the hole in the floor, the isolated 2 x 2 $m^2$ section of floor surrounding it and the metallic structure with a pulley. In (b) the cryostat is being installed in the hole. In (c) they are shown the pumps and the gas outlet. And (d) shows the equipment from Lisbon pre-installed in the Zaragoza laboratory.*

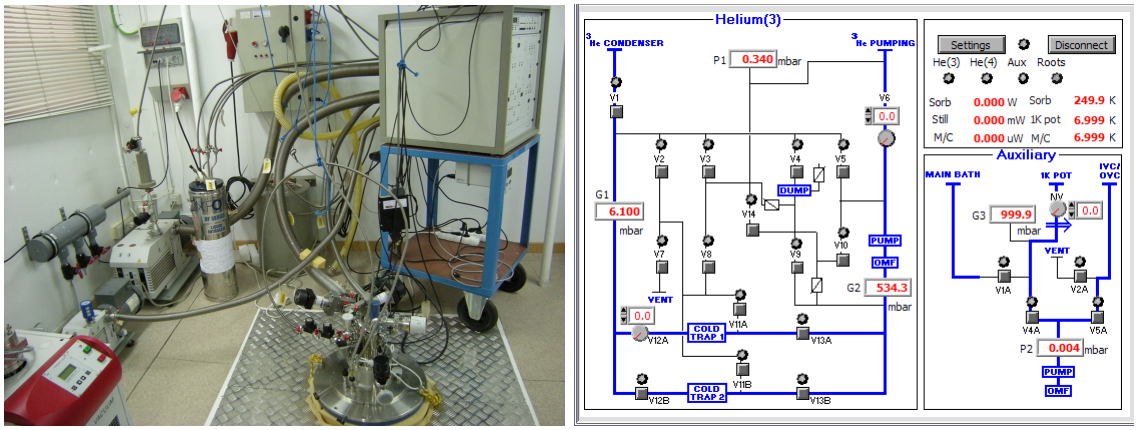


(a) (b)

Figure 6.2: *(a) GIFNA low temperature laboratory in the University of Zaragoza with the DR in operation. The DR and cryostat are inside the hole (only the upper part with connectors is visible). From left to right they are the pumps, the cold traps, the dump and the IGH box. In (b) it is shown the control panel of the Kelvinox IGH system.*

## 6.2 Leak detection and repairing

Several leak tests must be compulsory performed before each cooling down with the dilution refrigerator because of the importance of vacuum to minimize heat transfer from the outermost parts to the Mixing Chamber and bolometers. Unfortunately, a dilution refrigerator is full of joints that hold together its large number of pieces by soldering, soft soldering, indium seals, KF flanges, etc. and they are exposed to tough conditions as, e. g., extreme thermal cycles from room temperature to a few milikelvin. In addition, helium becomes superfluid under 2.18 K, so the requirements of the joints exposed to it are even more stringent.

Routine leak tests include checking the KF flanges that join together the refrigerator and gas handling systems (IGH, pumps, cold traps, etc.), the dilution circuit and the Inner Vacuum Chamber (IVC) coupling which is resealed for each running with a Kapton seal. A leak detector (Smart Test from Pfeiffer Vacuum[3]) is used for all these tests, using He as tracer gas.

In the first test runs of the dilution refrigerator in Zaragoza, a long–term instability problem was found. Temperatures down to 28 mK were reached but after some hours it suddenly increased. Although leak tests seemed to be fine, we

[3]http://www.pfeiffer-vacuum.com

contacted with experts that told us that there could be a so–called superleak; this is a small leak, below the limits of detection, which is problematic if the unit is exposed to superfluid helium, as was the case. We found that the leak became detectable in cold conditions, at 77 K and it was located in the dilution circuit, but the problem was to precisely locate the leak point. A suspicious point was an indium seal (circled in figure 6.3a) that was rebuilt several times and tested at 77 K, immersing the dilution refrigerator in liquid nitrogen (figure 6.3a) without success. The best method to perform the cold leak detection was keeping a part of the refrigerator inside the liquid nitrogen and blowing He on the outside part. We removed the refrigerator from the LN little by little and finally, a leak was found in a soldering beneath the previously tested indium seal that joined a copper piece with a NiCd tube (see figure 6.3b).

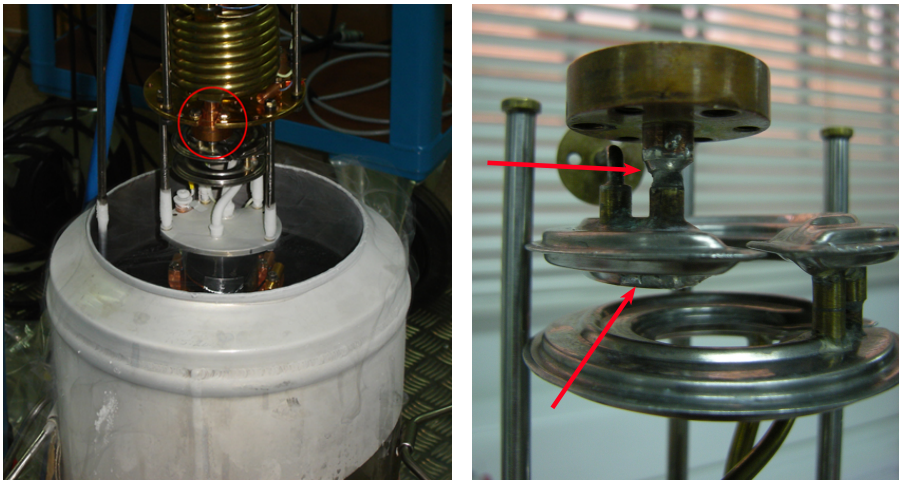

(a) (b)

Figure 6.3: *(a) Leak test of the dilution unit at 77 K. The suspicious joint, circled in red, was rebuilt several times. In (b) they are marked the two cold leaks that were finally found and fixed.*

The best solution for the leak was thought to be resoldering, and the bottom part of the refrigerator was dismounted for that. Several failed attempts were done, but the heat applied, despite being cautious, provoked a new small leak in a NiCd plate of a silvered heat exchanger (figure 6.3b), probably the heat had opened an old repaired leak. Finally, after contacting Oxford and some experts, the first leak was successfully soldered using a low melting point tin alloy and applying heat indirectly, with a small torch, through a copper piece in contact with the parts to join. The leak in the heat exchanger was also closed using a small solder and the same soldering composition as before. This repair solved the problem of instability in the long–term operation of the dilution unit. Since then we were able to reach 28 mK as base

temperature in stable conditions.

Last year, it appeared a third leak in a small capillary of the dilution circuit, in the injection side just over the 1 K pot (see figure 6.4a). It was detected in a routine leak test before a cooling down of the refrigerator. The section of the refrigerator could not be removed and it would have been difficult and hazardous to solder this leak on–site, so we sealed it with an epoxy reinforced with fiberglass. The epoxy used was Stycast 2850FT with catalyst 24LV, which has a low thermal expansion coefficient, similar to the metals. We also sealed a rusty area observed in the top of the same capillary. The sealed leak can be observed in figure 6.4b.

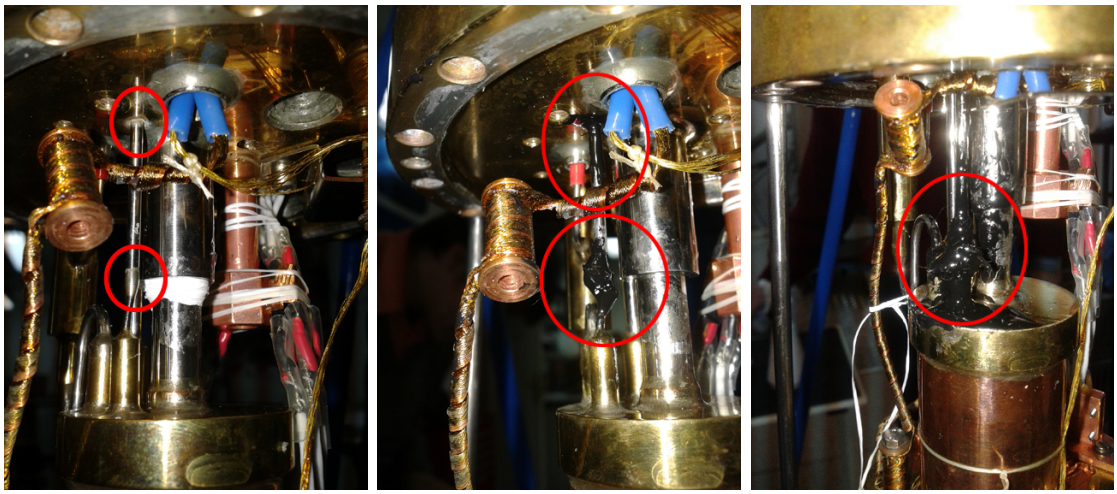

(a) (b) (c)

Figure 6.4: *Leak found in a small capillary (a) and its first (b) and second (c) sealing with epoxy. The top circles in (a) and (b) indicate a rusty area that was also sealed for prevention.*

After one successful run, the last repaired leak reopened. The old epoxy was removed with a scalpel while applying heat with a small solder. We repeated the procedure of the last time, but after some failed attempts we decided to cover a larger part of the capillary with Stycast (figure 6.4c). Finally, the leak was effectively sealed again and the dilution unit has operated without leaks up to date.

## 6.3 Thermometry and temperature

As explained in previous chapters, the temperature at which the bolometer is cooled affects the detector response. It is important to know well this temperature and its stability. For this reason low temperature thermistors are attached to the

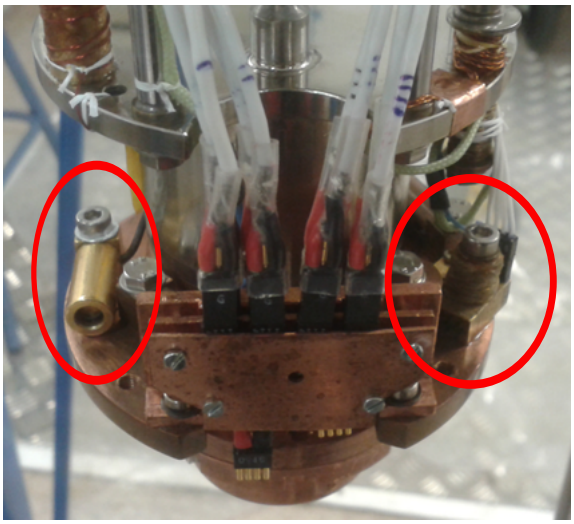

Figure 6.5: *Temperature sensors attached to the mixing chamber. Both $RuO_2$ resistors are circled in red, the one from Lisbon on the left and the other one from the IAS on the right.*

mixing chamber of the dilution refrigerator, to which bolometers are coupled. Other thermistors are placed in several stages of the refrigerator to control its operation.

The thermistors of our dilution refrigerator can be divided in two groups, those with less precision used during the cooling process, which are controlled by the IGH system and read through two wires, and those used at base temperature and with high precision, which are controlled through an AVS-47 resistance bridge, a device that performs four wires measurements by applying low excitation current (30 mA in the case of our thermistors) and is also prepared to be controlled remotely. In the first group are included a 270 Ω Allen Bradley resistor attached to the Sorb, and two 2200 Ω ruthenium oxide ($RuO_2$) resistors in the 1 K pot and Mixing Chamber (for use above 100 mK). The three thermistors of the second group are $RuO_2$ resistors, the ones placed in the Still and the Cold Plate are measured with two wires, and the Mixing Chamber one with four wires to increase its accuracy. Apart from these thermometers provided with the system by Oxford Instruments, a second $RuO_2$ sensor (calibrated under 50 mK against a $^{60}Co$ nuclear orientation thermometer by Oxford Instruments) was installed in the Mixing Chamber by the Lisbon group with the aim of having a crosschecked measurement and a spare device (the one on the left in figure 6.5).

$RuO_2$ are the most reliable thermistors for the temperatures reached by dilution refrigerators. They are a kind of oxide resistors consisting in a thick $RuO_2$ film mounted in a gold-plated copper holder. It is suitable for measurement below 4.2 K

and its R(T) dependence is approximately described by the Mott's Law (as in the Ge–NTD sensors):

$$R(T) = R_0 \exp\left(\frac{T_0}{T}\right)^n \tag{6.1}$$

where $n$ ranges between 0.25 and 0.6 and $T_0$ between ∼1 and ∼100 K, depending on the particular thermistor.

All thermistors were properly calibrated but some mismatching was observed in the measurement of the mixing chamber's temperature (as we will see in section 6.7 studying the Ge–NTD of a bolometer), maybe due to some degrading that had appeared with time. To assure our temperature measurement we added to the Mixing Chamber another $RuO_2$ thermistor provided by the IAS group (that on the right in figure 6.5), that had been recently calibrated with secondary thermometers in the *Centre de Spectrométrie Nucléaire et de Spectrométrie de Masse* of Orsay. We also remounted the other thermistors using GE Low Temperature Varnish to improve the thermal contact. The registered temperature of the sensor from IAS indicated a higher temperature than that from Lisbon in contrast to expectations, as is shown in table 6.1. More tests have to be done to solve the discrepancies. Meanwhile, we used with caution the temperature of the $RuO_2$ sensor mounted in Lisbon as the temperature reference.

| | Temperature (K) | | | | |
|---|---|---|---|---|---|
| Lisbon $RuO_2$ | 39 | 35 | 34 | 31 | 30 |
| IAS $RuO_2$ | 50 | 44 | 43 | 35 | 33 |

Table 6.1: *Comparison of the readout of the $RuO_2$ thermistors from Lisbon and from the IAS at different temperatures.*

Reaching a temperature as low as possible is an important goal to achieve a good performance of the bolometer, and the $^3$He/$^4$He mixture composition is a critical parameter. The leaks in the dilution circuit led us to think that some mixture was lost and the composition could be unbalanced. We measured the composition of the mixture with a mass spectrometer, finding out that we had a 11.0% of $^3$He and a 89.0% of $^4$He, while the nominal values from the documentation were 16.2% of $^3$He and a 83.8% of $^4$He. After some calculation we introduced two liters of $^3$He to re-balance the mixture. After that, we reached a lower temperature with our refrigerator: in continuous operation we measured 24.5 mK with good stability, as can be observed in figure 6.6.

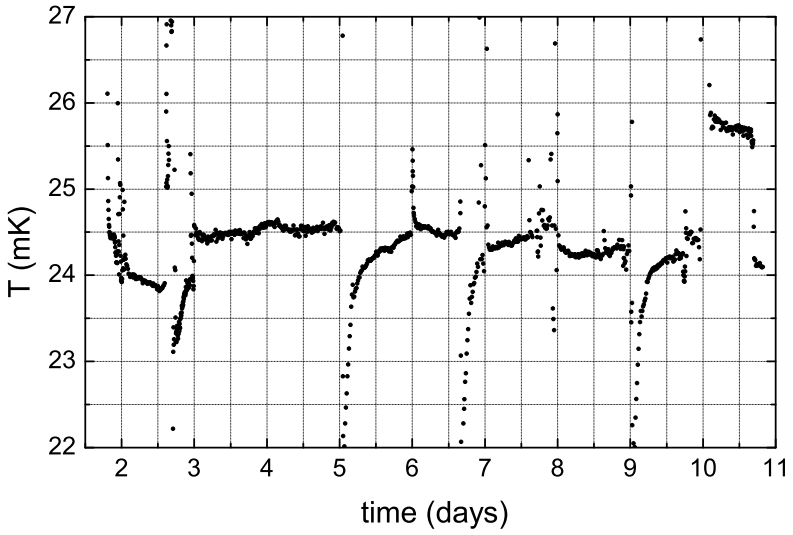


Figure 6.6: *Temperature registered by the $RuO_2$ thermistor from Lisbon placed in the Mixing Chamber of the dilution refrigerator during a running. Instabilities are mainly due to refillings of the liquid $^4$He bath.*

## 6.4 Slow Control System

In particle physics detectors and, in particular, in bolometers (cryogenic devices working near zero absolute temperature), it is of the utmost importance to monitor several system variables that are critical to achieve optimal detectors performance, guaranteeing their integrity and stability. These systems are normally known as Slow Control Systems (SCS) and respond to a double purpose: the monitoring and control of the conditions that could influence on the operation and data signals of the experiment, and the safety management of the potential risks of the experimental setup. In both cases an action, either automatic or manual, is required if a deviation from the predefined parameters is detected. We have implemented a SCS that allows to monitor the installation, its status and stability, and allows its remote monitoring.

The parameters included in the SCS are the pressure in the Inner Vacuum Chamber (IVC), the temperatures of the several $RuO_2$ sensors (mentioned in section 6.3) placed in the different stages of the refrigerator, the liquid helium level in the cryostat and a set of parameters measured by the Oxford IGH including other pressures, temperatures and heater powers. These parameters are measured by the following sensors and instruments (a scheme of the SCS is shown in figure 6.7):

- The pressure of the IVC is measured by a Compact Full-Range Gauge made by Pfeiffer Vacuum, a system that combines a Pirani and a cold cathode gauges

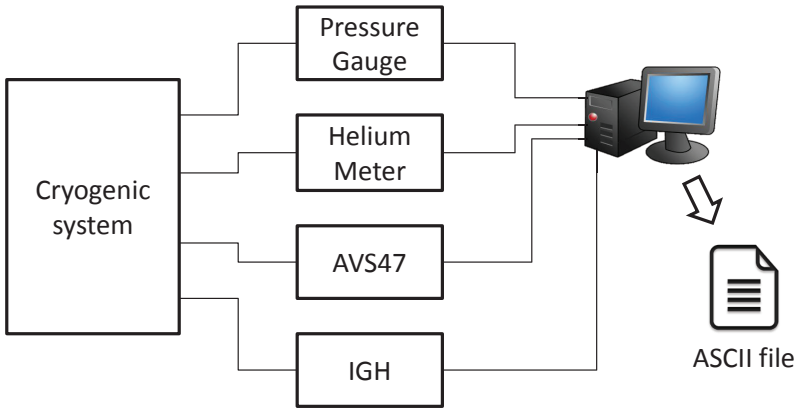


Figure 6.7: *Schematic view of the Slow Control System.*

to measure continuously in the pressure range from $10^{-9}$ to 1000 mbar. It is connected to a Single Gauge controller also from Pfeiffer. The IVC is the chamber where the bolometers are mounted, and high vacuum values are required to allow good thermal isolation between the mixing chamber (and bolometers) and the IVC copper vessel that is kept at 4.2 K.

- The $RuO_2$ thermometers are connected to the AVS47 resistor bridge. Temperature is a crucial factor in a cryogenic experiment because the bolometer response depends critically on it.

- The LHe level is measured by a resistive probe consisting of a superconductor filament to which a current is applied; the output voltage is inversely proportional to the level of liquid helium. The probe is connected to a Helium Level Meter module provided by the Electronic Instrumentation Service of the University of Zaragoza. It controls the parameters of the measurement and allows its remote control through a USB virtual serial port.

- The IGH provides values measured by several sensors: pressures at several points of the gas circulation system, temperatures of the Sorb, 1 K pot and Mixing Chamber (above 100 mK), and power supplied to the heaters placed in the Sorb, Still and Mixing Chamber. These parameters are relevant to achieve and keep the best performance of the dilution refrigerator.

All the instruments and sensors are connected to a PC using either a USB interface or a serial interface associated with the RS232 protocol. The SCS software is implemented in LabView, which allows a fast integration of the different instruments since most of them include LabView subroutines (called Virtual

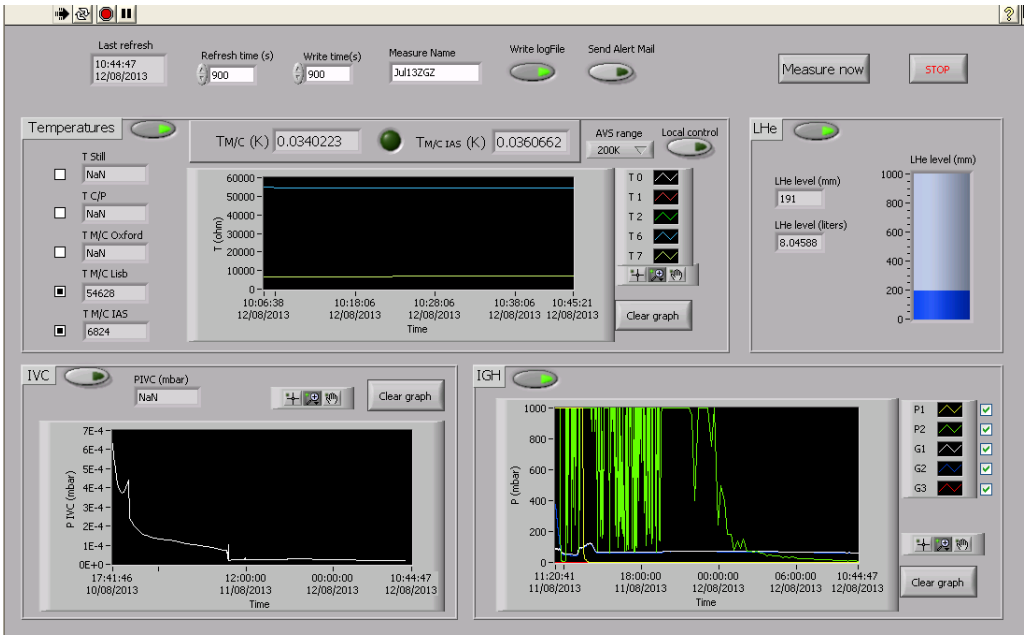


Figure 6.8: *User interface of the Slow Control System program implemented in LabView.*

Instruments) for their control and monitoring. The developed program allows real time visualization of the parameters, their recording and the control of alarms. The user interface is shown in figure 6.8. The record rate can be customized by the user and it is common to all the instruments. The measurements are time-stamped and written in ASCII log-files. An alarm is also included to send an email if the liquid helium level decreases below a selected value.

The SCS has worked correctly but some improvements can be carried out for future runs. It would be interesting to allow different sampling rate for each instrument because their variations have different timescales. Some alarms could be added, besides the one for the LHe level, for instance if there is a blockage in the circulation circuit (controlling the pressures G1 and G2 of the IGH, figure 6.2b), if the pumps power supply goes down, or if the Mixing Chamber temperatures overpasses a selected threshold. Also interesting, specially in the case of continuous operation, would be to send an email with a daily (or the required periodicity) report of the status of the cryogenic system.

## 6.5 Bolometers wiring and read-out

A wiring was designed, constructed and installed to read up to four bolometers. One of the problems of wiring is the thermal leak caused by the cables, which connect the Mixing Chamber (at 20–30 mK temperature) with the top of the refrigerator (at room temperature). Several aspects must be taken into account as the type of cable, its right thermalization at each temperature step and to avoid direct thermal leaks through the ports opened for the wires. Other requirements are imposed by their use to transmit weak signals: they must be properly shielded to avoid crosstalk among the different wires and electromagnetic noise from outside. We chose a cable composed by a twisted pair of constantan wires shielded by a braided screen made also of constantan.

The wiring was designed in three different stages coupled with connectors. The first one between the top of the fridge, where a specific brass piece with vacuum sealed Fisher connectors was built and installed (figure 6.9a), and the plate above the 1 K pot, with a copper thermalization piece in contact with the IVC joint (figure 6.9b). The second stage connects the 4.2 K plate with the Mixing Chamber at $\simeq$ 20 mK. To avoid the thermal leak, cables were thermalized in four copper pieces along the fridge (at approximately 1.5 K, 0.6 K, 50 mK and 20 mK of temperature in operation), shown in figure 6.9c. In the last of these pieces, the polarization and signal cables of each sensor are combined to enter in the four pins connector of the bolometer (figure 6.9d). The last stage of wiring connects the Mixing Chamber with each bolometer. In this stage there are no differences of temperature, so other kind of wires can be used (in our case copper ones).

The acquisition system for the bolometers data is quite similar to that used at IAS and LSC, previously explained in chapter 3. The analog signals arriving from the bolometers to the top of the dilution refrigerator are amplified by a Celians EPC1B preamplifier for each channel. Sometimes it is used a second amplification stage, a Stanford SR560 amplifier that allows an additional band-pass filtering of the signals. A NI4472 PCI acquisition card installed in a computer (24 bits of resolution and up to 100 kHz of sampling rate) triggers the signal and digitalizes the pulses, which are recorded using the same acquisition software as in IAS and LSC, expressly implemented for this kind of measurements.

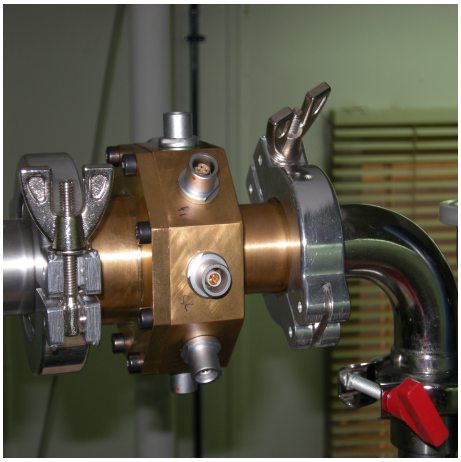

(a)

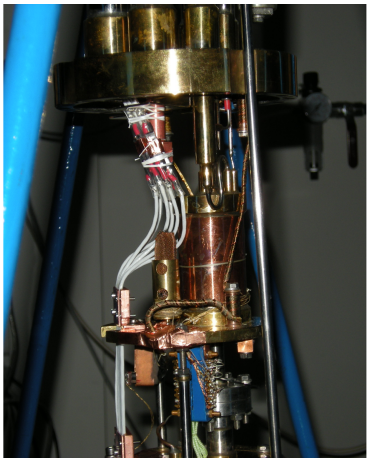

(b)

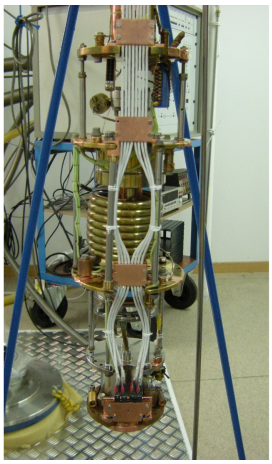

(c)

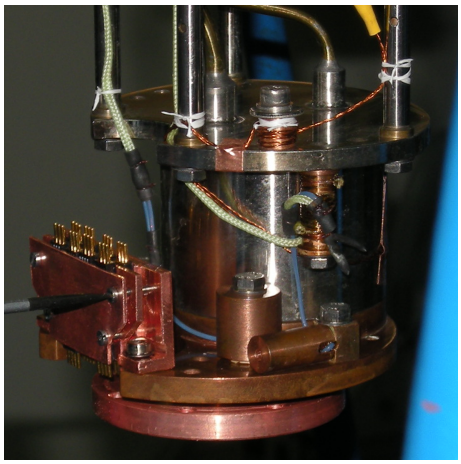

(d)

Figure 6.9: *Wiring of the dilution refrigerator to read four Ge–NTD sensors. (a) Fisher connectors in the top of the refrigerator. (b) Union between the first and second stages (see text), thermalized in the plate at the top of the picture (at 4.2 K). (c) Second stage of wiring from 4.2 K to* $\simeq 20$ *mK, thermalized in four copper pieces at intermediate temperatures. The last of these pieces, in the Mixing Chamber, is zoomed in (d). Here, the polarization and signal cables of each channel are combined to form a four wires cable that is directly connected to each bolometer.*

## 6.6 Microphonic and electromagnetic noise reduction

Bolometers are extremely sensitive to mechanical vibrations, or microphonics, since frictions or movements of the crystal with respect to the holder release an amount of energy that is converted into heat and detected by the Ge–NTD sensor inducing thermal noise in the measurements, or vibration of the wires, that modify their capacitance and generate noise. It is important to decouple the bolometers from the rest of the system to dump these vibrations. An important source of microphonics are vibrations originated by the cryogenic facility, mainly by the pumps, which are transmitted through the vacuum tubes. Other common sources of microphonic noise in dilution refrigerators are the 1 K pot (continuously filled with $^4$He) and the boiling liquid helium bath.

As previously stated, the low temperature laboratory was already designed so that the concrete block with the cryostat hole was isolated from the rest of the laboratory floor to avoid the transmission of pumps vibrations through it. Additional steps (addressed to reduce microphonic and electromagnetic noise) have been taken to improve the facility. These improvements are summarized in the next paragraphs.

We installed the pumps inside a wooden box internally covered with acoustic insulator (figure 6.10a), and we loaded the tubes with asphalt cover to dump oscillations. An important improvement was to include a sand filter to decouple the vibrations of the tubes before entering to the refrigerator (figure 6.10b).

Another set of upgrades was intended for isolating the cryostat from the hole floor; despite being concrete isolated, vibrations could be induced through the cryostat. The solution was to put an insulating structure between the floor and the cryostat. This structure was composed, from bottom to top, by a fine sand box of 5 cm high, a steel plate (90 x 90 cm$^2$) of 1 cm thickness to spread the load and compact the sand, three layer Stabren® dumping pads covering a total of 100 cm$^2$, another steel plate (50 x 50 cm$^2$) of 0.5 cm thickness and lead plates (50 x 50 cm$^2$ with a total thickness of 10 cm). The lead was included as the base of a future radioactivity shielding. Figure 6.11 shows the progressive installation of the anti-vibration structure below the cryostat.

Bolometric signals can be also affected by electromagnetic noise, that is an annoying disturbance due to either electromagnetic induction or electromagnetic radiation emitted from external sources as the electric network or other devices.

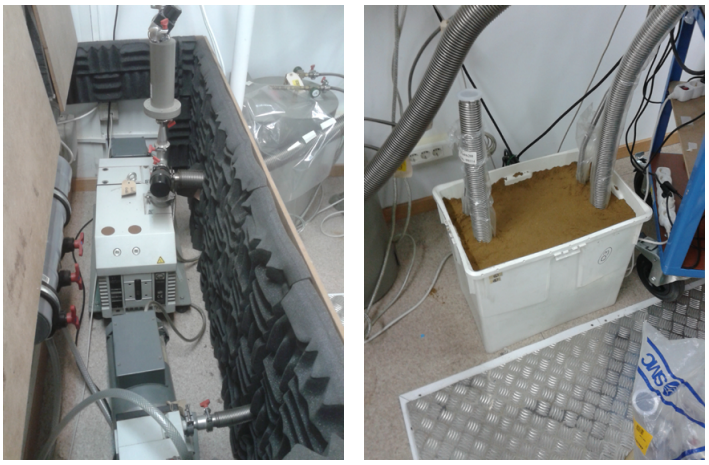

(a) (b)

Figure 6.10: *In (a) is shown the pumps box, internally covered with acoustic insulator. In (b) the sand box that decouples the vibrations of the tubes.*

Several issues must be considered to minimize these contributions. As much as possible we have tried to use a common electrical ground for all the devices of the system and avoided ground loops, some cables and instruments were screened to avoid external radiation and even some electronic components were installed inside a mu–metal box. As the electrical network is a source of noise, when possible we used devices powered by batteries, as in the case of the amplifiers and polarization sources. We also tested a PXI digitizer card not mounted in a PC and powered by batteries, instead of the PCI card, but noticeable differences were not found. Most of bolometric facilities are installed inside Faraday cages; in fact, the metallic structure in our laboratory was thought to facilitate in the future the building of a Faraday cage.

Quantifying the electromagnetic noise in a system is not easy because there are many sensitive parts on it. With this purpose we have used two figures of merit: measurements of the noise power spectral density (PSD) as function of frequency of the Ge–NTD sensors, and a relevant physical parameter of the detectors, their energy resolution, that will be studied in the next section. Figure 6.12 shows a typical PSD obtained with the Ge–NTD of the $SrF_2$ bolometer. The noise increase at frequencies below 100 Hz corresponds to the pulse power spectrum; labeled peaks are due to the 50 Hz pick-up from the electrical network; the region between 100 and 1000 Hz are probably due to microphonics, and higher frequency peaks presumably arise from electromagnetic noise sources.

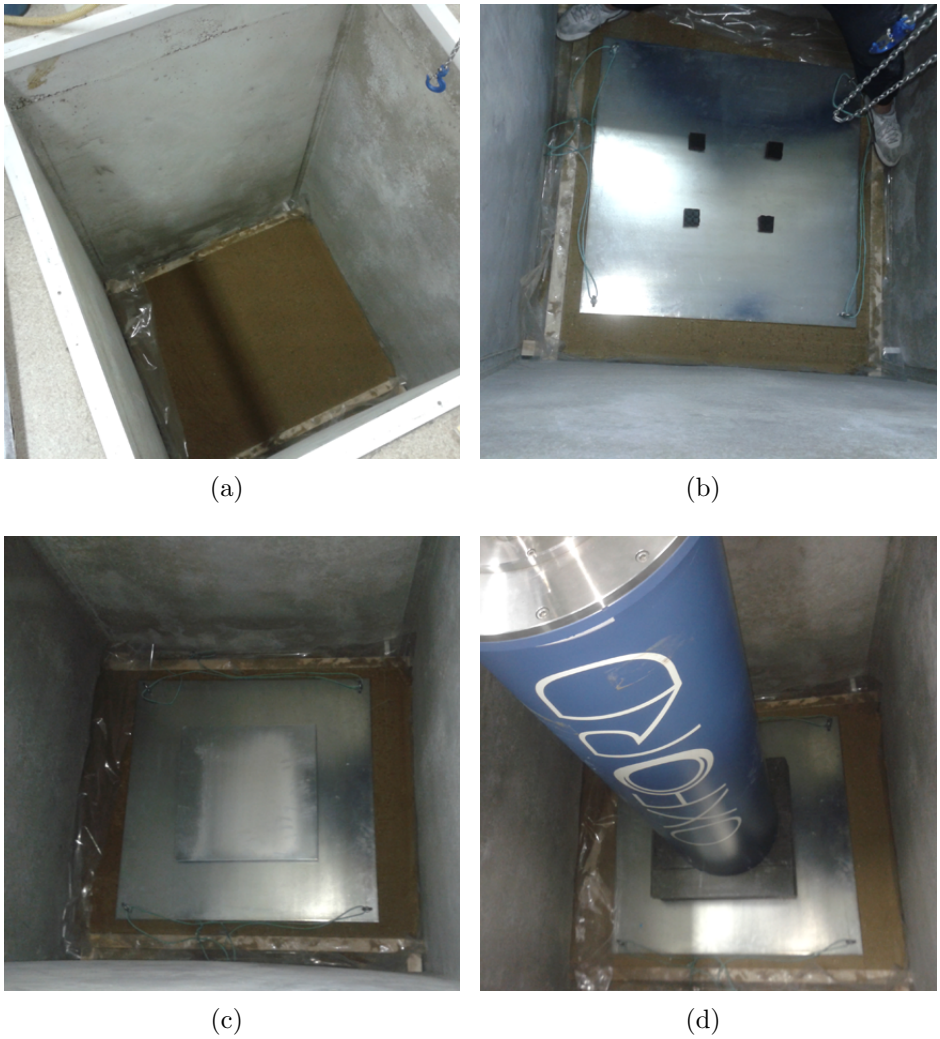

(a) (b)

(c) (d)

Figure 6.11: *Anti-vibration structure installed below the cryostat. It is composed, from bottom to top, by 5 cm of sand (a), 1 cm of steel and Stabren® dumping pads (b), 0.5 cm of steel (c) and 10 cm of lead (d).*

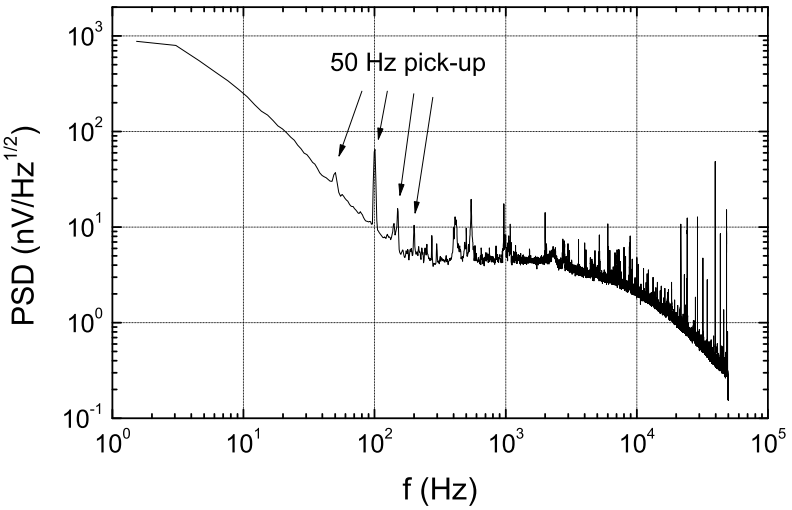


Figure 6.12: *Noise power spectral density of the $SrF_2$ bolometer Ge-NTD polarized. Different contributions are explained in text.*

## 6.7 First tests with a $SrF_2$ bolometer

The first bolometer attached to the mixing chamber was the thermal bolometer of $SrF_2$ characterized in section 5.1. The aim of using a known bolometer was to have a reference for testing the installation and monitoring its improvements. As it will be shown the $SrF_2$ bolometer is ideal for our first tests due to its internal radioactive contamination, mainly in $^{226}$Ra (activity of $0.52 \pm 0.01$ Bq/kg), which allows to calibrate in energy easily with the $\alpha$ peaks.

First tests with the $SrF_2$ bolometer were carried out to reproduce the excitation function of the Ge–NTD sensor and characterize it. We measured several voltage–current (V–I) curves at different temperatures. These measurements were done applying low currents to the Ge–NTD sensor with a Keithley 220 programmable current source and measuring the output voltage with a Keithley 2000 high performance digital multimeter. Different temperatures were reached by applying power to the Mixing Chamber heater. Curves are displayed in figure 6.13a. From the linear region of these curves we calculated the resistance of the Ge–NTD as function of temperature, that should follow the Mott's law (equation 6.1) with $n = 1/2$:

$$R(T) = R_0 \exp \sqrt{T_0/T}, \tag{6.2}$$

where $R_0$ and $T_0$ are characteristic parameters of each sensor. We fitted the equation to our data to obtain the values $T_0 = 10.6$ K and $R_0 = 21.1$ m$\Omega$. The data points and the fitted curve are displayed in figure 6.13b with the data and function obtained in the IAS for the same Ge–NTD. A disagreement between both measurements is

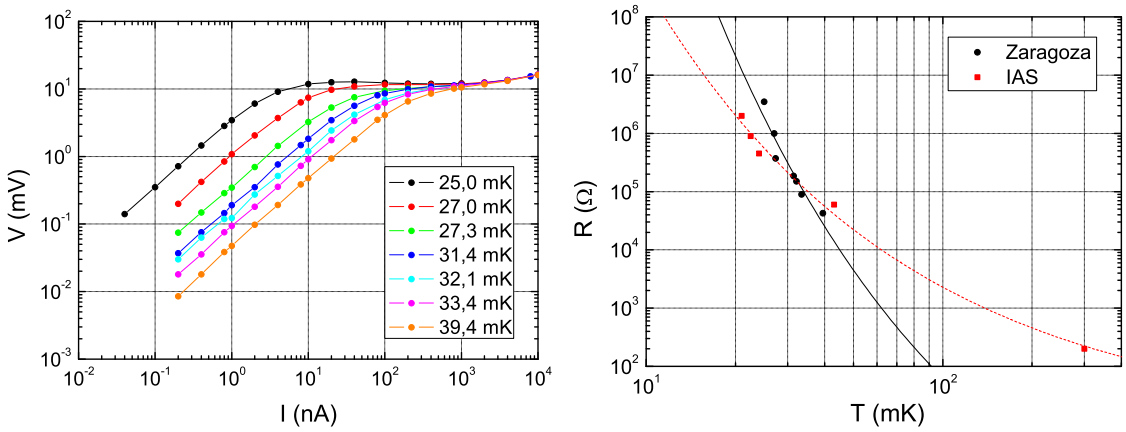


(a) (b)

Figure 6.13: *(a) Excitation functions V-I of the Ge–NTD sensor mounted in the $SrF_2$ bolometer measured at different temperatures. (b) R(T) law of the Ge–NTD sensor fitted to data measured in Zaragoza (black dots and solid line) and in IAS facilities (red squares and dashed line) for the same sensor.*

clearly visible, which led us to mistrust of the calibration of our temperature sensors.

Noise spectra were measured at different applied polarization voltages (see figure 6.14a). The noise level depends on the dynamic impedance that changes with the bias. In this way we can optimize the noise, but the magnitude that actually must be maximized is the signal-to-noise ratio. We also measured noise spectra at different temperatures. Figure 6.14b illustrates how the bolometer becomes more sensitive to noise when temperature goes down.

A background spectrum measured in Zaragoza is shown in figure 6.15. It has two well differentiated parts: a continuous component from 0 to 2 V and four peaks between 4 and 5.5 V. The continuous part of the spectrum is due to the radioactive background, consisting mainly of $\beta/\gamma$ interactions. Some peaks were hardly recognized as arising from natural radioactive background (natural chain of $^{232}$Th and $^{40}$K): they are listed in table 6.2 and tagged in the spectrum of figure 6.15a. The four peaks with higher amplitude were unambiguously identified as $\alpha$ decays of the inner contamination from the radioactive chain of $^{226}$Ra. This peaks are also listed in table 6.2 and labeled in figure 6.15b.

We performed two separated energy calibrations for the two parts of the spectrum with the peaks mentioned above. The already known linearity of the detector can be appreciated both for the $\beta/\gamma$ and $\alpha$ lines. Although the spectrum was self-calibrated in this case, when necessary, we used external gamma sources of $^{137}$Cs, $^{22}$Na and

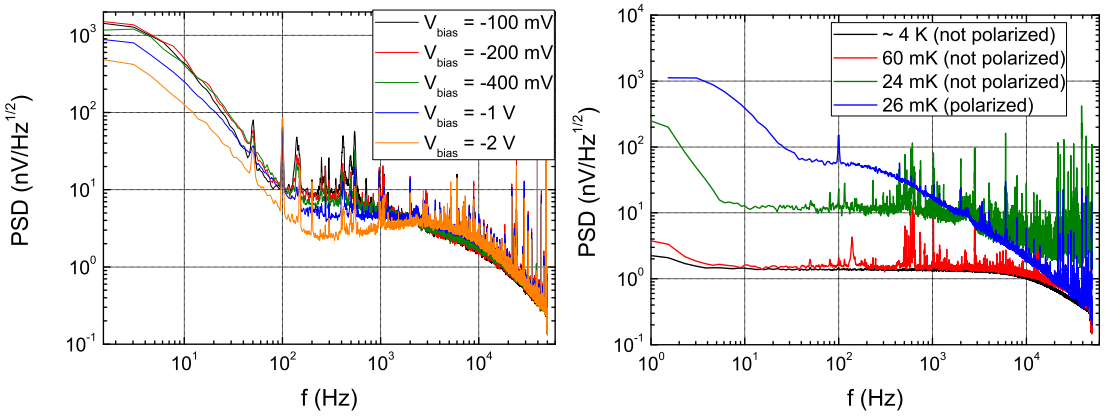


(a) (b)

Figure 6.14: *Noise power spectral density of the Ge–NTD sensor mounted in the $SrF_2$ bolometer measured with different biases (a) and at different temperatures (b). In (b) there were not bias applied, except in the spectrum at 26 mK to see the effect of polarization when comparing with the one at 24 mK.*

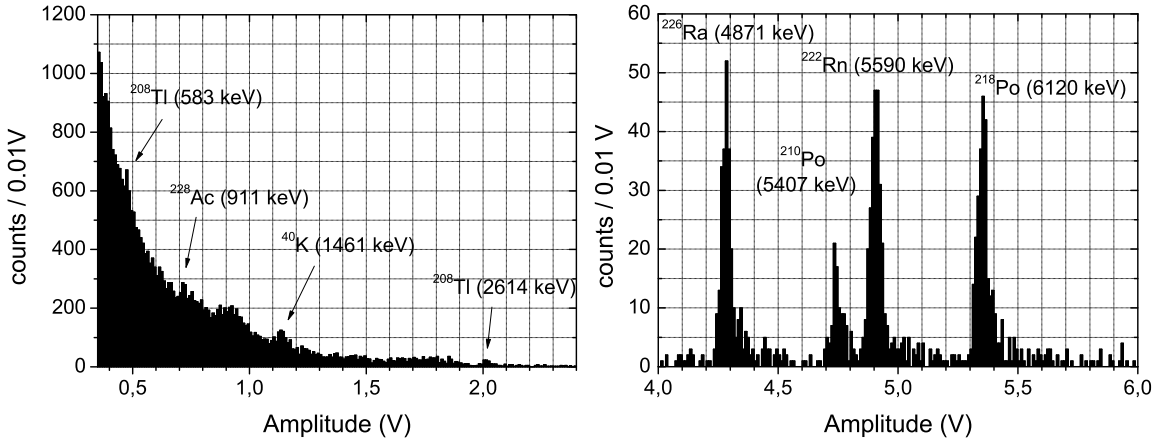


(a) (b)

Figure 6.15: *Pulse amplitude spectrum obtained with the $SrF_2$ bolometer in a background measurement of 2.6 h: continuous $\beta/\gamma$ background (a) and inner contamination $\alpha$ peaks (b).*

| Isotope | Amplitude (mV) | Energy (keV) | FWHM (keV) |
|---|---|---|---|
| $^{208}$Tl | 0.473±0.001 | 583.191 | – |
| $^{228}$Ac | 0.714±0.002 | 911.204 | – |
| $^{40}$K | 1.135±0.003 | 1460.83 | 56±10 |
| $^{208}$Tl | 2.012±0.003 | 2614.53 | 45±8 |
| $^{226}$Ra | 4.278±0.001 | 4870.63 | 49±2 |
| $^{210}$Po | 4.741±0.003 | 5407.46 | 57±6 |
| $^{222}$Rn | 4.902±0.002 | 5590.3 | 59±2 |
| $^{218}$Po | 5.3468±0.002 | 6119.68 | 59±2 |

Table 6.2: *Pulse amplitude and FWHM energy resolution of the identified $\gamma$ and $\alpha$ peaks with their corresponding energies [146]. The gamma peaks were hardly resolved and the resolution of some of them could not be estimated.*

$^{133}$Ba placed at the bolometer level.

One of the most important parameters of a particle detector is its energy resolution. As stated in section 6.6, bolometers are extremely sensitive to several factors that can worsen their energy resolution. The upgrades carried out in this line led to improve the energy resolution in the successive measurements, starting from FWHM energy resolutions of about 700 keV and achieving values of 56 keV for the $\alpha$ peaks. These values are far from the 8 keV obtained in the IAS facilities. The FWHM of the base line has been also improved from 300 to 14 keV. In figure 6.17 they are compared a Zaragoza energy spectrum with another one measured at IAS, both acquired with the $SrF_2$ bolometer.

A factor that also affects the energy resolution is the detection rate. A high rate produces pile-up, provoking instability in the signal base line. In figure 6.17 it can also be observed that the gamma background in our Zaragoza laboratory is more than one order of magnitude higher than the one in the IAS laboratory. Main differences in radio-purity terms are that, as explained in chapter 3, in the IAS laboratory there was an external lead shielding surrounding the cryostat.

Using the two energy calibrations, for $\beta/\gamma$ and $\alpha$ interactions, we estimated the $\mathrm{REF}_h(\alpha{:}\beta/\gamma)$. This value was already estimated with data from the IAS (chapter 5.1.2). Both estimations are shown in figure 6.18 with their $1\sigma$ error bands. Results are close each other but they are not compatible at $1\sigma$ C. L. This is an example of the fact that the REF depends on the experimental conditions and data treatment

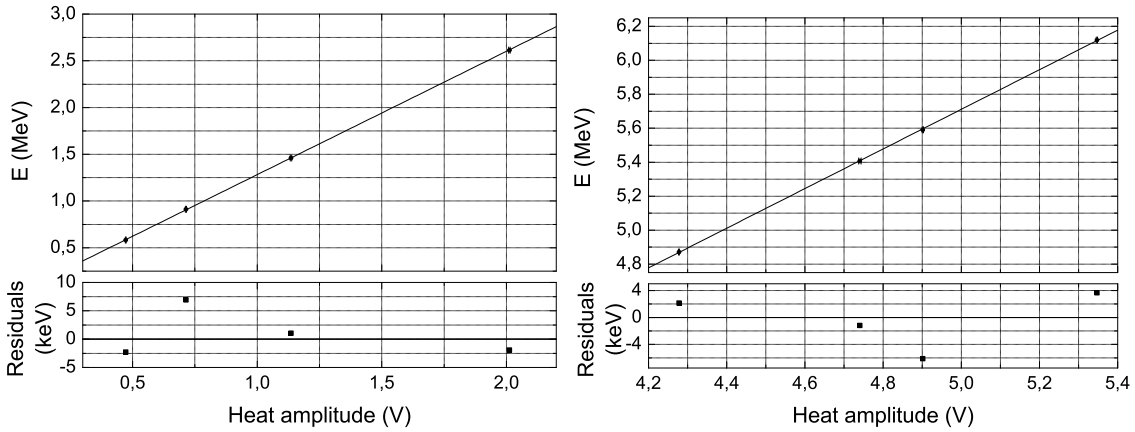


(a) (b)

Figure 6.16: *Energy calibrations of the gamma background peaks (a) and the alfa inner contamination peaks (b) for the $SrF_2$ bolometer measured in Zaragoza.*

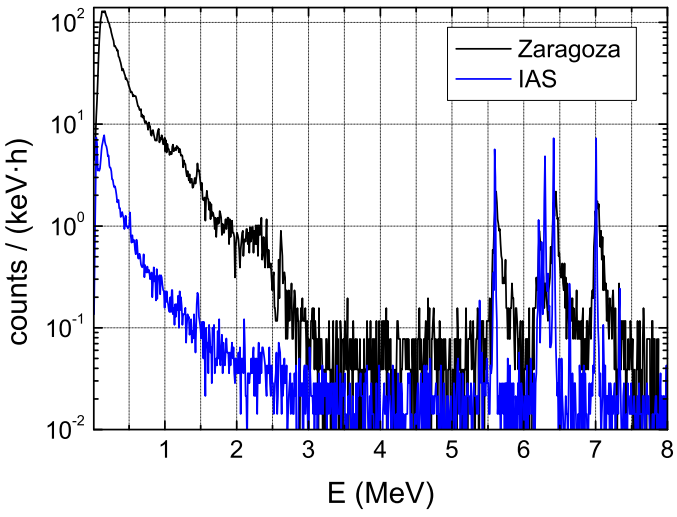


Figure 6.17: *Energy spectra of two background measurements carried out with the $SrF_2$ bolometer in the laboratories of Zaragoza (black line) and IAS (blue line). Both spectra are energy calibrated with gamma lines.*

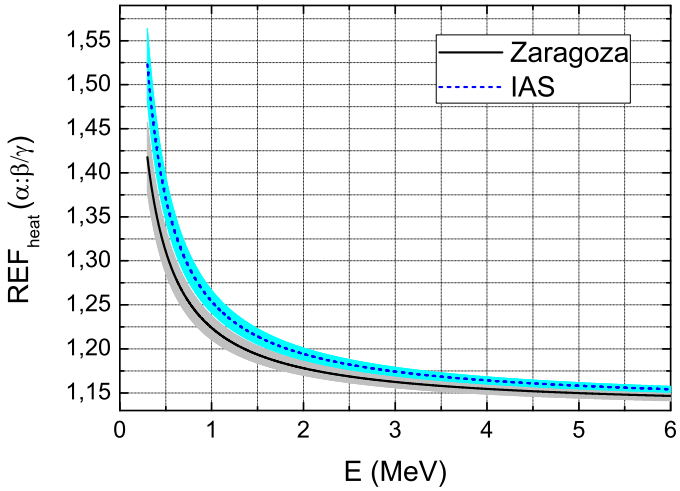


Figure 6.18: *Comparison of the estimates of $REF_h(\alpha{:}\beta/\gamma)$ obtained with data from Zaragoza (solid black line) and IAS (dashed blue line).* Shaded regions represent the $1\sigma$ error bands.

procedure, and in this case they are quite different.

The first tests carried out with the $SrF_2$ bolometer indicated that, although there is still hard work to do (specially to reduce microphonic and electromagnetic noises), we have progressed in the right direction to measure with cryogenic detectors in the laboratory of Zaragoza. Short-term improvements for our installation, apart from additional efforts in the reduction of microphonic and electromagnetic noises, are the building of an external lead shielding and the filling of the cryostat hole with radon-free air.

## 6.8 Scientific goals and prospects

Besides the work in the cryogenic installation, first steps have been taken in the design and construction of bolometers in the University of Zaragoza, with the long-term goal of developing a NaI scintillating bolometer and, if positive results are obtained, proposing to the LSC a new experimental project. All this work is being performed in collaboration with the ADG group of the Lisbon University, and with the advice and collaboration of some members of the STAP group of the IAS in cryogenic issues, and with the assistance of people from the Weak Interaction Group of the Milano-Bicocca University, who provided Ge–NTD sensors and their mounting technique.

NaI has shown its excellent scintillating properties in several experiments at room

temperature and it is an interesting target for dark matter searches (for instance, the experiments DAMA-LIBRA [190] and ANAIS [191]). However, its hygroscopicity makes it problematic for many applications, in particular to be used as a bolometer. To avoid the air exposition, NaI crystals were coated with vapor-deposited poly-p-xylylene (parylene) by Comelec[4], in Switzerland, and we studied their optical and mechanical behavior at low temperatures [32]. The crystals, cylindrical in shape, were covered with 5 $\mu$m thickness coat in the lateral face and 2-3 $\mu$m in the top and bottom faces. Coats as thin as possible are preferable to reduce the thermal capacity and allow the light transmission, but moisture permeability also depends on the film thickness.

We measured at IAS (see reference [32]) the scintillation spectra of the parylene coated crystals at 77, 4.2 and 1.5 K and also the relative light output as function of the temperature from 1.5 to 300 K, showing a light output below 10 K of at least 90% of the value at room temperature that suggest that parylene coated NaI should be a good scintillator at low temperatures.

In our cryogenic facility at Zaragoza we tested the resistance of the parylene coated NaI crystals to thermal cycles such as the ones suffered by bolometers in their operation. For that, a copper frame was designed to encapsulate the crystals, that were held with six small Teflon pieces (see figure 6.19a) that clamped the crystals when the system was cooled down. This design was thought as a prototype of a possible future bolometer. First, the mounting with a NaI(Tl) crystal was cooled down to 100 K through a cold finger immersed in liquid nitrogen (see figure 6.19b), and later, a mounting with pure NaI crystal was attached to the Mixing Chamber of our dilution refrigerator and cooled down to 80 mK (see figure 6.19c). The light output was measured before and after the thermal cycles with a HAMAMATSU R6233-100 photomultiplier (PMT) under gamma excitation ($^{137}$Cs source). The samples were mounted inside an aluminium cavity with a Teflon internal diffuser and the photocathode facing the crystal but not coupled to it, in an easily reproducible configuration. The PMT pulses were digitized with a Tektronix TDS5000 scope and digitally integrated to obtain the pulse area as energy estimator. A decrease of 7.5% was noticed after the cycle to 100 K, being the mean pulse area of the 662 keV photopeak 13.0 $V \cdot ns$ before the thermal cycle and 12.4 $V \cdot ns$ after it (see figure 6.20a). No optical deterioration was observed in the crystal, although the parylene adherence appeared to be lost in some areas. After the cycle to 80 mK the crystal seemed to be affected by humidity showing some white areas and the light output was reduced in a 35%, from 3.5 to 2.3 $V \cdot ns$ of mean pulse area in the

[4]Comelec S.A.: http://www.comelec.ch

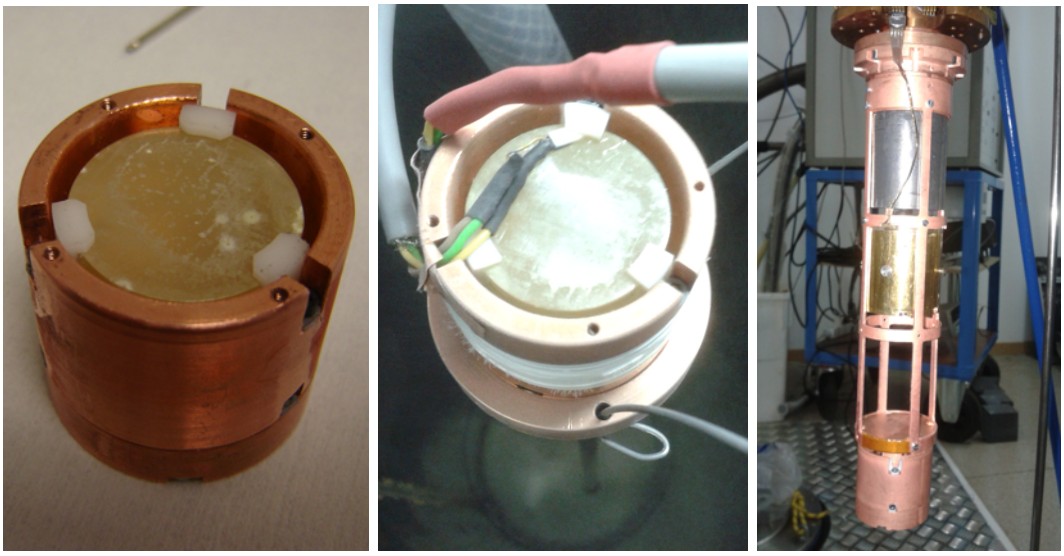

(a) (b) (c)

Figure 6.19: *In (a) it is shown the mounting of a parylene coated NaI crystal in a copper frame, being held by six Teflon clamps. In (b) it is shown the cooling down to 100 mK through a cold finger in contact with liquid nitrogen. In (c) the detectors holder is attached to the Mixing Chamber of the dilution refrigerator. The three coupled cylinders are, from top to bottom, a lead cylinder for shielding purposes, the $SrF_2$ bolometer and the parylene coated NaI crystal in its copper frame.*

photopeak (spectra are shown in figure 6.20b). In this case, the sample was exposed to normal humidity conditions for about one week to be mounted in the dilution refrigerator. For the future, a quicker procedure of mounting in the refrigerator must be designed to limit exposure to humidity. Our conclusion is that parylene allows a certain handling in normal humidity conditions, but it is not a 100% barrier against moisture. Some loss of adherence of the parylene to the crystal has been observed visually, limiting the reusability of the samples.

Next steps will be directed in the line of investigating other coatings for NaI crystals as alternative to parylene, as for example the deposition of $SiO_2$. In parallel, we are going to check the feasibility of our bolometer design with a non hygroscopic material. A $ZnWO_4$ crystal with a Ge–NTD sensor has been already mounted and experimental tests are ongoing.

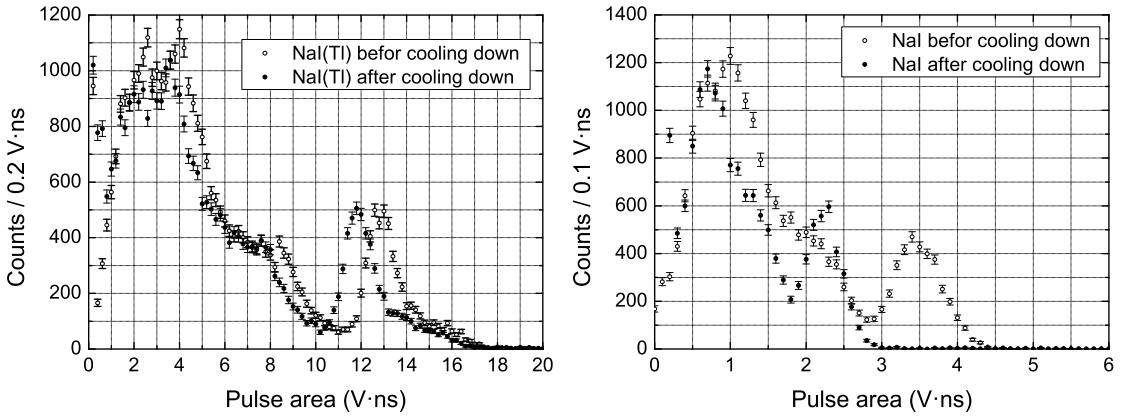


(a) (b)

Figure 6.20: *Pulse area spectra measured for the parylene coated NaI(Tl) crystal irradiated with a $^{137}Cs$ source before and after the cooling down process to 100 K (a), and for the parylene coated NaI crystal under the same irradiation before and after the thermal cycle to 80 mK (b).*

# Conclusions

The work presented in this thesis is organized under two main issues: first, the development and characterization of scintillating bolometers, carried out in the facilities of the Institut d'Astrophysique Spatiale (IAS) and the Laboratorio Subterráneo de Canfranc (LSC), for different applications in the field of nuclear and particle physics; and second, the installation of a cryogenic facility in the University of Zaragoza as a new bench to test bolometers and scintillating bolometers. The conclusions of this work are listed below:

- Scintillating bolometers of $SrF_2$, LiF, enriched $^6$LiF, LGBO, BGO and $Al_2O_3$ have been exposed to natural radioactive background and irradiated with different radioactive sources ($\alpha$ particles, $\gamma$ particles, neutrons and/or recoiling nuclei depending on the case). This has allowed their characterization, the study of their heat and light responses, and the estimation of their Relative Efficiency Factors (REF) and discrimination powers among the different types of interacting particles.

- We have compared the results obtained for the light REF in the different crystals with calculations of an existing model (a semi–empirical approach with only one parameter). The model underestimates the dependence on the energy of the light REF between $\gamma$ and $\alpha$ particles and does not reproduce our experimental data as the light REF between $\gamma$ particles and low energy nuclear recoils. That suggests that the model oversimplifies the complex scintillation process of inorganic crystals. Experimental measurements of light REFs becomes not only advisable but in some experiments even unavoidable because up to date models are not satisfactory enough.

- We have proved the viability of particle discrimination in the $SrF_2$ bolometer, without the need for the light channel, based only on the shape of the thermal pulses, obtaining a discrimination power between $\alpha$ and $\beta/\gamma$ particles of $3.9\sigma$ at energies from 4.5 to 6.5 MeV.

- We have studied the processes of double electron capture and $\beta^+$ decay and electron capture of the $^{84}$Sr nuclei present in the $SrF_2$ scintillating bolometer, obtaining lower limits to the half-lives of the processes $\varepsilon\beta^+0\nu$ between ground states ($T^{\varepsilon\beta^+0\nu}_{1/2}$(g.s. $\rightarrow$ g.s.) $\geq 4.2 \cdot 10^{16}$ yr), and the $2\varepsilon2\nu$ to the first excited state of the daughter nucleus ($T^{2\varepsilon2\nu}_{1/2}$(g.s. $\rightarrow$ 882.6 keV) $\geq 3.7 \cdot 10^{15}$ yr) at 90% C.L. These limits are competitive with or even better than the results published for these processes but are far from the theoretical calculations ($\sim 10^{24} - 10^{26}$ yr). We have estimated that, increasing the crystal mass, the isotopic abundance of $^{84}$Sr, the measurement time and optimizing the background conditions, sensitivities to the half-life of $\varepsilon\beta^+0\nu$ of $\sim 10^{21} - 10^{22}$ yr could be reached.

- In the $SrF_2$ scintillating bolometer, we have observed a positional dependence in the scintillation light that can be attributed to variations in the light yield (inhomogeneities in the crystal) and/or light collection. We have quantified the contribution of this effect to the energy resolution of the light channel, that worsens from 6% to 11%.

- We have proved that the scintillating bolometers of LiF, enriched $^6$LiF and LGBO are able to clearly discriminate the signal produced by neutron captures against other events in spite of their feeble light yield. The natural and enriched LiF crystals have energy resolutions (53 and 32 keV at 4.78 MeV respectively) that allow to completely resolve the thermal neutron peak (4.78 MeV) from the fast neutron one at the $^6$Li resonance (5.02 MeV). The presence of Gd, as in the LGBO crystal, could be a disadvantage since thermal neutrons are mostly captured by $^{55}$Gd and $^{57}$Gd whose products are difficult to detect, but an advantage for fast neutron detection by $^6$Li because the thermal neutrons peak becomes lower.

- We have studied the features of BGO and $Al_2O_3$ as dark matter detectors, obtaining excellent results in background rejection, with good discrimination powers of electron versus nuclear recoils down to energies of about 25–30 keV in BGO and 15–20 keV in $Al_2O_3$.

- We have installed a cryogenic laboratory in the University of Zaragoza to operate a dilution refrigerator: installation of the vacuum and gas handling systems, the cryostat and other cryogenic equipment, and development of a slow control system. We have tuned the dilution refrigerator to reach steady operational conditions at low enough temperatures to operate bolometers (leaks repairing, re-balancing of the mixture, etc.) and we have designed

and installed a wiring to read up to four bolometers. We have improved the installation to minimize the microphonic and electromagnetic noise contributions to the signals. The facility has been tested using a known bolometer of $SrF_2$ and proved its capability to operate such detectors. First tests of new bolometers developed at the University of Zaragoza are ongoing.

# Resumen y conclusiones

Nuestro Grupo de Investigación en Física Nuclear y Astropartículas (GIFNA) de la Universidad de Zaragoza, estableció una colaboración en 1997 con el grupo de Espectrometría Térmica para Astrofísica y Física (STAP) del Instituto de Astrofísica Espacial de Orsay (IAS) para medir inicialmente con bolómetros y posteriormente con bolómetros centellantes (diseñados y construidos por el grupo francés) en el antiguo Laboratorio Subterráneo de Canfranc (LSC), con el objetivo de llevar a cabo búsquedas de la materia oscura galáctica. Dentro de esta colaboración, llamada ROSEBUD (las siglas en inglés de "búsqueda subterránea de objetos poco probables con bolómetros"), se han realizado experimentos en el LSC con numerosos y variados detectores bolométricos desde el año 1999. Recientemente han sido desarrollados y probados nuevos materiales, no solo dedicados a búsquedas de materia oscura, sino también a espectroscopía de neutrones y a otros experimentos de física nuclear y de partículas. Las medidas de caracterización y aplicación de bolómetros centellantes presentadas en esta tesis se han llevado a cabo tanto en el laboratorio del IAS como en el LSC. El GIFNA ha establecido otra colaboración con el Grupo de Detectores Avanzados (ADG) de la Universidad de Lisboa (UL) para el préstamo y operación en Zaragoza (y a largo plazo en el LSC) de un refrigerador de dilución (propiedad de la UL) para probar bolómetros y bolómetros centellantes que serán desarrollados por el GIFNA. La última parte de esta tesis se centra en la preparación, puesta a punto y primeras pruebas de la nueva instalación criogénica de Zaragoza.

## Bolómetros y bolómetros centellantes

Cuando una partícula interacciona en el blanco de un detector, transfiere parte o toda su energía a éste produciendo algún tipo de excitación. Esta excitación puede recogerse principalmente en forma de calor, carga o luz. Un bolómetro es básicamente un detector de calor, un dispositivo capaz de detectar el incremento de temperatura producido por la interacción de una partícula en un cristal absorbente.

Cuando una partícula interactúa con el cristal cede un depósito de energía en forma de calor que se transmite por fonones a todo el cristal produciendo un incremento de temperatura en éste que es transformado en una señal eléctrica por medio de un termistor (sensor de fonones). Idealmente el bolómetro está formado por un conjunto absorbente+sensor caracterizado por su capacidad calorífica $C$, acoplado a un baño térmico a temperatura constante $T_b$ a través de un enlace térmico de conductancia térmica $G$, que devuelve el sistema a la temperatura base tras una interacción. El incremento de temperatura $\Delta T$ producido tras la interacción de una partícula es proporcional al depósito de energía $\Delta E$ e inversamente proporcional a la capacidad calorífica $C$ ($\Delta T = \Delta E/C$).

Con el objetivo de maximizar la respuesta térmica del bolómetro, es necesario utilizar absorbentes con valores de capacidad calorífica muy pequeños, lo que se consigue enfriando el bolómetro a temperaturas cercanas al cero absoluto (del orden de decenas de mK). Los materiales con menos contribuciones a la capacidad calorífica a bajas temperaturas son los dieléctricos y diamagnéticos (a bajas temperaturas siguen la ley de $T^3$ de Debye), lo que todavía deja un amplio abanico de posibles materiales para ser utilizados como absorbente. Los sensores de fonones son otra parte fundamental de un bolómetro; son los responsables de convertir las variaciones de temperatura en señales eléctricas. Normalmente se utilizan termistores superconductores operando en la región de la transición superconductora, donde la variación de resistencia con temperatura es más pronunciada, o termistores semiconductores (son los utilizados en esta tesis), dopados con impurezas en concentraciones muy cercanas a la transición metal-aislante, donde la dependencia de la conductividad con la temperatura es también grande.

Además de calor, es posible detectar una segunda forma de excitación (carga o luz) para obtener más información de las interacciones. En el caso de bolómetros centellantes, esta segunda magnitud detectada es luz. En un bolómetro centellante, el cristal es un material centellante, lo que significa que emite luz cuando es expuesto a ciertas formas de radiación. Esta luz es absorbida por otro detector, en nuestro caso un segundo bolómetro, llamado bolómetro óptico, consistente en un disco de Ge al que está acoplado un segundo sensor de fonones que transforma el incremento de temperatura producido por la absorción de fotones en una señal eléctrica. Ambos cristales están acoplados en una cavidad cerrada con paredes interiores reflectantes para favorecer la recogida de luz. De esta forma, son medidos simultáneamente el calor y la luz producidos por la interacción de una partícula en el cristal centellante. La medida de la luz permite identificar el tipo de partícula que interacciona, ya

que la cantidad de luz producida por la interacción de fotones, electrones o muones, es diferente de la producida por partículas alfa y diferente de la producida por retrocesos nucleares.

## Física nuclear y de partículas con bolómetros y bolómetros centellantes

Los bolómetros tienen excelentes propiedades como detectores de partículas: muy buena resolución en energía, umbrales de energía muy bajos, la posibilidad de elegir entre una amplia gama de materiales como blancos, y la posibilidad de diferenciar el tipo de partícula en el caso de bolómetro centellantes. Por todo esto, los detectores bolométricos se utilizan en numerosas aplicaciones, incluyendo algunos de los temas de más interés actual en física de partículas y astropartículas: la búsqueda de materia oscura, la física de neutrinos, la búsqueda de axiones o el estudio de desintegraciones muy poco probables.

La materia oscura es uno de los principales componentes del Universo según el modelo cosmológico más aceptado, el ΛCDM, sustentado por numerosos datos experimentales y observacionales, destacando especialmente las medidas del telescopio espacial Hubble de distancias y velocidades de galaxias, las observaciones de supernovas tipo Ia, y las medidas de anisotropías del fondo cósmico de microondas (CMB) de los satélites WMAP y Planck. Además, todo apunta a que la mayor parte de la materia oscura es fría (partículas no relativistas en la época de su desacoplo). Las características de las partículas que conforman esta materia oscura fría (no relativistas, masivas, neutras, estables, débilmente interaccionantes con la materia y no bariónicas) no se encuentran en ninguna partícula del Modelo Estándar (SM, siglas en inglés) de Física de Partículas, por lo que se buscan candidatos más allá de este modelo. Uno de los candidatos mejor motivados es el WIMP (las siglas en inglés de partículas masivas débilmente interaccionantes), y dentro de los WIMPs, en los modelos de supersimetría (extensiones del SM), el neutralino más ligero. Otro candidato viable es el axión, partícula propuesta para explicar el problema de la conservación de simetría CP en la Cromodinámica Cuántica (QCD), que podría constituir la materia oscura si su masa se encuentra entre el $\mu$eV y el meV. Diferentes experimentos han tratado y tratan de detectar materia oscura utilizando diferentes estrategias: detección directa, detección indirecta y búsqueda en aceleradores. El único resultado positivo hasta la fecha, aunque no ampliamente aceptado por la comunidad científica, es el publicado por el experimento italiano DAMA/LIBRA. Los experimentos de detección directa de materia oscura (detección de los retrocesos

de núcleos del detector producidos por WIMPs) requieren altas eficiencias, umbrales de energía muy bajos y un buen rechazo del fondo radiactivo. Los bolómetros se ajustan muy bien a estos requisitos y algunos de los principales experimentos y proyectos de búsqueda directa de materia oscura utilizan estos detectores (CDMS, EDELWEISS, CRESST, EURECA). Uno de los fondos radiactivos más peligrosos para los experimentos de materia oscura son los neutrones rápidos, ya que producen una señal muy similar a la producida por hipotéticos WIMPs. Por ello es muy importante conocer con precisión el flujo de neutrones rápidos en los experimentos de materia oscura. Los bolómetros centellantes pueden fabricarse con materiales sensibles a neutrones rápidos y medir flujos muy débiles; además, pueden situarse junto a los blancos de materia oscura y obtener así una medida directa de dicho flujo en la posición exacta del detector.

El neutrino es una partícula que aparece en el Modelo Estándar como neutra, de spin 1/2, que interacciona débilmente, sin masa y de la que existen tres familias o sabores ($\nu_e$, $\nu_\mu$, $\nu_\tau$); sin embargo, su estudio ha revelado algunas cualidades sorprendentes como el hecho de que su masa no es nula, las familias son en realidad una combinación lineal de estados de masa definida ($\nu_1$, $\nu_2$, $\nu_3$) que pueden cambiar, dando lugar a cambios de sabor u oscilaciones. Algunas propiedades quedan todavía por descubrir, como la escala absoluta de masas o su naturaleza de Dirac (neutrino $\neq$ antineutrino) o Majorana (neutrino = antineutrino). Algunos experimentos tratan de determinar estas propiedades por medio de enfoques como la desintegración doble beta (DBD) o el estudio del espectro de la desintegración beta simple. La DBD es un proceso de segundo orden en el que un núcleo (A,Z) se transforma en un isóbaro (A,Z$\pm$2) con la emisión de dos electrones o positrones (también has procesos con una o dos capturas electrónicas). Según el modelo estándar también se emiten dos antineutrinos o neutrinos; sin embargo, se ha propuesto también la desintegración sin neutrinos (no ha sido todavía observada), cuyo descubrimiento sería una prueba de física fuera del Modelo Estándar, revelando además la naturaleza de Majorana de los neutrinos. A partir de la la vida media del proceso DBD sin neutrinos, y utilizando modelos teóricos, podría obtenerse un valor de la masa efectiva de Majorana del neutrino $\langle m_\nu \rangle$. Los experimentos de DBD necesitan grandes masas de detección, muy buena resolución en energía y rechazo del fondo radiactivo. El experimento CUORE (y su precursor CUORICINO) y los proyectos LUCIFER y LUMINEU tratan de buscar la DBD con bolómetros, los dos últimos con bolómetros centellantes. La medida precisa del espectro de la desintegración beta es el método más directo para investigar la masa del neutrino, ya que es un continuo desde cero hasta una energía que corresponde con la diferencia de masas atómicas de la desintegración beta menos la masa efectiva del neutrino $m_\nu c^2$. Para esta medida se necesita una

resolución excelente, ya que la masa esperada del neutrino es del orden del meV. Los bolómetros, en este caso cadenas de microbolómetros, también se utilizan en este campo. Al igual que en la desintegración doble beta, se utilizan absorbentes que contienen el isótopo que se estudia. Los proyectos MARE y ECHO utilizan este tipo de detectores para medir el espectro beta de $^{187}$Re y $^{163}$Ho, respectivamente.

Los bolómetros también se han propuesto para detectar axiones. Algunos experimentos, diseñados principalmente con otros objetivos, han dado límites a los valores de las constantes de acoplo de axiones con fotones y electrones (por ejemplo, utilizando bolómetros, los ya mencionados CDMS, EDELWEISS o CUORE). Gracias a las excelentes propiedades de discriminación, eficiencia y resolución en energía de los bolómetros centellantes, se han dado medidas de algunos parámetros de física nuclear, como por ejemplo: la desintegración $\alpha$ del núcleo estable más pesado hasta la fecha, el $^{209}$Bi, con un bolómetro centelleador de BGO; otras desintegraciones $\alpha$ poco probables como las de algunos isótopos de plomo ($PbWO_4$) y wolframio ($CaWO_4$); o la medida de los cocientes L/K de captura electrónica de $^{207}$Bi and $^{7}$Be. Las buenas características de los bolómetros también permiten llevar a cabo medidas de radiopureza, alcanzando niveles de actividad muy bajos, del orden de algunos mBq/kg; y medidas de espectroscopía $\gamma$, seleccionando un absorbente adecuado (de alto número atómico).

## Montaje experimental

Para llevar a cabo medidas con bolómetros se necesita una instalación dedicada. En primer lugar, las muy bajas temperaturas a las que funcionan los bolómetros se alcanzan gracias a un refrigerador de dilución, que es un complejo dispositivo que utiliza las propiedades termodinámicas de una mezcla (dilución) de $^{3}$He-$^{4}$He para alcanzar, de forma continua, temperaturas del orden del mK. Estas propiedades aseguran que al forzar el paso de átomos de $^{3}$He de una fase concentrada en $^{3}$He a una diluida en una mezcla $^{3}$He-$^{4}$He por debajo de la temperatura crítica, la diferencia de entalpía sea positiva, lo que provoca el enfriamiento de la cámara de mezcla, que es el recipiente que contiene la mezcla $^{3}$He-$^{4}$He y está acoplada térmicamente a los bolómetros. La continuidad del proceso se consigue bombeando la fase gaseosa de una cámara intermedia llamada destilador conectada a la fase diluida de la cámara de mezcla. La mezcla bombeada se purifica y se reinyecta en la cámara de mezcla tras ser enfriada en diferentes estadios. El refrigerador junto con los detectores se introduce en un criostato que permite el aislamiento térmico. A su vez, el criostato y los primeros elementos de la cadena electrónica se encuentran en una caja de

Faraday que permite el apantallamiento electromagnético.

La señal primaria de los bolómetros se obtiene polarizando los sensores de fonones (en nuestro caso de Ge–NTD, i.e., Ge dopado por transmutación con neutrones) a través de una resistencia de carga. La señal es amplificada dentro de la caja de Faraday para minimizar el ruido electromagnético, y se envía fuera de la caja a través de fibras ópticas. Una vez fuera, la señal óptica se reconvierte en eléctrica y pasa por un filtro de frecuencias. Un módulo electrónico permite establecer el *trigger* para varias señales simultáneas con un OR lógico. Las señales pasan por una tarjeta digitalizadora y quedan registradas en un ordenador. La cadena electrónica descrita anteriormente puede variar ligeramente de una medida a otra. Se pueden adquirir en simultáneo varias señales, dos por cada bolómetro centelleador (calor y luz).

En ocasiones, la contaminación radiactiva interna del propio detector es suficiente para calibrarlo en energía, pero en la mayoría de los casos son necesarias fuentes externas. En este trabajo se han utilizado diferentes fuentes radiactivas con emisión de fotones, neutrones, partículas $\alpha$ y núcleos de retroceso, para realizar calibraciones de energía y estudiar la respuesta del detector a diferentes partículas. Se utiliza una fuente de pulsos infrarrojos (IR), de amplitud y frecuencia constantes, enviados a los bolómetros a través de fibras ópticas para monitorizar la estabilidad de la medida y la respuesta de los bolómetros. Esto también permite estimar el tiempo muerto contando los pulsos que no son registrados en la medida.

El estudio preliminar de los bolómetros y bolómetros centellantes se realiza en la instalación del IAS en un laboratorio en superficie. El criostato donde se aloja el refrigerador se encuentra dentro de la caja de Faraday, introducido en un agujero en el suelo forrado de plomo para reducir el fondo radiactivo. La caja de Faraday está forrada de aislante acústico y los tubos que vienen del sistema de bombeo pasan por filtros de plomo. Ambas medidas se toman para minimizar vibraciones y ruido microfónico. Los bolómetros más prometedores se miden en las instalaciones del LSC, laboratorio subterráneo situado en los Pirineos, entre los túneles de carretera y ferrocarril del Somport, bajo 850 m de roca (2450 m equivalentes de agua) que filtran los muones producidos en la atmósfera por rayos cósmicos. El laboratorio proporciona un entorno de ultra-bajo fondo radiactivo ideal para medidas de sucesos muy poco probables. El experimento ROSEBUD se encuentra en el Hall B del laboratorio, donde se ha construido una caja de Faraday y se han tomado diferentes medidas para reducir tanto el ruido mecánico (aislamiento acústico, filtros anti-vibraciones), ruido electromagnético (caja de Faraday) como el fondo radiactivo natural del propio laboratorio (blindaje externo de plomo, criostato radiopuro, etc.).

## Preanálisis de los pulsos

Las señales (pulsos digitalizados) adquiridas de los detectores deben ser tratadas para obtener información relevante de ellas. En primer lugar, los pulsos (consistentes en trazas de 4096 puntos) se reducen a N-tuplas con los 10-20 parámetros más relevantes del pulso: la posición del *trigger* y el canal que lo ha activado, el nivel de la línea de base y su desviación cuadrática media, la amplitud del pulso, la posición del máximo, los tiempos de subida y bajada del pulso, el área, el tiempo absoluto en el que se ha registrado, la diferencia de tiempo con el pulso anterior y el número identificativo del evento. Estos parámetros se representan en histogramas para ver la distribución de uno de ellos, o en diagramas de dispersión en los que se muestra los valores de dos parámetros para cada pulso (uno en cada eje). Es importante utilizar buenos estimadores de los parámetros, especialmente de la amplitud del pulso, ya que permite estimar la energía en el canal de calor, y en el caso del canal de luz identificar el tipo de partícula que ha interaccionado. Hemos probado diferentes estimadores: el punto máximo de la traza restando la línea de base, el ajuste a un pulso patrón, la aplicación de un filtro de suavizado, y la aplicación del filtro óptimo. Se ha concluido que el mejor estimador debe determinarse para cada medida concreta, ya que cada uno tiene sus ventajas e inconvenientes bajo determinadas condiciones experimentales. También se ha probado un tipo de adquisición continua de la señal de los bolómetros, que permite evitar la utilización del módulo de *trigger* y hacer éste *off-line*. Para ello se ha implementado un programa para localizar pulsos en la traza continua y obtener sus correspondientes N-tuplas.

Dado que las condiciones de una medida suelen variar con el tiempo, la respuesta de los bolómetros en medidas largas puede verse modificada (téngase en cuenta que la respuesta de un bolómetro es fuertemente dependiente de su temperatura de trabajo). Gracias a las señales de los pulsos IR podemos ver cómo cambia la respuesta y corregirla aplicando un factor multiplicativo a la amplitud de los pulsos en función del tiempo en el que se ha registrado. Entre los pulsos adquiridos, deben seleccionarse cuáles son de interés para el experimento que se realiza y cuáles no lo son. Para ello se aplican algunos cortes en función del valor de determinados parámetros como el ruido de la línea de base, las constantes de tiempo, la posición de los pulsos o su amplitud.

## Resultados y conclusiones

Los resultados presentados en esta tesis se organizan en dos categorías: en primer lugar, el desarrollo y la caracterización de bolómetros centellantes, medidos en las instalaciones del IAS y el LSC, para su utilización en diversas aplicaciones en el campo de la física nuclear y física de partículas; y en segundo lugar, la instalación de un laboratorio criogénico en la Universidad de Zaragoza para ser utilizado como banco de pruebas de bolómetros y bolómetros centellantes. Las conclusiones de este trabajo se presentan a continuación:

- Bolómetros centellantes de $SrF_2$, LiF, $^6$LiF enriquecido, LGBO, BGO y $Al_2O_3$ han sido expuestos al fondo radiactivo natural e irradiados con diversas fuentes radiactivas (partículas $\alpha$, fotones, neutrones y/o núcleos de retroceso, en función de cada bolómetro). Esto nos ha permitido caracterizarlos, estudiar sus respuestas de calor y luz, y estimar los Factores de Eficiencia Relativa (REF) y la capacidad de discriminación entre los diferentes tipos de partículas.

- Hemos comparado los resultados obtenidos para los REF del canal de luz en los diferentes cristales con los cálculos de un modelo existente (modelo semiempírico con un único parámetro libre). El modelo subestima la dependencia con la energía del REF de luz entre fotones y partículas $\alpha$ y no reproduce bien nuestros datos experimentales de REF de luz entre fotones y retrocesos nucleares de baja energía. Esto sugiere que el modelo simplifica en exceso el complejo proceso de centelleo de los cristales inorgánicos. Las medidas experimentales de REFs de luz son más que aconsejables, inevitables para algunos experimentos, ya que ningún modelo hasta la fecha es suficientemente satisfactorio.

- Hemos demostrado la viabilidad de discriminar partículas en el bolómetro de $SrF_2$ sin necesidad del canal de luz, utilizando solamente la forma de los pulsos de calor. Se han obtenido capacidades de discriminación entre partículas $\alpha$ y $\beta/\gamma$ de $3.9\sigma$ a energías de 4.5 a 6.5 MeV.

- Hemos estudiado los procesos de doble captura electrónica y desintegración $\beta^+$ con captura electrónica de los núcleos de $^{84}$Sr presentes en el bolómetro centellante de $SrF_2$, obteniendo límites inferiores a las vidas medias del proceso $\varepsilon\beta^+0\nu$ entre estados fundamentales ($T_{1/2}^{\varepsilon\beta^+0\nu}$(g.s. $\rightarrow$ g.s.) $\geq 4.2 \cdot 10^{16}$ años), y del $2\varepsilon2\nu$ al primer nivel excitado del núcleo hijo ($T_{1/2}^{2\varepsilon2\nu}$(g.s. $\rightarrow$ 882.6 keV) $\geq 3.7 \cdot 10^{15}$ años) al 90% de nivel de confianza. Estos límites son competitivos o incluso mejores que los resultados publicados para estos procesos, aunque están

lejos de las estimaciones teóricas ($\sim 10^{24} - 10^{26}$ años). Hemos estimado que, aumentando la masa del detector, la abundancia isotópica de $^{84}$Sr, el tiempo de medida y optimizando las condiciones de fondo radiactivo, podría llevarse a cabo un experimento sensible a una vida media del proceso $\varepsilon\beta^+0\nu$ del orden de $10^{21} - 10^{22}$ años.

- En el bolómetro centellante de $SrF_2$ hemos observado una dependencia posicional en la señal de luz que puede atribuirse a variaciones en la producción de luz (inhomogeneidades en el cristal) y/o en la recogida de luz. Hemos cuantificado la contribución de este efecto a la resolución en energía del canal de luz: la empeora del 6% al 11%.

- Hemos demostrado que los bolómetros centellantes de LiF, $^6$LiF enriquecido y LGBO son capaces de discriminar con claridad la señal producida por captura de neutrones frente a otros sucesos, a pesar de su débil producción de luz. Los cristales de LiF natural y enriquecido tienen resoluciones en energía (53 y 32 keV a 4.78 MeV respectivamente) que permiten resolver completamente el pico de neutrones térmicos (4.78 MeV) del de neutrones rápidos en la resonancia del $^6$Li (5.02 MeV). La presencia de Gd, como en el caso del cristal de LGBO, puede ser un inconveniente ya que la mayoría de neutrones térmicos son capturados por los isótopos $^{55}$Gd y $^{57}$Gd cuyos productos son difíciles de detectar, pero puede ser una ventaja para la detección de neutrones rápidos en $^6$Li, ya que el pico de neutrones térmicos se reduce.

- Hemos estudiado las características del BGO y el $Al_2O_3$ como detectores de materia oscura, obteniendo excelentes resultados en lo que respecta al rechazo del fondo radiactivo, con buenas capacidades de discriminación de fotones frente a retrocesos nucleares hasta energías tan bajas como 25-30 keV en BGO y 15–20 keV en $Al_2O_3$.

- Hemos instalado un laboratorio criogénico en la Universidad de Zaragoza para operar un refrigerador de dilución: instalación de los sistemas de vacío y manejo de gases, del criostato y otros equipos de criogenia, y desarrollo e implementación de un sistema de control. Hemos puesto a punto el refrigerador de dilución (reparación de fugas, equilibrado de la mezcla, etc.) para su correcto funcionamiento en condiciones estables a temperaturas suficientemente bajas como para llevar a cabo medidas con bolómetros. Hemos diseñado e instalado un cableado en el refrigerador de dilución para poder leer las señales de hasta cuatro bolómetros. Hemos optimizado la instalación minimizando las contribuciones de ruido microfónico y electromagnético a

las señales. La instalación se ha puesto a prueba utilizando un bolómetro conocido de $SrF_2$ y se ha demostrado su capacidad para realizar este tipo de medidas. Actualmente se están realizando las primeras pruebas de bolómetros desarrollados en la Universidad de Zaragoza.

# Agradecimientos

Antes de nada me gustaría decir que en estos cuatro años me he encontrado con un gran grupo profesional y humano que me ha hecho sentir como uno más desde el primer día, he trabajado realmente a gusto. El trabajo realizado durante la elaboración de esta tesis es fruto de un equipo, y sería injusto no agradecer el apoyo de todas aquellas personas que la han hecho posible:

En primer lugar tengo que dar las gracias a mi director, Eduardo García, por guiarme con paciencia y dedicación desde el principio, transmitiendo en todo momento su ilusión por la ciencia, sus ganas para mirar siempre hacia adelante, y su forma de trabajar con rigor y buen hacer.

Agradecer también a José Ángel Villar la oportunidad que me ofreció de hacer el doctorado en el Grupo de Física Nuclear y Astropartículas y el interés que mostró por mí para que así fuera.

A las personas más cercanas a este proyecto, que lo han hecho y lo hacen posible y con las que he compartido tantas horas de laboratorio, refrigerador, viajes, Canfranc, etc.: Ysrael Ortigoza, compañero de despacho, que me introdujo en el mundo de ROSEBUD y los bolómetros y no ha parado desde el primer día de ofrecerme su experiencia, consejos y ayuda. María Martínez, que ha aportado sus amplios conocimientos y está siempre dispuesta a resolver las dudas que me han surgido. Y Alfonso Ortíz de Solórzano, por su forma de trabajar, siempre encontrando soluciones más que problemas (y son muchos los que han surgido). Igualmente a Jorge Puimedón y a Marisa Sarsa, que me descrubrió la materia oscura y los detectores de partículas y despertó mi interés por este campo.

Al IAS como institución y en particular al grupo francés por acogerme durante mi estancia en Orsay: Nöel Coron, Pierre de Marcillac y Lidia Torres. Es un lujo haber aprendido de verdaderos expertos y pioneros en bolometría y criogenia. También a la Fundação para a Ciência e a Tecnologia de Portugal por la cesión del refrigerador y al grupo ADG de la Universidad de Lisboa, concretamente Thomas A. Girard y

Pavol Valko por su constante colaboración. Y gracias al LSC y su personal, siempre dispuesto a resolver nuestras necesidades durante las medidas en Canfranc.

También quiero agradecer a Gloria Luzón la oportunidad que me dio de conocer el CERN y el experimento CAST, y a Igor y Theopisti por acogerme allí. A Susana Cebrián, José Manuel Carmona y resto del grupo por tener siempre sus puertas abiertas: Clara, Laura, Miguel Ángel, Asun, Héctor, David, Diego.

Gracias a las personas con las que compartimos el rato del café y conversaciones, ya somos "expertos" en todo: Juanan, Javi, Paco, Diana, Alicia, Tomás, Javi, Alfredo, Victor, Ayalid, José Antonio, Patricia, Juán, Fredi.

Y por supuesto quiero agradecer este trabajo y mucho más a mi familia, especialmente a mis padres y mi hermano, y a Mapi, por su infinito apoyo.

Finalmente, debo agradecer el apoyo económico del Gobierno de Aragón, del Ministerio de Economía y Competitividad a través de los proyectos FPA 2008-03228 y FPA 2011-23749, y del proyecto Consolider MULTIDARK (CSD2009-00064), que han financiado los trabajos de esta tesis.

# Bibliography


[1] S. P. Langley. The bolometer and radiant energy. *Proceedings of the American Academy of Arts and Sciences*, 16:342–358, 1881.

[2] F. Simon. Application of low temeperature calorimetry to radioactive measurements. *Nature*, 135:763, 1935.

[3] R. C. Jones. The general theory of bolometer performance. *Journal of the Optical Scociety of America*, 43:1–14, 1953.

[4] S. H. Moseley, J. C. Mather, and D. McCammon. Thermal detectors as x-ray spectrometers. *J. Appl. Phys.*, 56:1257–1262, 1984.

[5] E. Fiorini and T. O. Niinikoski. Low-temperature calorimetry for rare decays. *Nucl. Instrum. Meth.*, 224:83–88, 1984.

[6] S. Cebrián et al. First underground light versus heat discrimination for dark matter search. *Phys. Lett. B*, 563:48–52, 2003.

[7] S. Cebrián et al. Bolometric WIMP search at Canfranc with different absorbers. *Astrop. Phys.*, 21:23–34, 2004.

[8] A. Calleja et al. Recent performance of scintillating bolometers developed for dark matter searches. *J. Low Temp. Phys.*, 151:848–853, 2008.

[9] W. R. Leo. *Techniques for Nuclear and Particle Physics Experiments.* Springer-Verlag, second revised edition, 1994.

[10] M. Chapellier. Physics of electrons and phonons in low-temperature detectors. *Nucl. Instr. Meth. A*, 520:21–26, 2004.

[11] A. Giuliani and S. Sanguinetti. Phonon-mediated particle detectors: physics and materials. *Mater. Sci. Eng.*, R 11:1–52, 1993.

[12] Y. Ortigoza et al. Energy partition in sapphire and BGO scintillating bolometers. *Astopart. Phys.*, 34:603–607, 2011.

[13] S. R. Bandler et al. Magnetically coupled microcalorimeters. *J. Low Temp. Phys.*, 167:1004–1014, 2012.

[14] W. S. Yoon et al. High energy resolution cryogenic alpha spectrometers using magnetic calorimeters. *J. Low Temp. Phys.*, 167:280–285, 2012.

[15] R. C. O. Ranitzsch et al. Development of metallic magnetic calorimeters for high precision measurements of calorimetric $^{187}$Re and $^{163}$Ho spectra. *J. Low Temp. Phys.*, 167:1004–1014, 2012.

[16] J. A. Bonetti et al. Characterization and fabrication of the TES arrays for the Spider, Keck and BICEP2 CMB polarimeters. *J. Low Temp. Phys.*, 167:146–151, 2012.

[17] R. A. Hijmering et al. Effect of magnetic fields on TiAu TES bolometers for the SAFARI instrument on the SPICA FIR telescope. *J. Low Temp. Phys.*, 167:242–247, 2012.

[18] G. Angloher et al. Results from 730 kg days of the CRESST-II Dark Matter search. *Eur. Phys. J. C*, 72(1971), 2012.

[19] D. S. Akerib et al. Exclusion limits on the WIMP-nucleon cross section from the first run of the Cryogenic Dark Matter Search in the Soudan Underground Laboratory. *Phys. Rev. D*, 72(052009), 2005.

[20] `http://www.cresst.de/bigpic_transition.php`.

[21] B. I. Shklovskii and A. L. Efros. *Electronic properties of doped semiconductors.* Springer-Verlag, 1984.

[22] D. McCammon. *Cryogenic Particle Detection*, chapter 1. Springer, 2005.

[23] W. Ootani et al. Sensitive germanium thermistors for cryogenic thermal detector of Tokyo dark matter search programme. *Nucl. Instr. Meth. A*, 374:534–538, 1996.

[24] L. C. Torres. *Bolómetros centelleadores para búsqueda de materia oscura.* PhD thesis, Universidad de Zaragoza, 2008.

[25] M. Pedretti. *The single module for Cuoricino and Cuore detectors: test, construction and modelling.* PhD thesis, Università degli Studi dell'Insubria, 2004.

[26] C. Arnaboldi et al. $CdWO_4$ scintillating bolometer for Double Beta Decay: Light and heat anticorrelation, light yield and quenching factors. *Astropart. Phys.*, 34:143–150, 2010.

[27] M. Pedretti et al. Measurements of thermal properties for modeling and optimization of large mass bolometers. *Physica B*, 329–333:1614–1615, 2003.

[28] L. Foggetta et al. Composite macro-bolometers for the rejection of surface radioactive background in rare-event experiments. *Astropart. Phys.*, 34:809–821, 2011.

[29] M. Galeazzi and D. McCammon. Microcalorimeter and bolometer model. *J. Appl. Phys.*, 93:4856–4869, 2003.

[30] J. B. Birks. *The Theory and Practice of Scintillation Counting*. Pergamon Press Ltd., 1964.

[31] P. Lecoq et al. *Inorganic Scintillators for Detector Systems*. Springer, 2006.

[32] N. Coron et al. Study of parylene–coated NaI(Tl) at low temperatures for bolometric applications. *Astropart. Phys.*, 47:31–37, 2013.

[33] C. Sailer et al. Low temperature light yield measurements in NaI and NaI(Tl). *Eur. Phys. J. C*, 72(2061), 2012.

[34] R. Strauss et al. Neutron scattering facility for the measurement of light quenching factors of dark matter detectors at low temperatures. *J. Low Temp. Phys.*, 167:1063–1068, 2012.

[35] J. W. Beeman et al. $ZnMoO_4$: a promising bolometer for neutrinoless double beta decay searches. *Astropart. Phys.*, 35:813–820, 2012.

[36] Y. Ortigoza. *Caracterización de un bolómetro centelleador de BGO ($Bi_4Ge_3O_{12}$) para su aplicación en la búsqueda directa de materia oscura*. PhD thesis, Universidad de Zaragoza, 2010.

[37] Y. Ortigoza et al. Light relative efficiency factors for ions in BGO and $Al_2O_3$ at 20 mk. *Submitted to Astropart. Phys.*

[38] C. Arnaboldi et al. Characterization of ZnSe scintillating bolometers for Double Beta Decay. *Astropart. Phys.*, 34:344–353, 2011.

[39] L. González-Mestres and D. Perret-Gallix, editors. *Low Temperature Detectors for Neutrinos and Dark Matter - II, Proceedings of LTD-2*. Editions Frontières, 1988.

[40] A. Alessandrello et al. Development of a thermal scintillating detector for double beta decay of $^{48}$Ca. *Nucl. Phys. B - Proc. Sup.*, 28:233–235, 1992.

[41] C. Bobin et al. Alpha/gamma discrimination with a $CaF_2$(Eu) target bolometer optically coupled to a composite infrared bolometer. *Nucl. Instr. Meth. A*, 386:453–457, 1997.

[42] L. Cardani et al. LUCIFER: A scintillating bolometer array for the search of neutrinoless double beta decay. *J. Phys. Conf. Ser.*, 375(042016), 2012.

[43] N. Coron et al. Highly sensitive large-area bolometers for scintillation studies below 100 mK. *Opt. Eng.*, 43:1568–1576, 2004.

[44] R. F. Lang et al. Discrimination of recoil backgrounds in scintillating calorimeters. *Astropart. Phys.*, 33:60–64, 2010.

[45] J. W. Beeman et al. Discrimination of $\alpha$ and $\beta/\gamma$ interactions in a $TeO_2$ bolometer. *Astropart. Phys.*, 35:558–562, 2012.

[46] J. W. Beeman et al. A next-generation neutrinoless double beta decay experiment based on $ZnMoO_4$ scintillating bolometers. *Phys. Lett. B*, 710:318–323, 2012.

[47] J. W. Beeman et al. Effect of $SiO_2$ coating in bolometric Ge light detectors for rare event searches. *Nucl. Instr. Meth. A*, 709:22–28, 2013.

[48] C. Isaila et al. Low-temperature light detectors: Neganov-Luke amplification and calibration. *Phys. Lett. B*, 716:160–164, 2012.

[49] C. Enss. *Journal of Low Temperature Physics, Special Issue: Low Temperature Detectors (LTD-14)*, volume 167. Springer, 2012.

[50] M. Trodden and S. M. Carroll. TASI lectures: Introduction to cosmology. *arXiv.org*, arXiv:astro-ph/0401547, 2004.

[51] G. F. Smoot et al. Structure in the COBE differential microwave radiometer first-year maps. *Astrophys. J. Lett.*, 396:L1–L5, 1992.

[52] G.F. Hinshaw et al. Nine-year Wilkinson Microwave Anisotropy Probe (WMAP) observations: Cosmologycal parameter results. *Astrophys. J. Suppl. S. In press:* `http://lambda.gsfc.nasa.gov/product/map/dr5/pub_papers/nineyear/cosmology/wmap_9yr_cosmology_results.pdf`, 2013.

[53] Planck collaboration. Planck 2013 results. XVI. Cosmological parameters. *Submitted to Astron. Astrophys. arXiv:1303.5076*, 2013.

[54] N. Suzuki et al. The Hubble Space Telescope Cluster Supernova Survey. V. Improving the dark energy constraints above $z > 1$ and building an early-type-hosted supernova sample. *Astrophys. J.*, 746(85), 2012.

[55] ESA and the Planck collaboration. `http://spaceinimages.esa.int/Images/2013/03/Planck_CMB`.

[56] J. D. Bekenstein. Relativistic gravitation theory for the modified Newtonian dynamics paradigm. *Phys. Rev. D*, 70(083509), 2004.

[57] J. H. Oort. The force exerted by the stellar system in the direction perpendicular to the galactic plane and some related problems. *Bull. Astron. Inst. Neth.*, 6:249–287, 1932.

[58] J. Beringer et al. (Particle Data Group). Review of particle physics. *Phys. Rev. D*, 86, 2012.

[59] F. Zwicky. Spectral displacement of extra galactic nebulae. *Helv. Phys. Acta*, 6:110–127, 1933.

[60] V. C. Rubin. The rotational of spiral galaxies. *Science*, 220:1339–1344, 1983.

[61] R. Massey, T. Kitching, and J. Richard. The dark matter of gravitational lensing. *Rep. Prog. Phys.*, 73(086901), 2010.

[62] D. Clowe et al. A direct empirical proof of the existence of dark matter. *Astrophys. J. Lett.*, 648:L109–L113, 2006.

[63] V. Springel et al. Simulations of the formation, evolution and clustering of galaxies and quasars. *Nature*, 435:629–636, 2005.

[64] M. Roos. Astrophysical and cosmological probes of dark matter. *J. Mod. Phys.*, 3:1152–1171, 2012.

[65] G. Bertone, D. Hooper, and J. Silk. Particle dark matter: evidence, candidates and constraints. *Phys. Rep.*, 405:279–390, 2005.

[66] S. van den Bergh. The early history of dark matter. *Publ. Astron. Soc. Pac.*, 111:657–660, 1999.

[67] `http://bustard.phys.nd.edu/Phys171/lectures/dm.html`.

[68] R. D. Peccei and H. R. Quinn. CP conservation in the presence of pseudoparticles. *Phys. Rev. Lett.*, 38:1440–1443, 1977.

[69] L. Visinelli and P. Gondolo. Dark matter axions revisited. *Phys. Rev. D*, 80(035024), 2009.

[70] M. Ackermann et al. Constraints on the galactic halo dark matter from Fermi-LAT diffuse measurements. *Astrophys. J.*, 761:91, 2012.

[71] J. Aleksić et al. Searches for dark matter annihilation signatures in the Segue 1 satellite galaxy with the MAGIC-I telescope. *J. Cosmol. Astropart. Phys.*, 6:35, 2011.

[72] M. Aguilar et al. First result from the Alpha Magnetic Spectrometer on the International Space Station: Precision measurement of the positron fraction in primary cosmic rays of 0.5–350 gev. *Phys. Rev. Lett.*, 110(141102), 2013.

[73] M. G. Aarsten et al. Search for dark matter annihilations in the Sun with the 79–String IceCube detector. *Phys. Rev.*, 110(131302), 2013.

[74] J. D. Zornoza et al. Dark matter search with the ANTARES neutrino telescope. *arXiv.org*, arXiv:1204.5066, 2013.

[75] G. Aad et al. Search for nonpointing photons in the diphoton and $E_T^{miss}$ final state in $\sqrt{s} = 7$ TeV proton-proton collisions using the ATLAS detector. *Phys. Rev. D*, 88(012001), 2013.

[76] L. Baudis. Direct dark matter detection: The next decade. *Dark Universe*, 1:94–108, 2012.

[77] D. G. Cerdeño and A. M. Green. *Particle Dark Matter: Observations, Models and Searches*, chapter 17 (Direct detection of WIMPs), pages 347–369. Cambridge University Press, 2010.

[78] R. Bernabei et al. New results from DAMA/LIBRA. *Eur. Phys. J. C*, 67:39–49, 2010.

[79] C. Aalseth et al. Search for an annual modulation in a p-type point contact germanium dark matter detector. *Phys. Rev. Lett.*, 107:141301, 2011.

[80] E. Aprile et al. Dark Matter results from 225 live days of XENON100 data. *Phys. Rev. Lett.*, 109(181301), 2012.

[81] R. Agnese et al. Dark matter search results using the silicon detectors of CDMS II. *arXiv.org*, arXiv:hep-ex/1304.4279, 2013.

[82] Z. Ahmed et al. Dark Matter search results from the CDMS II experiment. *Science*, 327(1619), 2010.

[83] Z. Ahmed et al. Search for annual modulation in low-energy CDMS-II data. *arXiv.org*, arXiv:1203.1309v2, 2012.

[84] E. Armengaud et al. Final results of the EDELWEISS-II WIMP search using a 4-kg array of cryogenic germanium detectors with interleaved electrodes. *Phys. Lett. B*, 702:329–335, 2011.

[85] E. Armengaud et al. A search for low-mass WIMPs with EDELWEISS-II heat-and-ionization detectors. *Phys. Rev. D*, 86(051701(R)), 2012.

[86] Z. Ahmed et al. Combined limits on WIMPs from the CDMS and EDELWEISS experiments. *Phys. Rev. D*, 84:011102, 2011.

[87] The CUORE collaboration. The low energy spectrum of $TeO_2$ bolometers: results and dark matter perspectives for the CUORE-0 and CUORE experiments. *J. Cosmol. Astropart. Phys.*, 1(38), 2013.

[88] S. Cebrián et al. First results of the ROSEBUD dark matter experiment. *Astropart. Phys.*, 15:79–85, 2001.

[89] CDMS collaboration. `http://cdms.berkeley.edu/gallery.html`.

[90] EDELWEISS collaboration. `http://edelweiss.in2p3.fr/`.

[91] CRESST collaboration. `http://www.cresst.de/pictures.php`.

[92] CUORE collaboration. `http://crio.mib.infn.it/wig/Cuoricinopage/CUORICINO.php`.

[93] The EURECA collaboration. EURECA conceptual design report 2012. *Submitted to Phys. Dark Universe*, 2013.

[94] R. L. Bramblett, R. I. Ewing, and T.W. Bonner. A new type of neutron spectrometer. *Nucl. Instrum. Meth.*, 9:1–12, 1960.

[95] G. F. Knoll. *Radiation Detection and Measurement*. John Wiley & Sons, third edition, 1999.

[96] M.B. Chadwick et al. ENDF/B-VII.1. `http://www.nndc.bnl.gov/exfor/endf00.jsp`, 2011.

[97] N. Coron et al. Measurement of the differential neutron flux inside a lead shielding in a cryogenic experiment. *J. Phys. Conf. Ser.*, 375(012018), 2012.

[98] T. Rolón. *Detección de neutrones con bolómetros centellantes de fluoruro de litio y zafiro y su aplicación en experimentos de búsqueda de materia oscura.* PhD thesis, Universidad de Zaragoza, 2013.

[99] T. Niedermayr et al. Unfolding of cryogenic neutron spectra. *Nucl. Instrum. Methods Phys. Res. A*, 579:165–168, 2007.

[100] K. Winter. *Neutrino Physics.* Cambridge University Press, second edition, 2000.

[101] B. Pontecorvo. Mesonium and antimesonium. *J. Exp. Theor. Phys.*, 33:549, 1957.

[102] Y. Abe et al. Indication of reactor $\bar{\nu}_e$ disappearance in the Double Chooz experiment. *Phys. Rev. Lett.*, 108(131801), 2012.

[103] K. Abe et al. Search for differences in oscillation parameters for atmospheric neutrinos and antineutrinos at Super-Kamiokande. *Phys. Rev. Lett.*, 107(241801), 2011.

[104] B. Aharmin et al. Measurement of the $\nu_e$ and total $^8$B solar neutrino fuxes with the Sudbury Neutrino Observatory phase-III data set. *Phys. Rev. C*, 87(015502), 2013.

[105] M. Goeppert-Mayer. Double beta-disintegration. *Phys. Rev.*, 48:512–516, 1935.

[106] W. H. Furry. On transition probabilities in double beta-disintegration. *Phys. Rev.*, 56:1184–1193, 1939.

[107] `http://next.ific.uv.es/next/experiment/physics.html`.

[108] H. V. Klapdor-Kleingrothaus et al. First evidence for neutrinoless double beta decay. *Part. Nucl. Lett.*, 110:57–79, 2002.

[109] H. V. Klapdor-Kleingrothaus and I. V. Krivosheina. The evidence for the observation of $0\nu\beta\beta$ decay: the identification of $0\nu\beta\beta$ events from the full spectra. *Mod. Phys. Lett. A*, 21:1547, 2006.

[110] M. Agostini et al. Results on neutrinoless double beta decay of $^{76}$Ge from GERDA Phase I. *arXiv.org*, arXiv:nucl-ex/1307.4720, 2013.

[111] V. Álvarez et al. Ionization and scintillation response of high-pressure xenon gas to alpha particles. *J. Inst.*, 8(P05025), 2012.

[112] M. Auger et al. Search for neutrinoless double-beta decay in $^{136}$Xe with EXO-200. *Phys. Rev. Lett.*, 109(032505), 2012.

[113] A. Gando et al. Measurement of the double-$\beta$ decay half-life of $^{136}$Xe with the KamLAND-Zen experiment. *Phys. Rev. C*, 85(045504), 2012.

[114] J. Hartnell et al. Neutrinoless Double Beta Decay with SNO+. *J. Phys. Conf. Ser.*, 375(042015), 2012.

[115] R. Arnold et al. Probing new physics models of neutrinoless double beta decay with SuperNEMO. *Eur. Phys. J. C*, 70:927–943, 2010.

[116] E. Andreotti et al. $^{130}$Te neutrinoless double-beta decay with CUORICINO. *Astropart. Phys.*, 34:822–831, 2011.

[117] F. Alessandria et al. CUORE crystal validation runs: Results on radioactive contamination and extrapolation to CUORE background. *Astropart. Phys.*, 35:839–849, 2012.

[118] H. Bhang et al. AMoRe experiment: a search for neutrinoless double beta decay of $^{100}$Mo isotope with $^{40}$Ca$^{100}$MoO$_4$ cryogenic scintillation detector. *J. Phys. Conf. Ser.*, 375(042023), 2012.

[119] M. Mancuso et al. An aboveground pulse tube based bolometric test facility for the validation of the LUMINEU $ZnMoO_4$ crystals. 15th International Workshop on Low Temperature Detectors, 2013.

[120] G. Drexlin et al. Current direct neutrino mass experiments. *Advances in High Energy Physics*, 2013(293986), 2013. `http://dx.doi.org/10.1155/2013/293986`.

[121] Ch. Krauss et al. Final results from phase II of the Mainz neutrino mass search in tritium $\beta$ decay. *Eur. Phys. J. C*, 40:447–468, 2005.

[122] V. M. Lobashev. Study of the Tritium beta-spectrum in experiment "Troitsk $\nu$-mass". *Prog. Part. Nucl. Phys.*, 48:123–131, 2002.

[123] A. Nucciotti, E. Ferri, and O. Cremonesi. Expectations for a new calorimetric neutrino mass experiment. *Astropart. Phys.*, 34:80–89, 2010.

[124] L. Gastaldo et al. Characterization of low temperature metallic magnetic calorimeters having gold absorbers with implanted $^{163}$Ho ions. *Nucl. Inst. Meth. A*, 711:150–159, 2013.

[125] B. Cabrera, L. M. Krauss, and F. Wilczek. Bolometric detection of neutrinos. *Phys. Rev. Lett.*, 55(1), 1985.

[126] A. J. Anderson et al. Coherent neutrino scattering in dark matter detectors. *Phys. Rev. D*, 84(013008), 2011.

[127] J. Monroe and P. Fisher. Neutrino backgrounds to dark matter searches. *Phys. Rev. D*, 76(033007), 2007.

[128] J. A. Formaggio, E. Figueroa-Feliciano, and A. J. Anderson. Sterile neutrinos, coherent scattering, and oscillometry measurements with low-temperature bolometers. *Phys. Rev. D*, 85(013009), 2012.

[129] M. Biassoni et al. Low threshold performance and coherent detection of supernova neutrinos in CUORE-0 and CUORE. *Nuovo Cimento C*, 36:251–254, 2013.

[130] K. Zioutas et al. Axion searches with helioscopes and astrophysical signatures for axion(-like) particles. *New J. Phys*, 11(105020), 2009.

[131] E. A. Paschos and K. Zioutas. A proposal for solar axion detection via Bragg scattering. *Phys. Lett. B*, 323:367–372, 1994.

[132] Z. Ahmed et al. Search for axions with the CDMS experiment. *Phys. Rev. Lett.*, 103(141802), 2009.

[133] E. Armengaud et al. Axion searches with the EDELWEISS-II experiment. *arXiv.org*, arXiv:astro-ph/1307.1488v1, 2013.

[134] The CUORE collaboration. Search for 14.4 kev solar axions from M1 transition of $^{57}$Fe with CUORE crystals. *J. Cosmol. Astropart. P.*, 5(7), 2013.

[135] P. De Marcillac et al. Experimental detection of $\alpha$–particles from the radioactive decay of natural bismuth. *Nature*, 422:876–878 and supplementary information, 2003.

[136] J. W. Beeman et al. First measurement of the partial widths of $^{209}$Bi decay to the ground and to the first excited states. *Phys. Rev. Lett.*, 108(962501), 2012.

[137] L. Pattavina et al. Scintillating bolometers: A promising tool for rare decays search. *Nucl. Instr. Met. A*, In press, `http://dx.doi.org/10.1016/j.nima.2013.06.009`, 2013.

[138] S. Cebrián et al. Improved limits for natural $\alpha$ radioactivity of tungsten with a $CaWO_4$ scintillating bolometer. *Phys. Lett. B*, 556:14–20, 2003.

[139] C. Cozzini et al. Detection of the natural $\alpha$ decay of tungsten. *Phys. Rev. C*, 70(064606), 2004.

[140] N. Coron et al. Measurement of the L/K electron capture ratio of the $^{207}$Bi decay to the 1633 keV level of $^{207}$Pb with a BGO scintillating bolometer. *Eur. Phys. J. A*, 48(89), 2012.

[141] P. A. Voytas et al. Direct measurement of the L/K ratio in $^{7}$Be electron capture. *Phys. Rev. Lett.*, 88(012501), 2002.

[142] A. Alessandrello et al. Measurements of internal radioactive contamination in samples of Roman lead to be used in experiments on rare events. *Nucl. Instrum. Meth. B*, 142:163–172, 1998.

[143] E. Leblanc et al. High-energy resolution alpha spectrometry using cryogenic detectors. *Appl. Radiat. Isotopes*, 64:1281–1286, 2006.

[144] M. W. Rabin. National and international security applications of cryogenic detectors–mostly nuclear safeguards. *AIP Conf. Proc.*, 1185:725–732, 2009.

[145] F. Pobell. *Matter and Methods at Low Temperatures*. Springer, third edition, 2007.

[146] S. Y. F. Chu, L. P. Ekstrom, and R. B. Firestone. The Lund/LBNL Nuclear Data Search, v2.0. `http://nucleardata.nuclear.lu.se/toi/`, 1999.

[147] MATLAB. *version 7.10.0 (R2010a)*. The MathWorks Inc. (`http://www.mathworks.es/products/matlab/`), Natick, U.S., 2010.

[148] R. Barlow. *STATISTICS. A Guide to the Use of Statistical Methods in the Physical Sciences*. John Wiley & Sons, 1989.

[149] T. A. Shutt. *A dark matter detector based on the simultaneous measurement of phonons and ionization at 20 mK*. PhD thesis, University of California at Berkeley, 1993.

[150] S. J. Collocott and J. G. Collins. Low-temperature heat capacity of alkaline-earth flourides: $SrF_2$, $BaF_2$. *J. Phys. C: Solid State Phys.*, 16:6179–6184, 1983.

[151] N. Coron. Private communication.

[152] C. Ginestra et al. Characterization of a $SrF_2$ scintillating bolometer. *J. Low Temp. Phys.*, 167:973–978, 2012.

[153] `http://www.world-nuclear.org/uploadedImages/org/info/radioactive_decay_series.png`.

[154] D. McCammon et al. *Low Temperature Detectors for Neutrinos and Dark Matter III.* Edited by L. Brogiato, D. V. Camin and E. Fiorini (Editions Frontières), 1990. (p. 213).

[155] M. Bass. *Handbook of Optics, second ed., vol. II.* McGraw–Hill, Inc., 1995.

[156] R. Shendrik, E. A. Radzhabov, and A. I. Nepomnyashchikh. Scintillation properties of pure and $Ce^{3+}$-doped $SrF_2$ crystals. *Radiat. Meas.*, In press, `http://dx.doi.org/10.1016/j.radmeas.2013.01.054`, 2013.

[157] V. I. Tretyak. Semi-empirical calculation of quenching factors for ions in scintillators. *Astropart. Phys.*, 33:40–53, 2010.

[158] J. B. Birks. Scintillations from organic crystals: specific flourescense and relative response to different radiations. *Proc. Phys. Soc. A*, 64:874–877, 1951.

[159] M. J. Berger et al. ESTAR: Stopping-power and range tables for electrons, version 1.2.3, 2005. National Institute of Standards and Technology, Gaithersburg, MD. `http://physics.nist.gov/PhysRefData/Star/Text/ESTAR.html`.

[160] J. F. Ziegler, M. D. Ziegler, and J. P. Biersack. SRIM: The stopping and range of ions in matter, version 2008.04. `http://www.srim.org`.

[161] N. Coron et al. Our short experience at IAS and within ROSEBUD with radioactive contaminations in scintillating bolometers: uses and needs. In *Radiopure Scintillators for EURECA RPScint'2008*, 2009. arXiv:0903.1539.

[162] G. Cowan. *Statistical Data Analysis.* Clarendon Press, Oxford, 1998.

[163] C. Arnaboldi et al. A novel technique of particle identification with bolometric detectors. *Astropart. Phys.*, 34:797–804, 2011.

[164] A. P. Meshik et al. Weak decay of $^{130}$Ba and $^{132}$Ba: geochemical measurements. *Phys. Rev. C*, 64(035205), 2001.

[165] P. Belli et al. Search for $2\beta$ processes in $^{64}$Zn with the help of $ZnWO_4$ crystal scintillator. *Phys. Lett. B*, 658:193–197, 2008.

[166] P. Belli et al. Radioactive contamination of $SrI_2$(Eu) crystal scintillator. *Nucl. Instrum. Meth. A*, 670:10–17, 2012.

[167] H. J. Kim. Review on neutrino-less double beta decay experiments. `http://old.apctp.org/conferences/2009/npap2009/Presentations/APCTP_NPAP2009_192_Kim.pdf`, 2009.

[168] R. B. Firestone et al. *Table of Isotopes, 8h ed.* John Wiley, New York, 1996.

[169] M. Doi and T. Kotani. Neutrinoless modes of double beta decay. *Prog. Theor. Phys.*, 89:139–159, 1993.

[170] G. J. Feldman and R. D. Cousins. Unified approach to the classical statistical analysis of small signals. *Phys. Rev. D*, 57:3873–3889, 1998.

[171] F. Salvat, J. M. Fernández-Varea, and J. Sempau. Penelope–2008: A code system for Monte Carlo simulation of electron and photon transport. Issy–les–Moulineaux, France: OECD/NEA data bank, 2008.

[172] R. Sahu and V. K. B. Kota. Deformed shell model results for two neutrino positron double beta decay of $^{84}$Sr. *Int. J. Mod. Phys. E*, 20:1723–1733, 2011.

[173] J. G. Tracy. High–purity enrichment of $^{84}$Sr. *Nucl. Instrum. Meth. A*, 438:1–6, 1999.

[174] J. D. Patterson and B. C. Bailey. *Solid-State Physics: Introduction to the Theory.* Springer, 2010.

[175] P. de Marcillac et al. Characterization of a 2 g LiF bolometer. *Nucl. Instrum. Meth. A*, 337:95–100, 1993.

[176] N. Coron et al. Scintillating and particle discrimination properties of selected crystals for low-temperature bolometers: from LiF to BGO. *Nucl. Instrum. Meth. A*, 520:159–162, 2004.

[177] J. Gironnet et al. Neutron spectroscopy with $^6$LiF bolometers. *AIP Conference Proceedings*, 1185:751–754, 2009.

[178] J. Gironnet. *Spectrométrie de neutrons rapides par bolomètres à cible lithium pour la réduction du fond des expériences de détection directe de matière noire.* PhD thesis, Université Paris Sud 11, 2010. `http://tel.archives-ouvertes.fr/tel-00633437`.

[179] C. S. Silver et al. Optimization of a $^6$LiF bolometric neutron detector. *Nucl. Instrum. Meth. A*, 485:615–623, 2002.

[180] T. Niedermayr et al. Unfolding of cryogenic neutron spectra. *Nucl. Instrum. Meth. A*, 579:165–168, 2007.

[181] M. Martínez et al. Scintillating bolometers for fast neutron spectroscopy in rare event searches. *J. Phys. Conf. Ser.*, 375(012025), 2012.

[182] J. Amaré et al. Light yield of undoped sapphire at low temperature under particle excitation. *Appl. Phys. Lett.*, 87(264102), 2005.

[183] J. Amaré et al. Recent developments on scintillating bolometers for WIMP searches: ROSEBUD status. *J. Phys. Conf. Ser.*, 39:133–135, 2006.

[184] N. Coron et al. A BGO scintillating bolometer as dark matter detector prototype. *Opt. Mater.*, 31:1393–1397, 2009.

[185] N. Coron et al. 2010 update on the ROSEBUD project. *PoS*, Identification of Dark Matter(054), 2010.

[186] D. G. Cerdeño et al. Complementarity of dark matter direct detection with bolometric targets. *J. Cosmol. Astropart. P.*, 07(028), 2013.

[187] N. Coron et al. Thermal relative efficiency factor for recoiling $^{206}$Pb nuclei in a sapphire bolometer. *Phys. Lett. B*, 659:113–118, 2008.

[188] N. Coron et al. Recent developments on scintillating bolometers for WIMP searches: ROSEBUD status. *J. Phys. Conf. Ser.*, 203(012038), 2010.

[189] M. Luca. *Sapphire scintillation tests for cryogenic detectors in the EDELWEISS dark matter search.* PhD thesis, Université Claude Bernard–Lyon 1, 2007. `http://tel.archives-ouvertes.fr/tel-00182326`.

[190] R. Bernabei et al. New results from DAMA/LIBRA and the combined results with DAMA/NaI. *Eur. Phys. J. C*, 67:39–49, 2010.

[191] S. Cebrián et al. Background model for a NaI (Tl) detector devoted to dark matter searches. *Astrop. Phys.*, 37:60–69, 2012.